



**HAL**  
open science

# X-ray absorption spectroelectrochemical studies of CO<sub>2</sub>-reducing iron porphyrins

Daniela Mendoza Franzese

► **To cite this version:**

Daniela Mendoza Franzese. X-ray absorption spectroelectrochemical studies of CO<sub>2</sub>-reducing iron porphyrins. Theoretical and/or physical chemistry. Université Paris Cité, 2022. English. NNT : 2022UNIP7075 . tel-04219351

**HAL Id: tel-04219351**

**<https://theses.hal.science/tel-04219351v1>**

Submitted on 27 Sep 2023

**HAL** is a multi-disciplinary open access archive for the deposit and dissemination of scientific research documents, whether they are published or not. The documents may come from teaching and research institutions in France or abroad, or from public or private research centers.

L'archive ouverte pluridisciplinaire **HAL**, est destinée au dépôt et à la diffusion de documents scientifiques de niveau recherche, publiés ou non, émanant des établissements d'enseignement et de recherche français ou étrangers, des laboratoires publics ou privés.

## Université Paris Cité

Ecole doctorale chimie physique et chimie analytique de Paris Centre ED 388

Laboratoire d'Electrochimie Moléculaire

---

# X-ray absorption spectroelectrochemical studies of CO<sub>2</sub>-reducing iron porphyrins

---

**Par Daniela MENDOZA-FRANZESE**

Thèse de doctorat en électrochimie moléculaire et biologique

Dirigée par Dr. Elodie ANXOLABEHERE-MALLART

Et par Prof. Marc ROBERT

Thèse présentée et soutenue publiquement le 29 mars 2022 devant un jury composé de :

Prof. Beatriz Roldan-Cuenya	PR, Fritz Haber Institute of the Max Planck Society, Germany	Rapportrice
Prof. Petra Hellwig	PR, Université de Strasbourg, France	Rapportrice
Prof. Ivana Ivanovic-Burmazovic	PR, Ludwig-Maximilians-Universität München, Germany	Examinatrice
Prof. Johannes Messinger	PR, Uppsala University Sweden	Examinateur
Dr. Elodie Anxolabéhère-Mallart	DR, Université de Paris, France	Directrice
Prof. Marc Robert	PR, Université de Paris, France	Co-directeur
<i>Membre invité</i>		
Dr. Benedikt Lassalle-Kaiser	DR, Synchrotron SOLEIL, France	Co-encadrant



## Abstract

---

*The atmospheric level of greenhouse gases, in particular carbon dioxide (CO<sub>2</sub>), has considerably increased in recent decades, leading to unprecedented changes in the climate. The electrochemical reduction of CO<sub>2</sub> into chemical building blocks or fuels is a promising strategy to recycle this gas, while mitigating its emission. However, this process is energetically demanding, requiring the use of catalysts. Only a few of them are currently known, which can perform this reaction in a controlled, selective, and efficient manner. Among homogeneous catalysts, iron porphyrins have shown some of the highest activities and stability. Thanks to the tunability of their structure, the performance of these catalysts has been improved both in organic and in aqueous solutions. Because they are based on earth-abundant elements, iron porphyrins are a promising class of materials for above-mentioned CO<sub>2</sub> conversion processes. However, to direct the CO<sub>2</sub> reduction reaction towards products of high value, a fundamental understanding of the reaction mechanism is essential.*

*The mechanism of the CO<sub>2</sub>-to-CO electrochemical reduction by iron porphyrins have been investigated since the 90's, mostly by electrochemical techniques. The structural and electronic characterization of the reaction intermediates involved in the reaction is, however, still missing. Providing such information would allow defining strategies to optimize the catalyst and/or orient the reaction towards specific products. To do so, spectroscopic measurements need to be performed in conditions relevant to electrocatalytic activity, which requires the development of specific instrumentation. These data will allow a correlation between kinetic (electrochemical) and structural (spectroscopic) information, strengthening the understanding of the catalytic mechanism.*

*The present project aims at answering, at least partially, to the above-mentioned challenges, by applying advanced spectroelectrochemical methods for the study of iron porphyrins during the electrocatalytic reduction of CO<sub>2</sub> into CO. We have use UV-Visible as well as synchrotron-based X-ray absorption spectroscopy as a main tool for our study. Specific spectroelectrochemical cells and data collection strategies were developed to analyze samples in organic solvents under applied electrochemical potential and under electrocatalytic conditions. Using these techniques, we determined the oxidation state and geometry of reduced iron porphyrins species under argon and CO<sub>2</sub> atmospheres. As a major result, we could show that CO<sub>2</sub> does interact with a reduced form of the iron porphyrin through a bond with the central iron. In light of these results, we propose electronic structures for key intermediates along the CO<sub>2</sub>-to-CO reduction reaction catalytic cycle.*

**Keywords:** Spectroelectrochemistry, iron porphyrins, CO<sub>2</sub> reduction; electronic structure; reaction intermediates; homogeneous catalysis; reaction mechanism





## Résumé

---

*Le niveau atmosphérique de gaz à effet de serre, en particulier du dioxyde de carbone (CO<sub>2</sub>), a considérablement augmenté au cours des dernières décennies, entraînant des changements climatiques sans précédent. La réduction électrochimique du CO<sub>2</sub> en composés chimiques ou en carburants est une stratégie prometteuse pour recycler ce gaz, tout en atténuant ses émissions. Cependant, le coût énergétique de ce procédé est élevée et nécessite l'utilisation de catalyseurs. Il n'en existe aujourd'hui que très peu qui soient capables de réaliser cette réaction de manière contrôlée, sélective et efficace. Parmi les catalyseurs homogènes, les porphyrines de fer ont montré une activité et une stabilité parmi les plus élevées. Grâce à la possibilité de modifier synthétiquement leurs structures, les performances de ces catalyseurs ont été améliorées tant en solutions organiques qu'en solutions aqueuses. Parce qu'elles sont basées sur des éléments abondants, les porphyrines de fer constituent une classe de matériaux prometteurs pour la conversion du CO<sub>2</sub> en CO. Cependant, pour orienter la réaction de réduction du CO<sub>2</sub> vers des produits à haute valeur-ajoutée, une compréhension fondamentale du mécanisme de la réaction est essentielle.*

*Le mécanisme de la réduction électrochimique du CO<sub>2</sub> en CO par les porphyrines de fer a été étudié depuis les années 90, principalement par des techniques électrochimiques. La caractérisation structurelle et électronique des intermédiaires réactionnels impliqués dans la réaction fait cependant toujours défaut. Fournir de telles informations permettrait de l'optimiser et/ou l'orienter vers des produits spécifiques. Pour ce faire, des mesures spectroscopiques doivent être réalisées dans des conditions électrocatalytique, ce qui nécessite une instrumentation spécifique. Ces données permettront une corrélation entre les informations cinétiques et structurelles, renforçant ainsi la compréhension du mécanisme catalytique.*

*Le présent projet vise à collecter ce type de données, en appliquant des méthodes spectroélectrochimiques avancées pour l'étude des porphyrines de fer au cours de la réduction électrocatalytique de réduction du CO<sub>2</sub> en CO. Nous avons utilisé les spectroscopies d'absorption UV-Visible et d'absorption des rayons X comme outils principaux pour notre étude. Des cellules spectroélectrochimiques et des stratégies de collecte de données spécifiques ont été développées pour analyser des échantillons en solutions dans des solvants organiques et en conditions électrochimiques. Grâce à ces techniques, nous avons déterminé le degré d'oxydation et la géométrie des espèces de porphyrines de fer réduites sous argon et sous CO<sub>2</sub>. Un résultat majeur est la mise en évidence d'une liaison entre le CO<sub>2</sub> et l'atome métallique d'une forme réduite de la porphyrine de fer. À la lumière de ces résultats, nous proposons des structures électroniques pour les intermédiaires clés du cycle catalytique de la réaction de réduction du CO<sub>2</sub> en CO.*

**Mots clefs :** Spectroélectrochimie ; porphyrines de fer ; réduction du CO<sub>2</sub> ; structure électronique ; intermédiaires de réaction ; catalyse homogène ; mécanisme de réaction



*“Nothing in life is to be feared, it is only to be understood.  
Now is the time to understand more, so that we may fear less.”*

---

- Marie Skłodowska Curie -



# Acknowledgements

---

*The present thesis could have not been possible without the financing granted by the Michem Labex and the Synchrotron SOLEIL.*

*I would like to express my gratitude to Dr. Jean Daillant, general director of Synchrotron SOLEIL, for hosting me in this synchrotron facilities. I acknowledged the peer-review committees of synchrotron SOLEIL for the beamline allocations.*

*I thank Dr. Elodie Anxolabéhère-Mallart not only for her mentorship and advices during these more than three years, but also for coupling that to her direction at LEM.*

*I would like to thank the members of the committee for their interest in this work. I am grateful to Prof. Beatriz Roldan-Cuenya and Prof. Petra Hellwig for reviewing this thesis as well as to Prof. Ivana Ivanovic and Prof. Johannes Messinger for their remarks and comments.*

*I would like to express my gratitude to Prof. Marc Robert for always believing in my capacities, for offering me this opportunity and for his lessons. I am extremely grateful to Dr. Benedikt Lassalle-Kaiser for all the scientific discussions, for encouraging and guiding me during all this time, but especially for his trust and faith.*

*I am grateful to all the members of the REACTE team of the Laboratoire d'Electrochimie Moléculaire, especially to Orestes, Etienne, Nikos, Niklas, Simon and Julian for their great contribution to the development of this project, but more importantly for the personal support and friendship during all this time. I thank all the LEM members for the administrative and scientific guidance during my project.*

*I would like to thank all the LUCIA beamline members for welcoming me as a part of the team. Special thanks to Dr. Delphine Vantelon for the in house allocated sessions. I also thank SAMBA beamline scientists, especially Dr. Andrea Zitolo and M. Guillaume Alizon, for all the engineering and scientific support. I would like to express my gratitude to the AILES beamline team, especially M. Jean-Blaise Brubach for your unconditional support and scientific discussions.*

*I am thankful to Mr. Victor Pinty of the mechanical engineering group, Dr. Kelly Rader of AILES beamline, M. Baptiste Maurice and M. Stephane Lefrancois of the microfluidic laboratory of Synchrotron SOLEIL, for the design, construction and support in the development of the spectroelectrochemical setups.*

*Last but not least, I would like to thank my family members and friends. I warmly thank Geny for always being there and encouraging me, Melanie for opening the doors of your home, Dilan for your unconditional support, Laura for all your help during the writing of this thesis, Jeni for being the best sister I could have asked for, Carmelina for bringing peace to my mind, my now angel tío Charles, thanks for giving me light in the darkest, I will always miss you.*

*I dedicate this to my parents, for always believing in myself, for your words, love, for encouraging me every day and being close to my heart even if an entire Ocean separates us. Gracias papá por ser mi ángel en la Tierra, por tu fuerza, por seguir aquí...*



# Table of contents

---

<b>List of figures</b> .....	xv
<b>List of schemes</b> .....	xix
<b>List of tables</b> .....	xxi
<b>List of structures</b> .....	xxii
<b>Notations and abbreviations</b> .....	xxiii
<b>Chapter I – General introduction</b> .....	<b>1</b>
1.1 Carbon dioxide (CO <sub>2</sub> ) reduction: from the macro to the atomic scale .....	3
1.2 Outline .....	4
1.3 References .....	6
<b>Chapter II – Introduction: electrochemical activation of CO<sub>2</sub> by iron porphyrins</b> .....	<b>7</b>
2.1 Catalysts are needed for the CO <sub>2</sub> reduction .....	10
2.2 Iron porphyrin as a 2e <sup>-</sup> CO <sub>2</sub> reducing molecular catalyst .....	12
2.2.1 Electrochemistry of iron porphyrins – no substrate .....	13
2.2.2 Electrochemical activation of CO <sub>2</sub> by iron porphyrins .....	14
2.2.3 Enhanced catalysis .....	17
2.3 Epilogue and next chapter outlook .....	19
2.4 References .....	21
<b>Chapter III – Introduction: X-ray absorption spectroelectrochemistry</b> .....	<b>25</b>
3.1 In situ spectroelectrochemical methods to study CO <sub>2</sub> reducing reactions .....	28
3.2 X-Ray Absorption spectroscopy (XAS) .....	29
3.2.1 Origin, description and useful terminology .....	29
3.2.2 What can we learn from a XAS spectrum? .....	30
3.2.3 Advantages and limitations .....	32
3.3 X-ray absorption spectroelectrochemistry as a tool for the study of CO <sub>2</sub> reducing molecular catalysts .....	33
3.4 References .....	35
<b>Chapter IV – Spectroscopic studies of the CO<sub>2</sub> reduction mechanism by iron porphyrins</b> .....	<b>41</b>
4.1 Electronic configuration and structures of iron porphyrins .....	43
4.1.1 Iron(III) porphyrins (d <sup>5</sup> ) .....	43



4.1.2 Iron(II) porphyrins (d <sup>6</sup> ) .....	45
4.1.3 Iron(I) porphyrins (d <sup>7</sup> ) .....	49
4.1.4 Iron(0) porphyrins (d <sup>8</sup> ) .....	50
4.1.5 Controversy in the electronic structure of highly reduced iron porphyrins .....	51
4.2 Spectroscopic characterization of adducts between CO <sub>2</sub> and iron porphyrins .....	52
4.2.1 Coordination chemistry of CO <sub>2</sub> .....	52
4.2.2 Theoretical calculation on the stabilization of the CO <sub>2</sub> -coordinated adduct .....	54
4.2.3 <i>Ex-situ</i> Raman spectroscopic measurements .....	54
4.2.4 <i>In situ</i> and <i>operando</i> spectroelectrochemical measurements .....	55
4.3 Spectroscopic characterization on the interaction between the CO and the iron center .....	57
4.3.1 Infrared spectroscopy .....	57
4.3.2 X-Ray absorption spectroscopy.....	58
4.3.3 UV-Vis spectroscopy .....	58
4.4 Outlook .....	59
4.5 References .....	61
<b>Chapter V – X-Ray Absorption Spectroelectrochemistry: instrumentation .....</b>	<b>65</b>
5.1 State of the art.....	67
5.1.1 Molecular catalyst immobilized in high surface area electrodes .....	67
5.1.2 Molecular catalysts in solution .....	68
5.2 Cell used during this thesis project .....	70
5.3 Cell parameters .....	71
5.3.1 Technical considerations .....	71
5.3.2 Spectroscopic parameters .....	74
5.3.3 Electrochemical parameters .....	75
5.4 Conclusion .....	77
5.5 References .....	78
<b>Chapter VI – Results and discussion: Insights in the understanding of the electronic structure of reduced [Fe<sup>III</sup>(TPP)]Cl species by spectroelectrochemical methods .....</b>	<b>81</b>
6.1 Iron porphyrin analysis at the Fe(III) state .....	83
6.1.1 Ring substituents effect .....	83
6.1.2 Solvent effect.....	85
6.2 <i>In situ</i> spectroelectrochemical measurements on reduced species of [Fe <sup>III</sup> (TPP)]Cl in an inert atmosphere .....	92

6.2.1 One electron reduction process: $[\text{Fe}^{\text{III}}(\text{TPP})]\text{Cl} + 1\text{e}^-$ .....	94
6.2.2 Two electron reduction process: $[\text{Fe}^{\text{III}}(\text{TPP})]\text{Cl} + 2\text{e}^-$ .....	98
6.2.3 Three electron reduction process: $[\text{Fe}^{\text{III}}(\text{TPP})]\text{Cl} + 3\text{e}^-$ .....	100
6.3 Summary and discussion .....	103
6.4 References .....	107
<b>Chapter VII – Structural and electronic changes in <math>[\text{Fe}^{\text{III}}(\text{TPP})]\text{Cl}</math> and its reduced states under <math>\text{CO}_2</math></b> .....	<b>109</b>
7.1 $[\text{Fe}^{\text{III}}(\text{TPP})]\text{Cl}$ analysis in the presence of $\text{CO}_2$ .....	111
7.2 <i>In situ</i> spectroelectrochemical measurements on reduced species of $[\text{Fe}^{\text{III}}(\text{TPP})]\text{Cl}$ in $\text{CO}_2$ atmosphere .....	114
7.2.1 One electron reduction process: $[\text{Fe}^{\text{III}}(\text{TPP})]\text{Cl} + 1\text{e}^-$ .....	114
7.2.2 Two electron reduction process: $[\text{Fe}^{\text{III}}(\text{TPP})]\text{Cl} + 2\text{e}^-$ .....	116
7.2.3 Three electron reduction process: $[\text{Fe}^{\text{III}}(\text{TPP})]\text{Cl} + 3\text{e}^-$ .....	120
7.3 Identification of $[\text{Fe}^{\text{II}}(\text{TPP})(\text{CO})]$ adduct .....	123
7.4 Discussion .....	125
7.5 References .....	127
<b>Chapter VIII – Conclusions and perspective</b> .....	<b>129</b>
8.1 Key findings .....	131
8.2 Perspectives .....	138
8.3 Final outlook .....	140
8.4 References .....	142
<b>Appendixes</b> .....	<b>145</b>
A. <i>Electrochemical experiments</i> .....	145
A.1 Cyclic voltammetry .....	147
A.2 Control potential electrolysis .....	147
A.3 Setting up an experiment .....	148
A.3.1 Electrodes .....	148
A.3.2 Solvent .....	148
A.3.3 Supporting electrolyte .....	149
A.4 Accessing to kinetic information .....	149
A.5 References .....	153
B. <i>X-Ray Absorption Spectroscopy</i> .....	155
B.1 XAS physical principles .....	157

B.2 Synchrotron radiation sources .....	160
B.2.1 Beamlines components .....	160
B.3 Synchrotron SOLEIL .....	163
B.3.1 General descriptions of the beamlines of SOLEIL used for this thesis .....	164
B.4 How to start a synchrotron-based experiment? .....	167
B.5 References .....	169
<i>C. Instrumentation and materials</i> .....	171
C.1 Materials .....	173
C.2 Instrumentation and experimental details .....	174
C.2.1 Electrochemical measurements .....	174
C.2.2 X-Ray Absorption spectroscopy .....	175
C.2.3 UV-Vis spectroscopy .....	177
C.2.4 Infrared spectroscopy .....	178
C.3 Sample preparation .....	179
C.3.1 Spectro(electro)chemical catalysts samples .....	179
C.3.2 Other samples .....	179
C.3.3 Synthesis .....	180
C.3.3.1 Catalyst preparation .....	180
C.3.3.2 Chemical reduction .....	181
C.4 References .....	184
<i>D. Spectroelectrochemical cells</i> .....	185
D.1 X-Ray Absorption (XAS) .....	187
D.1.1 Cell A .....	187
D.1.2 Cell B .....	191
D.2 Ultraviolet-Visible .....	195
D.3 Reflectance infrared <i>in situ</i> spectroelectrochemical cell .....	196
D.3.1 Constraints .....	196
D.3.2 A vacuum-chamber compatible cell .....	197
D.4 References .....	200
<b>French summary</b> .....	<b>202</b>
<b>Publications</b> .....	<b>220</b>

# List of figures

---

2.1. Catalytic Tafel Plot [TOF = f ( $\eta$ )] .....	11
2.2. CV for the molecular catalysis of a one-electron catalytic reaction .....	12
2.3. a. Structure [Fe <sup>III</sup> (TPP)]Cl .....	14
2.3. b. CV [Fe <sup>III</sup> (TPP)]Cl in DMF + 0.1 M TBAPF <sub>6</sub> under Ar .....	14
2.3. c. Reversible reactions occurring during electroreduction of CO <sub>2</sub> by [Fe <sup>III</sup> (TPP)]Cl .....	14
2.4. CV [Fe <sup>III</sup> (TPP)]Cl in DMF + 0.1 M TBAPF <sub>6</sub> under CO <sub>2</sub> .....	14
2.5. CV [Fe <sup>III</sup> (TPP)]Cl in DMF + 0.1 M TBAPF <sub>6</sub> under CO <sub>2</sub> + 5 mM phenol and under CO.....	17
3.1. a. Illustration of an XAS spectrum .....	32
3.1. b. Energy diagram for a hypothetical transition metal complex indicating the transitions that give rise to each part of an XAS spectrum .....	32
4.1. UV-Vis absorption spectrum of [Fe <sup>III</sup> (TPP)]Cl in DMF under Ar at room temperature.....	44
4.2. <i>Ex situ</i> Fe K-edge XANES spectra of iron(II) tetraphenyl porphyrin with different axial ligands and spin states.....	45
4.3. UV-Vis absorption spectrum of [Fe <sup>II</sup> (TPP)] in DMF + 0.1 M TEAP under Ar at room temperature.....	47
4.4. UV-Vis absorption spectrum of [(Fe <sup>III</sup> (TPP)) <sub>2</sub> O] in DMF + 0.1 M TEAP under Ar at room temperature .....	48
4.5. a. CV electrochemically prepared [(Fe <sup>III</sup> (TPP)) <sub>2</sub> O] in DMF + 0.1 M TBAPF <sub>6</sub> under Ar .....	49
4.5. b. UV-Vis absorption spectrum of [(Fe <sup>III</sup> (TPP)) <sub>2</sub> O] in DMSO + 0.1 M TEAP under Ar at room temperature.....	49
4.6. Fe K-edge XANES spectra of [Fe <sup>III</sup> (TPP)]Cl and its reduced species in the solid state .....	51
4.7. Binding modes of CO <sub>2</sub> to a metal center .....	53
4.8. a. Structure of [Fe(F <sub>20</sub> TPP)] .....	57
4.8. b. In situ – operando Fe K-edge XANES spectra of immobilized [Fe(F <sub>20</sub> TPP)] on carbon electrodes recorded at open circuit potential and t -0.6 V vs. RHE with comparison with reference iron samples .....	57
4.8. c. Zoom to the half edge jump position of figure 4.8 – a. ....	57
4.8. d. Zoom to the pre-edge region of figure 4.8 – a. ....	57
4.9. UV-Vis absorption spectrum of the [Fe <sup>II</sup> (TPP)(CO)] adduct .....	59

5.1. CV comparison of [Fe <sup>III</sup> (TPP)]Cl in DMF + 0.1 M TBAPF <sub>6</sub> recorded in cell A at room atmosphere and while having inert conditions around the cell .....	73
5.2. Fe K-edge XANES spectra of [Fe <sup>III</sup> (TPP)]Cl in the solid state with a beam size 50 x 100 μm at different irradiation times .....	75
5.3. Fe K-edge XANES spectra of Fe <sup>III</sup> Cl <sub>3</sub> .6H <sub>2</sub> O and Fe <sup>II</sup> Cl <sub>2</sub> in DMF + 0.1 M TBAPF <sub>6</sub> and while applying a CPE at -0.6 V vs Ag/Ag <sup>+</sup> to the initial Fe <sup>III</sup> Cl <sub>3</sub> .6H <sub>2</sub> O sample. Insert – CV of Fe <sup>III</sup> Cl <sub>3</sub> .6H <sub>2</sub> O in DMF + 0.1 M TBAPF <sub>6</sub> under Ar at a scan rate of 100 mV s <sup>-1</sup> .....	77
6.1. Fe K-edge XANES spectra of [Fe <sup>III</sup> (TPPS)]Cl, [Fe <sup>III</sup> (TPP)]Cl and [Fe <sup>III</sup> (-p-TMA)]Cl in the solid state .....	84
6.2. Fe K-edge XANES spectra of [Fe <sup>III</sup> (TPPS)]Cl in the solid state and in DMF.....	86
6.3. Fe K-edge XANES spectra of [Fe <sup>III</sup> (TPPS)]Cl in aqueous buffered solution as a function of the pH.....	88
6.4. a. Pre-edge peak intensity as a function of the pH for the [Fe <sup>III</sup> (TPPS)]Cl in aqueous buffered solution .....	88
6.4. b. Main edge energy position as a function of the pH for the [Fe <sup>III</sup> (TPPS)]Cl in aqueous buffered solution .....	88
6.5. UV-Vis spectra of the [Fe <sup>III</sup> (TPPS)]Cl in aqueous buffered solution as a function of the pH	89
6.6. Fe K-edge XANES spectra of [Fe <sup>III</sup> (TPP)]Cl in solid state and in DMF + 0.1 M TBAPF <sub>6</sub> under Ar (complex <i>I</i> ).....	92
6.7. CV [Fe <sup>III</sup> (TPP)]Cl in DMF + 0.1 M TBAPF <sub>6</sub> under Ar recorded in cell A under a vacuum of 10 <sup>-2</sup> mbar on the LUCIA Beamline at Synchrotron SOLEIL .....	93
6.8. Fe K-edge XANES spectra of complex <i>I</i> and its one-electron reduction species (complex <i>2a</i> ) generated by performing a CPE at $E = -0.8$ V vs Ag/Ag <sup>+</sup> in DMF + 0.1 M TBAPF <sub>6</sub> under Ar ....	94
6.9. UV-Vis spectral evolution from complex <i>I</i> to complex <i>2a</i> .....	95
6.10. Fe K-edge XANES spectra of complex <i>I</i> and complex <i>2b</i> , generated by chemical reduction .....	96
6.11. Fe K-edge XANES spectra comparison of complexes <i>2a</i> , <i>2b</i> and <i>2c</i> .....	97
6.12. Fe K-edge XANES spectra comparison of complexes <i>I</i> , <i>2a</i> and the doubly reduced species (complex <i>3</i> ) generated by performing a CPE at $E = -1.6$ V vs Ag/Ag <sup>+</sup> in DMF + 0.1 M TBAPF <sub>6</sub> under Ar .....	99
6.13. UV-Vis spectral evolution from complex <i>2a</i> to complex <i>3</i> .....	100
6.14. Fe K-edge XANES spectra comparison of complexes <i>I</i> , <i>2a</i> , <i>3</i> and the triply reduced species (complex <i>4</i> ) generated by performing a CPE at $E = -2.0$ V vs Ag/Ag <sup>+</sup> in DMF + 0.1 M TBAPF <sub>6</sub> under Ar .....	101
6.15. UV-Vis spectral evolution from complex <i>3</i> to complex <i>4</i> .....	102
6.16. Fe K-edge XANES spectra comparison of complexes <i>2a</i> , <i>3</i> and <i>4</i> with the spectrum of a metallic iron sample and of Fe <sup>III</sup> O(OH).NH <sub>2</sub> O oxide .....	103

6.17. UV-Vis profile of complexes <b>1</b> , <b>2a</b> , <b>3</b> and <b>4</b> generated <i>in situ</i> by spectroelectrochemical methods in DMF + 0.1 M TBAPF <sub>6</sub> under Ar .....	105
7.1. Fe K-edge XANES spectra of [Fe <sup>III</sup> (TPP)]Cl in DMF + 0.1 M TBAPF <sub>6</sub> under CO <sub>2</sub> atmosphere (complex <b>5</b> ).....	112
7.2. CV [Fe <sup>III</sup> (TPP)]Cl in DMF + 0.1 M TBAPF <sub>6</sub> under Ar and under CO <sub>2</sub> recorded in cell A under a vacuum of 10 <sup>-2</sup> mbar on the LUCIA Beamline at Synchrotron SOLEIL .....	113
7.3. Fe K-edge XANES spectra of [Fe <sup>III</sup> (TPP)]Cl in DMF + 0.1 M TBAPF <sub>6</sub> under Ar (complex <b>2a</b> ) and under CO <sub>2</sub> (complex <b>6</b> ).....	114
7.4. UV-Vis spectral evolution from complex <b>5</b> to <b>6</b> .....	116
7.5. Fe K-edge XANES comparative spectra of complexes <b>5</b> , <b>6</b> and <b>7</b> .....	117
7.6. Fe K-edge XANES spectra of [Fe <sup>III</sup> (TPP)]Cl + 2e <sup>-</sup> in DMF + 0.1 M TBAPF <sub>6</sub> under Ar (complex <b>3</b> ) and under CO <sub>2</sub> (complex <b>7</b> ) .....	118
7.7. UV-Vis spectral evolution from complex <b>6</b> to <b>7</b> .....	119
7.8. UV-Vis spectra comparison between the 2e <sup>-</sup> reduced species under argon (complex <b>6</b> ) and under CO <sub>2</sub> (complex <b>7</b> ) .....	119
7.9. Fe K-edge XANES spectra of [Fe <sup>III</sup> (TPP)]Cl + 3e <sup>-</sup> in DMF + 0.1 M TBAPF <sub>6</sub> under Ar (complex <b>4</b> ) and under CO <sub>2</sub> (complex <b>8</b> ) .....	120
7.10. Fe K-edge XANES spectra of [Fe <sup>III</sup> (TPP)]Cl + ne <sup>-</sup> (n = 0, 1, 2, 3) in DMF + 0.1 M TBAPF <sub>6</sub> under CO <sub>2</sub> .....	121
7.11. UV-Vis spectral evolution from complex <b>7</b> to <b>8</b> .....	122
7.12. UV-Vis spectra comparison between the 3e <sup>-</sup> reduced species under argon (complex <b>4</b> ) and under CO <sub>2</sub> (complex <b>8</b> ) .....	123
7.13. UV-Vis spectra of <b>8</b> and <b>9</b> .....	124
7.14. Mid-IR spectra of <b>8</b> and <b>9</b> .....	125
B.1. a. <i>k</i> -space representation for [Fe <sup>III</sup> (TPP)]Cl in the solid state recorded in transmission mode on the LUCIA beamline at Synchrotron SOLEIL .....	159
B.1. b. In-phase and out-phase interferences obtained for the same system .....	159
B.1. c. Fourier transform signal of the k-space - EXAFS .....	159
B.2. Aerial and internal views of the synchrotron SOLEIL .....	163
B.3. Beamlines at the Synchrotron SOLEIL classified by energy range .....	164
B.4. AILES beamline .....	165
B.5. LUCIA beamline.....	166
B.6. SAMBA beamline .....	167
C.1. Representation of the heart-shaped electrochemical cell used for CV experiments .....	174

C.2. CV of [Fe <sup>III</sup> (TPP)]Cl in DMF + 0.1 M TBAPF <sub>6</sub> under Ar, under CO <sub>2</sub> and under CO <sub>2</sub> after drying the catalysts and the electrolyte .....	175
C.3. Comparative first derivative spectra for 2 mM solution [Fe <sup>III</sup> (TPP)]Cl in DMF + 0.1 M TBAPF <sub>6</sub> under argon as raw data and after smothering .....	176
C.4. Determination of the pre-edge peak energy position in this manuscript .....	177
C.5. Photograph of the top view of the IR spectroelectrochemical cell in the AILES beamline station showing the beam path of the reflectance configuration .....	178
C.6 UV-Vis Q-bands of a 2 mM solution of [Fe <sup>III</sup> (TPP)]Cl and chemically generated [Fe <sup>II</sup> (TPP)] in DMF under Ar .....	182
C.6. CV of chemically prepared [Fe <sup>II</sup> (TPP)] in DMF + 0.1 M TBAPF <sub>6</sub> under Ar .....	182
D.1. Photographs of cell A installed on the LUCIA beamline .....	189
D.2. Fe K-edge spectra comparison of 20 mM solution [Fe <sup>III</sup> (TPPS)]Cl + 0.1 M KCl recorded in cell A using transmission and fluorescence mode .....	191
D.3. Photographs of cell B installed on the SAMBA beamline .....	194
D.4. CV [Fe <sup>III</sup> (TPP)]Cl in DMF + 0.1 M TBAPF <sub>6</sub> under Ar and under CO atmosphere .....	195
D.5. Photograph of the IR cell installed in the AILES-C beamline showing the flowing system indications .....	197

# List of schemes

---

2.1. Metal complexes based on Ni, Co and Fe used as molecular catalyst for $2e^-$ $\text{CO}_2\text{RR}$ .....	9
2.2. Iron protoporphyrin structure .....	13
2.3. Proposed mechanism for the electrocatalytic reduction $\text{CO}_2$ to $\text{CO}$ by $[\text{Fe}^{\text{III}}(\text{TPP})]\text{Cl}$ .....	15
2.4. $\text{Fe-CO}_2$ proposed adduct with the CAT catalyst .....	18
2.5. CAT and FCAT catalysts structures .....	19
2.6. $\text{Fe-o-TMA}$ structure and $\text{Fe-CO}_2$ proposed stabilization.....	19
3.1. Physical phenomena occurring during electron excitation by X-rays .....	30
4.1. a. Structure of $S = 5/2$ high spin $[\text{Fe}^{\text{III}}(\text{TPP})]\text{Cl}$ .....	44
4.1. b. Simplified d-orbital splitting representation for $[\text{Fe}^{\text{III}}(\text{TPP})]\text{Cl}$ .....	44
4.2. a. Structure and simplified d-orbital splitting of $S = 2$ high spin $[\text{Fe}^{\text{II}}(\text{TPP})(\text{THF})_2]$ .....	46
4.2. b. Structure and simplified d-orbital splitting of $S = 1$ intermediate spin $[\text{Fe}^{\text{II}}(\text{TPP})]$ .....	46
4.2. c. Structure and simplified d-orbital splitting of $S = 0$ low spin $[\text{Fe}^{\text{II}}(\text{TPP})(\text{Py})_2]$ .....	46
4.3. Structure of $[(\text{Fe}^{\text{III}}(\text{TPP}))_2\text{O}]$ .....	47
4.4. a. Structure of $S = 1/2$ low spin $[\text{Fe}^{\text{I}}(\text{TPP})]^-$ .....	50
4.4. b. Simplified d-orbital splitting of $S = 1/2$ low spin $[\text{Fe}^{\text{I}}(\text{TPP})]^-$ .....	50
4.5. a. Structure of $S = 0$ low spin $[\text{Fe}^0(\text{TPP})]^{2-}$ .....	50
4.5. b. Simplified d-orbital splitting of $S = 0$ low spin $[\text{Fe}^0(\text{TPP})]^{2-}$ .....	50
4.6. Molecular orbital diagram of $\text{CO}_2$ .....	53
4.7. a. Structure of substituted iron tetraphenyl porphyrin bearing hydroxyl groups in the phenyl moieties on the ring .....	54
4.7. b. Lateral view of the optimized structure of the $\text{Fe-CO}_2$ adduct obtained by DFT .....	54
4.8. Proposed reaction intermediates in the chemical reduction of an iron porphyrin in the presence of $\text{CO}_2$ obtained by <i>ex situ</i> Raman spectroscopy.....	55
5.1. Spectroelectrochemical XAS setup generally used for the study of immobilized molecular catalysts on high surface area working electrodes .....	68
5.2. Representation of a thin layer spectroelectrochemical flow cell .....	70
5.3. Cell used during the project – Cell A .....	71
5.4. Sample delivery system to the cell in the experimental station .....	73



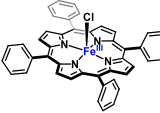
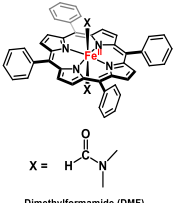
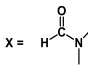
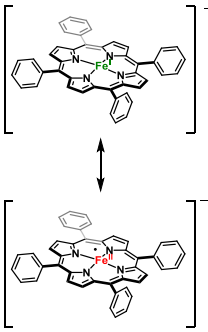
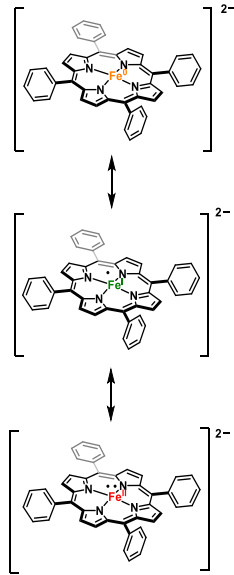
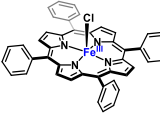
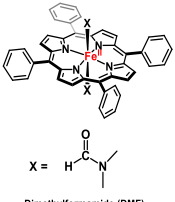
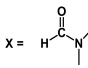
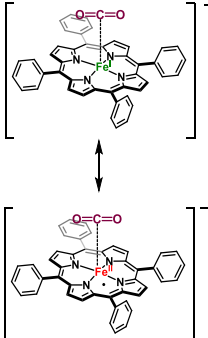
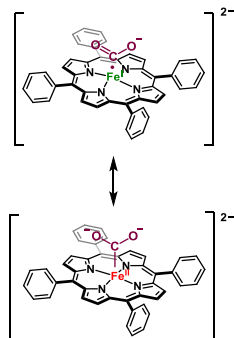
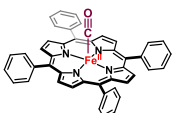
6.1. a. Structure of [Fe <sup>III</sup> (TPPS)]Cl .....	84
6.1. b. Structure of [Fe <sup>III</sup> (TPP)]Cl .....	84
6.1. c. Structure of [Fe <sup>III</sup> (-p-TMA)]Cl .....	84
6.2. a. Proposed structure of [Fe <sup>III</sup> (TPPS)]Cl in DMF .....	87
6.2. b. Proposed structure of [Fe <sup>III</sup> (TPPS)]Cl in water.....	87
6.3. Proposed structures of [Fe <sup>III</sup> (TPPS)]Cl as a function of the pH in aqueous media.....	91
6.4. Proposed structure of [Fe <sup>III</sup> (TPP)]Cl in DMF + 0.1 TBAPF <sub>6</sub> (complex <i>I</i> ).....	93
6.5. Proposed structures of complexes <i>2a</i> and <i>2b</i> .....	98
6.6. Formal representation of proposed structures for complexes <i>3</i> and <i>4</i> .....	106
7.1. Proposed structure of [Fe <sup>III</sup> (TPP)]Cl in DMF + 0.1 TBAPF <sub>6</sub> under CO <sub>2</sub> (complex <i>5</i> ) .....	112
7.2. Proposed structure of complex <i>6</i> .....	115
8.1. Proposed mechanism for the electrocatalytic reduction CO <sub>2</sub> to CO by [Fe <sup>III</sup> (TPP)]Cl based on electrochemical evidence .....	136
8.2. Simplified mechanism for the electrocatalytic reduction of CO <sub>2</sub> into CO by [Fe <sup>III</sup> (TPP)]Cl based on spectroelectrochemical evidence presented in the manuscript.....	137
A.1. Kinetic zone diagram with simulated CV forms .....	150
B.1. General synchrotron scheme .....	160
B.2. General beamline scheme.....	161
B.3. Representation of the two different detection modes usually used in hard XAS .....	162
D.1. Vacuum compatible XAS cell A: PEEK cell body and liquid feedthrough.....	188
D.2. Spectroelectrochemical cell B.....	192
D.3. “CO box” components .....	192
D.4. Gas flowing system for the “CO box” .....	193
D.5. Liquid circulation system for the “CO box” .....	194
D.6. UV-Vis spectroelectrochemical cell .....	196
D.7. Vacuum compatible IR spectroelectrochemical cell for reflectance measurements .....	198
D.8. Parts of the IR spectroelectrochemical cell .....	199

# List of tables

---

4.1. Experimental conditions and UV-Vis signatures obtained by Lu <i>et al.</i> ....	56
6.1. Main edge energy position for the Fe(III) porphyrins in the solid state .....	85
6.2. Main edge energy position for the [Fe <sup>III</sup> (TPPS)]Cl in different experimental conditions .....	86
6.3. Soret and Q-bands wavelength values of [Fe <sup>III</sup> (TPPS)]Cl in aqueous buffered solution as a function of the pH .....	90
6.4. Pre-edge peak and main energy position for [Fe <sup>III</sup> (TPP)]Cl in different experimental conditions .....	93
6.5. Pre-edge peak and main energy position for <b>2a</b> , <b>2b</b> and <b>2c</b> obtained in various experimental conditions .....	98
6.6. Comparison of the pre-edge peak and main energy position for <b>1</b> , <b>2a</b> , <b>2b</b> , <b>3</b> and <b>4</b> .....	104
6.7. UV-Vis Soret and Q-bands values observed in this work for complex <b>1</b> to <b>4</b> in DMF + 0.1 TBAPF <sub>6</sub> and comparison with reported values in the literature .....	105
7.1. Pre-edge peak and main edge energy position for <b>1</b> and <b>5</b> .....	112
7.2. Pre-edge peak and main edge energy position for <b>2a</b> and <b>6</b> .....	115
7.3. Summary of the pre-edge peak and main edge energy position values for <b>1</b> to <b>8</b> .....	121
8.1. Summary of the proposed structures, XANES and UV-Vis data for complexes <b>1</b> to <b>4</b> .....	133
8.2. Summary of the proposed structures, XANES and UV-Vis data for complexes <b>5</b> to <b>9</b> .....	135
C.1. Concentrations required for sample preparation .....	179
D.1. O-ring material resistance on DMF and vacuum .....	190

# List of structures

	electrons transferred	-	1e <sup>-</sup>	2e <sup>-</sup>	3e <sup>-</sup>
Gas used	Argon	<b>1</b> 	<b>2a</b>  X =  Dimethylformamide (DMF)	<b>3</b> 	<b>4</b> 
	CO <sub>2</sub>	<b>5</b> 	<b>6</b>  X =  Dimethylformamide (DMF)	<b>7</b> 	<b>8</b> 
	CO		<b>9</b> 		

# Notations

---

$\eta$	Overpotential	$e^-$	Electron
$k_{cat}$	Kinetic rate constant	V	Potential
$v$	Scan rate	R	Ideal gas constant
$q$	Charge	T	Temperature
$\gamma$	Excess factor	F	Faradaic constant
$\lambda$	Kinetic parameter	C	Concentration
$C_A^\circ$	Concentration of the substrate	eV	Electronvolts
$C_P^\circ$	Concentration of the catalyst	Dp	Diffusion coefficient
$\varepsilon$	Molar extinction coefficient	S	Working electrode surface
$\lambda$	Wavelength	$I_T$	Intensity after irradiation
$i$	Current	$I_0$	Intensity of the incident radiation
$\mu$	Linear absorption coefficient	d	Thickness of the sample
$c$	Speed of light		
$h$	Planck's constant		
$m_e$	Mass of the electron		
$E$	Applied potential		

# Abbreviations

---

AH	Weak acid
AILES	Advanced Infrared Line Exploited for Spectroscopy Scan rate
ATR	Attenuated total reflectance
BRB	Britton-Robinson Buffer
CO <sub>2</sub> RR	Carbon dioxide reduction reaction
CPE	Control potential electrolysis
CV	Cyclic voltammogram
CAT	Iron(III) tetra(2,6-dihydroxyphenyl)porphyrin
CE	Counter electrode
DMF	N,N'-dimethylformamide
DMSO	Dimethyl sulfoxide
DFT	Density functional theory
EXAFS	Extended X-Ray absorption fine structure
EPR	Electron paramagnetic resonance
ESRF	European Synchrotron Radiation Facility
EWE	Electron withdrawing effect
EPDM	Ethylene propylene diene monomer
FeTPP	Iron tetraphenyl porphyrin chloride
FE	Faradaic efficiency
FCAT	Iron(III) di(2,6-dihydroxyphenyl)di(pentafluorophenyl)porphyrin
FT	Fourier transform
FY	Fluorescence yield
FFKM	Perfluoroelastomer
FPM	Fluorocarbon
GC	Glassy carbon
GC/MS	Gas chromatography/mass spectrometry

HER	Hydrogen evolution reaction
HS	High spin
HOMO	Highest occupied molecular orbital
IR	Infrared spectroscopy
IS	Intermediate spin
IUPAC	International union of pure and applied chemistry
LEM	Laboratoire d'Electrochimie Moléculaire
LS	Low spin
LUMO	Lowest unoccupied molecular orbital
LUCIA	Line for Ultimate Characterization by Imaging and Absorption
LCF	Linear combination fitting
MO	Molecular orbital
MIR	Mid-infrared
MVQ	Methyl Vinyl Silicone rubber
NIR	Near infrared
NMR	Nuclear magnetic resonance
NOAA	National Oceanic and Atmospheric Administration
OTTLE	Optically transparent thin layer electrodes
PEEK	Polyether-ether ketone
PTFE	Polytetrafluoroethylene
P4VP	Poly-4-vinylpyridine
RDS	Rate determining step
RE	Reference electrode
RHE	Reversible hydrogen electrode
RT	Room temperature
SHE	Standard hydrogen electrode
SCE	Saturated calomel electrode
SEC	Spectroelectrochemistry
SOLEIL	Optimized light source of intermediate energy of LURE

SAMBA	Spectroscopy Applied to Material Based on Absorption
SDD	Silicon drift diode
S/N	Signal to noise
TOF	Turnover frequency
TON	Turnover number
TBA	Tetrabutylammonium
TD-DFT	Time-dependent density functional theory
TEAP	Triethylammonium phosphate
THF	Tetrahydrofuran
UV-Vis	Ultraviolet-visible spectroscopy
WE	Working electrode
XAS	X-Ray absorption spectroscopy
XANES	X-Ray absorption near edge structure







# Chapter I

---

**General introduction:  
The CO<sub>2</sub> clock is ticking...**

## **Content**

---

<b>1.1</b>	Carbon dioxide (CO <sub>2</sub> ) reduction: from the macro to the atomic scale .....	<b>3</b>
<b>1.2</b>	Outline .....	<b>4</b>
<b>1.3</b>	References .....	<b>6</b>



## 1.1 Carbon dioxide (CO<sub>2</sub>) reduction: from the macro to the atomic scale

CO<sub>2</sub> is essential to make life on Earth hospitable. In nature, its concentration has been regulated by geological activity and photosynthetic organisms, balancing, in a well-controlled manner, the production and consumption of this molecule. However, since the beginning of the Industrial Revolution, in the middle of the 18<sup>th</sup> century, the CO<sub>2</sub> concentration in the atmosphere has drastically increased, perturbing the equilibrium of the natural carbon cycle. It has been demonstrated that this increase is due to anthropogenic CO<sub>2</sub> sources, such as transportation, cement and chemicals production, power generation or agriculture. Certainly, this has impacted the Earth's climate, with current atmospheric CO<sub>2</sub> concentrations being the highest ever observed in human history. For instance, in May 2021 it reached 419 parts per million (ppm), according to the National Oceanic and Atmospheric Administration (NOAA) Global Monitoring Laboratory reports, the highest value since precise measurements started 63 years ago.<sup>1</sup> Notwithstanding the continuous warning alerts from the scientific community and the climate agreements, only a small fraction, around 0.6%, of the generated CO<sub>2</sub> is recycled and fossil fuels still dominate the global energy consumption.<sup>2,3</sup> Along with this, there are also important economic consequences since these non-renewable resources are on their way to exhaustion. Some reports even suggest that production of oil, gas and coal will run out faster than expected, if the current demand keeps growing.<sup>4</sup>

Due to the detrimental effects of the CO<sub>2</sub> accumulation on the Earth climate and environment, as well as the economical and geopolitical consequences that this situation is generating, the scientific community has come together to find solutions. One proposed option to cope with energetic needs is to store and convert energy coming from renewable sources, such as solar light. Taking inspiration from Nature, artificial photosynthesis aims to convert water and CO<sub>2</sub> into oxygen and carbon-derived molecules, storing solar energy into chemical bonds.<sup>2</sup> Considering that solar light is best converted into electrical energy using solar panels, electrochemistry can then be used to reduce CO<sub>2</sub> into carbon building blocks, such as carbon monoxide (CO), which can be used in industrial processes or for the synthesis of more valuable chemicals. However, the CO<sub>2</sub> reduction reaction (CO<sub>2</sub>RR) is a difficult and energetically demanding process due to the high stability and inertness of this molecule, requiring the use of catalysts.

The CO<sub>2</sub> reduction reaction catalysts development, that allows overcoming energetic barriers and making the reaction more selective towards the generation of a specific product, has shown an accelerated progress in the late years. Several elements were shown to be successful electrocatalysts for CO<sub>2</sub> reduction as pure metals, such as silver, palladium, and copper.<sup>5</sup> Transition metal complexes, involving macrocyclic or polypyridine ligands, were also shown to be efficient, economical and selective catalysts, notably towards the reduction of CO<sub>2</sub> to

CO.<sup>6-8</sup> These molecular catalysts present several advantages as compared to pure metals or materials :

- i) Their electronic structures (and hence their activity) can be tuned by synthetic modifications.
- ii) They can be isolated as pure species and therefore be precisely characterized under chemical states relevant to their catalytic activity.
- iii) There are no effects of surface vs. bulk behavior as in metals or materials.

These catalysts nevertheless present activities that need to be improved in terms of efficiency and selectivity to be used on large scales. This process requires understanding the mechanism by which they function as well as their structures along the catalytic cycle. The mechanism of electrochemical CO<sub>2</sub>RR by molecular catalysts have been extensively studied, especially with cyclic voltammetry. There are still, however, uncertainties on the local and electronic structure of intermediate species that play a key role in the catalytic cycle, by which spectroscopic techniques can be useful to observe these species. The present manuscript provides *in situ* spectroelectrochemical characterizations for one of the most active family of CO<sub>2</sub>-reducing molecular catalysts: iron porphyrins. Even if conventional spectroscopic techniques, such as ultraviolet-visible (UV-Vis), Raman and infrared (IR) spectroscopies have been used to study iron porphyrins, the electronic structures of reduced species of this family are still poorly understood. Therefore, in this project, X-Ray Absorption Spectroscopy (XAS), was coupled to electrochemistry to provide spectroscopic insights on the reduced forms of this molecular catalyst. Data were collected under inert and CO<sub>2</sub> atmosphere to understand the nature of the interaction between CO<sub>2</sub> and the reduced iron porphyrin species. These data are discussed with the aim to contribute to the understanding of the mechanism of the electrochemical reduction of CO<sub>2</sub> by these catalysts.

## 1.2 Outline

The present text is organized in eight chapters, including this general introduction. *Chapter 2* is devoted to previous electrochemical studies performed on iron porphyrins towards the activation of CO<sub>2</sub>. In order to complement mechanistic data known to date, we introduce in *Chapter 3* the coupling of this technique with X-Ray absorption spectroscopy. *Chapter 4* is dedicated to describing previous spectroscopic studies on iron porphyrins by UV-Vis, Raman and IR spectroscopies but also by XAS, including initial *ex situ* measurements but also recent results by *in situ* and *operando* spectroelectrochemistry.

A specific challenge for spectroelectrochemical measurements is the development of instrumentation. We portrait in *Chapter 5* the spectroelectrochemical cell that was developed and used during this project, as well as the parameters that need to be controlled to avoid

experimental artifacts. The following two chapters summarize the results obtained with spectroelectrochemical methods on the iron tetraphenyl porphyrin chloride [Fe<sup>III</sup>(TPP)]Cl in solution. *Chapter 6* is devoted to the *in situ* analysis of the electronic structure of a series of iron porphyrins both in water and dimethylformamide (DMF) under argon. *In situ* spectroelectrochemical measurements were also performed under applied reductive potentials. *Chapter 7* describes the UV-Vis, IR and XAS spectroscopic information obtained on [Fe<sup>III</sup>(TPP)]Cl under reductive potentials in the presence of CO<sub>2</sub>. By comparing the data collected under inert conditions and under CO<sub>2</sub> atmosphere, we can describe metal-substrate interactions and further contribute to mechanistic hypothesis previously proposed. This analysis, as well as conclusions and perspectives are summarized in *Chapter 8*. *Several appendices* are inserted at the end of this manuscript, where technical and theoretical aspects of the techniques used throughout this thesis are described.

### 1.3 References Chapter I

- (1) National Oceanic and Atmospheric Administration (NOAA). Carbon dioxide peaks near 420 parts per million at Mauna Loa observatory. *NOAA Research News*. **2021**. Source: <https://research.noaa.gov/article/ArtMID/587/ArticleID/2764/Coronavirus-response-barely-slows-rising-carbon-dioxide>.
- (2) Robert, M. Running the Clock: CO<sub>2</sub> Catalysis in the Age of Anthropocene. *ACS Energy Lett.* **2016**, *1* (1), 281–282.
- (3) Masson-Delmotte, V., P. Zhai, A. Pirani, S. L. Connors, C. Péan, S. Berger, N. Caud, Y. Chen, L. Goldfarb, M. I. Gomis, M. Huang, K. Leitzell, E. Lonnoy, J.B.R. Matthews, T. K. Maycock, T. Waterfield, O. Yelekçi, R. Yu and B. Zhou (eds.). *IPCC, 2021: Summary for Policymakers. In: Climate Change 2021: The Physical Science Basis. Contribution of Working Group I to the Sixth Assessment Report of the Intergovernmental Panel on Climate Change*. **2021** Cambridge University Press. In Press.
- (4) Murray, J.; King, D. Oil's Tipping Point Has Passed. *Nature*. **2012**, *481* (7382), 433–435.
- (5) Kortlever, R.; Shen, J.; Schouten, K. J. P.; Calle-Vallejo, F.; Koper, M. T. M. Catalysts and Reaction Pathways for the Electrochemical Reduction of Carbon Dioxide. *J. Phys. Chem. Lett.* **2015**, *6* (20), 4073–4082.
- (6) Zhang, S.; Fan, Q.; Xia, R.; Meyer, T. J. CO<sub>2</sub> Reduction: From Homogeneous to Heterogeneous Electrocatalysis. *Acc. Chem. Res.* **2020**, *53* (1), 255–264.
- (7) Kinzel, N. W.; Werlé, C.; Leitner, W. Transition Metal Complexes as Catalysts for the Electroconversion of CO<sub>2</sub>: An Organometallic Perspective. *Angew. Chem. Int. Ed.* **2021**, *60* (21), 11628–11686.
- (8) Boutin, E.; Merakeb, L.; Ma, B.; Boudy, B.; Wang, M.; Bonin, J.; Anxolabéhère-Mallart, E.; Robert, M. Molecular Catalysis of CO<sub>2</sub> Reduction: Recent Advances and Perspectives in Electrochemical and Light-Driven Processes with Selected Fe, Ni and Co Aza Macrocyclic and Polypyridine Complexes. *Chem. Soc. Rev.* **2020**, *49* (16), 5772–5809.

# Chapter II

---

## - Introduction -

### Electrochemical activation of CO<sub>2</sub> by iron porphyrins

#### Content

---

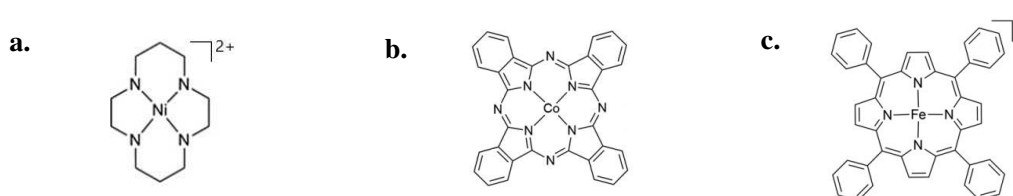
<b>2.1</b>	Catalysts are needed for the reduction of CO <sub>2</sub> .....	<b>10</b>
<b>2.2</b>	Iron porphyrins as a 2e <sup>-</sup> CO <sub>2</sub> reducing molecular catalyst .....	<b>12</b>
<b>2.2.1</b>	Electrochemistry of iron porphyrins – no substrate .....	<b>13</b>
<b>2.2.2</b>	Electrochemical activation of CO <sub>2</sub> by iron porphyrins .....	<b>14</b>
<b>2.2.3</b>	Enhanced catalysis .....	<b>17</b>
<b>2.3</b>	Epilogue and next chapter outlook .....	<b>19</b>
<b>2.4</b>	References .....	<b>21</b>





Even if CO<sub>2</sub> reduction by using electrochemical methods has been known since the 50s',<sup>1</sup> the research in this field intensified in the decade of the 80s' due to the oil crisis. However, during the early 2000s' it drastically slowed down, only re-emerging in the recent years with the need for finding energy alternatives to reduce the effects of global warming.<sup>2</sup> Hence, CO<sub>2</sub> reduction has become an intense field of research.

Pioneering work on the field was achieved by Y. Hori *et al.* who initially showed the detection of gaseous products, such as CO and even CH<sub>4</sub> by using metal electrodes.<sup>3</sup> Following these reports, C<sub>2</sub> products generation studies also flourished, by the detection of ethylene also reported by this group<sup>4</sup> and by the A. Bard group.<sup>5</sup> However, these early reports lacked on the ability of controlling the catalytic properties. Notably, transition metal complexes started to capture the attention of the scientific community. The advantage of tuning both, the metal center, and the ligand, along with studying the steric and electrostatics effects opened a path of endless possibilities.<sup>6</sup> First attempts used noble metals, such as rhenium and ruthenium complexes, but their high-cost prevented the scaling-up of these systems.<sup>7-9</sup> Therefore, metal complexes based on more abundant transition metals for instance nickel, with the pioneering work of J.-P. Sauvage in nickel cyclams,<sup>10</sup> but also by using macrocycles complexes of cobalt<sup>11-15</sup> and iron<sup>16-22</sup> as metal centers have been envisioned, providing convenient platforms for molecular engineering (scheme 2.1). Among them, iron, as being the most abundant metal on Earth, has been chosen as the best alternative due to lowering production costs and the ethical and environmental impacts that, for instance, cobalt mining generates.<sup>23,24</sup>



**Scheme 2.1. Examples of metal complexes based on abundant metals: a. Nickel cyclam; b. Cobalt phthalocyanine; c. Iron porphyrin which have been used as molecular catalysts for the 2 electrons reduction of CO<sub>2</sub>.**

This chapter aims at presenting the fundamental aspects of the electrochemical activation of CO<sub>2</sub> focusing on the use of iron porphyrins as molecular catalyst. The Laboratoire d'Electrochimie Moléculaire (LEM) has been a pioneer in the study of these systems for the electrochemical activation of small molecules, among them CO<sub>2</sub>. However, before furthering in the description of these molecules and its role in the CO<sub>2</sub>RR, the fundamental reasons why a catalyst is required to activate CO<sub>2</sub> are introduced. Furthermore, mechanistic studies performed on these systems, based on electrochemistry, will be described in detail, due to the relevance of these results for the development of this project.

## 2.1. Catalysts are needed for the reduction of CO<sub>2</sub>

The introduction of one electron to reduce CO<sub>2</sub> into its radical anion form, CO<sub>2</sub><sup>•-</sup>, requires a potential as negative as -1.85 V vs. SHE (standard hydrogen electrode) in aqueous media at pH 7,<sup>25</sup> and of -1.97 V vs. SHE in aprotic solvent, such as DMF (N,N'-dimethylformamide).<sup>26</sup> This energetic requirement is associated to a large barrier due to an internal reorganization to transform the linear CO<sub>2</sub> molecule to a bent CO<sub>2</sub><sup>•-</sup> radical anion form, and to a solvation reorganization. Therefore, a catalyst is required to lower the high activation barrier and to efficiently and selectively transform CO<sub>2</sub> into its reduced products.<sup>6,27</sup>

The thermodynamic cost for the reaction to occur is called overpotential ( $\eta$ ). It can be described as the difference between the potential that is applied versus the standard potential of the target reaction, the minimum required to drive the reaction (equation 2.1).<sup>28,29</sup> Hence, a good catalyst will minimize  $\eta$ .

$$\eta = E_{CO_2/product}^{\circ} - E_{electrode} \quad \text{Eq. 2.1}$$

For a catalyst to be *efficient*, the reaction must be ideally fast, selective and the catalyst should remain stable over time. Therefore, one can define the efficiency of the catalysts in terms of its *turnover frequency (TOF)*, with the number of cycles a catalyst can perform over time. More specifically, TOF, as described in equation 2.2, relate the moles ( $n$ ) of products that are formed divided by the amount of active catalyst per unit of time.<sup>30</sup>

$$TOF = \frac{1}{n(t)_{active\ catalyst}} \frac{dn(t)_{product}}{dt} \quad \text{Eq. 2.2}$$

By plotting the TOF (eq. 2.2) as a function of the overpotential  $\eta$  (eq. 2.1) the intrinsic activity of a catalyst can be estimated, as shown in figure 2.1, also known as catalytic Tafel plot.<sup>31-33</sup> Indeed, TOF is related to  $\eta$  since the amount of active catalyst increases when  $\eta$  becomes larger. A plateau value can be reached, which will be equal to the rate constant of the catalytic process ( $k_{cat}$ ), providing a pure kinetic regime, as described in more detail in appendix A.

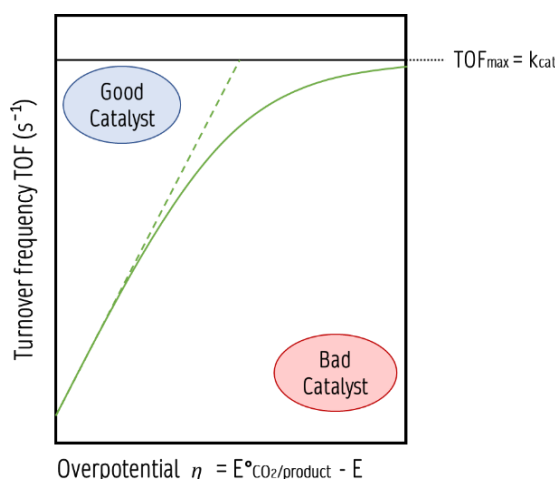


**Figure 2.1. Catalytic Tafel Plot [TOF = f( $\eta$ )].**

*Adapted from reference 6.*

The *durability* of a catalyst is obtained by calculating its *turnover number (TON)* which refers to the total amount of product obtained once the catalysts has stopped its activity divided by the initial amount of the catalyst. Usually, TON is measured by performing control potential electrolysis (CPE) during long time or until the catalysts shows signal of damage or destruction.

Finally, the selectivity can be described as the ability of the catalyst to generate a specific product. For an electrocatalytic reaction, it can be quantified in terms of the *Faradaic Efficiency (FE)*, which indicates the ratio between the charge ( $q$ ) that has been requested to generate the targeted product and the total charge that has passed through the electrode.<sup>30</sup> In an ideal case, all the electrons passing through the electrode should be used to generate a specific product. However, this almost never occurs due to competing reactions. For instance, for CO<sub>2</sub>RR, the hydrogen evolution reaction (HER) is usually the most difficult reaction to avoid, due to the proximity of the reduction potential of this reaction to generate hydrogen, with an apparent standard potential at pH 7 of -0.42 V vs. SHE, in comparison with the ones to generate C1 related products, such as CO with an apparent standard potential at pH 7 of -0.20 V vs. SHE.

To study reaction mechanisms a useful electrochemical tool is cyclic voltammetry. The generated plot of the electrical response of the species (current) as a function of the applied potential, known as a cyclic voltammogram (CV), gives valuable information related to the kinetics of the system. A brief introduction of its application in homogeneous catalysts, in which both, the catalyst and the substrate, are dissolved in the electrolyte solution, is described as follow. When no catalyst is present in the electrolyte solution, the substrate (A) is directly reduced at the electrode surface (blue CV, figure 2.2). In the presence of the active form of the catalyst (Q), catalytic reduction of A occurs, and the current is amplified (red CV,

figure 2.2). In this case, the transformation of the substrate A to the product B occurs at a more positive potential than without the presence of the catalysts. A loss of the reversibility, that is observed in the absence of the substrate (green CV figure 2.2), is also observed. From the exact shape and location of the catalytic response as a function of the scan rate, substrate concentration, and possibly co-substrate concentration such as protons, kinetic information, such as the rate constant, can be obtained from the cyclic voltammogram.

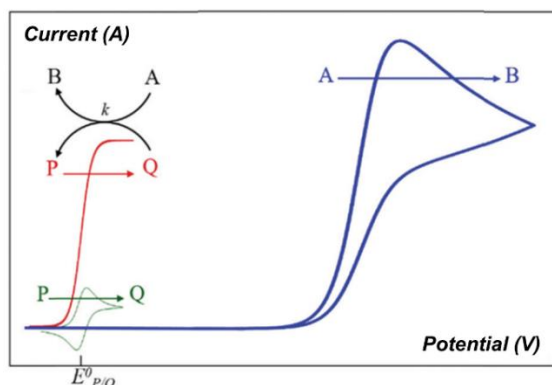


**Figure 2.2.** Cyclic voltammogram for the reduction of A to B. Blue: direct reduction of A at the electrode surface in the absence of catalyst. Red: catalytic reduction of A by the reduced form of the catalyst (Q). Green: reversible one-electron catalyst (P) reduction.

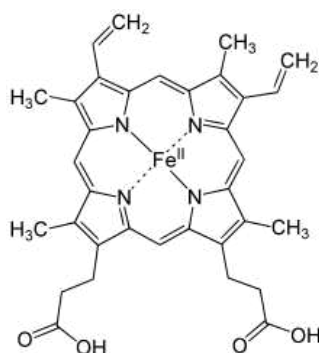
*Adapted from reference 6.*

The various kinetic regimes can be identified through the determination of the minimum set of adimensional parameters describing the system (in the previous case the excess factor that relate the substrate and catalyst concentration  $\gamma = C_A^0/C_P^0$  and the kinetic parameter  $\lambda = k_{cat}C_P^0RT/Fv$  which are represented on a so-called zone diagram (see appendix A).<sup>31,33,34</sup>

Where  $R$  is the ideal gas constant (J/mol.K),  $T$  is the temperature in Kelvin (K),  $F$  is the Faradaic constant (C/mol),  $k_{cat}$  the kinetic rate constant,  $C_A^0$  and  $C_P^0$  as the concentration of the substrate and the catalyst respectively in (mol/cm<sup>3</sup>) respectively and  $v$  the scan rate (V/s).

## 2.2 Iron porphyrins as 2e<sup>-</sup> CO<sub>2</sub> reducing molecular catalysts

Porphyrin ligands, a hydrophobic and planar ring that contains four pyrrole subunits bonded by methine bridges, are known for being the backbone of the heme proteins, essential components for living organisms (scheme 2.2). In particular, iron porphyrins are extensively found in nature as proteins that have vital roles in processes such as oxygen transport and storage, performed by the hemoglobin; electron transport in the respiratory chain, degradation of organic substrates, executed by the cytochrome P450, along many other reported processes.<sup>35-37</sup> Due to their relevance in nature, iron porphyrins have driven the attention for many decades.



**Scheme 2.2.** Structure of the protoporphyrin ring with a central bound iron atom commonly found in nature.

In 1988, researchers from LEM and the Institute Curie in Orsay – France, reported that the iron tetraphenyl porphyrin chloride [ $\text{Fe}^{\text{III}}(\text{TPP})\text{Cl}$ ] (figure 2.3 – a.), the most simple model of the iron porphyrin family, was able to reduce  $\text{CO}_2$  into  $\text{CO}$ .<sup>38</sup> From these studies, many substituted iron porphyrins have been developed, which, as described later in this chapter, have incredibly enhanced the activity of the iron porphyrins, being considered as one of the most efficient and robust molecular catalysts known so far.

### 2.2.1 Electrochemistry of iron porphyrins – No substrate

The cyclic voltammogram of [ $\text{Fe}^{\text{III}}(\text{TPP})\text{Cl}$ ] in a dry, aprotic solvent, such as DMF in the presence of an electrolyte, for instance tetrabutylammonium hexafluorophosphate ( $\text{TBAPF}_6$ ) and under an inert atmosphere, such as argon (Ar), displays three defined waves, as shown in figure 2.3 - b. Each of these waves have been proposed as electronic transitions at the metal center. For instance,  $\text{Fe}^{\text{III}}$  to  $\text{Fe}^{\text{II}}$  is being reduced at  $-0.13 \text{ V vs. SCE}$ ,  $\text{Fe}^{\text{II}}$  to formal “ $\text{Fe}^{\text{I}}$ ” at  $-1.00 \text{ V vs. SCE}$ , and finally “ $\text{Fe}^{\text{I}}$ ” to formal “ $\text{Fe}^{\text{0}}$ ” at the last wave potential at  $-1.67 \text{ V vs. SCE}$  (figure 2.3 – c).<sup>16,38,39</sup> These waves are electronically reversible (fast electron transfer) and monoelectronic.  $\text{Fe}^{\text{II}}/\text{“Fe}^{\text{I}}\text{”}$  and “ $\text{Fe}^{\text{I}}\text{”}/\text{“Fe}^{\text{0}}\text{”}$  waves are chemically reversible. At the  $\text{Fe}^{\text{III}}/\text{Fe}^{\text{II}}$  wave, however, decoordination of chloride have been proposed to occur.<sup>40</sup>

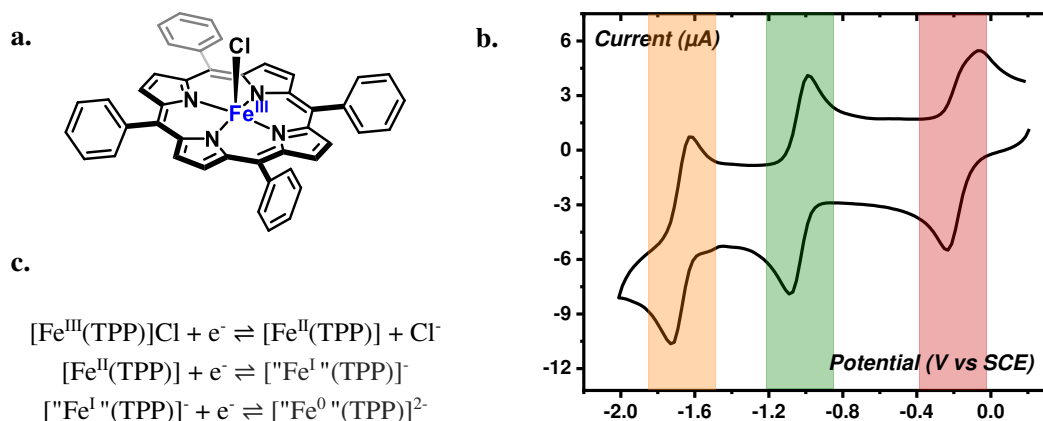


Figure 2.3. a. Structure of iron tetraphenyl porphyrin chloride  $[\text{Fe}^{\text{III}}(\text{TPP})]\text{Cl}$ ; b. Cyclic voltammogram of 2 mM solution of  $[\text{Fe}^{\text{III}}(\text{TPP})]\text{Cl}$  in dry DMF + 0.1 M TBAPF<sub>6</sub> under Ar atmosphere at room temperature (RT) and a scan rate of  $\nu = 100 \text{ mV}\cdot\text{s}^{-1}$ ; c. Reversible reactions occurring at each potential region.

Each section indicates the reducing regions:  $\text{Fe}^{\text{III}}/\text{Fe}^{\text{II}}$  (red),  $\text{Fe}^{\text{II}}/^{\text{I}}\text{Fe}^{\text{I}}$  (green) and  $^{\text{I}}\text{Fe}^{\text{I}}/^{\text{0}}\text{Fe}^{\text{0}}$  (orange).

## 2.2.2 Electrochemical activation of CO<sub>2</sub> by iron porphyrins

Figure 2.4. shows the CV of a 2 mM solution of  $[\text{Fe}^{\text{III}}(\text{TPP})]\text{Cl}$  in DMF + 0.1 M TBAPF<sub>6</sub> under Ar (black trace) and CO<sub>2</sub> (red trace) atmosphere. Under CO<sub>2</sub>, an increase of the current intensity together with a loss of reversibility is observed at -1.67 V vs. SCE. These new features attest a catalytic activity at the  $^{\text{I}}\text{Fe}^{\text{I}}/^{\text{0}}\text{Fe}^{\text{0}}$  wave. Therefore, the formal reduced state  $^{\text{0}}\text{Fe}^{\text{0}}$  is considered as the active form of the catalyst. Further control potential electrolysis at -1.8 V vs. SCE confirmed the formation of CO.<sup>41</sup> Since protons are required for the reaction to proceed (scheme 2.3), residual water in the DMF is considered as the proton source in this case (see figure C.2 - appendix C for details).

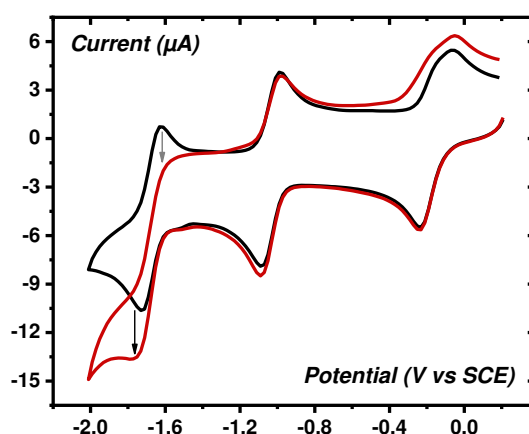
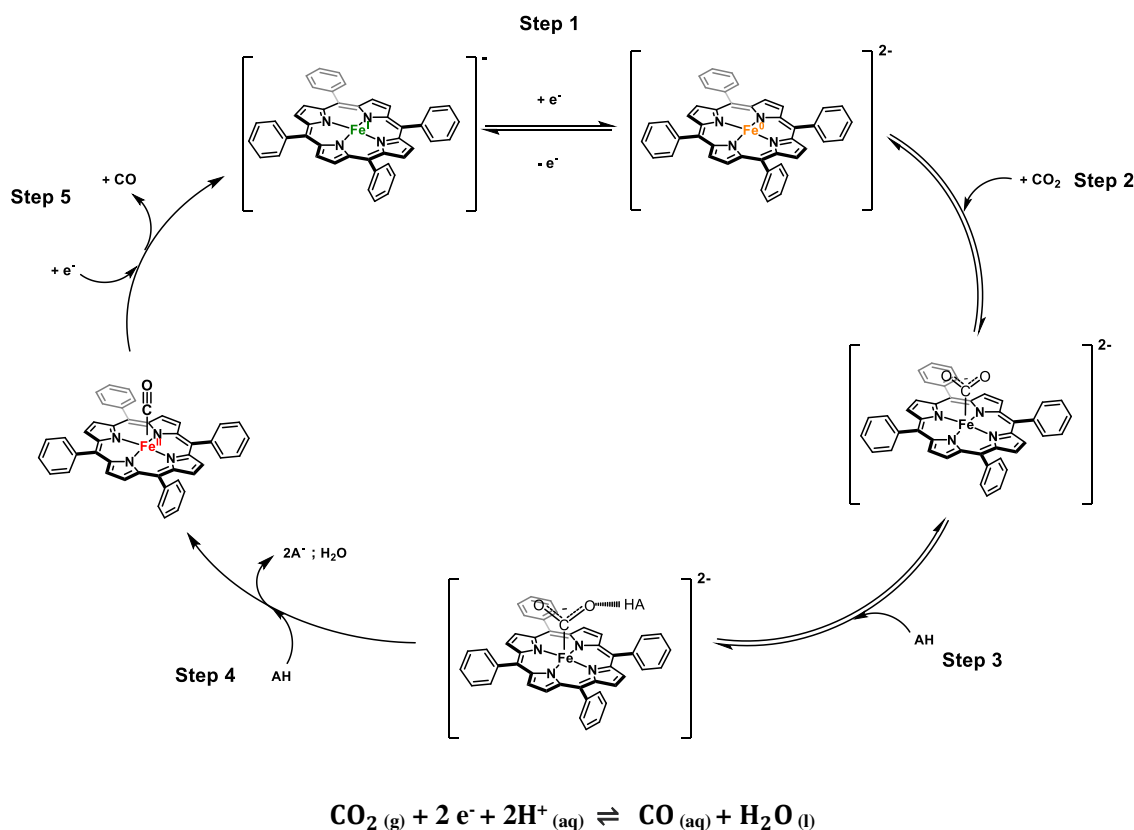


Figure 2.4. Cyclic voltammogram of 2 mM solution of  $[\text{Fe}^{\text{III}}(\text{TPP})]\text{Cl}$  in dry DMF + 0.1 M TBAPF<sub>6</sub> under Ar (black) and saturated with CO<sub>2</sub> (C = 0.2 M) (red) at room temperature (RT) and a scan rate of  $\nu = 100 \text{ mV}\cdot\text{s}^{-1}$ .

Arrows indicate the observed changes in the presence of CO<sub>2</sub> in comparison with Argon data: grey arrow – loss of reversibility; black arrow – catalytic current increase.

Based on electrochemical methods, a mechanism for the CO<sub>2</sub> reduction to CO mediated by [Fe<sup>III</sup>(TPP)]Cl has been proposed (scheme 2.3).<sup>16,42,43</sup>



**Scheme 2.3.** Proposed mechanism for the electrocatalytic reduction of CO<sub>2</sub> to CO mediated by [Fe<sup>III</sup>(TPP)]Cl in the presence of a weak acid (AH).

Adapted from reference 39.

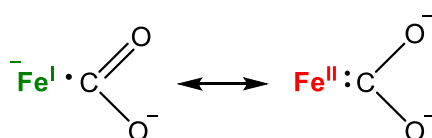
The mechanism can be summarized in the following steps:

### **Step 1 – Generation of the electron-rich metal complex**

The catalytic cycle starts with the formation of the formal “Fe<sup>0</sup>” by a three-electron transfer process, as described above.

### **Step 2 – Fe-CO<sub>2</sub> adduct formation**

The generated electron-rich metal center binds the electrophilic carbon on the CO<sub>2</sub> molecule, forming an initial adduct which can be represented as the mesomeric forms:





In which a form with a formal “Fe<sup>I</sup>” is asymmetric while the other form, with an Fe<sup>II</sup> center, is symmetrical.<sup>43</sup>

### Step 3 – Hydrogen bonding stabilization

This adduct can be stabilized by hydrogen bonding in the presence of the acid. In this context, the selection of this acid is pivotal to make the catalysis durable and to direct the reaction towards the generation of a determined product, as discussed in more detail in section 2.2.3.<sup>16,44</sup>

### Step 4 – Bond cleavage

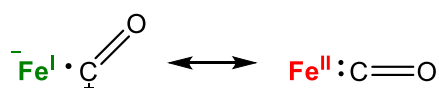
The push-pull effect obtained by the protonation weakens the C-O bond, leading to water release and the formation of the stable Fe<sup>II</sup>-CO adduct.

### Step 5 – Product release

In the following step, the Fe<sup>II</sup>-CO adduct is reduced regenerating the catalyst active form “Fe<sup>I</sup>” and the release of CO.

It has been suggested that the CO<sub>2</sub> adduct is not symmetric. This is expected since the major product of the reaction is CO, meaning that while one C-O bond is broken during the proton-coupled intramolecular electron transfer the other is conserved as CO. This observation allowed to Costentin *et al.* to propose the “Fe<sup>I</sup>” asymmetrical adduct (as shown in scheme 2.3), rather than the Fe<sup>II</sup> symmetrical one.<sup>43</sup>

In the same order of ideas, the CO adduct can be also described as the mesomeric forms



However, due to the high affinity of Fe<sup>II</sup> centers in porphyrins towards CO, the Fe<sup>II</sup> adduct has been considered in this case rather than the “Fe<sup>I</sup>” adduct. This has been observed by CV with the presence of the anodic wave “Fe<sup>I</sup>”/Fe<sup>II</sup> being shifted. Figure 2.5 shows the CV of the [Fe<sup>III</sup>(TPP)]Cl under argon (black trace), under CO<sub>2</sub> (red trace), under CO<sub>2</sub> with 5 mM of an added proton source, for instance phenol (brown), and under CO (green). In the presence of CO an oxidative wave is observed close to the potential of the “Fe<sup>I</sup>”/Fe<sup>II</sup> in the presence of CO<sub>2</sub> and a proton source, supporting the formation of the Fe<sup>II</sup>-CO adduct.<sup>16,39,45</sup>

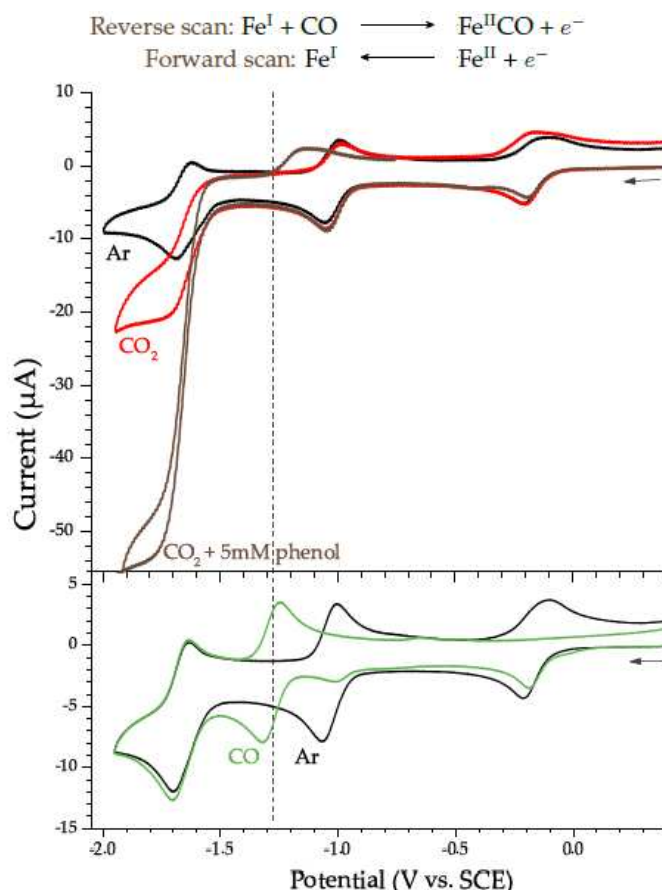


**Figure 2.5.** Cyclic voltammogram of 2 mM solution of  $[\text{Fe}^{\text{III}}(\text{TPP})]\text{Cl}$  in dry DMF + 0.1 M  $\text{TBAPF}_6$  under Ar (black); saturated with  $\text{CO}_2$  ( $C = 0.2$  M) (red); saturated with  $\text{CO}_2$  ( $C = 0.2$  M) + 5 mM phenol (brown). Bottom: same solution under Ar (black) and under CO (green). All the experiments were performed at room temperature (RT) and a scan rate of  $\nu = 100 \text{ mV}\cdot\text{s}^{-1}$ .

*Adapted from reference 39. Credits to Dr. Iban Azcarate.*

### 2.2.3 Enhanced catalysis

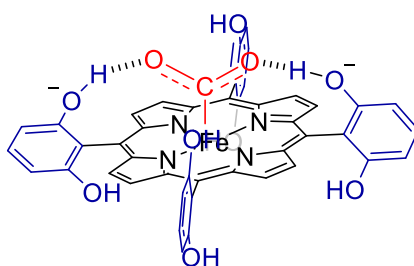
#### - Addition of Lewis or Brønsted acid

The addition of a Brønsted acid evidence an even more pronounced current increase at the last wave, as illustrated in figure 2.5 - brown trace, suggesting an influence in catalysis. Further kinetic analysis suggested a synergistic assistance by a push-pull mechanism. Therefore, electrons are pushed from the iron center into the electrophilic carbon in the  $\text{CO}_2$ , while the doublet on the oxygen is pulled by the formation of an hydrogen bond. This effect weakens the C-O bond and favors its cleavage. Preparative-scale electrolysis performed in  $[\text{Fe}(\text{TPP})]\text{Cl}$  in DMF + 0.1 M  $\text{Et}_4\text{NClO}_4$  at 1.7 V vs. SCE in the presence of  $\text{CO}_2$  and trifluoroethanol showed an improvement in the metrics for assessing the catalytic performance. For instance, a TOF of  $40 \text{ h}^{-1}$  while not significant degradation of the catalysts was detected.<sup>16</sup> Studies in the same system in the presence of different proton sources addressed to the role on the nature of the acid to drive the selectivity of the reaction. For

instance, while in the presence of trifluoroethanol a 96% CO was formed, the addition of a slightly more acidic source, such as triethylammonium chloride, favored the HER while the use of 1-propanol lead to the generation of formate.<sup>16,45,46</sup> The addition of Lewis acids, such as magnesium and calcium cations, also showed a positive effect, boosting the conversion of CO<sub>2</sub>.<sup>41,44</sup>

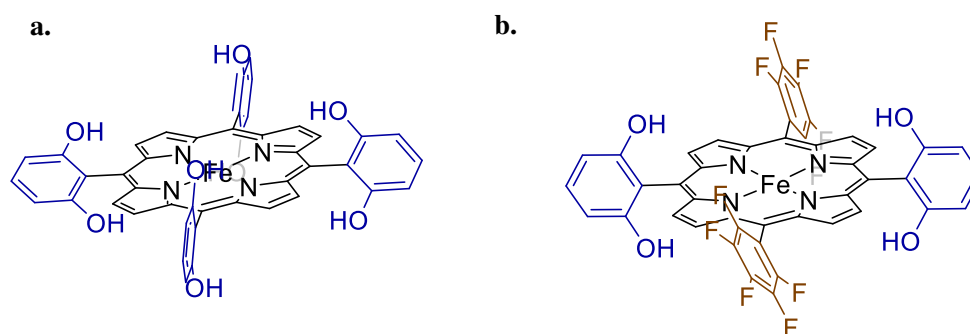
#### - Through-structure/space effects

The results obtained in the presence of Brønsted and Lewis acids led to the development of substituted porphyrins. The incorporation of hydroxyl groups in the phenyl substituents of the porphyrin ring in close proximity to the metal center, for instance at ortho position, named CAT, significantly enhanced catalysis. It was concluded that the presence of pendant acidic groups in the porphyrin ring has a synergic effect. Therefore, they serve both as hydrogen bond promoters, that being in close proximity to the metal center help in the stabilization of the CO<sub>2</sub> intermediate, as shown in scheme 2.4, but also as proton relay.<sup>47</sup> The incorporation of these functionalities induced fast kinetics with a TOF of 10<sup>3.8</sup> s<sup>-1</sup> at a low overpotential (0.465 V) while no degradation of the catalyst was observed.<sup>18</sup>



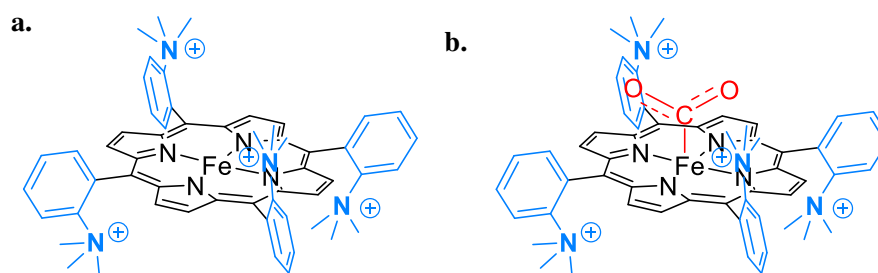
**Scheme 2.4. Fe-CO<sub>2</sub> adduct stabilized by the presence of phenolic functionalities in the ortho position of the porphyrin ring in the CAT catalyst.**

The substitution of the hydroxyl groups by methoxy moieties led to a TOF of 10<sup>1.3</sup> s<sup>-1</sup> at a 1.04 V overpotential, confirming the enhancement of catalysis by the presence of a local proton source at the porphyrin ring.<sup>18</sup> The incorporation of fluorine moieties, in contrast, allowed to decrease the overpotential but at the same time, it lowered the catalytic activity. It was suggested that the presence of electron-withdrawing substituents influence catalysis by making the iron center less nucleophilic, and therefore slows down the coordination of CO<sub>2</sub> into the metal.<sup>47</sup> These results lead to the suggestion of combining the effect of electron-withdrawing groups at the ligand (through-structure effect) with the presence of a local proton source (through-space effects), generating the FCAT catalyst (scheme 2.5). By doing this, the catalytic activity was maintained at the range of TOF = 10<sup>4</sup> s<sup>-1</sup> while the overpotential was reduced when compared with CAT.<sup>6,47</sup>



Scheme 2.5. Iron porphyrins derivatives: a. CAT ; b. FCAT.

The introduction of four positively charged trimethylanilinium substituents in the phenyl groups of the porphyrin ring resulted in an incredibly enhanced catalysis.<sup>17,39,48</sup> For instance, long run (84 h) electrolysis performed in the presence of an iron porphyrin bearing these charged groups in the ortho position of the phenyl groups (Fe-o-TMA – scheme 2.6 - a) in the presence of a large concentration of a weak acid (3 M phenol) and under CO<sub>2</sub> showed an incredible efficiency with a TOF = 10<sup>6</sup> s<sup>-1</sup> without showing any degradation of the catalyst. This porphyrin shows a total conversion of CO<sub>2</sub> to CO, despite the large presence of the acid that could drive the reaction towards the H<sub>2</sub> generation.<sup>17</sup> The presence of positively charged groups was, therefore, suggested to favorize both effects: a “Fe<sup>1+</sup>”/“Fe<sup>0</sup>” wave found at more positive potentials and a stabilization of the expected Fe-CO<sub>2</sub> adduct, due to the interaction between the positive charges of the substituent and the negatively charged oxygens in the CO<sub>2</sub> (scheme 2.6 - b). In contrast, negatively charged groups, such as the presence of sulfonate groups, evidenced a contrary effect reducing catalytic efficiency.<sup>17</sup>



Scheme 2.6. a. Structure of the iron porphyrin derivative Fe-o-TMA; b. Fe-CO<sub>2</sub> adduct stabilized by the presence of positively charged functionalities in the ortho position of the porphyrin ring.

### 2.3. Epilogue and next chapter outlook

Iron porphyrins are efficient, abundant and economical molecular electrocatalysts used for the activation of CO<sub>2</sub>. The improvement of their catalytic properties has been possible due to their structural tunability. Iron porphyrins have been described as robust since they do not degrade during long periods of electrolysis and as very selective catalysts towards the

formation of CO. Electrochemical methods, mostly based on cyclic voltammetry and preparative scale electrolysis, have been widely used for many decades to characterize iron porphyrins, leading to a proposed mechanism. It has been possible to suggest that the efficiency of iron porphyrins is related to several factors: (i) the presence of an electron rich iron center as active site of catalysis; (ii) the possible stability of the generated adducts, Fe-CO<sub>2</sub> and Fe-CO and (iii) the nature of the added acid. Certainly, this last aspect has been described as pivotal in catalysis, directing the reaction towards the generation of a specific product depending on the acidic properties of the media.

Ideally, a complete understanding of the reaction mechanism should lead to the catalyst optimization. Although electrochemistry has been used for decades to describe the mechanism, still spectroscopic evidence of the intermediates is missing, especially during *operando* conditions. By having a well-defined site of catalysis, iron porphyrins can benefit from *in situ-operando* spectroelectrochemical methods, in which “reaction-oriented electrochemistry” can be coupled to “species focused spectroscopy” allowing the identification of reaction intermediates.

Spectroscopic techniques, such as UV-Vis and vibrational spectroscopies, have been used for many years to describe the CO<sub>2</sub>RR mechanism catalyzed by iron porphyrin. While UV-Vis spectroscopy has given insights in the electronic configurations of iron porphyrins, vibrational methods, such as IR and Raman spectroscopy, have been used to monitor the (de)-coordination and evolution of the CO<sub>2</sub> to CO transformation. However, more evidence is required in order to conclude over the generated species.

During this project, X-Ray absorption (XAS) spectroelectrochemistry was selected as the main tool for the studying the CO<sub>2</sub>RR mechanism catalyzed by iron porphyrin since it allows an element specific analysis. Therefore, it is possible to directly probe the iron center and observe the changes occurring at it. In this way, much information regarding the redox state but also structural variations can be suggested. *In situ* XAS spectroelectrochemistry collected in the absence of substrate allowed to reach further insights in the determination of the electronic configuration of the iron porphyrin at the catalyst active site. Incorporation of the substrate, allowed to complement already existing mechanistic information, suggesting the presence of the different adducts and concluding over the rate determining step of the reaction in the *in situ* experimental conditions.

Due to the relevance of XAS for the development of this project, the next chapter will present an introduction to this technique, with some theoretical aspects as well as key definitions.

## 2.4. References – Chapter II

- (1) Teeter, T. E.; Van Rysselberghe, P. Reduction of Carbon Dioxide on Mercury Cathodes. *J. Chem. Phys.* **1954**, *22* (4), 759–760.
- (2) Kas, R.; Yang, K.; Bohra, D.; Kortlever, R.; Burdyny, T.; A. Smith, W. Electrochemical CO<sub>2</sub> Reduction on Nanostructured Metal Electrodes: Fact or Defect? *Chem Sci.* **2020**, *11* (7), 1738–1749.
- (3) Hori, Y.; Kikuchi, K.; Suzuki, S. Production of CO and CH<sub>4</sub> in Electrochemical Reduction of CO<sub>2</sub> at Metal Electrodes in Aqueous Hydrogencarbonate Solution. *Chem. Lett.* **1985**, *14* (11), 1695–1698.
- (4) Hori, Y.; Kikuchi, K.; Murata, A.; Suzuki, S. Production of Methane and Ethylene in Electrochemical Reduction of Carbon Dioxide at Copper Electrode in Aqueous Hydrogencarbonate Solution. *Chem. Lett.* **1986**, *15* (6), 897–898.
- (5) DeWulf, D. W.; Jin, T.; Bard, A. J. Electrochemical and Surface Studies of Carbon Dioxide Reduction to Methane and Ethylene at Copper Electrodes in Aqueous Solutions. *J. Electrochem. Soc.* **1989**, *136* (6), 1686.
- (6) Boutin, E.; Merakeb, L.; Ma, B.; Boudy, B.; Wang, M.; Bonin, J.; Anxolabéhère-Mallart, E.; Robert, M. Molecular Catalysis of CO<sub>2</sub> Reduction: Recent Advances and Perspectives in Electrochemical and Light-Driven Processes with Selected Fe, Ni and Co Aza Macrocyclic and Polypyridine Complexes. *Chem. Soc. Rev.* **2020**, *49* (16), 5772–5809.
- (7) Hawecker, J.; Lehn, J.-M.; Ziessel, R. Electrocatalytic Reduction of Carbon Dioxide Mediated by Re(Bipy)(CO)<sub>3</sub>Cl (Bipy = 2,2'-Bipyridine). *J. Chem. Soc., Chem. Commun.* **1984**, *6*, 328–330.
- (8) Sullivan, B. P.; Bolinger, C. M.; Conrad, D.; Vining, W. J.; Meyer, T. J. One- and Two-Electron Pathways in the Electrocatalytic Reduction of CO<sub>2</sub> by Fac-Re(Bpy)(CO)<sub>3</sub>Cl (Bpy = 2,2'-Bipyridine). *J. Chem. Soc., Chem. Commun.* **1985**, *20*, 1414–1416.
- (9) Ishida, H.; Tanaka, H.; Tanaka, K.; Tanaka, T. Selective Formation of HCOO<sup>-</sup> in the Electrochemical CO<sub>2</sub> Reduction Catalyzed by [Ru(Bpy)<sub>2</sub>(CO)<sub>2</sub>]<sup>2+</sup> (Bpy = 2,2'-Bipyridine). *J. Chem. Soc., Chem. Commun.* **1987**, *2*, 131–132.
- (10) Beley, M.; Collin, J.-P.; Ruppert, R.; Sauvage, J.-P. Nickel(II)-Cyclam: An Extremely Selective Electrocatalyst for Reduction of CO<sub>2</sub> in Water. *J. Chem. Soc., Chem. Commun.* **1984**, (19), 1315–1316.
- (11) Lieber, C. M.; Lewis, N. S. Catalytic reduction of carbon dioxide at carbon electrodes modified with cobalt phthalocyanine. *J. Am. Chem. Soc.* **1984**, *106*, 17, 5033–5034.
- (12) Han, N.; Wang, Y.; Ma, L.; Wen, J.; Li, J.; Zheng, H.; Nie, K.; Wang, X.; Zhao, F.; Li, Y.; Fan, J.; Zhong, J.; Wu, T.; Miller, D. J.; Lu, J.; Lee, S.-T.; Li, Y. Supported Cobalt Polyphthalocyanine for High-Performance Electrocatalytic CO<sub>2</sub> Reduction. *Chem.* **2017**, *3* (4), 652–664.

- (13) Wang, M.; Torbensen, K.; Salvatore, D.; Ren, S.; Joulié, D.; Dumoulin, F.; Mendoza, D.; Lassalle-Kaiser, B.; Isci, U.; Berlinguette, C.P.; Robert, M. CO<sub>2</sub> electrochemical catalytic reduction with a highly active cobalt phthalocyanine. *Nat. Comm.* **2019**, 10, 3602.
- (14) Boutin, E.; Wang, M.; Lin, J. C.; Mesnage, M.; Mendoza, D.; Lassalle-Kaiser, B.; Hahn, C.; Jaramillo, T. F.; Robert, M. Aqueous Electrochemical Reduction of Carbon Dioxide and Carbon Monoxide into Methanol with Cobalt Phthalocyanine. *Angew. Chem. Int. Ed.* **2019**, 58 (45), 16172–16176.
- (15) Ren, S.; Joulié, D.; Salvatore, D.; Torbensen, K.; Wang, M.; Robert, M.; Berlinguette, C.P. Molecular electrocatalysts can mediate fast, selective CO<sub>2</sub> reduction in a flow cell. *Science*. **2019**, 365, 6451, 367-369.
- (16) Bhugun, I.; Lexa, D.; Savéant, J.-M. Catalysis of the Electrochemical Reduction of Carbon Dioxide by Iron(0) Porphyrins: Synergistic Effect of Weak Brønsted Acids. *J. Am. Chem. Soc.* **1996**, 118 (7), 1769–1776.
- (17) Azcarate, I.; Costentin, C.; Robert, M.; Savéant, J.-M. Through-Space Charge Interaction Substituent Effects in Molecular Catalysis Leading to the Design of the Most Efficient Catalyst of CO<sub>2</sub>-to-CO Electrochemical Conversion. *J. Am. Chem. Soc.* **2016**, 138 (51),
- (18) Costentin, C.; Drouet, S.; Robert, M.; Savéant, J.-M. A Local Proton Source Enhances CO<sub>2</sub> Electroreduction to CO by a Molecular Fe Catalyst. *Science*. **2012**, 338, 6103, 90-94.
- (19) Khadhraoui, A.; Gotico, P.; Boitrel, B.; Leibl, W.; Halime, Z.; Aukauloo, A. Local Ionic Liquid Environment at a Modified Iron Porphyrin Catalyst Enhances the Electrocatalytic Performance of CO<sub>2</sub> to CO Reduction in Water. *Chem. Comm.* **2018**, 54 (82), 11630–11633.
- (20) Gotico, P.; Boitrel, B.; Guillot, R.; Sircoglou, M.; Quaranta, A.; Halime, Z.; Leibl, W.; Aukauloo, A. Second-Sphere Biomimetic Multipoint Hydrogen-Bonding Patterns to Boost CO<sub>2</sub> Reduction of Iron Porphyrins. *Angew. Chem. Int. Ed.* **2019**, 58 (14), 4504–4509.
- (21) Maurin, A.; Robert, M. Noncovalent Immobilization of a Molecular Iron-Based Electrocatalyst on Carbon Electrodes for Selective, Efficient CO<sub>2</sub>-to-CO Conversion in Water. *J. Am. Chem. Soc.* **2016**, 138, 8, 2492-2495.
- (22) Rao, H.; Schmidt, L. C.; Bonin, J.; Robert, M. Visible-Light-Driven Methane Formation from CO<sub>2</sub> with a Molecular Iron Catalyst. *Nature* **2017**, 548 (7665), 74–77.
- (23) Calvão, F.; McDonald, C. E. A.; Bolay, M. Cobalt Mining and the Corporate Outsourcing of Responsibility in the Democratic Republic of Congo. *Extr. Ind. Soc.* **2021**, 8 (4), 100884.
- (24) Sovacool, B. K. When Subterranean Slavery Supports Sustainability Transitions? Power, Patriarchy, and Child Labor in Artisanal Congolese Cobalt Mining. *Extr. Ind. Soc.* **2021**, 8 (1), 271–293.
- (25) Surdhar, P. S.; Mezyk, S. P.; Armstrong, D. A. Reduction Potential of the Carboxyl Radical Anion in Aqueous Solutions. *J. Phys. Chem.* **1989**, 93 (8), 3360–3363.
- (26) Lamy, E.; Nadjo, L.; Savéant, J.-M. Standard Potential and Kinetic Parameters of the Electrochemical Reduction of Carbon Dioxide in Dimethylformamide. *J. Electroanal. Chem. Interf. Electrochem.* **1977**, 78 (2), 403–407.



- (27) Kinzel, N. W.; Werlé, C.; Leitner, W. Transition Metal Complexes as Catalysts for the Electroconversion of CO<sub>2</sub>: An Organometallic Perspective. *Angew. Chem. Int. Ed.* **2021**, *60* (21), 11628–11686.
- (28) Bard, A.J.; Faulkner, L.R. *Electrochemical Methods: Fundamentals and Applications*. Wiley, 2<sup>nd</sup> edition, **2000**.
- (29) Appel, A. M.; Helm, M. L. Determining the Overpotential for a Molecular Electrocatalyst. *ACS Catal.* **2014**, *4* (2), 630–633.
- (30) Boutin, E. Sequential Electrochemical Reduction of Carbon Dioxide into Methanol, in Aqueous Media with Cobalt Phthalocyanines. *Doctoral Thesis - Université de Paris*. **2019**, pp. 11 - 25.
- (31) Costentin, C.; Drouet, S.; Robert, M.; Savéant, J.-M. Turnover Numbers, Turnover Frequencies, and Overpotential in Molecular Catalysis of Electrochemical Reactions. Cyclic Voltammetry and Preparative-Scale Electrolysis. *J. Am. Chem. Soc.* **2012**, *134* (27), 11235–11242.
- (32) Costentin, C.; Passard, G.; Savéant, J.-M. Benchmarking of Homogeneous Electrocatalysts: Overpotential, Turnover Frequency, Limiting Turnover Number. *J. Am. Chem. Soc.* **2015**, *137* (16), 5461–5467.
- (33) Costentin, C.; Robert, M.; Savéant, J.-M. Catalysis of the Electrochemical Reduction of Carbon Dioxide. *Chemical Society Reviews* **2013**, *42* (6), 2423–2436.
- (34) Savéant, J.-M. *Elements of Molecular and Biomolecular Electrochemistry: An Electrochemical Approach to Electron Transfer Chemistry*, John Wiley & Sons. **2006**, pp. 78 - 181.
- (35) Walker, F. A.; Simonis, U. Iron Porphyrin Chemistry. *Encyclopedia of Inorganic Chemistry*. Volume IV. John Wiley & Sons. 2<sup>nd</sup> edition. **2006**. pp: 2390-2521.
- (36) Everse, J. Heme Proteins. *Encyclopedia of Biological Chemistry*. Lennarz, W. J., Lane, M. D., Eds.; Academic Press: Waltham, 2<sup>nd</sup> edition. **2013**. pp 532–538.
- (37) Cook, D. J.; Finnigan, J. D.; Cook, K.; Black, G. W.; Charnock, S. J. Chapter Five - Cytochromes P450: History, Classes, Catalytic Mechanism, and Industrial Application. *Advances in Protein Chemistry and Structural Biology*. Christov, C. Z., Ed.; Insights into Enzyme Mechanisms and Functions from Experimental and Computational Methods; Academic Press, **2016**; Vol. 105, pp 105–126.
- (38) Hammouche, M.; Lexa, D.; Savéant, J.-M.; Momenteau, M. Catalysis of the Electrochemical Reduction of Carbon Dioxide by Iron(“0”) Porphyrins. *J. Electroanal. Chem. Interf. Electrochem.* **1988**, *249* (1), 347–351.
- (39) Tatin, A. Electrochemical CO<sub>2</sub> Splitting into CO and O<sub>2</sub> in Neutral Water Using Earth-Abundant Materials. *Doctoral Thesis - Université Paris Diderot*. **2016**. pp. 35 - 45.
- (40) Lexa, D.; Rentien, P.; Savéant, J.-M.; Xu, F. Methods for Investigating the Mechanistic and Kinetic Role of Ligand Exchange Reactions in Coordination Electrochemistry: Cyclic Voltammetry of Chloroiron(III)Tetraphenylporphyrin in Dimethylformamide. *J. Electroanal. Chem. Interf. Electrochem.* **1985**, *191* (2), 253–279.
- (41) Hammouche, M.; Lexa, D.; Momenteau, M.; Savéant, J.-M. Chemical Catalysis of Electrochemical Reactions. Homogeneous Catalysis of the Electrochemical Reduction of



- Carbon Dioxide by Iron(“0”) Porphyrins. Role of the Addition of Magnesium Cations. *J. Am. Chem. Soc.* **1991**, *113* (22), 8455–8466.
- (42) Passard, G. Transfert Couple Électron/Proton et Rupture de Liaison Dans Les Processus Électrocatalytiques. *These de doctorat, Paris 7*, **2014**. pp. 35 - 45.
- (43) Costentin, C.; Drouet, S.; Passard, G.; Robert, M.; Savéant, J.-M. Proton-Coupled Electron Transfer Cleavage of Heavy-Atom Bonds in Electrocatalytic Processes. Cleavage of a C–O Bond in the Catalyzed Electrochemical Reduction of CO<sub>2</sub>. *J. Am. Chem. Soc.* **2013**, *135*, 24, 9023 - 9031.
- (44) Bhugun, I.; Lexa, D.; Savéant, J.-M. Catalysis of the Electrochemical Reduction of Carbon Dioxide by Iron(0) Porphyrins. Synergistic Effect of Lewis Acid Cations. *J. Phys. Chem.* **1996**, *100* (51), 19981–19985.
- (45) Bhugun, I.; Lexa, D.; Savéant, J.-M. Ultraefficient Selective Homogeneous Catalysis of the Electrochemical Reduction of Carbon Dioxide by an Iron(0) Porphyrin Associated with a Weak Bronsted Acid Cocatalyst. *J. Am. Chem. Soc.* **1994**, *116* (11), 5015–5016.
- (46) Bhugun, I.; Lexa, D.; Savéant, J.-M. Homogeneous Catalysis of Electrochemical Hydrogen Evolution by Iron(0) Porphyrins. *J. Am. Chem. Soc.* **1996**, *118*, 16, 3982 - 3983.
- (47) Costentin, C.; Passard, G.; Robert, M.; Savéant, J.-M. Pendant Acid–Base Groups in Molecular Catalysts: H-Bond Promoters or Proton Relays? Mechanisms of the Conversion of CO<sub>2</sub> to CO by Electrogenenerated Iron(0)Porphyrins Bearing Prepositioned Phenol Functionalities. *J. Am. Chem. Soc.* **2014**, *136*, 33, 11821 - 11829.
- (48) Costentin, C.; Robert, M.; Savéant, J.-M.; Tatin, A. Efficient and selective molecular catalyst for the CO<sub>2</sub>-to-CO electrochemical conversion in water. *PNAS.* **2015**, *112* (22), 6882 - 6886.

# Chapter III

---

## - Introduction -

### X-Ray Absorption Spectroelectrochemistry

#### Content

---

3.1	<i>In situ</i> spectroelectrochemical methods to study CO <sub>2</sub> reducing reactions.....	28
3.2	X-Ray Absorption Spectroscopy (XAS) .....	29
3.2.1	Origins, description, and useful terminology .....	29
3.2.2	What can we learn from a XAS spectrum? .....	30
3.2.3	Advantages and limitations .....	32
3.3	X-Ray absorption spectroelectrochemistry as a tool for the study of CO <sub>2</sub> reducing molecular catalysts .....	33
3.4	References .....	35



Electrochemistry is a prevalent technique broadly used in many scientific fields both as an analytical tool in the laboratory but also as a production mean at industrial scales.<sup>1,2</sup> Traditional electrochemical methods, such as cyclic voltammetry or chronoamperometry have been widely used to determine redox potentials, to follow changes at the electrode surface, to elucidate kinetics parameters, and therefore, to propose reactions mechanism. Hence, the information gained by using this technique to study the CO<sub>2</sub> reducing reaction has undoubtedly been very substantial, obtaining many kinetic data that has allowed to propose catalytic pathways.<sup>3-5</sup>

While electrochemistry can provide information regarding reaction kinetics, it provides little information on the local and electronic structure of the species studied. On the contrary, spectroscopy can provide this information, either in the solid or liquid states. Therefore, both techniques can complement each other for the identification of intermediate species.<sup>6</sup> The main advantage of spectroelectrochemistry (SEC) is that the two measurements are recorded concomitantly, reducing the risks of misinterpretations due to different experimental conditions.<sup>7</sup>

To date, many spectroscopic studies on electrochemical systems are performed in an *ex situ* manner, meaning that the electrochemical activation is performed prior the spectroscopic characterization in an external device, the sample being then transferred for analysis.<sup>7</sup> Such studies include molecular catalysts immobilized on high surface area electrodes, which are probed before and after controlled potential electrolysis (CPE), addressing changes at the electrode induced by the application of an electrochemical potential.<sup>8-12</sup> Other studies have been reported in homogeneous conditions by performing CPE at a set potential to generate a specific species, followed by freezing of the solution and its later analysis by spectroscopic techniques under cryogenic conditions.<sup>13,14</sup> Other *ex situ* methods include the chemical preparation of reduced/oxidized species and their analysis by spectroscopic tools in the solid state.<sup>15-17</sup> However, *ex situ* methods are limited since the analysis is performed only after activation and not during working conditions, which impedes tracking the changes directly correlated with the activity. In addition to this, washing, drying and/or transporting the materials to the spectrometer after its electrochemical activation can alter the material composition leading to inaccurate measurements and conclusions.<sup>18,19</sup> Hence, *in situ* and *operando* spectroelectrochemistry was developed to follow chemical transformations during working conditions.

A distinction needs to be made between *in situ* and *operando* spectroelectrochemical experiments. An experiment is considered *in situ* when the reactants or products of a reaction (not catalytic, *i.e.* an electron transfer, the formation/breaking of a bond, a reaction between two species) can be observed directly in their reaction conditions. An experiment is considered *operando* when it is probing an electrocatalytic reaction under conditions that are

as close as possible to those in which the catalyst performance has been established. *In situ* and/or *operando* measurements require the development of specific instrumentation related to the conditions in which the reactions occur, often adding complexity to spectroelectrochemical experiments.<sup>20</sup>

*In situ* and/or *operando* measurements can be classified based on the spectral response time, which usually depend on the instrumentation and experimental conditions. Therefore, one can perform *steady-state* experiments, in which generally controlled potential electrolysis is performed while the spectroscopic measurement is recorded. The majority of spectroelectrochemical cells developed so far allow the recording of data in this manner, with timescales of a few seconds to minutes.

### 3.1 *In situ* spectroelectrochemical methods to study CO<sub>2</sub> reducing reactions

Although important progresses have been achieved in the last decade in the study of electrocatalytic CO<sub>2</sub> reduction by molecular catalyst, the identification of key intermediates, described by their local and electronic structure, is still missing. Hence, following the evolution of these catalysts under *in situ* and/or *operando* conditions is a pre-requisite to the catalyst optimization.<sup>21</sup>

To date, many spectroelectrochemical methods have been used to study the CO<sub>2</sub> reduction reaction. Each of these techniques provide specific information on the oxidation or spin states, ligand binding, as well as on the electronic density localization and on the local structure of the species of interest.<sup>22</sup> These techniques require, however, dedicated instrumentation (photon sources, detectors) and sample conditions that impose constraints on the development of spectroelectrochemical tools to perform *in situ* or *operando* measurements.

For the study of the CO<sub>2</sub>RR, UV-Vis spectroelectrochemistry (UV-Vis-SEC) has been used to follow electronic transitions driven by electrochemical activation, most often in homogeneous system.<sup>23–25</sup> However, even if the instrumentation required is usually less complex than for other spectroscopic techniques, the analysis of the data is limited to literature comparisons, unless theoretical calculations are performed.<sup>26</sup>

Because the CO<sub>2</sub> molecule and its reaction products have strong polarized chemical bonds, vibrational spectroelectrochemical methods have been used to follow changes during the CO<sub>2</sub>RR.<sup>22</sup> Regarding Raman spectroscopy, it is usually used to study the coordination of species to the catalysts, although it sometimes leads to photodegradation of the sample.<sup>21</sup> Concerning IR spectroscopy, due to its wide spectral range, this technique has been used to study the binding modes of CO<sub>2</sub> to the catalyst,<sup>27–29</sup> although recent studies have also shown

its ability to identify the valence state and structural changes.<sup>30,31</sup> However, the sensitivity of internal sources, and the impact of the solvent-electrolyte in the detection make the analysis rather limited and/or challenging.

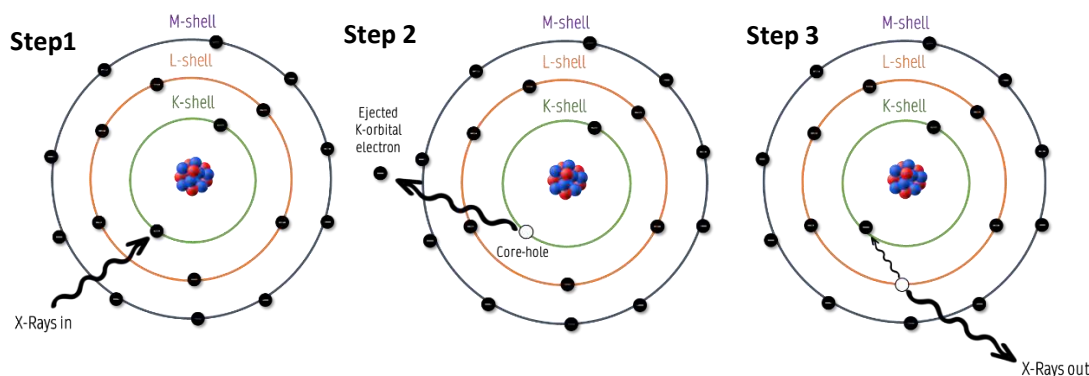
Even if UV-Vis, IR and Raman spectroscopy have been traditionally employed for studying the CO<sub>2</sub> reduction reaction catalyzed by iron porphyrins, as further described in chapter IV, they usually lack sensitivity, show the signature of other elements presented in the sample or depend on the state of the sample making its application limited. Therefore, we decided to use X-ray absorption spectroscopy (XAS), which has many spectroscopic advantages but is also more demanding in terms of instrumentation.

## 3.2 X-Ray Absorption Spectroscopy (XAS)

### 3.2.1 Origins, definition and useful terminology

After the discovery of X-rays in 1895 by W. Röntgen, it took some time to obtain the first XAS spectrum.<sup>32</sup> Indeed, it was only until 1913 when H. Moseley quantified the atomic number by measuring the emitted X-ray<sup>33</sup> followed by Fricke who measured the sudden increase of the absorption for several elements, from magnesium to chromium in 1920.<sup>34</sup> Since then, the understanding of XAS techniques grew along with the continuous comprehension of the atomic structure. However, it was only in the 70s' that absorption edges were finally measured at the synchrotron becoming a breakthrough for XAS applicability.<sup>35</sup> The brilliance of the synchrotron radiation allowed the decrease of a single measurement from weeks to hours, later pushed to minutes and nowadays to the picosecond scale. The impact of XAS measurements is evident for many scientific fields, which is continuously in progress and substantially increasing every year.

X-Ray absorption spectroscopy is a characterization technique in which an electron is excited by the absorption of an X-ray photon, providing information on unoccupied electronic levels.<sup>36,37</sup> As represented in scheme 3.1, in order for this to happen, an electron must be excited. Initially, the incident energy is absorbed by an electron in the inner-core shell (step 1). After this, the excitation of the deep-core electron occurs towards an unoccupied state beyond the Fermi level, leaving a core-hole (step 2). Finally, this hole is further filled by the recombination of a higher-level electron, which in the process emits a photon of lower energy than the one promoting the core electron in step 1 (step 3).<sup>38</sup>



**Scheme 3.1.** Simplified representation of the physical phenomena occurring during electron excitation by X-rays.

Adapted from reference 38.

In XAS, the electron gets excited from the core level towards an unoccupied orbital above the Fermi level. For this reason, the excited electron is known as a **core electron** and the empty space left in the resulting atom is known as a **core hole**. When the binding energy of the core electron matches the energy of the incident energy a sharp signal increase is observed in the XAS spectrum, known as the **absorption edge or rising edge**.<sup>20,37</sup> The X-ray notation defines the energy level from where the electron has been excited. For instance, when the electron that gets promoted is located at the innermost shell the absorption that occurs is defined as the **K-edge**.<sup>37,38</sup>

### 3.2.2 What can we learn from an XAS spectrum?

An XAS spectrum can be divided in two regions, XANES and EXAFS, defined by their energy range, as described in figure 3.1. The physical principles of both regions are briefly described in appendix B. This section is devoted to explaining the different information that one can get by analyzing these regions.

**X-Ray Absorption Near Edge Structure (XANES):** the K-edge main feature is due to an allowed transition from the  $1s$  orbital to the lowest unoccupied orbital  $np$ . Its position is usually used to assess the *oxidation state* of the absorbing atom. Therefore, the higher the oxidation state of the metal, the more energy will be required to ionize a core-electron, resulting in an edge shift towards higher energies.<sup>37</sup> As a rule of thumb, a shift of 1 to 2 eV at the rising edge energy is translated to a change in the oxidation state by 1 unit.<sup>36</sup> This edge value can be obtained by measuring the energy position either at the peak top of the first derivative of the absorption edge, or at half the intensity of the normalized spectrum (so-called *half edge jump*).<sup>39</sup> Both methods are, however, not absolute since the different transitions that compose a XANES spectrum can lead to complex features and hence a difficult reading of the edge energy position. It should therefore be considered with care and adapted to each situation, ideally comparing systems with similar molecular structures. In

this manuscript, we have chosen to report edge energy positions measured at the half edge jump, unless notified.

The **pre-edge** is a specific region observed just before the main edge. In transition metal complexes it is present due to a transition from the  $1s$  orbital to the  $(n-1)d$  orbitals, as described in figure 3.1 - b. In centrosymmetric complexes, such as octahedral structures, this transition is spectroscopically forbidden, generating weak pre-edge intensities. When the geometry around the excited ion deviates from a perfect octahedron, such as in a tetrahedron,  $3d$  and  $4p$  orbitals mix and the transition to  $p$ -containing orbitals becomes allowed, leading to a pre-edge with a higher intensity.<sup>36</sup> More generally, any change in the organization of the valence levels that lead to a rearrangement of the  $p$ - $d$  mixing will lead to changes in the pre-edge transitions, both in energy and intensity. Hence, this region is extremely useful in determining *site symmetry*, *spin states*, *ligands exchange* or any *geometrical changes*. These variations have been illustrated, for example, by Westre *et al.* for a series of iron complexes, serving as a guide when analyzing this region.<sup>40</sup> Pre-edge peak energies can be obtained by measuring either the peak top of the first derivative (which represents the 1st inflection point of the pre-edge in the normalized spectrum) or by taking the 0-crossing point of the first derivative. In this manuscript, we have chosen to report the pre-edge peak positions measured at the peak top of the first derivative (further information in appendix D).

**Extended X-Ray Absorption Fine Structure (EXAFS):** corresponds to the oscillations observed in the energy region from *ca.* 50 eV to *ca.* a thousand eV after the edge. These oscillations arise from the interaction of the ionized core-electron, which can also be described as a wave function, with surrounding atoms of the excited element. These interactions generate constructive and destructive interferences because of the scattering of the neighboring atoms and produce the EXAFS pattern.<sup>37</sup> Therefore, EXAFS provides information relative to the *number of ligands* around the absorber atom and their *atomic distances*. As described in appendix B, the Fourier transform of the raw signal allows not only to obtain qualitative information, but also quantitative data.

Because of the low concentration of the samples (*e.g.* 2 mM) imposed by electrochemical conditions, this thesis was focused on the use of XANES at the iron K-edge rather than EXAFS. Conclusions shown in this thesis are based on purely qualitative data supported by comparison of chemically reduced, electrogenerated species and references of the literature. Basically, two aspects were considered:

- 1) The position of the main absorption edge to get insights into oxidation state changes.
- 2) The presence, intensity, and shape of the pre-edge to get insights into the spin state and structural changes.



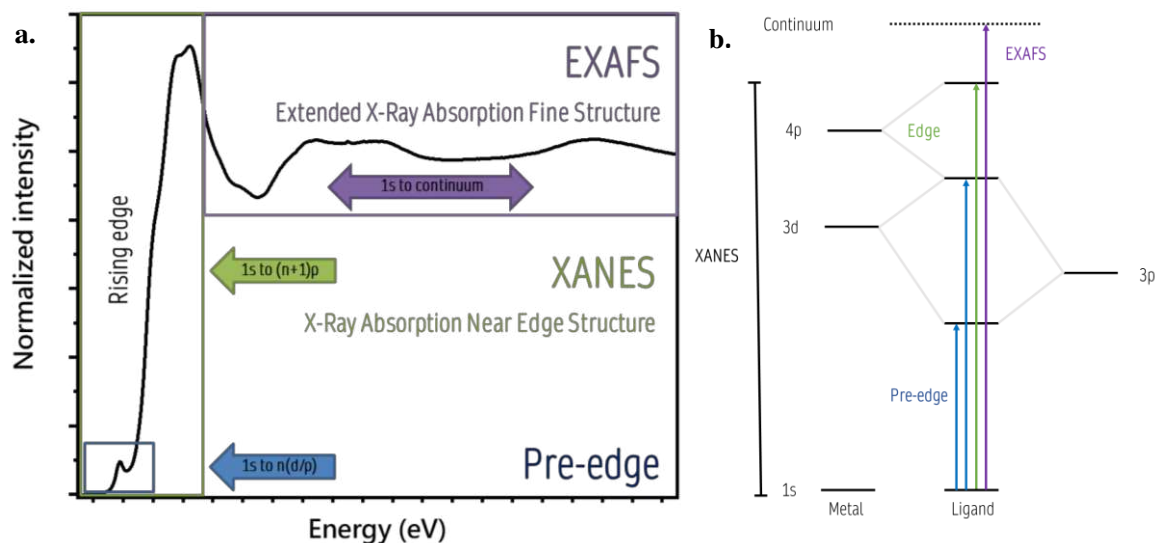


Figure 3.1. a. X-Ray absorption spectrum showing its two main regions: XANES, including the pre-edge feature and EXAFS; b. Energy diagram for a transition metal complex, indicating the transition that gives rise to each part of an XAS spectrum.

Adapted from reference 36.

### 3.2.3 Advantages and limitations

The advantages offered by XAS can be summarized as follows:

1) It is an **element-specific** technique, meaning that only the absorber atom is singled out during measurement. This reduces the risks of parasitic signal from the electrolyte, the solvent or other elements in the sample or the medium. This is a clear advantage over techniques such as IR, Raman or even UV-Vis spectroscopy.

2) In contrast to electron paramagnetic studies (EPR) or nuclear magnetic resonance (NMR), the absorbing atoms probed by XAS are **never silent**, ensuring that the element of interest will always produce a signal.

3) As opposed to diffraction methods that require crystalline samples, XAS is **not restricted to the state of the sample**. Therefore, solid samples, solutions or gases can be analyzed by XAS. In addition, samples are not required to be perfectly homogenous, allowing the study of heterogeneous and disorder systems.

4) In contrast to UV-Vis experiments, XAS is **not limited to transmission measurements**. Therefore, several detection modes (transmission, fluorescence, or electron yield) can be used to adapt to complex experimental conditions. More details on these data collection modes can be found in appendix B.

5) It is a **non-destructive** technique. Even though X-rays can cause damage due to radiations, as further discussed in chapter V, with the right experimental precautions, one can obtain reliable data without destroying the sample.

6) It is a **complete** technique that allows obtaining an **extensive amount of information** in a single experiment, as previously described. Therefore, due to the large range of energy sweep in a single spectrum, a complete mapping of the molecular orbital can be obtained.

7) The **high penetration depth** of X-rays is high (*ca.* 0.6mm at an X-ray energy of 7.0 keV in a material with a density of 1)<sup>41</sup>, which allows complex *in situ* or *operando* experimental setups.

XAS also implies some limitations, which can be summarized as follows:

- 1) The experimental timeframe due to the limited access to synchrotron, requires long waiting times, proposal acceptance and a careful planning as further described in appendix B.
- 2) The data generated by XANES is complex to analyze and interpret, usually requiring the use of another complementarity technique, comparison with well-established reference samples or analysis by quantum chemistry calculations.
- 3) Challenges of instrumentation development for *in situ* or *operando* experiments as further describe in chapter V. Parameters such as radiation damage, signal to noise and attenuation as well as high electrochemical conversion are key to address reproducible and optimal spectroscopic signatures.

### 3.3 X-ray absorption spectroelectrochemistry as a tool for the study of CO<sub>2</sub> reducing molecular catalysts.

The use of X-ray absorption spectroelectrochemistry to study the CO<sub>2</sub>RR has gained interest in recent years, along with the development of more efficient catalysts. Many reports have shown the applicability of this technique to give valuable information regarding the study of metallic and nanoparticles-based electrocatalysts. Even though many metals are known to convert CO<sub>2</sub> to C1 products, copper-based electrodes are the ones showing the best conversion of CO<sub>2</sub> to light hydrocarbons (mostly methane and ethylene). For this reason, copper-based catalysts have been extensively studied using *operando* X-ray spectroscopy in the last years.<sup>42-49</sup> Nitrogen-doped carbon materials have also gained importance in the late years due to the promising results they have shown in the conversion of CO<sub>2</sub> to C2 products.<sup>50-52</sup> By having a single dispersed metal site, these materials constitute the frontier between materials and molecular catalysts.

X-ray absorption spectroelectrochemical (XAS-EC) studies of the CO<sub>2</sub>RR catalyzed by molecular catalysts have been rather limited to *ex situ* characterization as described above.

However, important advances have been performed in the late years in the study of immobilized molecular catalysts over high surface carbon materials. For instance, Weng *et al.* have used *in situ operando* XAS-EC techniques in order to probe the electronic and structural changes occurring during working condition on a deposited copper(II) phthalocyanine (CuPc) complex onto carbon paper. This improved material showed a high faradaic efficiency (66%) towards the generation of methane. Using XANES, they were able to show that *ca.* 2 nm copper particles were formed upon application of a reductive potential, and were responsible for catalysis.<sup>53</sup> Interestingly, Karapinar *et al.* also reached a similar conclusion after analyzing an electrode containing copper polyphthalocyanine in a carbon-based material. By probing the electrode by XANES, they concluded that copper nanoparticles were the active species for the production of CO (with a faradaic efficiency of 80%), which could be converted back to the initial copper species by applying an oxidative potential.<sup>54</sup> Liu *et al.* showed that encapsulating cobalt phthalocyanine (CoPc) in a polymer matrix (poly-4-vinylpyridine - P4VP) and deposited over a carbon paper reduces CO<sub>2</sub> to CO at fast rates. The enhanced catalysis was attributed to coordination effects which was confirmed by *in situ* XANES. It was confirmed that the geometry of the CoPc-P4VP remains the same (square pyramidal structure) even if a potential was applied or CO<sub>2</sub> was incorporated in the media<sup>55</sup>.

A heterogenized zinc porphyrin complex into carbon fiber paper has also being analyzed by *in situ* XAS. The results indicate that the zinc center remains in the Zn(II) oxidation state, even at a potential as negative as -1.7 V vs. SHE. These results show that metallic zinc particles did not form during electroreduction and that the reduction occurs rather on the molecular catalyst itself.<sup>56</sup> Recent *in situ-operando* spectroelectrochemical XAS studies of iron porphyrin immobilized on a carbon material have shown that catalytic activity occurs at the Fe(II) level, with accumulation of the Fe-CO adduct throughout the experiment.<sup>57</sup> We will address this report in more details in the next chapter.

Despite the increased growth and popularity of XAS spectroelectrochemical measurements to study CO<sub>2</sub>RR in heterogenized molecular catalyst, *in situ/operando* studies on homogeneous catalysts is very limited. This project aims at filling this lack, by studying iron porphyrins in homogeneous conditions with *in situ* XAS spectroelectrochemistry. By using homogeneous conditions in an environment close to experimental conditions used in the laboratory, a better correlation between electrochemical and spectroscopic data can be achieved. Insights into the electronic and structural changes of iron porphyrins during electroreduction but also during CO<sub>2</sub>RR are described in chapter VI and VII, respectively. The next chapter gives an introduction to the electronic structures of iron porphyrins and on some spectroscopic studies that have been performed on this system during the last decades.

### 3.4. References – Chapter III

- (1) Tanbouza, N.; Ollevier, T.; Lam, K. Bridging Lab and Industry with Flow Electrochemistry. *iScience* **2020**, *23* (11), 101720.
- (2) Thonemann, N.; Schulte, A. From Laboratory to Industrial Scale: A Prospective LCA for Electrochemical Reduction of CO<sub>2</sub> to Formic Acid. *Environ. Sci. Technol.* **2019**, *53* (21), 12320–12329.
- (3) Francke, R.; Schille, B.; Roemelt, M. Homogeneously Catalyzed Electroreduction of Carbon Dioxide-Methods, Mechanisms, and Catalysts. *Chem Rev.* **2018**, *118* (9), 4631–4701.
- (4) Costentin, C.; Robert, M.; Savéant, J.-M. Catalysis of the Electrochemical Reduction of Carbon Dioxide. *Chem. Soc. Rev.* **2013**, *42* (6), 2423–2436.
- (5) Garza, A. J.; Bell, A. T.; Head-Gordon, M. Mechanism of CO<sub>2</sub> Reduction at Copper Surfaces: Pathways to C<sub>2</sub> Products. *ACS Catal.* **2018**, *8* (2), 1490–1499.
- (6) Kaim, W.; Fiedler, J. Spectroelectrochemistry: The Best of Two Worlds. *Chem. Soc. Rev.* **2009**, *38* (12), 3373–3382.
- (7) León, L.; Mozo, J. D. Designing Spectroelectrochemical Cells: A Review. *Trends Analyt. Chem.* **2018**, *102*, 147–169.
- (8) Xia, Y.; Kashtanov, S.; Yu, P.; Chang, L.-Y.; Feng, K.; Zhong, J.; Guo, J.; Sun, X. Identification of Dual-Active Sites in Cobalt Phthalocyanine for Electrochemical Carbon Dioxide Reduction. *Nano Energy* **2020**, *67*, 104163.
- (9) Torbensen, K.; Han, C.; Boudy, B.; Wolff, N. von; Bertail, C.; Braun, W.; Robert, M. Iron Porphyrin Allows Fast and Selective Electrocatalytic Conversion of CO<sub>2</sub> to CO in a Flow Cell. *Chem. Eur. J.* **2020**, *26* (14), 3034–3038.
- (10) Li, N.; Lu, W.; Pei, K.; Chen, W. Interfacial Peroxidase-like Catalytic Activity of Surface-Immobilized Cobalt Phthalocyanine on Multiwall Carbon Nanotubes. *RSC Adv.* **2015**, *5* (13), 9374–9380.
- (11) Boutin, E.; Wang, M.; Lin, J. C.; Mesnage, M.; Mendoza, D.; Lassalle-Kaiser, B.; Hahn, C.; Jaramillo, T. F.; Robert, M. Aqueous Electrochemical Reduction of Carbon Dioxide and Carbon Monoxide into Methanol with Cobalt Phthalocyanine. *Angew Chem Int Ed.* **2019**, *58* (45), 16172–16176.
- (12) Cometto, C.; Chen, L.; Mendoza, D.; Lassalle-Kaiser, B.; Lau, T.-C.; Robert, M. An Iron Quaterpyridine Complex as Precursor for the Electrocatalytic Reduction of CO<sub>2</sub> to Methane. *ChemSusChem* **2019**, *12* (19), 4500–4505.
- (13) Fernández, S.; Franco, F.; Casadevall, C.; Martin-Diaconescu, V.; Luis, J. M.; Lloret-Fillol, J. A Unified Electro- and Photocatalytic CO<sub>2</sub> to CO Reduction Mechanism with Aminopyridine Cobalt Complexes. *J. Am. Chem. Soc.* **2020**, *142* (1), 120–133.
- (14) Mondal, B.; Rana, A.; Sen, P.; Dey, A. Intermediates Involved in the 2e<sup>-</sup>/2H<sup>+</sup> Reduction of CO<sub>2</sub> to CO by Iron(0) Porphyrin. *J. Am. Chem. Soc.* **2015**, *137* (35), 11214–11217.

- (15) Römelt, C.; Song, J.; Tarrago, M.; Rees, J. A.; van Gastel, M.; Weyhermüller, T.; DeBeer, S.; Bill, E.; Neese, F.; Ye, S. Electronic Structure of a Formal Iron(0) Porphyrin Complex Relevant to CO<sub>2</sub> Reduction. *Inorg. Chem.* **2017**, *56* (8), 4745–4750.
- (16) Cartier, C.; Momenteau, M.; Dartyge, P.; Fontaine, A.; Tourillon, G.; Michalowicz, A. X-Ray Absorption Spectroscopy of Iron-(II) and -(III) Basket-Handle Porphyrin. *J. Chem. Soc. Dalton Trans.* **1992**, 10.
- (17) Römelt, C.; Ye, S.; Bill, E.; Weyhermüller, T.; van Gastel, M.; Neese, F. Electronic Structure and Spin Multiplicity of Iron Tetraphenylporphyrins in Their Reduced States as Determined by a Combination of Resonance Raman Spectroscopy and Quantum Chemistry. *Inorg. Chem.* **2018**, *57* (4), 2141–2148.
- (18) Weckhuysen, B. M. Determining the Active Site in a Catalytic Process: Operando Spectroscopy Is More than a Buzzword. *Phys. Chem. Chem. Phys.* **2003**, *5* (20), 4351–4360.
- (19) Nakanishi, K.; Kato, D.; Arai, H.; Tanida, H.; Mori, T.; Orikasa, Y.; Uchimoto, Y.; Ohta, T.; Ogumi, Z. Novel Spectro-Electrochemical Cell for in Situ/Operando Observation of Common Composite Electrode with Liquid Electrolyte by X-Ray Absorption Spectroscopy in the Tender X-Ray Region. *Rev. Sci. Instrum.* **2014**, *85* (8), 084103.
- (20) Timoshenko, J.; Roldan Cuenya, B. In Situ/Operando Electrocatalyst Characterization by X-Ray Absorption Spectroscopy. *Chem. Rev.* **2021**, *121* (2), 882–961.
- (21) Li, X.; Wang, S.; Li, L.; Sun, Y.; Xie, Y. Progress and Perspective for In Situ Studies of CO<sub>2</sub> Reduction. *J. Am. Chem. Soc.* **2020**, *142* (21), 9567–9581.
- (22) Bunea, S.; Urakawa, A. Chapter 9: In Situ Spectroscopic Methods to Study Electrochemical CO<sub>2</sub> Reduction. In *Carbon Dioxide Electrochemistry*; **2020**; pp 347–407.
- (23) Isaacs, M.; Armijo, F.; Ramírez, G.; Trollund, E.; Biaggio, S. R.; Costamagna, J.; Aguirre, M. J. Electrochemical Reduction of CO<sub>2</sub> Mediated by Poly-M-Aminophthalocyanines (M=Co, Ni, Fe): Poly-Co-Tetraaminophthalocyanine, a Selective Catalyst. *J. Mol. Catal A: Chem.* **2005**, *229* (1), 249–257.
- (24) Bourrez, M.; Molton, F.; Chardon-Noblat, S.; Deronzier, A. [Mn(Bipyridyl)(CO)<sub>3</sub>Br]: An Abundant Metal Carbonyl Complex as Efficient Electrocatalyst for CO<sub>2</sub> Reduction. *Angew Chem Int Ed.* **2011**, *50* (42), 9903–9906.
- (25) Tory, J.; Gobaille-Shaw, G.; Chippindale, A. M.; Hartl, F. Spectroelectrochemical Study of Complexes [Mo(CO)<sub>2</sub>(H<sub>3</sub>-Allyl)( $\alpha$ -Diimine)(NCS)] ( $\alpha$ -Diimine = Bis(2,6-Dimethylphenyl)-Acenaphthenequinonediimine and 2,2'-Bipyridine) Exhibiting Different Molecular Structure and Redox Reactivity. *J. Organomet. Chem.* **2014**, *760*, 30–41.
- (26) Anxolabéhère, E.; Chottard, G.; Lexa, D. Highly reduced iron porphyrin: UV-Vis and resonance Raman spectroelectrochemical studies of FeTPP and FeTF<sub>3</sub>PP. *New. J. Chem.* **1994**, *18*, 889-899.
- (27) Machan, C. W.; Sampson, M. D.; Chabolla, S. A.; Dang, T.; Kubiak, C. P. Developing a Mechanistic Understanding of Molecular Electrocatalysts for CO<sub>2</sub> Reduction Using Infrared Spectroelectrochemistry. *Organometallics* **2014**, *33* (18), 4550–4559.

- (28) Machan, C. W.; Stanton, C. J.; Vandezande, J. E.; Majetich, G. F.; Schaefer, H. F.; Kubiak, C. P.; Agarwal, J. Electrocatalytic Reduction of Carbon Dioxide by Mn(CN)(2,2'-Bipyridine)(CO)<sub>3</sub>: CN Coordination Alters Mechanism. *Inorg. Chem.* **2015**, *54* (17), 8849–8856.
- (29) Guo, Z.; Chen, G.; Cometto, C.; Ma, B.; Zhao, H.; Groizard, T.; Chen, L.; Fan, H.; Man, W.-L.; Yiu, S.-M.; Lau, K.-C.; Lau, T.-C.; Robert, M. Selectivity Control of CO versus HCOO<sup>-</sup> Production in the Visible-Light-Driven Catalytic Reduction of CO<sub>2</sub> with Two Cooperative Metal Sites. *Nat Catal.* **2019**, *2* (9), 801–808.
- (30) Lejeune, J.; Brubach, J.-B.; Roy, P.; Bleuzen, A. Application of the Infrared Spectroscopy to the Structural Study of Prussian Blue Analogues. *C. R. Chim.* **2014**, *17* (6), 534–540.
- (31) Vita, N.; Brubach, J.-B.; Hienerwadel, R.; Bremond, N.; Berthomieu, D.; Roy, P.; Berthomieu, C. Electrochemically Induced Far-Infrared Difference Spectroscopy on Metalloproteins Using Advanced Synchrotron Technology. *Anal. Chem.* **2013**, *85* (5), 2891–2898.
- (32) Lamberti, C.; van Bokhoven, J. A. Introduction: Historical Perspective on XAS. In *X-Ray Absorption and X-Ray Emission Spectroscopy*; John Wiley & Sons, Ltd, 2016; pp 1–21.
- (33) Moseley, H. G. J. XCIII. The High-Frequency Spectra of the Elements. *The London, Edinburgh, and Dublin Philosophical Magazine and Journal of Science* **1913**, *26* (156), 1024–1034.
- (34) Fricke., H. The K-Characteristic Absorption Frequencies for the Chemical Elements Magnesium to Chromium. *Phys. Rev.* **1920**, *16* (3), 202–215.
- (35) Malzer, W.; Schlesiger, C.; Kanngießner, B. A Century of Laboratory X-Ray Absorption Spectroscopy – A Review and an Optimistic Outlook. *Spectrochim Acta. B.* **2021**, *177* (C).
- (36) Kowalska, J.; DeBeer, S. The Role of X-Ray Spectroscopy in Understanding the Geometric and Electronic Structure of Nitrogenase. *Biochim Biophys.* **2015**, *1853* (6), 1406–1415.
- (37) Yano, J.; Yachandra, V. K. X-Ray Absorption Spectroscopy. *Photosynth Res* **2009**, *102* (2), 241–254.
- (38) Ravel, B. Introduction to X-Ray Absorption Spectroscopy. *Columbia University*. Lecture 4. **2015**. p 6 - 9.
- (39) Lassalle-Kaiser, B.; Gul, S.; Kern, J.; Yachandra, V. K.; Yano, J. In Situ/Operando Studies of Electrocatalysts Using Hard X-Ray Spectroscopy. *Journal of Electron Spectroscopy and Related Phenomena* **2017**, *221*, 18–27.
- (40) Westre, T. E.; Kennepohl, P.; DeWitt, J. G.; Hedman, B.; Hodgson, K. O.; Solomon, E. I. A Multiplet Analysis of Fe K-Edge 1s → 3d Pre-Edge Features of Iron Complexes. *J. Am. Chem. Soc.* **1997**, *119* (27), 6297–6314.
- (41) Kirz, J.; Attwood, D.; Henke, B.; Howells, M.; Kennedy, K.; Kim, K., et al. Center for X-ray Optics, X-ray Data Booklet. Lawrence Berkeley National Laboratory. **1986**.
- (42) Mistry, H.; Varela, A. S.; Bonifacio, C. S.; Zegkinoglou, I.; Sinev, I.; Choi, Y.-W.; Kisslinger, K.; Stach, E. A.; Yang, J. C.; Strasser, P.; Roldan Cuenya, B. Highly Selective Plasma-



- Activated Copper Catalysts for Carbon Dioxide Reduction to Ethylene. *Nat Commun* **2016**, *7* (1), 12123.
- (43) Jeon, H. S.; Timoshenko, J.; Scholten, F.; Sinev, I.; Herzog, A.; Haase, F. T.; Roldan Cuenya, B. Operando Insight into the Correlation between the Structure and Composition of CuZn Nanoparticles and Their Selectivity for the Electrochemical CO<sub>2</sub> Reduction. *J. Am. Chem. Soc.* **2019**, *141* (50), 19879–19887.
- (44) Herzog, A.; Bergmann, A.; Jeon, H. S.; Timoshenko, J.; Kühn, S.; Rettenmaier, C.; Lopez Luna, M.; Haase, F. T.; Roldan Cuenya, B. Operando Investigation of Ag-Decorated Cu<sub>2</sub>O Nanocube Catalysts with Enhanced CO<sub>2</sub> Electroreduction toward Liquid Products. *Angew Chem Int Ed.* **2021**, *60* (13), 7426–7435.
- (45) Behnaz Varandili, S.; Stoian, D.; Vavra, J.; Rossi, K.; R. Pankhurst, J.; T. Guntern, Y.; López, N.; Buonsanti, R. Elucidating the Structure-Dependent Selectivity of CuZn towards Methane and Ethanol in CO<sub>2</sub> Electroreduction Using Tailored Cu/ZnO Precatalysts. *Chem. Sci.* **2021**, *12* (43), 14484–14493.
- (46) Strach, M.; Mantella, V.; Pankhurst, J. R.; Iyengar, P.; Loiudice, A.; Das, S.; Corminboeuf, C.; van Beek, W.; Buonsanti, R. Insights into Reaction Intermediates to Predict Synthetic Pathways for Shape-Controlled Metal Nanocrystals. *J. Am. Chem. Soc.* **2019**, *141* (41), 16312–16322.
- (47) Vavra, J.; Shen, T.-H.; Stoian, D.; Tileli, V.; Buonsanti, R. Real-Time Monitoring Reveals Dissolution/Redeposition Mechanism in Copper Nanocatalysts during the Initial Stages of the CO<sub>2</sub> Reduction Reaction. *Angew. Chem. Intern. Ed.* **2021**, *60* (3), 1347–1354.
- (48) Eilert, A.; Roberts, F. S.; Friebel, D.; Nilsson, A. Formation of Copper Catalysts for CO<sub>2</sub> Reduction with High Ethylene/Methane Product Ratio Investigated with In Situ X-Ray Absorption Spectroscopy. *J. Phys. Chem. Lett.* **2016**, *7* (8), 1466–1470.
- (49) Friebel, D.; Mbuga, F.; Rajasekaran, S.; Miller, D. J.; Ogasawara, H.; Alonso-Mori, R.; Sokaras, D.; Nordlund, D.; Weng, T.-C.; Nilsson, A. Structure, Redox Chemistry, and Interfacial Alloy Formation in Monolayer and Multilayer Cu/Au(111) Model Catalysts for CO<sub>2</sub> Electroreduction. *J. Phys. Chem. C* **2014**, *118* (15), 7954–7961.
- (50) Genovese, C.; Schuster, M. E.; Gibson, E. K.; Gianolio, D.; Posligua, V.; Grau-Crespo, R.; Cibin, G.; Wells, P. P.; Garai, D.; Solokha, V.; Krick Calderon, S.; Velasco-Velez, J. J.; Ampelli, C.; Perathoner, S.; Held, G.; Centi, G.; Arrigo, R. Operando Spectroscopy Study of the Carbon Dioxide Electro-Reduction by Iron Species on Nitrogen-Doped Carbon. *Nat Commun* **2018**, *9* (1), 935.
- (51) Karapinar, D.; Huan, N. T.; Sahraie, N. R.; Li, J.; Wakerley, D.; Touati, N.; Zanna, S.; Taverna, D.; Tizei, L. H. G.; Zitolo, A.; Jaouen, F.; Mougél, V.; Fontecave, M. Electroreduction of CO<sub>2</sub> on Single-Site Copper-Nitrogen-Doped Carbon Material: Selective Formation of Ethanol and Reversible Restructuration of the Metal Sites. *Angew. Chem. Int. Ed.* **2019**, *58* (42), 15098–15103.



- (52) Pan, F.; Zhang, H.; Liu, K.; Cullen, D.; More, K.; Wang, M.; Feng, Z.; Wang, G.; Wu, G.; Li, Y. Unveiling Active Sites of CO<sub>2</sub> Reduction on Nitrogen-Coordinated and Atomically Dispersed Iron and Cobalt Catalysts. *ACS Catal.* **2018**, *8* (4), 3116–3122.
- (53) Weng, Z.; Wu, Y.; Wang, M.; Jiang, J.; Yang, K.; Huo, S.; Wang, X.-F.; Ma, Q.; Brudvig, G. W.; Batista, V. S.; Liang, Y.; Feng, Z.; Wang, H. Active Sites of Copper-Complex Catalytic Materials for Electrochemical Carbon Dioxide Reduction. *Nat Comm.* **2018**, *9* (1), 1–9.
- (54) Karapinar, D.; Zitolo, A.; Huan, T. N.; Zanna, S.; Taverna, D.; Galvão Tizei, L. H.; Giaume, D.; Marcus, P.; Mougél, V.; Fontecave, M. Carbon-Nanotube-Supported Copper Polyphthalocyanine for Efficient and Selective Electrocatalytic CO<sub>2</sub> Reduction to CO. *ChemSusChem* **2020**, *13* (1), 173–179.
- (55) Liu, Y.; Deb, A.; Leung, K. Y.; Nie, W.; Dean, W. S.; Penner-Hahn, J. E.; McCrory, C. C. L. Determining the Coordination Environment and Electronic Structure of Polymer-Encapsulated Cobalt Phthalocyanine under Electrocatalytic CO<sub>2</sub> Reduction Conditions Using in Situ X-Ray Absorption Spectroscopy. *Dalton Trans.* **2020**, *49* (45), 16329–16339.
- (56) Wu, Y.; Jiang, J.; Weng, Z.; Wang, M.; Broere, D. L. J.; Zhong, Y.; Brudvig, G. W.; Feng, Z.; Wang, H. Electroreduction of CO<sub>2</sub> Catalyzed by a Heterogenized Zn–Porphyrin Complex with a Redox-Innocent Metal Center. *ACS Cent. Sci.* **2017**, *3* (8), 847–852.
- (57) Lu, X.; Ahsaine, H. A.; Dereli, B.; Garcia-Esparza, A. T.; Reinhard, M.; Shinagawa, T.; Li, D.; Adil, K.; Tchalala, M. R.; Kroll, T.; Eddaoudi, M.; Sokaras, D.; Cavallo, L.; Takanabe, K. Operando Elucidation on the Working State of Immobilized Fluorinated Iron Porphyrin for Selective Aqueous Electroreduction of CO<sub>2</sub> to CO. *ACS Catal.* **2021**, *11* (11), 6499–6509.





# Chapter IV

---

## Spectroscopic studies of the CO<sub>2</sub> reduction mechanism by iron porphyrins

### Content

---

4.1	Electronic configuration and structures of iron porphyrins .....	43
4.1.1	Iron(III) porphyrins (d <sup>5</sup> ) .....	43
4.1.2	Iron(II) porphyrins (d <sup>6</sup> ) .....	45
4.1.3	Iron(I) porphyrins (d <sup>7</sup> ) .....	49
4.1.4	Iron(0) porphyrins (d <sup>8</sup> ) .....	50
4.1.5	Controversy in the electronic structure of highly reduced iron porphyrins .....	51
4.2	Spectroscopic characterization of adducts between CO <sub>2</sub> and iron porphyrins ..	52
4.2.1	Coordination chemistry of CO <sub>2</sub> .....	52
4.2.2	Theoretical calculation on the stabilization of a CO <sub>2</sub> -coordinated adduct .....	54
4.2.3	<i>Ex situ</i> Raman spectroscopic measurements .....	54
4.2.4	<i>In situ</i> and <i>operando</i> spectroelectrochemical measurements .....	55
4.3	Spectroscopic characterization on the interaction between the CO and the iron centre .....	57
4.3.1	Infrared spectroscopy .....	57
4.3.2	X-Ray absorption spectroscopy .....	58
4.3.3	UV-Vis spectroscopy .....	58
4.4	Outlook .....	59
4.5	References .....	61





The *d-orbitals* analysis in metal complexes can offer many insights in the electronic structures of these systems. The present chapter aims to summarize some of the spectroscopic information available in the literature describing the electronic structure of iron porphyrins in various oxidation states and the possible interaction of the iron center with CO<sub>2</sub> and CO.

#### 4.1. Electronic configuration and structures of iron porphyrins

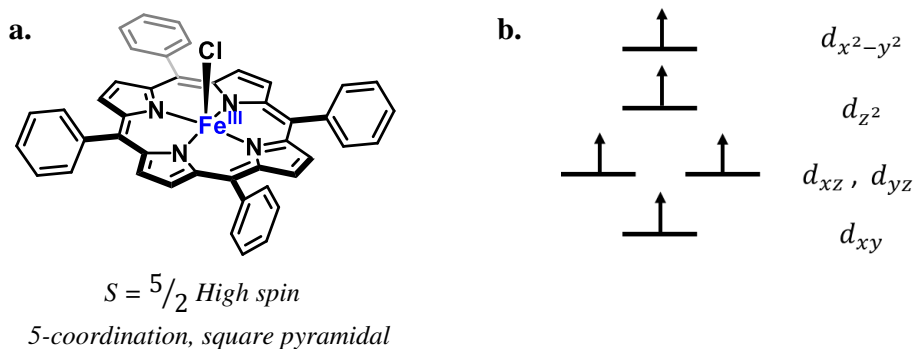
In iron porphyrins, the metal center is chelated by four nitrogen atoms from pyrrole groups, conferring it a square planar geometry. However, in some cases, the iron can be coordinated by one or two other axial ligands, yielding square pyramidal or distorted octahedral structures.<sup>1-3</sup> This arrangement confers to the iron porphyrins a characteristic *d-orbital* configuration, depending on their valence and spin states. The most important effect of the square planar geometry is observed by a destabilization of the  $d_{x^2-y^2}$  orbital in the *d-block*. The other e<sub>g</sub>-orbital, the  $d_{z^2}$ , only interacts weakly with the nitrogen atoms from the pyrroles. However, when other ligands coordinate the metal center in the axial positions, the  $d_{z^2}$  orbital is strongly destabilized. Concerning the t<sub>2g</sub>-orbitals, the  $d_{xz}$  and  $d_{yz}$  can combine with the porphyrin  $\pi$  orbitals. Nonetheless, the  $d_{xy}$  orbital does not possess the right symmetry to interact with the porphyrin ring orbitals, being lower in energy when compared with the other t<sub>2g</sub>-orbitals.<sup>1</sup>

In this thesis we will discuss only oxidation states going from Fe(III) ( $d^5$ ) to formally Fe(0) ( $d^8$ ) of iron porphyrin complexes, with spin states that may vary from high, intermediate to low spin.

##### 4.1.1 Iron(III) porphyrins ( $d^5$ )

Three spin states can be observed in Fe(III) porphyrins. The iron(III) species considered in this thesis, containing a chloride ligand coordinating the iron in axial position, have been reported as high spin (HS  $S = 5/2$ ).<sup>4</sup> The molecular orbital (MO) diagram for the high spin, five-coordinated iron tetraphenyl porphyrin chloride [Fe<sup>III</sup>(TPP)]Cl has been reported.<sup>4</sup> In this case, the  $d_{x^2-y^2}$  orbitals of the metal (highest in energy) strongly interact with the  $\sigma$  orbitals of the pyrrole ligands. As indicated by Paulat *et al.* the  $p_z$  orbital of the chloride ligand interacts with the  $d_{z^2}$  orbital of the metal, giving rise to a strong  $\sigma$  bond. Theoretical calculations (TD-DFT) have shown that the iron in the [Fe<sup>III</sup>(TPP)]Cl is out of the porphyrin plane, directed towards the chloride ligand, due to its radius and polarization.<sup>4</sup> A simplified *d-orbitals* representation for the HS [Fe<sup>III</sup>(TPP)]Cl complex is given in scheme 4.1. All the five *d-orbitals* are occupied by one electron, impacting the spectroscopic signatures of this porphyrin.

•••



**Scheme 4.1.** a. Structure of the  $S = 5/2$  high spin  $[\text{Fe}^{\text{III}}(\text{TPP})]\text{Cl}$ . b. Simplified  $d$ -orbital splitting representation.

The UV-Vis spectrum of iron porphyrins is very characteristic, showing an intense Soret band at around 400-500 nm and weaker Q-bands at higher wavelengths. The UV-Vis spectrum of  $[\text{Fe}^{\text{III}}(\text{TPP})]\text{Cl}$  in DMF at room temperature (see figure 4.1) exhibits an intense Soret band at 417 nm and lower Q-bands observed at 510 nm, 578 nm and a shoulder between 654 and 692 nm.<sup>5</sup> As detailed by Paulat *et al.* a broad band at 379 nm also rises due to a chloride to Fe charge transfer (CT).<sup>4</sup>

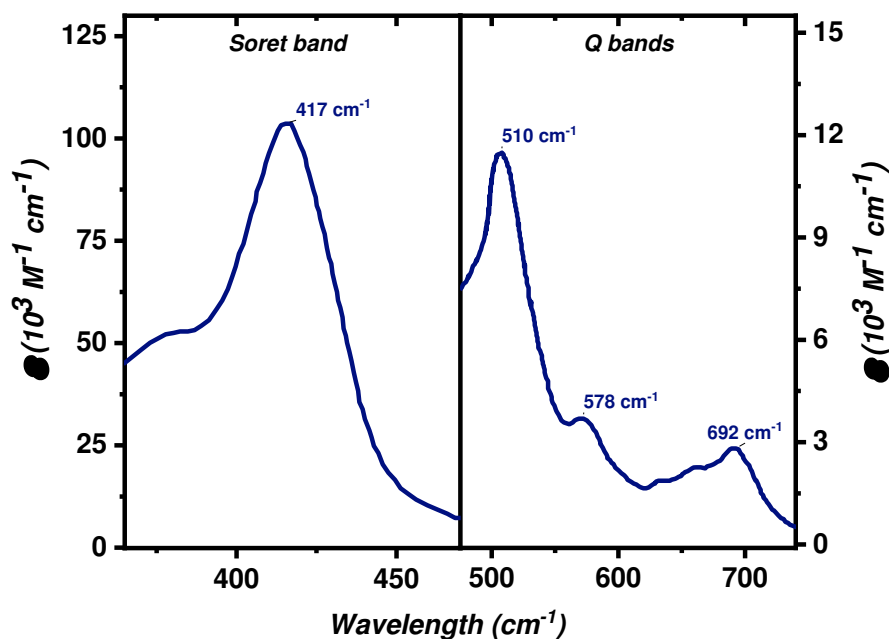


**Figure 4.1.** UV-Vis absorption spectrum of  $[\text{Fe}^{\text{III}}(\text{TPP})]\text{Cl}$  measured in DMF under Ar at room temperature.

Adapted from reference 5.

The XAS spectrum at the Fe K-edge of the  $[\text{Fe}^{\text{III}}(\text{TPP})]\text{Cl}$  in the solid state has also been reported by Römelt *et al.* and by Yamashige *et al.*<sup>6,7</sup> It exhibits a pre-edge peak, which is due

to a mixing of  $4p$  orbitals with  $3d$  orbitals of the metal due to the noncentrosymmetry imposed by the presence of the chloride axial ligand.<sup>8</sup> The single peak is also a qualitative evidence of the filled  $d$ -orbitals at the Fe(III) state.

#### 4.1.2 Iron(II) porphyrins ( $d^6$ )

Fe(II) species have been extensively studied due to their relevance to biochemical processes that occur in Nature.<sup>3,9</sup> The spin state of iron(II) porphyrins have been specifically studied in this context, and is still the subject of research efforts.<sup>10</sup> For example, while the deoxy-hemoglobin, an Fe(II) center without  $O_2$  coordination, is high spin ( $S = 2$ ), the binding of  $O_2$  generates the low spin oxy-hemoglobin complex ( $S = 0$ ). Early Fe K-edge X-Ray absorption spectroscopic studies at the Fe(II) level were performed by Verdagner *et al.* in model complexes, such as iron basket handle porphyrins, that allowed stabilization of  $O_2$ , avoiding dimerization or metal oxidation.<sup>11,12</sup> These studies were followed by Kim *et al.* who performed *in situ* spectroelectrochemical measurements on iron porphyrins immobilized on carbon substrates.<sup>13,14</sup> Years after these initial reports, Wilson *et al.*<sup>15</sup> reported a complete study on the electronic structure of iron(II) porphyrins, using Fe K-edge X-ray absorption spectroscopy. Data recorded on the hemoglobin system were compared to a frequently used model, iron(II) tetraphenyl porphyrin [Fe(TPP)], as illustrated in figure 4.2. Their study showed that the nature of the axial ligand coordinated to [Fe<sup>II</sup>(TPP)] complexes affects its spin state and therefore its pre-edge and rising edge positions. It was observed that, for the same oxidation state, a shift of at least 2 eV could be observed at the rising edge position for different spin states.<sup>15</sup> The use of spectroscopy is critical in this case since spin states cannot be directly differentiated by cyclic voltammetry.<sup>16</sup>

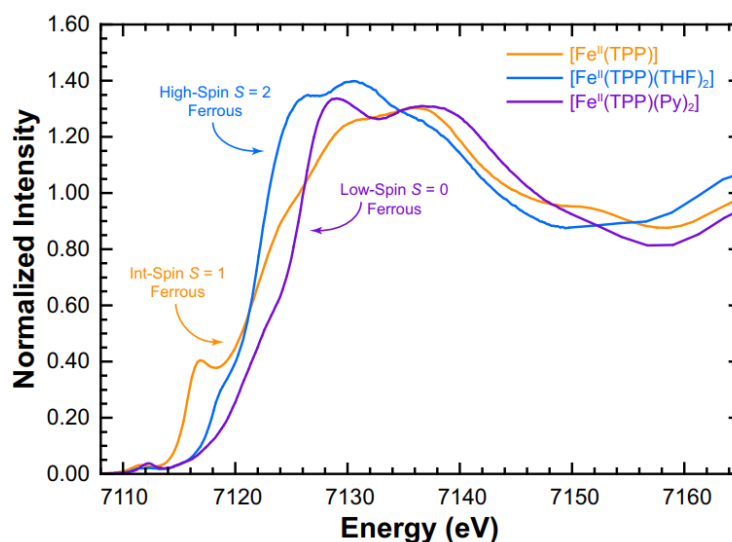
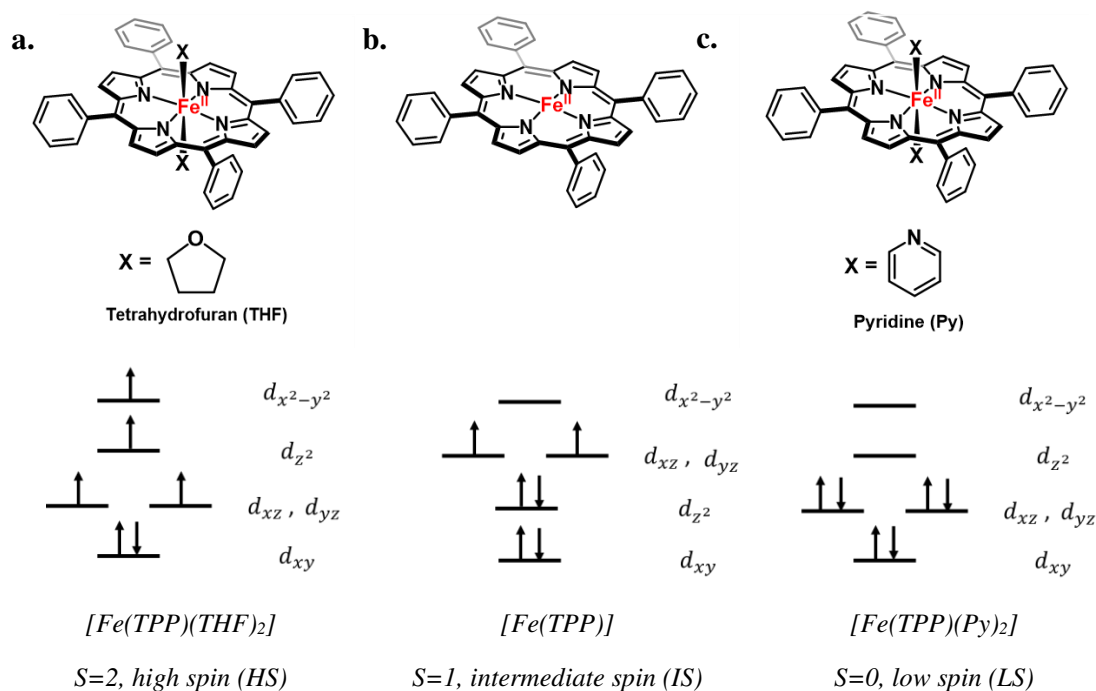


**Figure 4.2.** *Ex situ* Fe K-edge XANES spectra of iron(II) tetraphenyl porphyrin with different axial ligands and in different spin states. These data were recorded as frozen samples.

Reprinted from reference 15. Copyright 2013 PNAS



Based on these observations, three electronic configurations for the iron(II) tetraphenyl porphyrin can be described, as shown in scheme 4.2.



**Scheme 4.2.** Schematic representation of the three possible spin states of iron(II) tetraphenyl porphyrins (top) and the simplified d-orbital splitting for each of these structures (bottom). **a.** High spin; **b.** Intermediate spin; **c.** Low spin.

The UV-Vis spectrum of  $[\text{Fe}^{\text{II}}(\text{TPP})]$  species in DMF and 0.1 M triethylammonium phosphate (TEAP) under Ar (figure 4.3), shows that the Soret band is red-shifted towards 431 nm, being also more intense and sharper when compared to  $[\text{Fe}^{\text{III}}(\text{TPP})]\text{Cl}$ . With respect to the Q-bands, two well-defined bands are observed at 563 nm and at 605 nm.<sup>17,18</sup> In addition to these studies, electronic paramagnetic resonance (EPR) measurements performed on the one electron reduced  $[\text{Fe}^{\text{III}}(\text{TPP})]\text{Cl}$  complex in DMF implies diamagnetism supporting a low spin character of this complex due to the presence of DMF.<sup>18</sup> An extensive electrochemical analysis was also performed, regarding the (de)-coordination of the chloride anion. It has been shown that the chloride is not an axial ligand after reduction of the  $[\text{Fe}^{\text{III}}(\text{TPP})]\text{Cl}$  by one electron.<sup>19</sup>

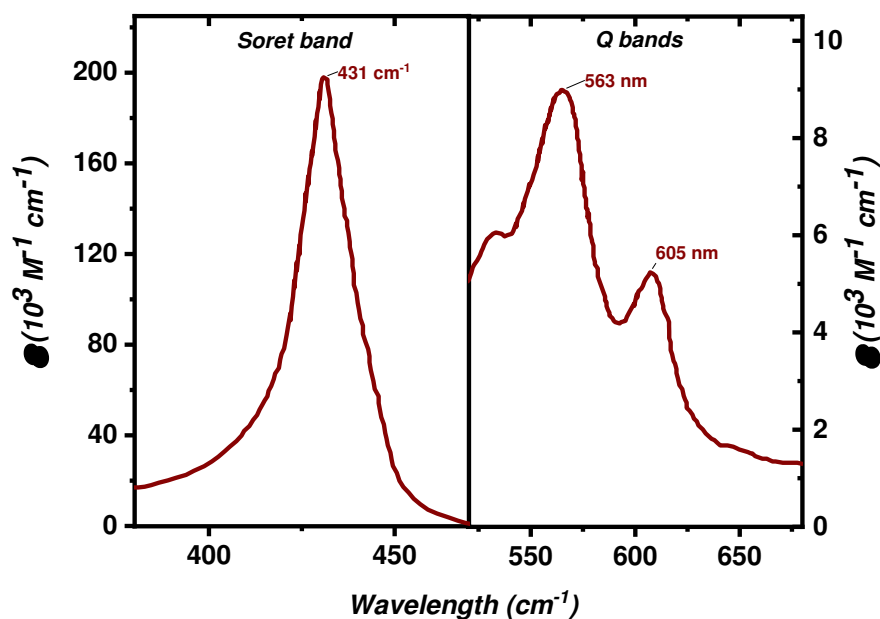
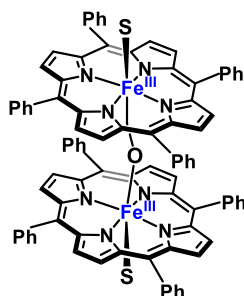


**Figure 4.3.** UV-Vis absorption spectrum of [Fe<sup>II</sup>(TPP)] measured in DMF + 0.1 M TEAP under Ar at room temperature.

*Adapted from reference 5.*

Early studies showed that the presence of water in the media could trigger the formation of an [(Fe<sup>III</sup>(TPP))<sub>2</sub>O] dimer, named μ-oxo iron porphyrin (scheme 4.3), upon reduction of the [Fe<sup>III</sup>(TPP)]Cl.<sup>16</sup> This new species would lead to a different optical absorption spectrum than the one observed for the Fe<sup>II</sup> species. Indeed, the Soret band changes from the one reported for the [Fe<sup>II</sup>(TPP)] species, being blue-shifted to 406 nm, while the Q-bands are maintained at 569 and 609 nm (figure 4.4).<sup>16,17,20</sup>



**Scheme 4.3.** Schematic representation of the [(Fe<sup>III</sup>(TPP))<sub>2</sub>O]. S = solvent.

*Phenyl groups in the porphyrin ring omitted for clarity.*



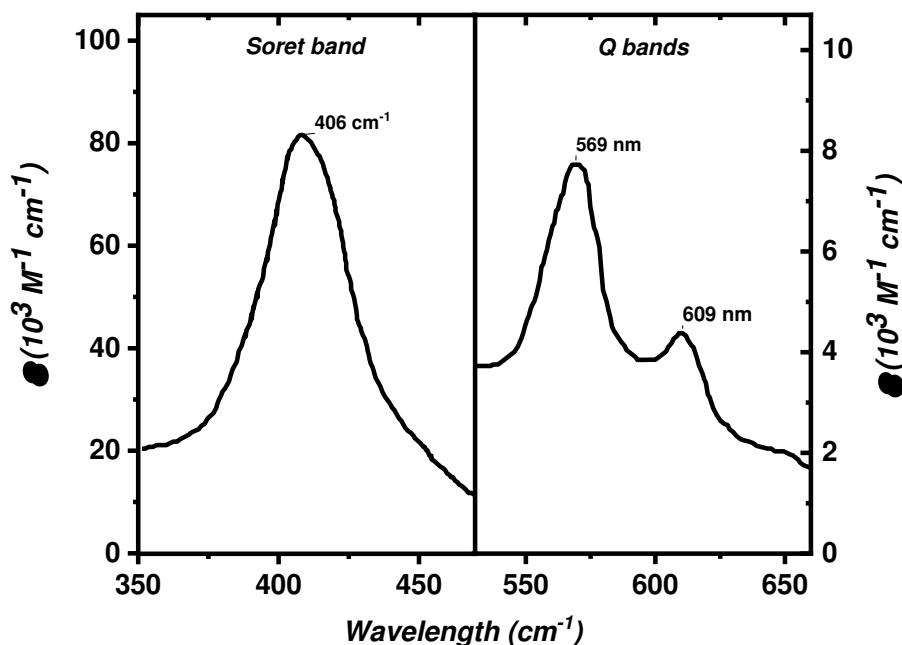


**Figure 4.4.** UV-Vis absorption spectrum of  $[(\text{Fe}^{\text{III}}(\text{TPP}))_2\text{O}]$  measured in DMF + 0.1 M TEAP under Ar at room temperature.

*Adapted from reference 5.*

Kadish *et al.* performed a detailed electrochemical study of the  $[(\text{Fe}^{\text{III}}(\text{TPP}))_2\text{O}]$  complex by cyclic voltammetry (figure 4.5 – a). It was concluded that the reduction of this dimer species proceed via multiple steps initially yielding the ferric-ferrous dimer at a potential close to  $-0.93 \text{ V vs. SCE}$ , at more negative potential the ferrous dimer and at a potential between  $-1.03$  and  $-1.38 \text{ V vs SCE}$  and, depending on the proton presence, a yellow-green compound described as the ferrous monomer  $[\text{Fe}^{\text{I}}(\text{TPP})]^-$ . UV-Vis spectroelectrochemical measurements evidenced a splitting of the Soret band, at  $390 \text{ nm}$  and  $420 \text{ nm}$  for this complex (figure 4.5 - b).<sup>17,21,22</sup>

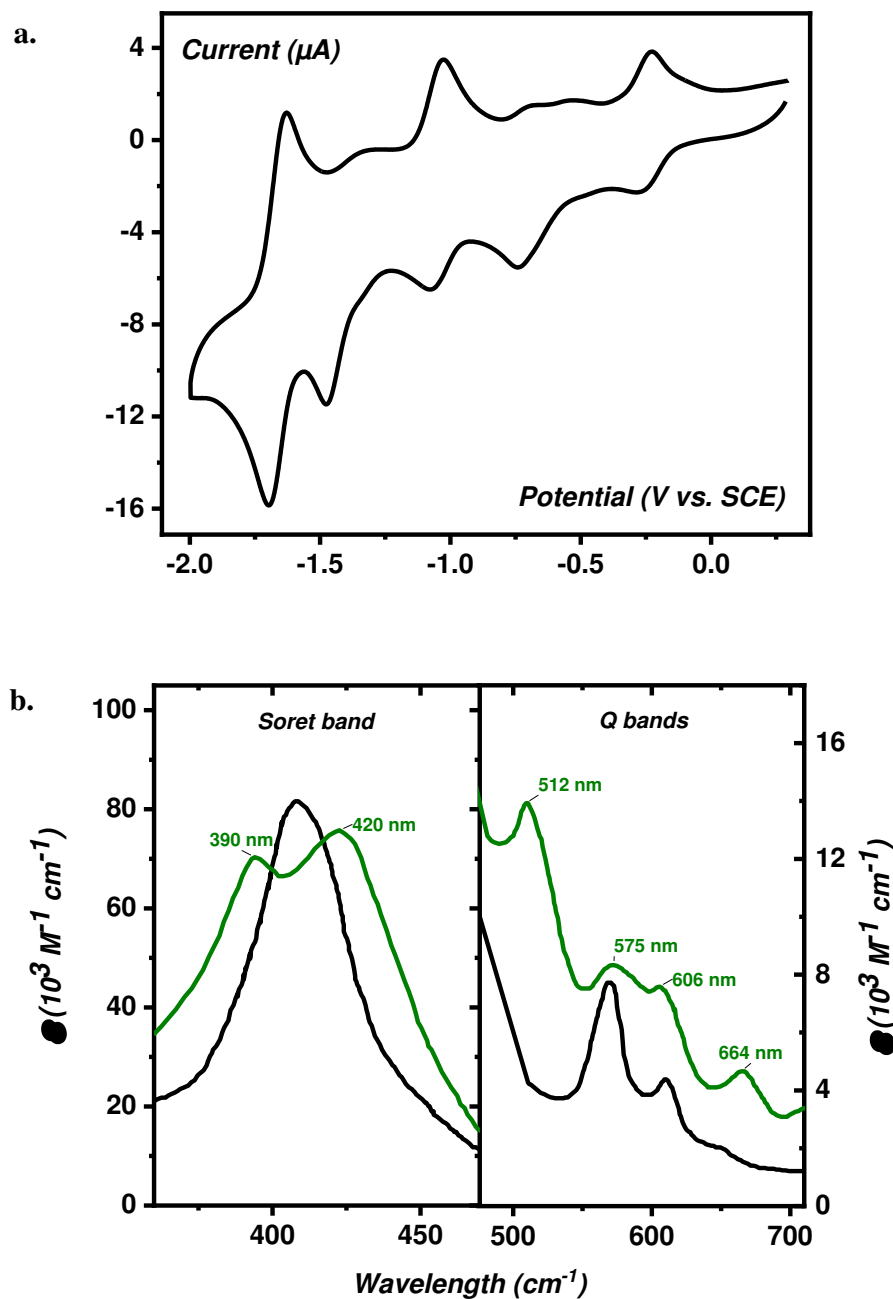


Figure 4.5. a. Cyclic voltammogram of electrochemically prepared  $[(\text{Fe}^{\text{III}}(\text{TPP}))_2\text{O}]$  in DMF + 0.1 M TBAPF<sub>6</sub> under Ar at room temperature; b. UV-Vis absorption spectrum of  $[(\text{Fe}^{\text{III}}(\text{TPP}))_2\text{O}]$  (black) and  $[\text{Fe}^{\text{I}}(\text{TPP})]^-$  (green) measured in DMSO + 0.1 M TEAP at room temperature.

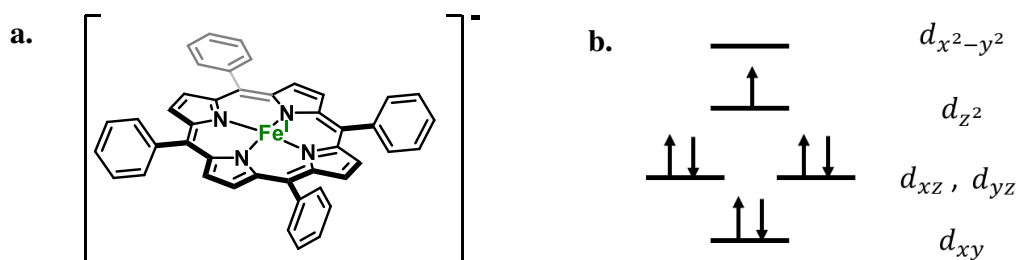
Credits to: a. Mrs. A. Salame; b. Adapted from reference 5.

#### 4.1.3 Iron(I) porphyrins ( $d^7$ )

Hence, due to the difficulties to stabilize the monomer species of Fe(I) porphyrins, there has been less spectrochemical reports on highly reduced iron porphyrins. Cohen *et al.* showed that the chemical reduction of  $[(\text{Fe}^{\text{III}}(\text{TPP}))_2\text{O}]$  induced a change on the EPR signal.<sup>23</sup> Indeed,  $[(\text{Fe}^{\text{III}}(\text{TPP}))_2\text{O}]$  presents no signal, due to the antiferromagnetic coupling of the two Fe(III)



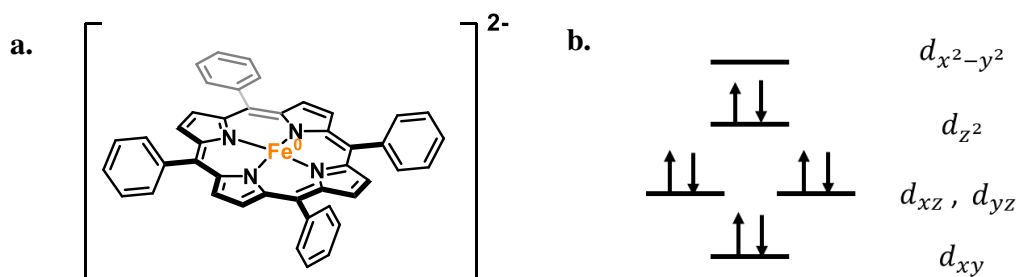
moieties. However, the EPR spectrum of the reduced species of  $[(\text{Fe}^{\text{III}}(\text{TPP}))_2\text{O}]$  at 77 K yield a signal with  $g$  values at 1.93 and 2.30, which were indicative of a low spin  $S = 1/2$  complex, with an unpaired electron in the  $d_{z^2}$  orbital.<sup>23</sup> Further UV-Vis and Raman spectroelectrochemical measurements performed by Anxolabéhère *et al.* also suggested the formation of the  $[\text{Fe}^{\text{I}}(\text{TPP})]^-$  complex by electrochemical reduction of  $[\text{Fe}^{\text{III}}(\text{TPP})]\text{Cl}$  at -1.4 V *vs.* SCE in DMSO + 0.1 M TEAP under Ar atmosphere by using a platinum electrode.<sup>17,22</sup> The electronic structure for the expected  $[\text{Fe}^{\text{I}}(\text{TPP})]^-$  is therefore presented in scheme 4.4.



Scheme 4.4. a. Schematic representation of the possible  $S = 1/2$  low spin Fe(I) tetraphenyl porphyrin complex; b. Simplified d-orbital splitting representation.

#### 4.1.4 Iron(0) porphyrins ( $d^8$ )

Lexa *et al.* reported that the chemical and electrochemical reduction of iron porphyrins, *i.e.* at more negative potential values than -1.7 V *vs.* SCE (see figure 2.3 – chapter II), yields a compound that does not show an EPR signal at 77 K or at higher temperatures. They suggested that this species corresponds to the localization of the electron transferred to the system on the porphyrin ring. In the presence of oxygen, this species was reconverted into  $[(\text{Fe}^{\text{III}}(\text{TPP}))_2\text{O}]$ , allowing to conclude that no structural modifications occurred in the ring, *e.g.* a hydrogenation of the porphyrin.<sup>18</sup> Nonetheless, a decade later, Mashiko *et al.* reported the crystal structure of the  $[\text{Fe}^0(\text{TPP})]^{2-}$  by chemical reduction with sodium anthracenide in anaerobic conditions and by stabilization with  $[\text{Na}(\text{THF})_3]_2$  cations.<sup>24</sup> The  $[\text{Fe}^0(\text{TPP})]^{2-}$  was described to have a square-planar structure and a diamagnetic electronic configuration, pointing towards a low spin,  $S = 0$  complex, as represented on scheme 4.5.



Scheme 4.5. a. Schematic representation of the possible  $S = 0$  low spin iron(0) tetraphenyl porphyrin complex; b. simplified d-orbital splitting.

More recently, Ye *et al.* reported XANES spectra on the solid state of  $[\text{Fe}^{\text{III}}(\text{TPP})]\text{Cl}$  and its reduced species, obtained by chemical reduction.<sup>6</sup> All the reduced species possess the same pre-edge values, *i.e.*, 7111 eV (figure 4.6), concluding that the iron center of these species have the same valence state, Fe(II). These results were supported by Mössbauer spectroscopy and DFT calculations, as well as by Raman spectroscopy studies performed by the same research group.<sup>6,25</sup> Therefore, they were able to suggest that ligand-centered reduction occurs at the second and third reduction steps.

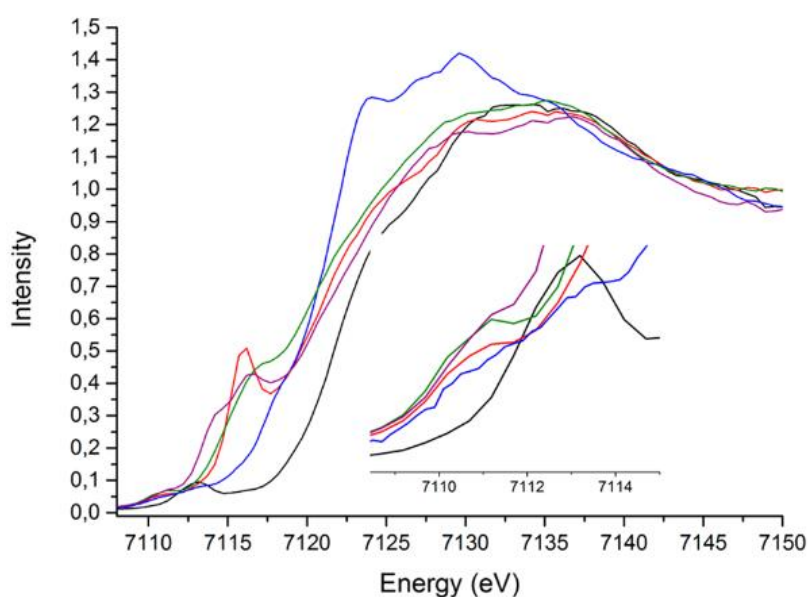
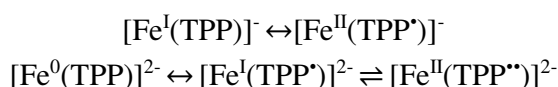


**Figure 4.6.** Fe K-edge XAS spectra of  $[\text{Fe}^{\text{III}}(\text{TPP})]\text{Cl}$  (black) and its reduced species: high spin  $[\text{Fe}^{\text{II}}(\text{TPP})(\text{THF})_2]$  (blue); intermediate spin  $[\text{Fe}^{\text{II}}(\text{TPP})]$  (red);  $[\text{Fe}^{\text{II}}(\text{TPP}^*)]^-$  (green);  $[\text{Fe}^{\text{II}}(\text{TPP}'')]^{2-}$  (purple) samples in the solid state (diluted in boron nitride) recorded as frozen samples at  $\sim 10$  K at the European Synchrotron Radiation Facility - ESRF beamline BM23.

*Reprinted from references 6. Copyright 2017 American Chemical Society.*

#### 4.1.5 Controversy in the electronic structure of highly reduced iron porphyrins

Despite electrochemical and spectroscopic studies, there is still a controversy regarding the exact electronic configuration of the highly reduced species of iron porphyrins. One can formulate the two and three electrons reduced species of  $[\text{Fe}^{\text{III}}(\text{TPP})]\text{Cl}$ , as formal “ $\text{Fe}^{\text{I}}$ ” and “ $\text{Fe}^{\text{0}}$ ” complexes (reduction occurring on the metal center), or as Fe(II) single and di-radicals (reduction occurring on the porphyrin ring) species, as follow:





Resonance Raman spectroelectrochemical studies performed in solution (DMSO) conducted by Anxolabéhère *et al.* supported the metal centered reduction. Indeed, the authors were able to observe distinctive signatures for both “Fe(I)” and “Fe(0)” complexes. Comparison with [Zn<sup>II</sup>(TPP)] and its known radical anion species were pointing towards the formulation of the highly reduced species of iron porphyrins as [Fe<sup>I</sup>(TPP)]<sup>-</sup> and [Fe<sup>0</sup>(TPP)]<sup>2-</sup> for the two and three electron reduced species respectively, at least under the conditions presented on the report.<sup>22</sup>

However, the more recent data presented by Ye *et al.* suggest that the reduction might occur at the ligand rather than on the metal center, describing the species as [Fe<sup>II</sup>(TPP<sup>•</sup>)]<sup>-</sup> and [Fe<sup>II</sup>(TPP<sup>••</sup>)]<sup>2-</sup> for the two and three reduction steps respectively.<sup>6</sup> Nonetheless, it is important to emphasize that the spectroscopic results shown here have been performed in the solid state, which means that the effect of solvent or electrolytes is not taken into account. Therefore, the experimental conditions might play a pivotal role in the determination of the spectroscopic signatures.

Finally, reactivity studies performed in the presence of alkyl halides have supported the idea that the metal is the reactive site on iron porphyrins and not the ligand. Even though the different resonance forms for iron porphyrins, as shown above, can contribute in the electronic configuration of these systems, it was shown that the iron center is the site that gets alkylated.<sup>26-28</sup> However, as different spectroscopic measurements, electrochemical techniques and quantum chemistry calculations have given contradictory results, no consensus has been reached to date. Therefore, *in situ* XAS and UV-Vis spectroelectrochemical measurements shown in chapter VI aim to give further insights in this point.

## 4.2 Spectroscopic characterization of adducts between CO<sub>2</sub> and iron porphyrins

### 4.2.1 Coordination chemistry of CO<sub>2</sub>

CO<sub>2</sub> is a 16e<sup>-</sup> molecule with a linear geometry in its ground state, belonging to the  $D_{\infty h}$  site symmetry group.<sup>29</sup> As described in chapter II, CO<sub>2</sub> is an extremely stable molecule which requires catalysts for its activation. The strong C=O bonds, having a bond energy of 806 kJ.mol<sup>-1</sup><sup>30</sup> and a short distance of 1.16 Å,<sup>31</sup> confers to this molecule its high stability. Despite being a non-polar molecule, there is an important electronegative difference between its electrophilic carbon center and the nucleophilic oxygen atoms. This confers to CO<sub>2</sub> the possibility to bind low oxidation state metal centers by the carbon ( $\eta^1$ -C mode), to bind higher oxidation state metal centers by the oxygen atom ( $\eta^1$ -O or  $\eta^2$ -(O,O) mode), or to bind to metal center through the  $\pi$  electron density of the C-O bond ( $\eta^2$ -(C,O) mode), as shown in figure 4.7.

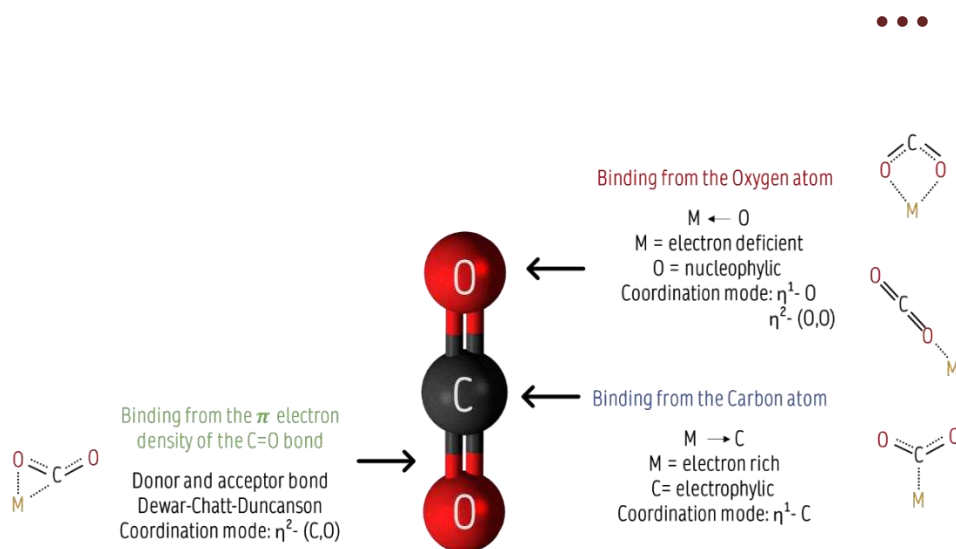
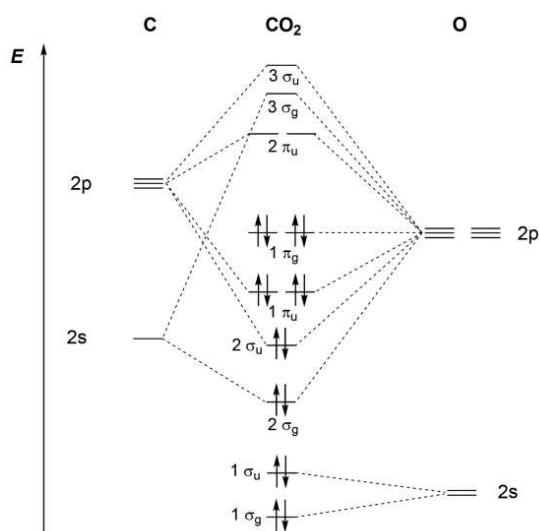


**Figure 4.7. Binding modes of CO<sub>2</sub> to a metal center.**

*Adapted from reference 29.*

The MO energy diagram of CO<sub>2</sub> (scheme 4.6) shows that the two most available orbitals for reactivity are the  $1\pi_g$  and the  $2\pi_u$  which are the highest occupied molecular orbital (HOMO) and the lowest unoccupied molecular orbital (LUMO), respectively. The doubly occupied HOMO is mainly centered on the oxygen atom, while the empty antibonding  $2\pi_u$  orbitals are mostly localized, with at least 60% weight, on the carbon atom.<sup>32</sup> Due to this, the CO<sub>2</sub> molecule is considered as amphoteric, meaning that the carbon atom possesses a Lewis acid character, while the oxygen atoms are Lewis bases. Overall, CO<sub>2</sub> has more acceptor than donor character, and therefore, the carbon atom is more reactive than the oxygen atoms.<sup>33</sup>



**Scheme 4.6. Molecular orbital diagram of CO<sub>2</sub>.**

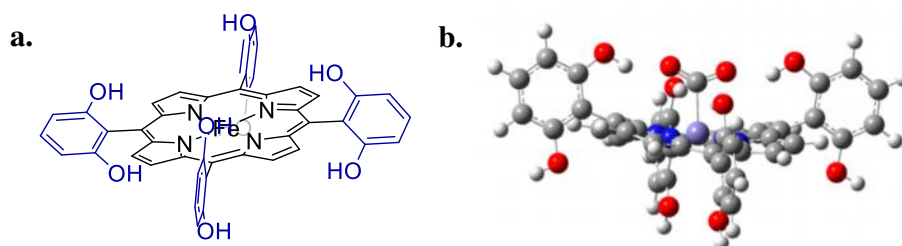
*Reprinted from reference 33. Copyright 2018 American Chemical Society.*



Upon one electron reduction, its LUMO orbitals get occupied with a resulting lowest energy state that corresponds to a bent geometry. Therefore, according to Walsh's rules, the  $\text{CO}_2^-$  radical anion has an O-C-O angle of  $134^\circ$  in contrast with the  $180^\circ$  linear  $\text{CO}_2$  structure.<sup>34</sup> When  $\text{CO}_2$  binds an electron-rich metal center in a  $\eta^1\text{-C}$  coordination mode, the loss of linearity has been observed, as reported in 1983 with the  $[\text{Rh}(\text{diars})_2(\text{Cl})(\text{CO}_2)]$  (diars = o-phenylene-bis(dimethyl)arsine) complex.<sup>35</sup> Similarly, it has been proposed that  $\text{CO}_2$  coordinates iron porphyrins in a  $\eta^1\text{-C}$  mode. This has been supported by the fact that the iron center in these complexes is expected to be in a low oxidation state "Fe(0)", being nucleophilic enough to allow the coordination of the electrophilic carbon of  $\text{CO}_2$ .

#### 4.2.2 Theoretical calculations on the stabilization of a $\text{CO}_2$ -coordinated adduct.

Costentin *et al.* proposed that the presence of hydroxyl groups in ortho positions of the phenyl groups of the porphyrin ring (scheme 4.7 - a) could stabilize an Fe- $\text{CO}_2$  adduct, acting as hydrogen bond donors.<sup>36</sup> Density functional theory (DFT) calculations supported the presence of hydrogen bonds stabilizing the Fe- $\text{CO}_2$  adduct during catalysis (scheme 4.7 - b). The authors concluded that this  $[\text{Fe}(\text{CO}_2)]^-$  species could be described as an Fe(I) complex with spin density being mostly localized on the iron but having some contribution on the ligand too.<sup>37</sup>



**Scheme 4.7. a. Schematic representation of the iron tetraphenyl porphyrin bearing hydroxyl substituents on the phenyl groups of the porphyrin ring; b: Lateral view of the optimized structure of the Fe- $\text{CO}_2$  adduct obtained by DFT calculations.**

*Reprinted from reference 37. Copyright 2014 American Chemical Society.*

Atoms color identification: grey: carbon; white: hydrogen; red: oxygen; blue: nitrogen; light purple: iron.

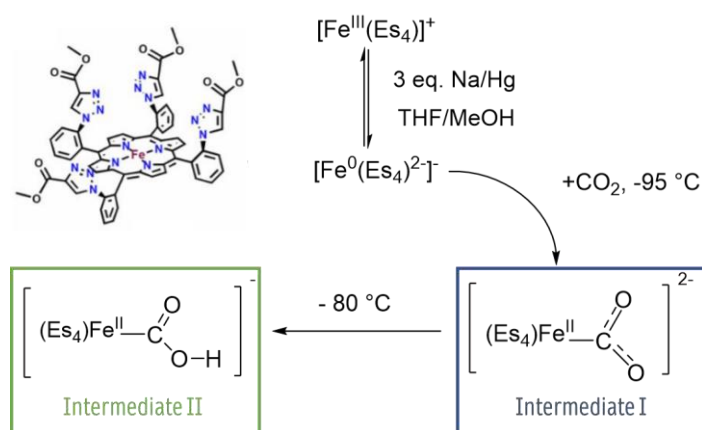
#### 4.2.3 *Ex situ* Raman spectroscopic measurements

Due to the highly polarized bonds in the  $\text{CO}_2$  molecule, *ex situ* Raman spectroscopy was used by Mondal *et al.* in order to spectroscopically obtain possible intermediates involved in the reduction of  $\text{CO}_2$  to CO by iron porphyrins.<sup>38</sup> An iron porphyrin, bearing a triazole moiety as substituent on the phenyl group of the porphyrin (scheme 4.8 – insert), was analyzed in a THF-methanol solution. The generation of the formally "Fe(0)" state, by observing a Raman shift of the  $\nu_4$  and  $\nu_2$  bands towards lower wavelengths when compared with the Fe(III) and Fe(II) species, was proposed. By bubbling  $\text{CO}_2$  at cryogenic temperatures ( $-95^\circ\text{C}$ ) they



observed changes of the vibrational bands, especially the one at  $590\text{ cm}^{-1}$ , which likely represents the Fe-C stretching. Since the  $\nu_4$  and  $\nu_2$  bands were close in values to the ones reported for high spin (HS)  $\text{Fe}^{\text{II}}$  porphyrins, they described the intermediate I as a HS  $[\text{Fe}^{\text{II}}(\text{Es})_4\text{CO}_2]^{2-}$ , which, as described by the authors, was only observable for a few second at very low temperatures.

By raising the temperature to  $-80\text{ }^\circ\text{C}$ , a shift in the Raman signatures was observed. A transition was proposed from intermediate I to intermediate II, the protonated form  $[\text{Fe}^{\text{II}}(\text{Es})_4(\text{COOH})]^-$  exists for longer time than intermediate I (minutes instead of seconds). They proposed these species due to the presence of methanol in the reduction mixture, which could act as proton source. The  $\nu_4$  and  $\nu_2$  signatures of this intermediate were similar to the ones obtained for low spin (LS)  $\text{Fe}^{\text{II}}$  porphyrins. Therefore, the authors concluded that intermediate II was better described as LS  $[\text{Fe}^{\text{II}}(\text{Es})_4(\text{COOH})]^-$  species.



**Scheme 4.8.** Proposed  $\text{CO}_2$  reduction intermediates for the chemical reduction of the  $\text{FeEs}_4$  (insert) based on *ex situ* Raman spectroscopic measurements.

*Adapted from reference 38.*

#### 4.2.4 *In situ* and *operando* XAS spectroelectrochemical measurements

An *in situ* and *operando* spectroelectrochemical characterization of the  $\text{CO}_2$  reduction to CO by an iron porphyrin was very recently described by Lu *et al.*<sup>39</sup> Studies were performed in immobilized iron (pentafluorophenyl)-porphyrin, named  $[\text{Fe}(\text{F}_{20}\text{TPP})]$ , on high surface carbon materials in aqueous solution.

Initial UV-Vis spectroelectrochemical experiments performed at an open circuit potential ( $+0.9\text{ V vs RHE}$ ) in the presence of argon and sodium bicarbonate ( $\text{NaHCO}_3$ ) as electrolyte shows a band at  $410\text{ nm}$ , which was ascribed to the Soret band of the  $\text{Fe}(\text{III})$  state. By applying a potential of  $-0.2\text{ V vs RHE}$  under the same conditions, a red shift on the Soret band to  $433\text{ nm}$  while a decrease of the band at  $410\text{ nm}$  was observed, in line with the reduction of the





iron center by one electron towards the generation of the Fe(II) species. When a potential of -0.5 V *vs* RHE is applied, a shoulder at 417 nm is observed. These same characteristic UV-Vis signatures were evidenced in the presence of CO<sub>2</sub>. When the supporting electrolyte was changed to a phosphate buffer pH 7.2 and experiments were performed under argon atmosphere only a band at 430 nm was observed when potential was swept from -0.2 V to -0.8 V *vs* RHE. No band at 417 nm was observable, which was further ascribed to correspond to the UV-Vis signature of the Fe(II)-CO adduct. Hence, the authors finally suggested that CO<sub>2</sub> is present in the bicarbonate solution leading to its reduction towards CO even under argon atmosphere. Table 4.1 summarized the experimental conditions while performing UV-Vis spectroelectrochemical measurements as well as the Soret band obtained values.

**Table 4.1. Experimental conditions and UV-Vis signatures obtained by Lu *et al.*<sup>39</sup>**

<i>Applied potential (V vs RHE)</i>	<i>Electrolyte</i>	<i>pH</i>	<i>Atmosphere</i>	<i>Soret band (nm)</i>	<i>Description</i>
<b>+0.9</b>	0.5 M NaHCO <sub>3</sub>	8.3	Argon	410	[Fe <sup>III</sup> (F <sub>20</sub> TPP)]
<b>-0.2</b>	0.5 M NaHCO <sub>3</sub>	8.3	Argon	433	[Fe <sup>II</sup> (F <sub>20</sub> TPP)]
<b>-0.5</b>	0.5 M NaHCO <sub>3</sub>	8.3	Argon	417	[Fe <sup>II</sup> (F <sub>20</sub> TPP)(CO)]
<b>+0.9</b>	0.5 M NaHCO <sub>3</sub>	7.2	CO <sub>2</sub>	410	[Fe <sup>III</sup> (F <sub>20</sub> TPP)]
<b>-0.2</b>	0.5 M NaHCO <sub>3</sub>	7.2	CO <sub>2</sub>	433	[Fe <sup>II</sup> (F <sub>20</sub> TPP)]
<b>-0.5</b>	0.5 M NaHCO <sub>3</sub>	7.2	CO <sub>2</sub>	417	[Fe <sup>II</sup> (F <sub>20</sub> TPP)(CO)]
<b>-0.2 to -0.8</b>	0.5 M K-phosphate	7.2	Argon	433	[Fe <sup>II</sup> (F <sub>20</sub> TPP)]

Spectroelectrochemical XAS measurements were also performed on this system in the presence of a CO<sub>2</sub> atmosphere. When a potential of -0.6 V *vs* RHE is applied, an edge shift of -0.8 eV was observed when compared with the XAS of the initial compound. In addition to this, two pre-edge peaks were observed with a  $\Delta E = 2.6$  eV difference between them (figure 4.8). The authors suggested that these observations are in line with the reduction of the iron center from a Fe(III) to a Fe(II) state, by comparing the generated spectra with standard references of Fe. Furthermore, the observed pre-edge splitting was described as an evidence for the formation of the Fe<sup>II</sup>-CO adduct, supporting their observations by UV-Vis spectroelectrochemistry.

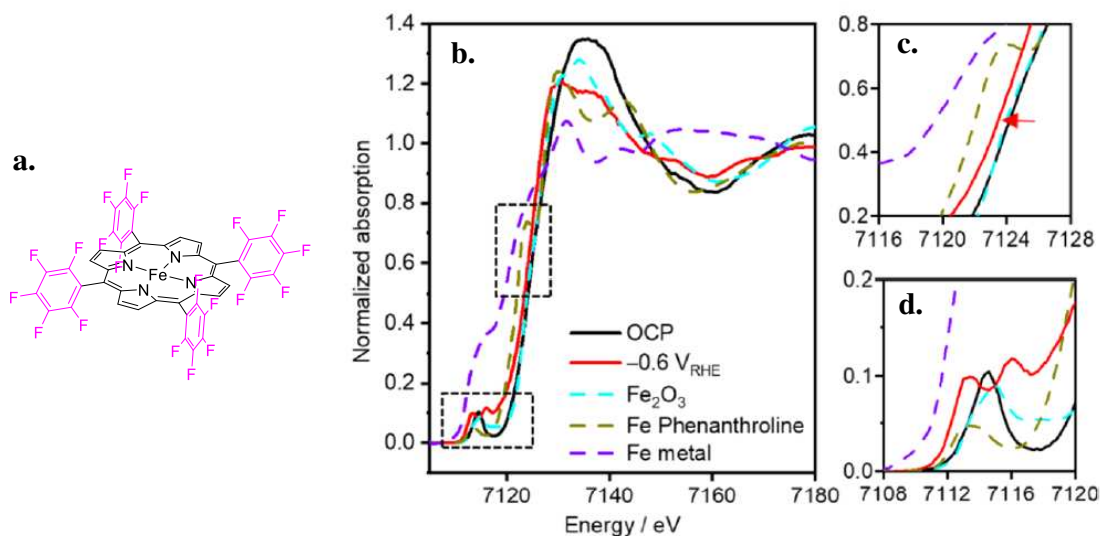


**Figure 4.8.** a. Structure of  $[\text{Fe}(\text{F}_{20}\text{TPP})]$ ; b. *In situ/operando* Fe K-edge XANES spectra of immobilized  $[\text{Fe}(\text{F}_{20}\text{TPP})]$  on carbon material electrode recorded at open circuit potential (black), at  $E = -0.6 \text{ V}$  vs RHE (red) and comparison with the Fe K-edge XANES spectra of iron standard references of  $\text{Fe}_2\text{O}_3$  (blue), Fe phenanthroline (green) and metallic iron (purple). c. Zoom section of the main edge. d. Zoom section of the pre-edge.

Reprinted from reference 39. Copyright 2021 American Chemical Society.

To date only this very recent data has been reported on *in situ/operando* spectroelectrochemical studies on the iron porphyrin system. Nonetheless, there are some discrepancies in this study with electrochemical data already known, for instance the  $\text{CO}_2$  activation occurring at the Fe(II) state. In addition to this, the experimental conditions in these studies are different from the ones employed during the electrochemical analysis. This thesis aims to give further suggestions in this Fe- $\text{CO}_2$  adduct, as presented in chapter VII.

### 4.3 Spectroscopic characterization on the interaction between the CO and the iron center

#### 4.3.1 Infrared spectroscopy

Carbon monoxide has been intensely investigated due to its importance as a reagent in many reactions and its well-known biological toxicity.<sup>40,41</sup> CO is characterized to strongly bind metal centers, especially electron rich ones, since it possesses a lone electron pair for  $\sigma$  donation to the metal. However, it can also accept electronic density from the metal through  $\pi$  backdonation. This effect has been widely studied by vibrational spectroscopy, allowing to determine the coordination modes of the CO ligand. Hence, CO formation has been determined at around  $2143 \text{ cm}^{-1}$ , while coordination has been reported to shift the band towards lower wavenumbers depending on the nature of the metal-CO bonding. Indirect detection of CO is also possible by following the diminution of the band around  $2342 \text{ cm}^{-1}$ , which has been reported to be related to the  $\text{CO}_2$  consumption.<sup>41</sup>

Infrared spectroscopy (IR) has been used to study heme carbonyls. A single sharp band at  $1951\text{ cm}^{-1}$  has served as an indication of the CO binding the iron center in a  $\eta^1$  mode through the carbon.<sup>40,41</sup> Croisy *et al.* used IR spectroscopy in order to examine the coordination of CO to iron porphyrins and the stability of the Fe-CO adduct. They conclude that CO can bind iron porphyrins in the Fe(II) state to form a monomeric Fe<sup>II</sup>-CO adduct, characterized by only one IR signature at around  $1960\text{ cm}^{-1}$ .<sup>42</sup>

### 4.3.2 X-ray absorption spectroscopy

The Fe<sup>II</sup>-CO bond in iron porphyrins was analyzed in the 80s' by Ascone *et al.* using *ex situ* Fe K-edge XAS.<sup>43</sup> They analyzed porphyrins bearing “picket fence” structures and coordinating ligands, such as 1-methyl-imidazole, in order to stabilize the CO-coordinated adducts previously proposed on the basis of IR measurements.<sup>42</sup> The carbonyl intermediate was obtained by bubbling CO in the reduced iron porphyrin dissolved in toluene or as precipitated solid samples.<sup>43,44</sup> With the help of EXAFS fittings analysis, they reported a bonding angle between the Fe and the CO of  $180^\circ \pm 10^\circ$ , confirming the linearity of the Fe-C-O unit.

Years later, Bae *et al.* were able to perform *in situ* XANES spectroelectrochemical studies on an iron porphyrin immobilized on a carbon material in the presence of CO.<sup>45</sup> Fe K-edge XANES on an Fe(II) porphyrin in the presence of CO shows a shift towards higher energy values. It was concluded that this shift was observed due to a charge transfer from the Fe(II) to the CO molecule (backdonation), decreasing the electronic density on the metal center. In addition to this, the presence of two pre-edge peaks at 7112 and 7115 eV was evidenced, which have also been identified in previously reported Fe(II)-CO porphyrins.<sup>42,43</sup> These studies suggested that the presence of this double peak was possibly due to a low spin iron center and that the relatively intense pre-edge peaks were due to the asymmetrical environment obtained by the coordination of CO.

### 4.3.3 UV-Vis spectroscopy

Thin layer spectroelectrochemistry was used by Croisy *et al.* in order to characterize the Fe<sup>II</sup>-CO intermediate, by using a structured “picket-fence” porphyrin as described for IR measurements. When a potential of  $-0.7\text{ V vs SCE}$  was applied to the porphyrin solution under CO atmosphere, a Soret band at 420 nm and a single Q-band at 540 nm were observed.<sup>42</sup> Years later, Routier *et al.* described evidences for an Fe<sup>II</sup>-CO intermediate by photochemical methods by using a sacrificial electron donor triethylamine (Et<sub>3</sub>N) in the presence of CO<sub>2</sub> saturated [Fe<sup>III</sup>(TPP)]Cl in acetonitrile, observing the same signatures as previously reported of a Soret band at 420 nm and Q-bands at 535 and 610 nm (Figure 4.9).

This adduct formation was further confirmed by performing UV-Vis measurements in the presence of CO.<sup>46</sup>

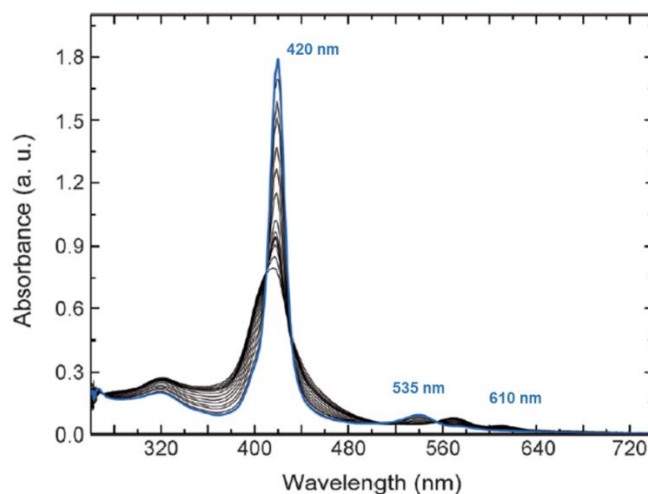


**Figure 4.9.** UV-Vis evolution for CO-saturated  $[\text{Fe}^{\text{III}}(\text{TPP})]\text{Cl}$  and  $\text{Et}_3\text{N}$  in acetonitrile upon irradiation. Blue spectrum correspond to the formation of the  $[\text{Fe}^{\text{II}}(\text{TPP})(\text{CO})]$  adduct.

*Adapted from references 46.*

#### 4.4 Outlook

We have shown along these introductory chapters that electrochemical and spectroscopic methods have been used for decades in order to understand the structure of adduct between  $\text{CO}_2$  or CO and iron porphyrins sometimes in their reduced forms. Even though many insights on the electronic structure of these systems have been performed by chemical reduction and *ex situ* processes, controversies on the electronic configuration of iron porphyrins, especially for the highly reduced oxidation states, are still present to date. Kinetic information obtained by electrochemical methods have allowed proposing the reaction mechanism. However, the electronic and geometric characterization of the intermediate species is still missing.

In the following chapters, we will present the major results obtained during this thesis project to get insights on the electronic configuration of iron porphyrins under conditions that are relevant to  $\text{CO}_2$  reduction electrocatalysis. Therefore, we will start in chapter V by presenting the tools that have been developed and used to perform these spectroelectrochemical measurements. In chapter VI, we will present the results obtained with *in situ* XAS and UV-Vis spectroelectrochemical measurements under argon atmosphere. The results will be compared to previous references described in the current chapter, in order to identify the highly reduced iron porphyrins species generated in solution. In chapter VII, the same procedure will be followed, under a  $\text{CO}_2$  atmosphere. Finally, the results obtained under both inert and  $\text{CO}_2$  atmospheres will be compared and discussed in light of the literature in chapter



VIII. Implications for the CO<sub>2</sub> reduction reaction mechanism will be provided and perspectives for future work will be given.

#### 4.5. References Chapter IV

- (1) McClure, D. S. Electronic Structure of Transition-Metal Complex Ions. *Radiat Res. Suppl.* **1960**, 2, 218–242.
- (2) Fierro, C.; Anderson, A. B.; Scherson, D. A. Electron Donor-Acceptor Properties of Porphyrins, Phthalocyanines, and Related Ring Chelates: A Molecular Orbital Approach. *J. Phys. Chem.* **1988**, 92 (24), 6902–6907.
- (3) Walker, F.A.; Simonis, U. Iron Porphyrin Chemistry. *Encyclopedia of Inorganic Chemistry*. Volume IV. John Wiley & Sons. 2<sup>nd</sup> edition. **2006**. pp: 2390-2521.
- (4) Paulat, F.; Lehnert, N. Detailed Assignment of the Magnetic Circular Dichroism and UV–vis Spectra of Five-Coordinate High-Spin Ferric [Fe(TPP)(Cl)]. *Inorg. Chem.* **2008**, 47 (11), 4963–
- (5) Jones, S. E.; Srivatsa, G. S.; Sawyer, D. T.; Traylor, T. G.; Mincey, T. C. Redox Chemistry of Iron Tetraphenylporphyrin Imidazolate-Chelated Protoheme, and of Their Iron(II)-Superoxide Adducts in Dimethyl Sulfoxide. *Inorg. Chem.* **1983**, 22 (26), 3903–3910.
- (6) Römel, C.; Song, J.; Tarrago, M.; Rees, J. A.; van Gastel, M.; Weyhermüller, T.; DeBeer, S.; Bill, E.; Neese, F.; Ye, S. Electronic Structure of a Formal Iron(0) Porphyrin Complex Relevant to CO<sub>2</sub> Reduction. *Inorg. Chem.* **2017**, 56 (8), 4745–4750.
- (7) Yamashige, H.; Matsuo, S.; Kurisaki, T.; Perera, R. C. C.; Wakita, H. Electronic Structure Analysis of Iron(III)-Porphyrin Complexes by X-Ray Absorption Spectra at the C, N and Fe K-Edges. *Anal. Sci.* **2005**, 21 (3), 309–314.
- (8) Westre, T. E.; Kennepohl, P.; DeWitt, J. G.; Hedman, B.; Hodgson, K. O.; Solomon, E. I. A Multiplet Analysis of Fe K-Edge 1s → 3d Pre-Edge Features of Iron Complexes. *J. Am. Chem. Soc.* **1997**, 119 (27), 6297–6314.
- (9) Collins, D. P.; Dawson, J. H. 3.05 - Recent History of Heme-Containing Proteins: Advances in Structure, Functions, and Reaction Intermediate Determination. In *Comprehensive Inorganic Chemistry II (Second Edition)*; Reedijk, J., Poepelmeier, K., Eds.; Elsevier: Amsterdam, **2013**; pp 65–102.
- (10) Tarrago, M.; Römel, C.; Nehr Korn, J.; Schnegg, A.; Neese, F.; Bill, E.; Ye, S. Experimental and Theoretical Evidence for an Unusual Almost Triply Degenerate Electronic Ground State of Ferrous Tetraphenylporphyrin. *Inorg. Chem.* **2021**, 60 (7), 4966–4985.
- (11) Verdager, M.; Cartier, C.; Momenteau, M.; Dartyge, E.; Fontaine, A.; Tourillon, G.; Michalowicz, A. From iron(II) to iron(III) basket handle porphyrins : static and kinetics X-ray absorption studies. *J. Phys. Colloq.* **1986**, 47 (C8), C8-649-C8-652.
- (12) Cartier, C.; Momenteau, M.; Dartyge, E.; Fontaine, A.; Tourillon, G.; Michalowicz, A.; Verdager, M. X-Ray Absorption Spectroscopy of Iron-(II) and -(III) Basket-Handle Porphyrins. *J. Chem. Soc., Dalton Trans.* **1992**, No. 4, 609–618.
- (13) Kim, S.; Tryk, D.; Bae, I. T.; Sandifer, M.; Carr, R.; Antonio, M. R.; Scherson, D. A. In Situ Extended X-Ray Absorption Fine Structure of an Iron Porphyrin Irreversibly Adsorbed on an Electrode Surface. *J. Phys. Chem.* **1995**, 99 (25), 10359–10364.



- (14) Kim, S.; Bae, I. T.; Sandifer, M.; Ross, P. N.; Carr, R.; Woicik, J.; Antonio, M. R.; Scherson, D. A. In Situ XANES of an Iron Porphyrin Irreversibly Adsorbed on an Electrode Surface. *J. Am. Chem. Soc.* **1991**, *113* (24), 9063–9066.
- (15) Wilson, S. A.; Green, E.; Mathews, I. I.; Benfatto, M.; Hodgson, K. O.; Hedman, B.; Sarangi, R. X-Ray Absorption Spectroscopic Investigation of the Electronic Structure Differences in Solution and Crystalline Oxyhemoglobin. *PNAS* **2013**, *110* (41), 16333–16338.
- (16) Lexa, D.; Momenteau, M.; Mispelter, J.; Lhoste, J. M. Electrochemical Study of the Effect of Axial Coordination upon the Redox Behavior of Iron Porphyrins in Dimethylformamide. *Bioelectrochem Bioenerg.* **1974**, *1* (1), 108–117.
- (17) Anxolabéhère, E. Influences supramoléculaires sur la réaction redox Fe(I)/Fe(0) (ou Fe(0)?) dans les porphyrines de fer. These de doctorat, *Paris 7*, **1991**.
- (18) Lexa, D.; Momenteau, M.; Mispelter, J. Characterization of the Reduction Steps of Fe(III) Porphyrins. *Biochim Biophys.* **1974**, *338* (1), 151–163.
- (19) Lexa, D.; Rentien, P.; Savéant, J. M.; Xu, F. Methods for Investigating the Mechanistic and Kinetic Role of Ligand Exchange Reactions in Coordination Electrochemistry: Cyclic Voltammetry of Chloroiron(III)Tetraphenylporphyrin in Dimethylformamide. *J. Electroanal. Chem. Interf. Electrochem.* **1985**, *191* (2), 253–279.
- (20) Pegis, M. L.; Martin, D. J.; Wise, C. F.; Brezny, A. C.; Johnson, S. I.; Johnson, L. E.; Kumar, N.; Rauegi, S.; Mayer, J. M. Mechanism of Catalytic O<sub>2</sub> Reduction by Iron Tetraphenylporphyrin. *J. Am. Chem. Soc.* **2019**, *141* (20), 8315–8326.
- (21) Kadish, K. M.; Larson, G.; Lexa, D.; Momenteau, M. Electrochemical and Spectral Characterization of the Reduction Steps of .Mu.-Oxo-Bis(Iron Tetraphenylporphyrin) Dimer in Dimethylformamide. *J. Am. Chem. Soc.* **1975**, *97* (2), 282–288.
- (22) Anxolabéhère, E.; Chottard, G.; Lexa, D. Highly reduced iron porphyrin: UV-Vis and resonance Raman spectroelectrochemical studies of FeTPP and FeTF<sub>5</sub>PP. *New. J. Chem.* **1994**, *18*, 889–899.
- (23) Cohen, I. A.; Ostfeld, D.; Lichtenstein, B. Characterization of a d<sup>7</sup> Iron System. Tetraphenylporphineiron(I) Anion. *J. Am. Chem. Soc.* **1972**, *94* (13), 4522–4525.
- (24) Mashiko, T.; Reed, C. A.; Haller, K. J.; Scheidt, W. R. Nature of Iron(I) and Iron(0) Tetraphenylporphyrin Complexes. Synthesis and Molecular Structure of (Dibenzo-18-Crown-6) Bis(Tetrahydrofuran) Sodium (Meso-Tetraphenylporphinato) Ferrate and Bis[Tris(Tetrahydrofuran)Sodium] (Meso-Tetraphenylporphinato) Ferrate. *Inorg. Chem.* **1984**, *23* (20), 3192–3196.
- (25) Römelt, C.; Ye, S.; Bill, E.; Weyhermüller, T.; van Gastel, M.; Neese, F. Electronic Structure and Spin Multiplicity of Iron Tetraphenylporphyrins in Their Reduced States as Determined by a Combination of Resonance Raman Spectroscopy and Quantum Chemistry. *Inorg. Chem.* **2018**, *57* (4), 2141–2148.





- (26) Lexa, D.; Mispelter, J.; Savéant, J.-M. Electroreductive Alkylation of Iron in Porphyrin Complexes. Electrochemical and Spectral Characteristics of  $\sigma$ -Alkylironporphyrins. *J. Am. Chem. Soc.* **1981**, *103* (23), 6806–6812.
- (27) Lexa, D.; Saveant, J. M.; Wang, D. L. Electroreductive Alkylation of Iron Porphyrins. Iron(III), Iron(II) and Iron(I) Alkyl Complexes from the Reaction of Doubly Reduced Iron(II) Porphyrins with Alkyl Halides. *Organometallics* **1986**, *5* (7), 1428–1434.
- (28) Gueutin, C.; Lexa, D. Low temperature spectroelectrochemistry for the characterization of highly reduced  $\sigma$ -alkyl iron halogenated porphyrins. *Electroanal.* **1996**, *8*, 11, 1029–1033.
- (29) Mascetti, J. Carbon Dioxide Coordination Chemistry and Reactivity of Coordinated CO<sub>2</sub>. In *Carbon Dioxide as Chemical Feedstock*; John Wiley & Sons, Ltd, 2010; pp 55–88.
- (30) Zhang, S.; Fan, Q.; Xia, R.; Meyer, T. J. CO<sub>2</sub> Reduction: From Homogeneous to Heterogeneous Electrocatalysis. *Acc. Chem. Res.* **2020**, *53* (1), 255–264.
- (31) Leitner, W. The coordination chemistry of carbon dioxide and its relevance for catalysis: A Critical Survey. *Coord. Chem. Rev.* **1996**, *153*, 257–284.
- (32) Roy, L.; Mondal, B.; Neese, F.; Ye, S. Chapter 5: Theoretical Approach to Homogeneous Catalytic Reduction of CO<sub>2</sub>: Mechanistic Understanding to Build New Catalysts. In *Carbon Dioxide Electrochemistry*; 2020; pp 197–225.
- (33) Francke, R.; Schille, B.; Roemelt, M. Homogeneously Catalyzed Electroreduction of Carbon Dioxide-Methods, Mechanisms, and Catalysts. *Chem Rev* **2018**, *118* (9), 4631–4701.
- (34) Walsh, A. D. The Electronic Orbitals, Shapes, and Spectra of Polyatomic Molecules. Part I. AH<sub>2</sub> Molecules. *J. Chem. Soc.* **1953**, 2260–2266.
- (35) Calabrese, J. C.; Herskovitz, T.; Kinney, J. B. Carbon Dioxide Coordination Chemistry. 5. The Preparation and Structure of the Rhodium Complex Rh( $\eta$ -1-CO<sub>2</sub>)(Cl)(Diars)<sub>2</sub>. *J. Am. Chem. Soc.* **1983**, *105* (18), 5914–5915.
- (36) Costentin, C.; Drouet, S.; Robert, M.; Savéant, J.-M. A Local Proton Source Enhances CO<sub>2</sub> Electroreduction to CO by a Molecular Fe Catalyst. *Science* **2012**, *338* (6103), 90–94.
- (37) Costentin, C.; Passard, G.; Robert, M.; Savéant, J.-M. Pendant Acid–Base Groups in Molecular Catalysts: H-Bond Promoters or Proton Relays? Mechanisms of the Conversion of CO<sub>2</sub> to CO by Electrogenenerated Iron(0)Porphyrins Bearing Prepositioned Phenol Functionalities. *J. Am. Chem. Soc.* **2014**, *136* (33), 11821–11829.
- (38) Mondal, B.; Rana, A.; Sen, P.; Dey, A. Intermediates Involved in the 2e<sup>-</sup>/2H<sup>+</sup> Reduction of CO<sub>2</sub> to CO by Iron(0) Porphyrin. *J. Am. Chem. Soc.* **2015**, *137* (35), 11214–11217.
- (39) Lu, X.; Ahsaine, H. A.; Dereli, B.; Garcia-Esparza, A. T.; Reinhard, M.; Shinagawa, T.; Li, D.; Adil, K.; Tchalala, M. R.; Kroll, T.; Eddaoudi, M.; Sokaras, D.; Cavallo, L.; Takanabe, K. Operando Elucidation on the Working State of Immobilized Fluorinated Iron Porphyrin for Selective Aqueous Electroreduction of CO<sub>2</sub> to CO. *ACS Catal.* **2021**, *11* (11), 6499–6509.
- (40) Yoshikawa, S.; Choc, M. G.; O’Toole, M. C.; Caughey, W. S. An Infrared Study of CO Binding to Heart Cytochrome c Oxidase and Hemoglobin A. Implications Re O<sub>2</sub> Reactions. *J. Biol. Chem.* **1977**, *252* (15), 5498–5508.





- (41) Aubke, F.; Wang, C. Carbon Monoxide as a  $\sigma$ -Donor Ligand in Coordination Chemistry. *Coord. Chem. Rev.* **1994**, *137*, 483–524.
- (42) Croisy, A.; Lexa, D.; Momenteau, M.; Savéant, J.-M. Integrated Molecular Systems. Fixation of Carbon Monoxide on Iron(I) in Simple and Superstructured Porphyrins. *Organometallics* **1985**, *4* (9), 1574–1579.
- (43) Ascone, I.; Bianconi, A.; Dartyge, E.; Della Longa, S.; Fontaine, A.; Momenteau, M. Linear Fe-C-O Configuration in Carbonyl 1-Methylimidazole Iron(II) Porphyrin Detected by XANES in Dispersive Mode. *Biochim. Biophys.* **1987**, *915* (2), 168–171.
- (44) Cartier, C.; Momenteau, M.; Dartyge, E.; Fontaine, A.; Tourillon, G.; Bianconi, A.; Verdagner, M. X-Ray Absorption Spectroscopy of Carbonyl Basket Handle Fe(II) Porphyrins: The Distortion of the Tetrapyrrolic Macrocycle. *Biochim. Biophys.* **1992**, *1119* (2), 169–174.
- (45) Bae, I. T.; Scherson, D. A. In Situ X-Ray Absorption of a Carbon Monoxide–Iron Porphyrin Adduct Adsorbed on High-Area Carbon in an Aqueous Electrolyte. *J. Phys. Chem. B* **1998**, *102* (14), 2519–2522.
- (46) Bonin, J.; Chaussemier, M.; Robert, M.; Routier, M. Homogeneous Photocatalytic Reduction of CO<sub>2</sub> to CO Using Iron(0) Porphyrin Catalysts: Mechanism and Intrinsic Limitations. *ChemCatChem* **2014**, *6* (11), 3200–3207.

# Chapter V

---

## X-Ray Absorption Spectroelectrochemistry: Instrumentation

### Content

---

<b>5.1</b> State of the art .....	<b>67</b>
<b>5.1.1</b> Molecular catalyst immobilized in high surface area electrode .....	<b>67</b>
<b>5.1.2</b> Molecular catalyst in solution .....	<b>68</b>
<b>5.2</b> Cell used during this thesis project .....	<b>70</b>
<b>5.3</b> Cell parameters .....	<b>71</b>
<b>5.3.1</b> Technical considerations .....	<b>71</b>
<b>5.3.2</b> Spectroscopic parameters .....	<b>74</b>
<b>5.3.3</b> Electrochemical parameters .....	<b>76</b>
<b>5.4</b> Conclusion .....	<b>77</b>
<b>5.5</b> References .....	<b>78</b>



As detailed in chapter III, X-ray absorption spectroelectrochemical (XAS-EC) experiments have gained more attention in the latest years. This is mostly because of the significant amount of information that can be obtained from a single spectrum on a broad number of systems and in various experimental conditions. As for other spectroelectrochemical techniques, XAS-EC must ensure high-quality data for both spectroscopic and electrochemical measurements. In contrast with other spectroelectrochemical techniques such as UV-Vis or IR, for which experimental setups are commercially available, XAS-EC requires the development of specific spectroelectrochemical cells adapted to the techniques and scientific goals of interest.

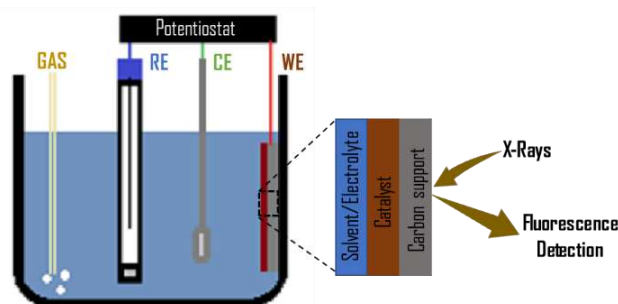
In order to perform *in situ* XAS spectroelectrochemical measurement on homogeneous samples of iron porphyrins, the development of an adequate XAS spectroelectrochemical cell was the first task required. The description regarding the synchrotron and beamlines used to acquire the data as well as the experimental procedures, cells and instrumentation information can be found in appendices B and D. This chapter is dedicated to some of the experiments performed in order to reach optimal XAS-EC performances with the setup used.

### 5.1 State of the art

Some important aspects are necessary to take into consideration when designing spectroelectrochemical cells.<sup>1</sup> For instance, the setup must ensure the complete electrochemical conversion of species, while minimizing cell resistance and diffusion pathways so that the conversion is performed in the shortest time. In addition to this, a sufficient amount of material must be probed, while solvent and electrolyte thickness must be reduced in order to obtain a good signal to noise data. The cell parts, such as the cell window, body, electrodes and other components, must be resistant and transparent to X-rays. Taking these aspects into consideration, many spectroelectrochemical cells have been developed, which have been used in some cases in order to study molecular catalysts, as briefly described below.

#### 5.1.1. Molecular catalyst immobilized in high surface area electrodes

One strategy to ensure a complete conversion of species in the shortest time while obtaining spectra with good signal-to-noise ratio is to use high surface electrodes. In some reported cases, an ink containing the catalysts is deposited on a conductive material that serves as the surface for the working electrode. First *in situ/operando* XAS-EC experiments for the analysis of molecular catalysts have been recorded by using these materials and a general setup as described in scheme 5.1.<sup>2,3</sup> Some examples illustrating the use of these electrodes for the study of the CO<sub>2</sub>RR was briefly presented in section 3.3.



**Scheme 5.1.** Schematic representation of a XAS-EC setup for the study of molecular catalysts electrocatalysts heterogenized on a high surface area working electrode.

*Adapted from reference 3*

*WE: working electrode, CE: counter electrode, RE: reference electrode.*

Although *in situ/operando* analysis using immobilized materials provides direct information under electrocatalytic conditions, it lacks precision when it comes to identifying intermediates. Indeed, the high loading of high surface area electrodes leads to a signal that can be dominated by inactive materials rather than the active one, as previously suggested by King *et al.*<sup>4</sup> In addition to this, the electrochemical analysis of immobilized catalyst by cyclic voltammetry is very challenging, electron transfer processes being hidden by electrode effects. The stepwise generation of reduced intermediates towards catalytic potential is therefore hampered, jeopardizing the identification of the catalytic species involved. On the contrary, the study of molecular catalysts in homogeneous conditions, allows a better correlation with electrochemical measurements, thus providing more accurate information on the chemical state of the catalyst as a function of the potential.

### 5.1.2. Molecular catalyst in solution

#### - *Thin-layer configuration*

The first XAS spectroelectrochemical cell for studies of transition metal complexes in solution was developed in 1986 by the Heineman group,<sup>5</sup> taking inspiration from previous cell development.<sup>6-9</sup> This cell has a reticulated vitreous carbon as working electrode, a platinum wire as counter electrode and a Ag/AgCl reference electrode. Kapton (polyamide) or Mylar (poly(ethylene terephthalate)) were used as cell windows to reduce X-ray attenuation. A platinum needle was used as both filling port and to ensure electrical contact. The time required (*ca.* 30 min) to achieve electrochemical conversion was, however, quite long to be compatible with an XAS experiment and the filling port could incorporate oxygen into the sample solution.

To allow a fast conversion of species while probing enough material to ensure a proper signal and reduce attenuation by the solvent, a thin-layer configuration is required. Charnock *et al.* presented in 1997 a novel XAS spectroelectrochemical cell inspired from the previous report

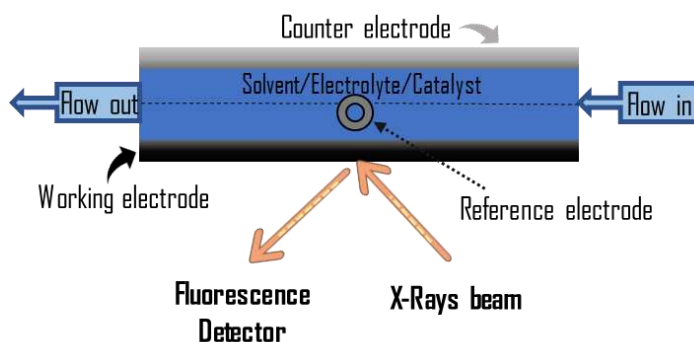
from the Heineman group and the optically transparent thin layer electrodes (OTTLE) cell used for UV-Vis spectroelectrochemistry. This setup allowed XAS analysis on metallic complexes in solution, however, by keeping long period of electrolysis time (*ca.* 20 min).<sup>10</sup> Continuing these early designs, Ascone *et al.* developed a cell in which the sample volume was reduced, allowing not only to minimize cell resistance but also a faster conversion of species.<sup>11</sup> Anxolabéhère-Mallart *et al.* performed sulfur K-edge measurements using a spectroelectrochemical cell inspired from these previous reports.<sup>12</sup>

#### - Thin layer flow cells

Spectroelectrochemical flow cells has also been reported. For instance, Igo *et al.* reported in 1991 a setup in which a flow-cell was connected to a bulk-electrolysis cell.<sup>13</sup> This setup permitted the continuous flow of electrochemically generated solution towards the interaction point with the X-rays. A disadvantage is that the electrogenerated species were not produced *in situ* in the X-ray chamber, therefore changes in the composition could occur during the flow time. The development of thin-layer spectroelectrochemical flow cells for *in situ-operando* experiments appears as a good alternative to generate species directly at the interaction point with X-rays, while being able to regenerate them by circulation.

An example of a flow spectroelectrochemical cell used for the *in situ* study of homogeneous solutions was reported by the Lassalle-Kaiser team in 2019.<sup>14</sup> By using a 3D printed cell, single-electron transfer processes could be spectroscopically followed with good signal-to-noise ratio for the  $\text{Fe}^{\text{III}}\text{Cl}_3/\text{Fe}^{\text{II}}\text{Cl}$  redox couple, with a 90% conversion without noticeable radiation damage. This was possible due to the simultaneous use of a high surface area electrode and the high concentration of the sample. Disadvantages include a complex geometry that prevented mechanical machining with chemical resistant materials to allow its use in organic media. Nonetheless, it should be noted that the development of 3D printing technology has revolutionized the field due to the convenience to produce home-made designed setups in a faster and more economical way. The use of this technology allows producing devices with precise patterns that can otherwise be difficult to build by mechanical machining procedures.<sup>15,16</sup>

Guo *et al.* reported an *in-situ* spectroelectrochemical flow cell which was designed for soft X-Ray studies in ultra-high vacuum chambers.<sup>17</sup> This cell, which general representation is shown in scheme 5.2, is a good example in which the solution can be continuously flown inside the chamber in order to reduce possible radiation damage. Apart from the advantage of performing experiments under vacuum atmosphere while flowing, the cell was also built-in polyether-ether ketone (PEEK), a material that is vacuum compatible, offers excellent chemical resistance to many solvents as well as good mechanical properties. This cell served as an inspiration for the cell presented in this manuscript, named as “cell A”, which will be further discussed in this chapter.

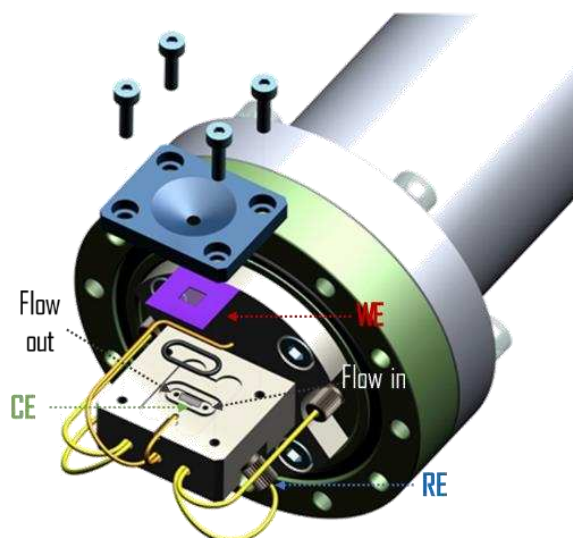


**Scheme 5.2.** Schematic representation of a thin layer spectroelectrochemical flow cell used for fluorescence detection of molecular species in solution.

## 5.2 Cell used during this thesis project

Scheme 5.3 shows a general view of cell A, with additional figures and pictures presented in appendix D. Similarly to a conventional electrochemical setup, this cell features three electrodes. A thin (60  $\mu\text{m}$ ) glassy carbon (GC) film is used as working electrode. The use of GC electrodes allows X-ray penetration down to *ca.* 4 keV, while providing electrochemical performances similar to those used in a conventional electrochemical setup. A platinum grid is used as counter electrode placed in front of the working electrode, while the reference electrode is a silver ( $\text{Ag}/\text{Ag}^+$ ) wire (pseudoreference) electrode inserted on the side of the liquid path.

Cell A allows the simultaneous recording of electrochemical data while XAS spectra are collected. The liquid layer of 200  $\mu\text{m}$  allows an almost total electrochemical conversion of species as further described. The cell is built in PEEK, allowing the use of organic solvents such as DMF and providing good mechanical properties. Additionally, this cell also allows flowing solutions through the electrochemical chamber by means of Teflon tubing and a syringe pump or peristaltic pump. Even if during the measurements performed during this project the sample was stationary, the possibility to empty and refill the cell without unmounting it from the experimental chamber (which is under vacuum) allows saving a significant amount of time while avoiding contamination from air. Finally, cell A allows performing experiments inside of a vacuum chamber (namely, the LUCIA beamline at Synchrotron SOLEIL), reducing the risk for oxygen presence that would react with the species of interest.



**Scheme 5.3. General scheme of the cell used during the present project.**

*WE: working electrode, CE: counter electrode, RE: reference electrode.*

### 5.3 Cell parameters

As indicated above, to ensure an optimal and reproducible experiments many parameters need to be considered. They are related to the following requirements:

- 1) Technical aspects: the materials used for the cell construction need to be carefully chosen in order to resist chemicals and to ensure liquid and gas tightness.
- 2) Spectroscopic control: the detection mode, material quantity and beam-induced damages significantly influence the data quality and time resolution.
- 3) Electrochemical control: a total electrochemical conversion of species during the spectrum recording time should be achieved. The experimental conditions should favor a minimal resistance and a stabilized current. The possibility to record cyclic voltammograms with profiles similar to what is observed in a classical three-electrode setup is also required for appropriate comparison.

In this section, the most important parameters examined during this project will be discussed.

#### 5.3.1. Technical considerations

##### - Cell material

One important practical consideration when studying reaction mechanism in homogeneous catalysis is related to the nature of the solvent. In particular, the use of dry aprotic solvents, such as DMF as in the present case, has many advantages, especially:

- DMF dissolves the iron porphyrin and the commonly used supporting electrolytes, such as tetrabutylammonium hexafluorophosphate.



- DMF offers a large potential window, reported between -2.5 to +1.8 V *vs* SCE, which is appropriate for the study of reduced species.<sup>18</sup>

- CO<sub>2</sub> is five times more soluble in DMF than in water. Indeed, solubility of CO<sub>2</sub> in DMF has been reported to be of 0.2 M<sup>19</sup> whereas in water is only of 0.04 M, even though this solubility can be enhanced by pH variation.<sup>20,21</sup>

Although 3D printing technology offers a fast and economical cell fabrication with complex designs, the used materials are not resistant to DMF. The cell design was therefore modified, from the previous version developed by the team,<sup>14</sup> to allow mechanical machining of PEEK as a solvent resistant polymer.

### - Liquid and gas tightness

In order to perform experiments under vacuum conditions, the o-ring sealing the working electrode with the cell was carefully selected (see appendix D). The geometry of the cell allows the flow of liquids without bubble formation. In order to check for the liquid and gas tightness of cell A, it was filled with an argon purged DMF + 0.1 MTBAPF<sub>6</sub> solution of [Fe<sup>III</sup>(TPP)]Cl. Cyclic voltammograms were recorded with the cell directly placed at room atmosphere (green trace – figure 5.1). Waves observed at ~ -1.0 V and at ~ -1.4 V *vs* SCE correspond to the reduction process of the [(Fe<sup>III</sup>(TPP))<sub>2</sub>O] dimeric species, as described in chapter IV.<sup>22</sup> These peaks are not observed on the CV when the cell is located in an inert atmosphere, *i.e.* inside a glove bag filled with argon, or under vacuum (black trace – figure 5.1). From these observations we can conclude that performing XAS-EC experiments on reduced species of iron porphyrins requires an inert atmosphere (Ar or N<sub>2</sub> atmosphere or vacuum) in order to avoid O<sub>2</sub> contamination during the experiment. We shall add that the presence of O<sub>2</sub> was shown to be deleterious to our studies since iron porphyrins shows catalytic activation of O<sub>2</sub> at more positive potential than CO<sub>2</sub> (-0.95 V *vs* SCE in the case of [Fe<sup>III</sup>(TPP)]Cl in DMF), which hampers their catalytic activity towards CO<sub>2</sub> reduction.<sup>23,24</sup> Inert conditions around the cell (particularly vacuum) are also beneficial to avoid moisture in the analyzed solution, which can be detrimental to the stability of intermediates or to catalysis. The effect of the presence of water/moisture in the sample and their minimization are further described in appendix C.

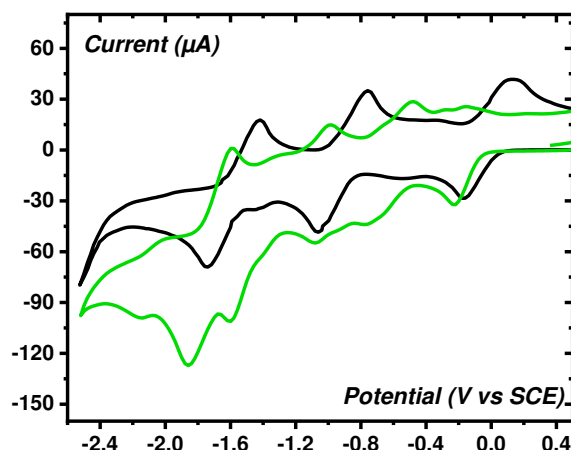
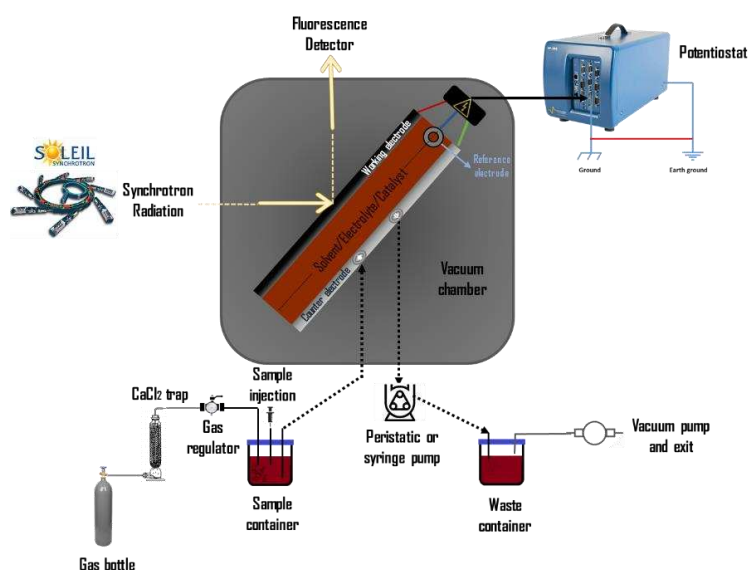


Figure 5.1. Cyclic voltammograms of a 2 mM solution  $[\text{Fe}^{\text{III}}(\text{TPP})]\text{Cl}$  in  $\text{DMF}+\text{TBAPF}_6$  0.1 M recorded in cell A at room atmosphere (green) and while keeping the cell inside a glove bag filled with Argon (black). Scan rate  $\nu = 100 \text{ mV}\cdot\text{s}^{-1}$ . The solution is saturated with argon in both experiments.

### - Sample delivery

Early experimental setup did not allow the sample delivery through pumping of the electrolyte and/or catalyst solution to the interaction point with the X-rays. Here we show that a better control of the experimental atmosphere can be obtained by using a flow system. The use of sealed containers for the solution allows saturating it with the required gas outside the spectroscopic cell or mixing it with reactants before flowing it into the chamber/cell without any air contact (see scheme 5.4). In addition to this, the sample, which was stationary during experiments, can be changed without removal of the cell from the experimental stage saving a considerable amount of time that is valuable during synchrotron experiences.



Scheme 5.4. Sample delivery system to the cell once installed on the LUCIA beamline experimental station.

Finally, the working electrode surface should remain as clean as possible throughout the experience. In order to avoid a time-consuming manipulation to remove the electrode and polish it, a DMF cleaning solution can be circulated to clean the cell and the electrode surface. The quality of the electrode surface, and in particular, the absence of any metallic deposition was probed by recording blank XAS spectra.

### 5.3.2 Spectroscopic parameters

#### - Detection mode

An XAS spectrum can be measured with different detection modes, which are detailed in appendix B. The experiments performed in this work were done in fluorescence mode, which can afford lower concentrations (in the mMol range) than transmission mode.<sup>14</sup> CO<sub>2</sub> reduction by iron porphyrins uses concentrations in the range 0.5 to 2 mM, which makes *fluorescence* detection an appropriate choice. More details regarding to this parameter are extended in appendix D.

#### - Radiation damages

In general terms, radiation damages describe the changes occurring on the sample due to its interaction with X-rays. They can be detected when modifications of the spectra are observed without any other external interference than the one with X-rays. They need to be carefully monitored to avoid misinterpretation of the data and experimental conditions should be optimized to reduce them as much possible.

There are several ways to reduce photodamage but not all of these strategies can be implemented while performing *in situ/operando* spectroelectrochemical measurements.<sup>4,25</sup> For instance, cryogenic cooling is usually used when collecting *ex situ* data on frozen samples, with temperatures in the range 20-100 K. Such temperatures cannot be reached, however, for *in situ/operando* conditions, and using higher temperatures would lead to cumbersome modifications of the *in situ* systems while provide little benefit in terms of radiation damage prevention. Other strategies to reduce radiation damage include recording data at different sample positions or lowering the X-ray dose deposited on a given sample spot. The concept of “spot” is hardly relevant in the case of liquids, since the species can diffuse in solution, making it irrelevant to probe different positions. The photon density of the beam can nonetheless be tuned (depending on the beamline) to make it as low as possible. The ideal situation is a large beam with a high total amount of photons, so that the signal to noise ratio remains reasonable while avoiding too high X-ray doses on each spot.

In order to study this effect during this project, spectra were recorded with two different beam sizes. As observed in figure 5.2, when using a beam size of *ca* 0.05 x 0.1 mm with a high flux of photons at the GALAXIES beamline of Synchrotron SOLEIL, a shift towards lower

energies was observed when compared to the initial spectra or to the spectra recorded with the larger beam (*ca.* 1 x 2 mm) of the LUCIA beamline. After recording 8 spectra (approximately 4 minutes of recording time) at GALAXIES a more pronounced shift towards lower energies and pre-edge changes were observed on the spectrum. This indicates that a focused beam (*ca.* 3 - 6 orders of magnitude more dense on GALAXIES than LUCIA beamline) strongly affects the signal by damaging the sample in a few minutes of irradiation. This was important to address since a shift of the rising edge could correspond to a change in the oxidation state of the element of interest, *i.e.* iron.<sup>26</sup> In this case, photoreduction processes could interfere with the electrochemical process of interest. Therefore, all experiments were performed using a beam of at least 1 x 2 mm on the LUCIA beamline.

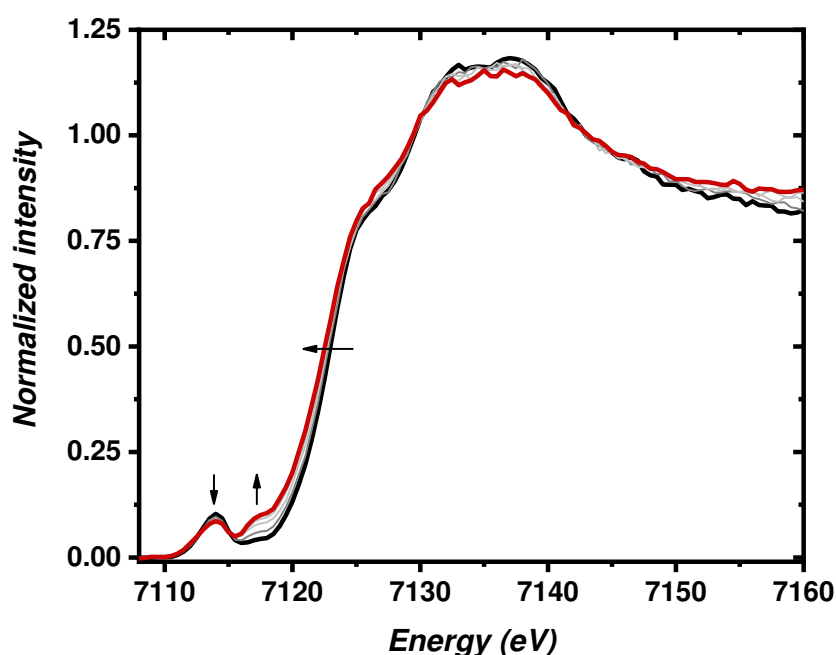


Figure 5.2. Fe K-edge XANES spectra of  $[\text{Fe}^{\text{III}}(\text{TPP})]\text{Cl}$  in the solid state recorded on the GALAXIES beamline (Synchrotron SOLEIL) with a beam size of  $50 \times 100 \mu\text{m}$  at different irradiation times. Initial (black), intermediate (grey) and final spectra (red). The recording time of each spectrum is one minute; the final spectrum corresponds to a 4 minutes irradiation time.

### 5.3.3 Electrochemical parameters

#### - Working electrode materials

Glassy carbon was selected as working electrode due to its electrochemical, mechanical and X-ray properties. From the electrochemistry point of view, this material is widely used in laboratory measurements, since it is highly conductive, and it is stable in the potential range of interest. Hence, its use in the spectroelectrochemical setup allows a direct correlation between synchrotron based and laboratory experiments. Additionally, GC requires a lower potential than platinum or gold electrodes to reduce protons into  $\text{H}_2$ , which is a competitive

reaction to the CO<sub>2</sub>RR. Moreover, GC does not present non-covalent interaction with iron porphyrins, on the contrary to gold electrodes. Considering spectroscopic aspects, GC is X-Ray transparent down to 4 keV (for a 60 μm thick electrode), chemically resistant and can withstand a pressure difference between sample compartment (room pressure) and the measurement chamber (primary vacuum). Therefore, this material was selected as working electrode and cell window for XAS-EC studies.

### - Electrochemical conversion

The use of a thin layer spectroelectrochemical cell is an important parameter on the electrochemical conversion of the species of interest. To assess the rate of conversion of the spectroelectrochemical cells, an initial study using iron chloride as standard reference was carried out, since the XAS spectra of these species is widely known in its solid and aqueous forms, both at the Fe(II) and Fe(III) oxidation states.<sup>27</sup> Hence, 2 mM solutions of Fe<sup>III</sup>Cl<sub>3</sub>·6H<sub>2</sub>O and Fe<sup>II</sup>Cl<sub>2</sub> were prepared under anaerobic conditions in DMF and 0.1 M TBAPF<sub>6</sub> as electrolyte. The cyclic voltammogram performed in cell A under argon at a scan rate of 100 mV·s<sup>-1</sup> shows an anodic peak at -0.10 V and a cathodic peak at -0.22 V vs SCE as evidenced in figure 5.3 - insert.

Figure 5.3 shows the Fe K-edge XANES recorded on both the ferric and ferrous solutions under anaerobic conditions during a 15 minutes scan. The spectrum of the Fe<sup>III</sup>Cl<sub>3</sub> solution (blue line) displays a low intensity white line (main edge peak top), a pronounced pre-edge peak and a main edge position at 7122.3 eV. The spectrum of the Fe<sup>II</sup>Cl<sub>2</sub> solution (red line) presents a more intense white line and a rising edge that is shifted to lower values by 2 eV in comparison with the spectrum of the Fe(III) species. In addition to these observations, the intensity of the pre-edge peak clearly decreases and is also shifted towards lower energies. The differences in the edge position, as well as in the pre-edge, are in agreement with previously reported data<sup>14</sup> and confirms the one electron difference between the two species.

When a constant potential of  $E = -0.6$  V vs. Ag/Ag<sup>+</sup> is applied during 15 minutes to an Fe<sup>III</sup>Cl<sub>3</sub> solution in DMF + 0.1 M TBAPF<sub>6</sub>, a shift of 2 eV towards lower energies is observed on the main edge, yielding a spectrum that closely matches the one of the Fe<sup>II</sup>Cl<sub>2</sub> reference sample (figure 5.3 – black dotted line). Linear combination fittings (LCF) performed on the XANES spectrum of the final species using the reference spectra of the Fe<sup>III</sup>Cl<sub>3</sub> and Fe<sup>II</sup>Cl<sub>2</sub> solutions, yield a conversion of 96%. This value is higher than what was obtained with the transmission spectroelectrochemical cell recently developed by our team (90%), confirming the importance of a thin layer configuration for a complete electrochemical conversion.<sup>14</sup>

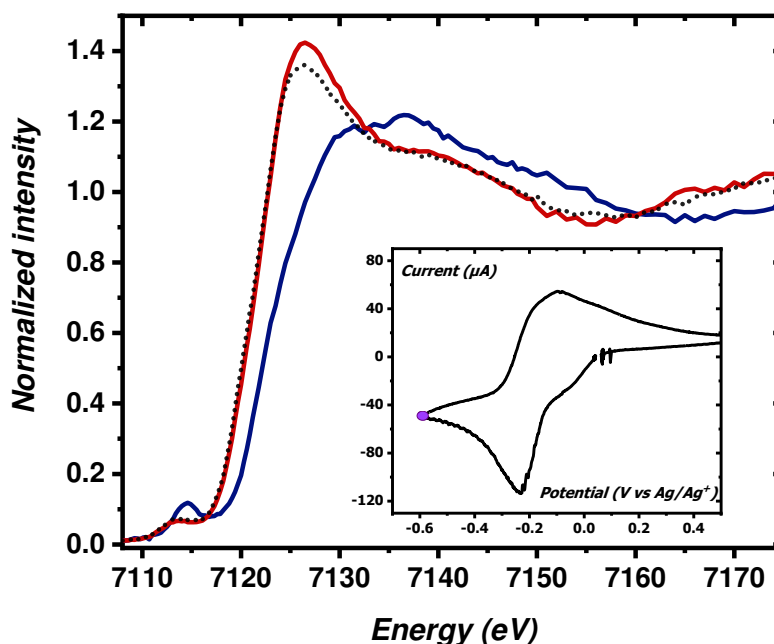


**Figure 5.3.** Fe K-edge XANES spectra recorded in the LUCIA Beamline of synchrotron SOLEIL in cell A of 2 mM solution of  $\text{Fe}^{\text{III}}\text{Cl}_3 \cdot 6\text{H}_2\text{O}$  (blue) and  $\text{Fe}^{\text{II}}\text{Cl}_2$  (red) in DMF + 0.1 M TBAPF<sub>6</sub> and while applying a potential of  $E = -0.6 \text{ V vs Ag/AgCl}^+$  starting from a  $\text{Fe}^{\text{III}}\text{Cl}_3 \cdot 6\text{H}_2\text{O}$  sample (black – dotted line). Insert: Cyclic voltammogram of  $\text{Fe}^{\text{III}}\text{Cl}_3 \cdot 6\text{H}_2\text{O}$  in DMF + 0.1 M TBAPF<sub>6</sub>, recorded under Ar at a scan rate  $\nu = 100 \text{ mV} \cdot \text{s}^{-1}$ .

The purple dot at the CV indicates the potential at which the electrolysis was performed.

All the experiments were performed inside of the primary vacuum chamber, while keeping the sample vial under Argon atmosphere.

## 5.4 Conclusion

As shown in this chapter, an XAS spectroelectrochemical cell has been optimized to perform fluorescence-detected experiments on homogeneous solutions of organic solvents and under vacuum. These conditions, together with the sample purging (with an inert gas or as sample gas) and circulation system ensures anaerobic conditions during the measurement and the stability of the species formed *in situ*. Based on the study of a model system, the  $\text{Fe}^{\text{III}}\text{Cl}_3/\text{Fe}^{\text{II}}\text{Cl}_2$  couple, the electrochemical performances of the cell were shown to allow a complete (96%) conversion of the species. The use of fluorescence detection was required to reach good signal to noise ratio given the concentration of the solutions studied. Finally, we have shown that a focused and small beam size  $50 \times 100 \mu\text{m}$  causes damages to the system, therefore a large beam size of  $1 \times 2 \text{ mm}$  and a less focused beam was requested.

## 5.5 References Chapter V

- (1) Sharpe, L. R.; Heineman, W. R.; Elder, R. C. EXAFS Spectroelectrochemistry. *Chem. Rev.* **1990**, *90* (5), 705–722.
- (2) Lassalle-Kaiser, B.; Zitolo, A.; Fonda, E.; Robert, M.; Anxolabéhère-Mallart, E. In Situ Observation of the Formation and Structure of Hydrogen-Evolving Amorphous Cobalt Electrocatalysts. *ACS Energy Lett.* **2017**, *2* (11), 2545–2551.
- (3) Weng, Z.; Wu, Y.; Wang, M.; Jiang, J.; Yang, K.; Huo, S.; Wang, X.-F.; Ma, Q.; Brudvig, G. W.; Batista, V. S.; Liang, Y.; Feng, Z.; Wang, H. Active Sites of Copper-Complex Catalytic Materials for Electrochemical Carbon Dioxide Reduction. *Nat. Comm.* **2018**, *9* (1), 1–9.
- (4) King, H. J.; Fournier, M.; Bonke, S. A.; Seeman, E.; Chatti, M.; Jumabekov, A. N.; Johannessen, B.; Kappen, P.; Simonov, A. N.; Hocking, R. K. Photon-Induced, Timescale, and Electrode Effects Critical for the in Situ X-Ray Spectroscopic Analysis of Electrocatalysts: The Water Oxidation Case. *J. Phys. Chem. C* **2019**, *123* (47), 28533–28549.
- (5) Dewald, H. D.; Watkins, J. W.; Elder, R. C.; Heineman, W. R. Development of Extended X-Ray Absorption Fine Structure Spectroelectrochemistry and Its Application to Structural Studies of Transition-Metal Ions in Aqueous Solution. *Anal. Chem.* **1986**, *58* (14), 2968–2975.
- (6) DeAngelis, T. P.; Heineman, W. R. An Electrochemical Experiment Using an Optically Transparent Thin Layer Electrode. *J. Chem. Educ.* **1976**, *53* (9), 594.
- (7) Murray, R. W.; Heineman, W. R.; O'Dom, G. W. An Optically Transparent Thin Layer Electrochemical Cell. *Anal. Chem.* **1967**, *39* (13), 1666–1668.
- (8) Smith, D. A.; Heeg, M. J.; Heineman, W. R.; Elder, R. C. Direct Determination of Fe-C Bond Lengths in Iron(II) and Iron(III) Cyanide Solutions Using EXAFS Spectroelectrochemistry. *J. Am. Chem. Soc.* **1984**, *106* (10), 3053–3054.
- (9) Smith, D. A.; Elder, R. C.; Heineman, W. R. Extended X-Ray Absorption Fine Structure Thin-Layer Spectroelectrochemistry. *Anal. Chem.* **1985**, *57* (12), 2361–2365.
- (10) Charnock, J. M.; Collison, D.; Garner, C. D.; McInnes, E. J. L.; Mosselmans, J. F. W.; Wilson, C. R. XAS of Ni and Cu Quinoxaline-2,3-Dithiolene Complexes in Solution Using a Novel In Situ Electrochemical Cell. *J. Phys. IV France* **1997**, *7* (C2), C2-658.
- (11) Ascone, I.; Cognigni, A.; Giorgetti, M.; Berrettoni, M.; Zamponi, S.; Marassi, R. X-ray absorption spectroscopy and electrochemistry on biological samples. *J. Synchrotron Rad.* **1999**, *6*, 384 - 386.
- (12) Anxolabéhère-Mallart, E.; Glaser, T.; Frank, P.; Aliverti, A.; Zanetti, G.; Hedman, B.; Hodgson, K. O.; Solomon, E. I. Sulfur K-Edge X-Ray Absorption Spectroscopy of 2Fe–2S Ferredoxin: Covalency of the Oxidized and Reduced 2Fe Forms and Comparison to Model Complexes. *J. Am. Chem. Soc.* **2001**, *123* (23), 5444–5452.
- (13) Igo, D. H.; Elder, R. C.; Heineman, W. R.; Dewald, H. D. Bulk-Electrolysis Flow-Cell System for UV-Visible and X-ray Absorption Spectroelectrochemical Analysis. *Anal. Chem.* **1991**, *63* (21), 2535–2539.



- (14) Cheaib, K.; Maurice, B.; Mateo, T.; Halime, Z.; Lassalle-Kaiser, B. Time-Resolved X-Ray Absorption Spectroelectrochemistry of Redox Active Species in Solution. *J. Synchrotron Rad.* **2019**, *26* (6), 1980–1985.
- (15) Ambrosi, A.; Shi, R. R. S.; Webster, R. D. 3D-Printing for Electrolytic Processes and Electrochemical Flow Systems. *J. Mater. Chem. A* **2020**, *8* (42), 21902–21929.
- (16) Achilli, E.; Minguzzi, A.; Visibile, A.; Locatelli, C.; Vertova, A.; Naldoni, A.; Rondinini, S.; Auricchio, F.; Marconi, S.; Fracchia, M.; Ghigna, P. 3D-Printed Photo-Spectroelectrochemical Devices for in Situ and in Operando X-ray Absorption Spectroscopy Investigation. *Journal of Synchrotron Radiation* **2016**, *23* (2), 622–628.
- (17) Bora, D. K.; Glans, P.-A.; Pepper, J.; Liu, Y.-S.; Du, C.; Wang, D.; Guo, J.-H. An Ultra-High Vacuum Electrochemical Flow Cell for in Situ/Operando Soft X-Ray Spectroscopy Study. *Rev Sci Inst.* **2014**, *85* (4), 043106.
- (18) Elgrishi, N.; Rountree, K. J.; McCarthy, B. D.; Rountree, E. S.; Eisenhart, T. T.; Dempsey, J. L. A Practical Beginner's Guide to Cyclic Voltammetry. *J. Chem. Educ.* **2018**, *95* (2), 197–
- (19) Francke, R.; Schille, B.; Roemelt, M. Homogeneously Catalyzed Electroreduction of Carbon Dioxide-Methods, Mechanisms, and Catalysts. *Chem Rev* **2018**, *118* (9), 4631–4701.
- (20) Savéant, J.-M. *Elements of Molecular and Biomolecular Electrochemistry: An Electrochemical Approach to Electron Transfer Chemistry*, John Wiley & Sons. **2006**, pp. 78 - 181.
- (21) Costentin, C.; Drouet, S.; Robert, M.; Savéant, J.-M. A Local Proton Source Enhances CO<sub>2</sub> Electroreduction to CO by a Molecular Fe Catalyst. *Science* **2012**, *338* (6103), 90–94.
- (22) Kadish, K. M.; Larson, G.; Lexa, D.; Momenteau, M. Electrochemical and Spectral Characterization of the Reduction Steps of .Mu.-Oxo-Bis(Iron Tetrphenylporphyrin) Dimer in Dimethylformamide. *J. Am. Chem. Soc.* **1975**, *97* (2), 282–288.
- (23) Oliveira, R.; Zouari, W.; Herrero, C.; Banse, F.; Schöllhorn, B.; Fave, C.; Anxolabéhère-Mallart, E. Characterization and Subsequent Reactivity of an Fe-Peroxo Porphyrin Generated by Electrochemical Reductive Activation of O<sub>2</sub>. *Inorg. Chem.* **2016**, *55* (23), 12204–12210.
- (24) Pegis, M. L.; Martin, D. J.; Wise, C. F.; Brezny, A. C.; Johnson, S. I.; Johnson, L. E.; Kumar, N.; Raugei, S.; Mayer, J. M. Mechanism of Catalytic O<sub>2</sub> Reduction by Iron Tetrphenylporphyrin. *J. Am. Chem. Soc.* **2019**, *141* (20), 8315–8326.
- (25) Yano, J.; Yachandra, V. K. X-Ray Absorption Spectroscopy. *Photosynth Res* **2009**, *102* (2), 241–254.
- (26) Westre, T. E.; Kennepohl, P.; DeWitt, J. G.; Hedman, B.; Hodgson, K. O.; Solomon, E. I. A Multiplet Analysis of Fe K-Edge 1s → 3d Pre-Edge Features of Iron Complexes. *J. Am. Chem. Soc.* **1997**, *119* (27), 6297–6314.
- (27) Apted, M. J.; Waychunas, G. A.; Brown, G. E. Structure and Specification of Iron Complexes in Aqueous Solutions Determined by X-Ray Absorption Spectroscopy. *Geochim Cosmochim Acta.* **1985**, *49* (10), 2081–2089.





# Chapter VI

---

## - Results and Discussion -

### Insights in the understanding of the electronic structure of reduced $[\text{Fe}^{\text{III}}(\text{TPP})]\text{Cl}$ species by spectroelectrochemical methods

#### Content

---

6.1	Iron porphyrin analysis at the Fe(III) state .....	83
6.1.1	Ring substituents effect .....	83
6.1.2	Solvent effect .....	85
6.2	<i>In situ</i> spectroelectrochemical measurements on reduced species of $[\text{Fe}^{\text{III}}(\text{TPP})]\text{Cl}$ in an inert atmosphere .....	92
6.2.1	One electron reduction process: $[\text{Fe}^{\text{III}}(\text{TPP})]\text{Cl} + 1\text{e}^-$ .....	94
6.2.2	Two electron reduction process: $[\text{Fe}^{\text{III}}(\text{TPP})]\text{Cl} + 2\text{e}^-$ .....	98
6.2.3	Three electron reduction process: $[\text{Fe}^{\text{III}}(\text{TPP})]\text{Cl} + 3\text{e}^-$ .....	100
6.3	Summary and Discussion .....	103
6.4	References .....	107



An electrochemical activation with coordination complexes starts with uptake or removal of one electron from the resting state of the catalyst. As suggested by Costentin *et al.* if this first step is an outer-sphere electron transfer process, distribution over the metal and/or the ligand is of minor importance.<sup>1</sup> However, this is different when chemical reactions are at play. In this case, interactions between the electron-activated catalysts and a substrate usually occurs in an inner-sphere manner, with the generation of a catalysts-substrate adduct. In this case, the electron density localization, on the ligand, on the metal center or with a mixed distribution, as well as its impact on the catalyst structure, become important to consider.

In this chapter, we present the UV-Vis and XANES spectro(electro)chemical studies performed on iron porphyrins in the absence of CO<sub>2</sub>, both in solid state and in solution (aqueous solution and in DMF). These studies will provide helpful data to describe electronic structures of the various species and to discuss the propositions from literature results.

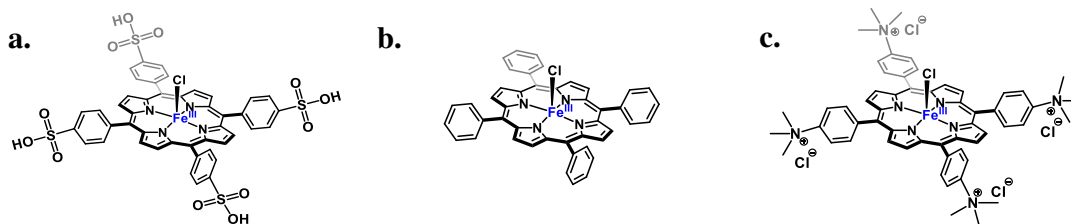
## 6.1 Iron porphyrins analysis at the Fe(III) state

In order to compare the spectroscopic data obtained by electroreduction, further describe in this chapter, the XANES fingerprints of the studied iron porphyrins at the initial oxidation state, Fe(III), are provided.

### 6.1.1. Ring substituents effect

The effects of substituents on the iron porphyrins catalytic activity have been widely studied by electrochemical methods.<sup>2-5</sup> However, direct evidence of this effect, by means of spectroscopic techniques, have not been yet investigated. In order to obtain electronic information related to the ligand substituents at the Fe(III) state, three porphyrins, shown in scheme 6.1, were selected:

- Iron 5, 10, 15, 20-Tetrakis-(4-sulfonatophenyl) porphyrin chloride, **[Fe<sup>III</sup>(TPPS)]Cl**, having electron withdrawing negatively charged sulfonate substituents at the phenyl groups of the porphyrin ring (Figure 6.1 – a).
- Iron tetraphenyl porphyrin chloride, **[Fe<sup>III</sup>(TPP)]Cl**, the most electrochemically studied, as shown in chapter II, and the structural base of the iron porphyrins (Figure 6.1 – b).
- Iron para-tetra(N,N,N-trimethyl-4-anilinium) porphyrin chloride, **[Fe<sup>III</sup>(-p-TMA)]Cl** containing electron withdrawing positively charged, anilinium groups, at the phenyl groups of the porphyrin ring (Figure 6.1 – c).



Scheme 6.1. Structures of the iron porphyrins studied during this project: a.  $[\text{Fe}^{\text{III}}(\text{TPPS})]\text{Cl}$ ; b.  $[\text{Fe}^{\text{III}}(\text{TPP})]\text{Cl}$ ; c.  $[\text{Fe}^{\text{III}}(-\text{p-TMA})]\text{Cl}$

The initial XAS characterization of the Fe(III) porphyrins was performed on the solid state - pellets, prepared as described in appendix C. Figure 6.1 shows the XANES spectra at the Fe K-edge of the solid-state samples of  $[\text{Fe}^{\text{III}}(\text{TPPS})]\text{Cl}$ ,  $[\text{Fe}^{\text{III}}(-\text{p-TMA})]\text{Cl}$  and  $[\text{Fe}^{\text{III}}(\text{TPP})]\text{Cl}$ . As observed, there is a slight main edge energy shift towards higher energies at the rising edge position, as summarized in table 6.1 appearing in the order of

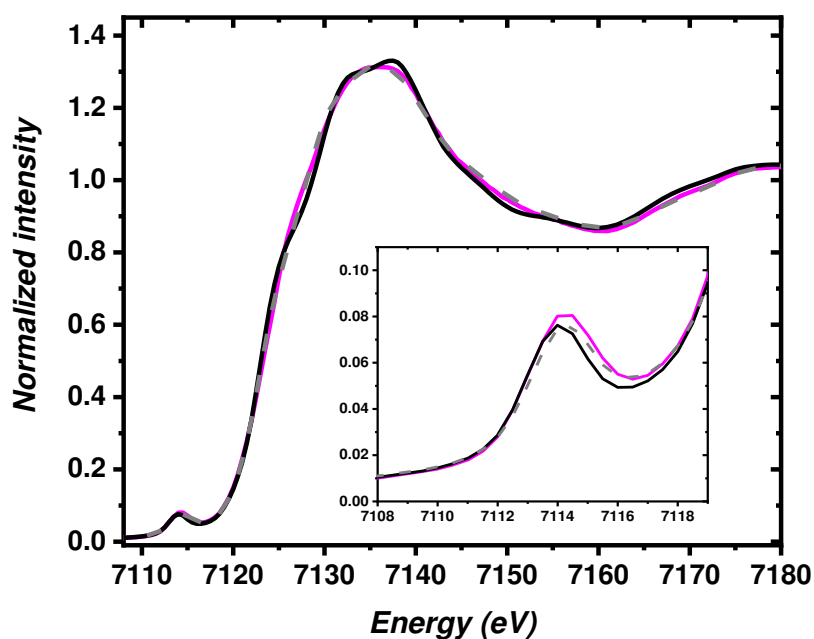


Figure 6.1. Iron porphyrin substituents effect: Fe K-edge XANES spectra of the solid-state  $\text{Fe}^{\text{III}}$  iron porphyrins:  $[\text{Fe}^{\text{III}}(\text{TPP})]\text{Cl}$  (solid line – black),  $[\text{Fe}^{\text{III}}(\text{TPPS})]\text{Cl}$  (dash lines - grey),  $[\text{Fe}^{\text{III}}(-\text{p-TMA})]\text{Cl}$  (solid line - magenta). Inset: pre-edge peak of each spectrum.

**Table 6.1. Main edge energy position for the Fe<sup>III</sup> porphyrins in the solid state**

<i>Complex</i>	<i>Main edge energy position (eV)</i>
[Fe <sup>III</sup> (TPP)]Cl	7123.0
[Fe <sup>III</sup> (TPPS)]Cl	7123.1
[Fe <sup>III</sup> (-p-TMA)]Cl	7123.2

*Main edge energy position measured at the half intensity of the normalized spectrum*

As described in chapter III, the metal electronic density can be estimated by analyzing the XANES rising edge.<sup>6,7</sup> In the present case, this effect is validated by following the substituents electron withdrawing effect (EWE) strength going from



It is expected that the electronic density on the metal center is going to vary, with the stronger EWE, the more positive character the iron center possesses. Therefore, a shift towards higher energies is observed when [Fe<sup>III</sup>(-p-TMA)]Cl is compared, for instance, with [Fe<sup>III</sup>(TPP)]Cl. These observations are in agreement with previous published data on [Fe<sup>III</sup>(TPP)]Cl and [Fe<sup>III</sup>(TPPS)]Cl and evidence that electronic withdrawing effect on the ligand has an impact on the metal center.<sup>8</sup> However, this evidence is only slightly observable by XANES.

### 6.1.2 Solvent effect

Although a major part of this thesis focuses on data obtained with [Fe<sup>III</sup>(TPP)]Cl, and its electroreduced species, in DMF solution, our initial experiments were performed on [Fe<sup>III</sup>(TPPS)]Cl. This porphyrin is soluble in both water and DMF, is commercially available and shows CO<sub>2</sub> reduction activity.<sup>4</sup>

Figure 6.2 shows the Fe K-edge XANES spectra of [Fe<sup>III</sup>(TPPS)]Cl in solid state (black trace), in water (light blue trace) and in DMF (dark blue dotted line). As observed in the figure and summarized in table 6.2, the XANES spectra of the solid sample and the solution in DMF shows the main edge energy value at 7123.1 eV, with a pre-edge peak being slightly more intense in DMF than in the solid state. This could indicate a subtle structural modification around the metal center, by a possible interaction with DMF. There are additional noteworthy observations in the presence of water. A significant shift (1 eV) of the rising edge position towards higher energies is observed when compared to the solid state and the DMF spectra, while the pre-edge peak intensity significantly decreases.

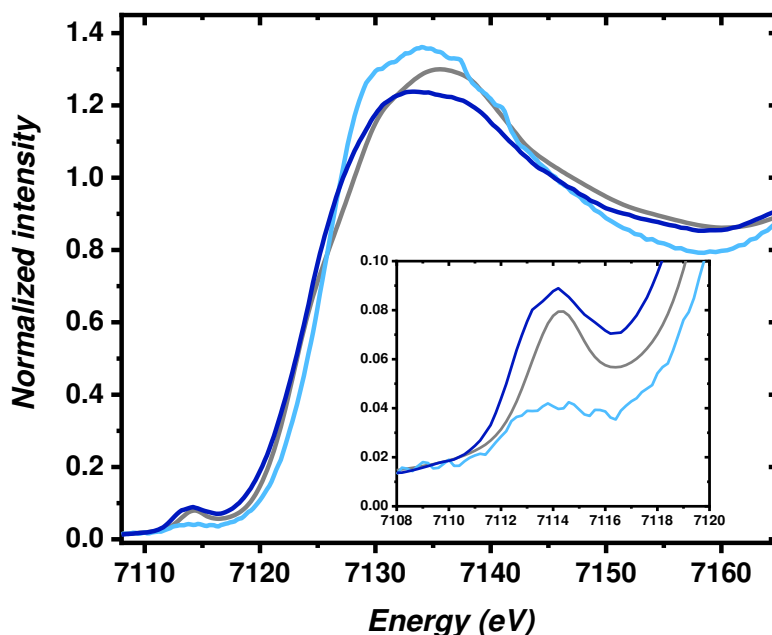


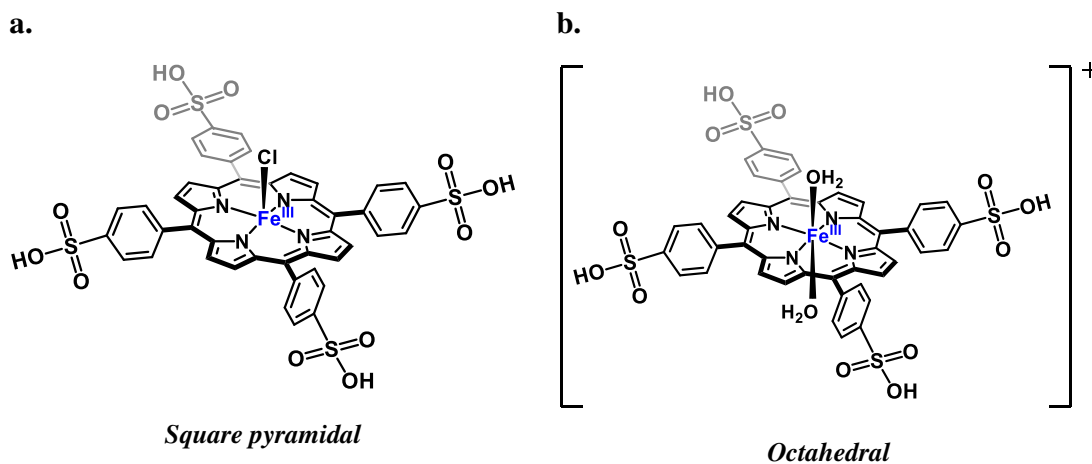
Figure 6.2. Iron porphyrin solvent effect: Fe K-edge XANES spectra of the iron sulphonatophenyl chloride  $[\text{Fe}^{\text{III}}(\text{TPPS})]\text{Cl}$  complex in solid state (grey), in DMF (dark blue) and in water (light blue)

Table 6.2. Main edge energy position for  $[\text{Fe}^{\text{III}}(\text{TPPS})]\text{Cl}$  in different experimental conditions

<i>Experimental conditions</i>	<i>Main edge energy position (eV)</i>
<b>Solid-state</b>	7123.1
<b>DMF solution</b>	7123.1
<b>Aqueous solution</b>	7124.1

*Main edge energy position measured at the half intensity of the normalized spectrum*

As indicated in chapter III, a change in the pre-edge peak indicates a structural or electronic modification at the metal center. This has been widely reported for other systems and summarized in a well-documented manner by Solomon *et al.*<sup>6</sup> In the present case, the differences at the pre-edge peak intensity can suggest that the metal center undergoes a structural change from a square pyramidal geometry, known for Fe(III) porphyrins with a chloride ligand binding the iron in an axial position, towards an octahedral geometry with the coordination of water as axial ligand (scheme 6.2). This is also supported by the main edge being shifted towards higher energies in the presence of water, suggesting a variation of the electronic structure at the iron center. A gain of a more positive character compared to the solid-state suggest a possible removal of the chloride ligand in axial position. These observations emphasize the fact that the nature of the solvent plays a role in both structural and electronic character of the metal center.



**Scheme 6.2.** Structural changes proposed to occur in the  $[\text{Fe}^{\text{III}}(\text{TPPS})]\text{Cl}$  complex with variation of the experimental conditions: a. In DMF. b. In aqueous solution.

In order to complement this study, XANES spectra were collected for  $[\text{Fe}^{\text{III}}(\text{TPPS})]\text{Cl}$  in aqueous solution at different pH values. Figure 6.3 shows the Fe K-edge XANES spectra of  $[\text{Fe}^{\text{III}}(\text{TPPS})]\text{Cl}$  in aqueous solution for pH values of 1.92, 3.89, 5.72, 8.51 and 11.77. Due to the presence of highly acidic sulfonate groups at the porphyrin ring,  $[\text{Fe}^{\text{III}}(\text{TPPS})]\text{Cl}$  dissolved in water drives the pH to a very low value, close to 2. The use of a buffered solution was necessary.<sup>9</sup> Britton-Robinson Buffer (BRB) was selected since electrochemical experiments has been previously reported on iron porphyrins by LEM researchers with this buffer.<sup>10</sup> Important changes in the pre-edge are observed which are correlated to the pH values (figure 6.4 – a.). The spectrum at low pH value shows a low intensity pre-edge peak. This spectrum presents the same features as the one described for the sample in a water solution, in agreement with the low pH value obtained in non-buffered solution due to the presence of the sulfonate groups. At pH 5.72, an increase of the pre-edge intensity is observed along with a slight shift towards lower energies of the rising edge (figure 6.4 – b). More interestingly, when pH is raised a more intense pre-edge peak appears with an important shift (almost 1 eV when compared with the complex at pH 1.92) towards lower energies at the rising edge. From figures 6.4 and 6.5 we can infer that the complex structure remains the same at low pH values (pH < 4) and is modified at more basic pH values (pH > 8.5).



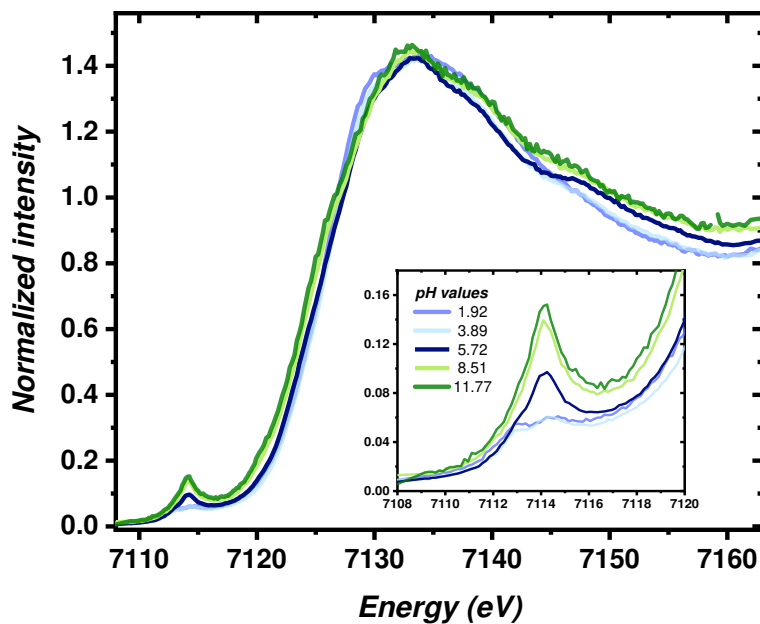


Figure 6.3. Iron porphyrin pH effect: Fe K-edge XANES spectra of the iron sulphonatophenyl chloride  $[\text{Fe}^{\text{III}}(\text{TPPS})]\text{Cl}$  complex in aqueous buffered solution as a function of the pH.

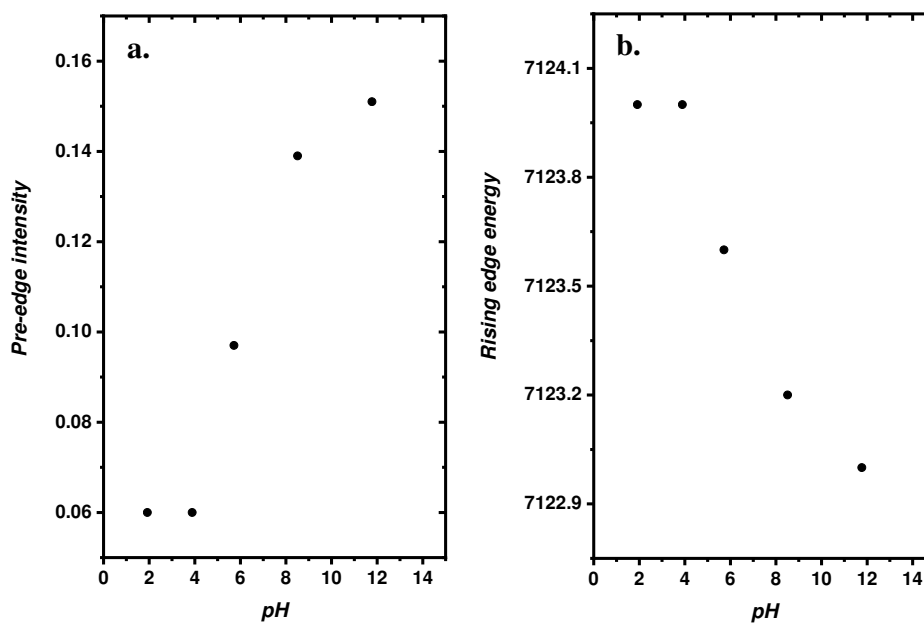
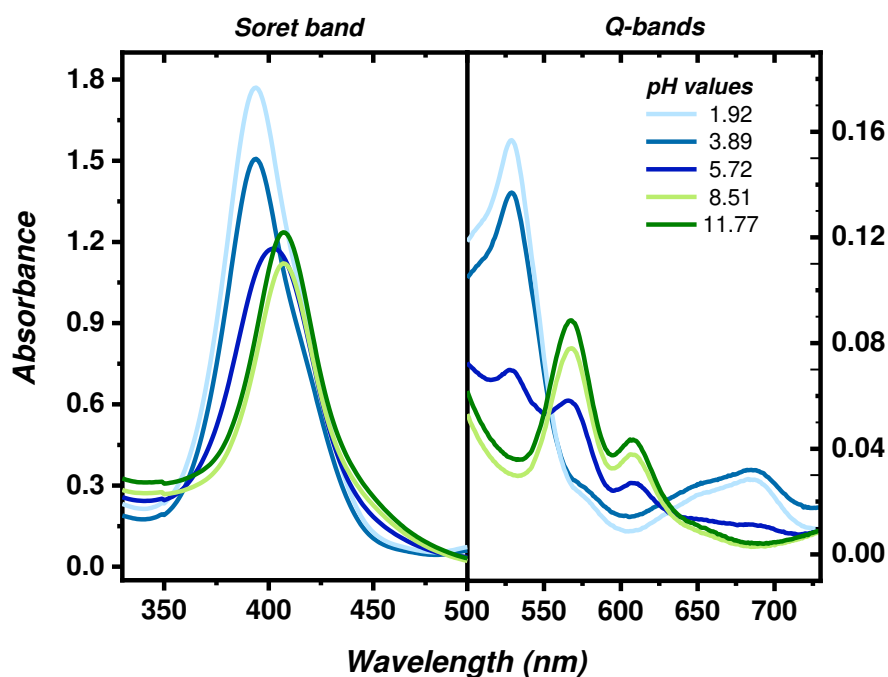


Figure 6.4. Iron porphyrin pH effect: a. Pre-edge peak intensity and b. Main edge energy position as a function of the pH. Values obtained from the Fe K-edge XANES spectra of the iron sulphonatophenyl chloride  $[\text{Fe}^{\text{III}}(\text{TPPS})]\text{Cl}$  complex in aqueous buffered solution (BRB).

In order to further understand the changes observed by XANES, UV-Vis spectroscopy was also performed as a function of pH (Figure 6.5 – table 6.3) The Soret band is located at 394 nm at pH going from 1.92 to 3.89, with no significant changes at the Q-bands. However, at pH 5.72, both Soret and Q-bands are modified. While the Soret band is shifted from 394 nm to 402 nm, the Q-bands are altered with the decrease of the bands at 528 and 684 nm, and the appearance of two new bands at 567 and 611 nm. At higher pH, the Soret band is red-shifted to a wavelength value of 407 nm while the Q-bands at 567 and 611 nm rise sharply and the other two at 528 and 684 nm disappear. These observations are related to the increase of the pre-edge intensity and main edge shift towards lower energies in the XANES spectra when  $\text{pH} > 8.5$ . Hence, XANES and UV-Vis results are both in agreement with the presence of two different species, one at low pH ( $\text{pH} < 4.0$ ) and one at high pH ( $\text{pH} > 9.0$ ) values. It is expected that the range of pH values in between corresponds to a transition zone in which several aqua/hydroxo species are in equilibrium.



**Figure 6.5. Iron porphyrin pH effect: UV-Vis spectra of the iron sulphonatophenyl chloride  $[\text{Fe}^{\text{III}}(\text{TPPS})]\text{Cl}$  complex in aqueous buffered solution as a function of pH.**

*pH values are detailed in the legend.*

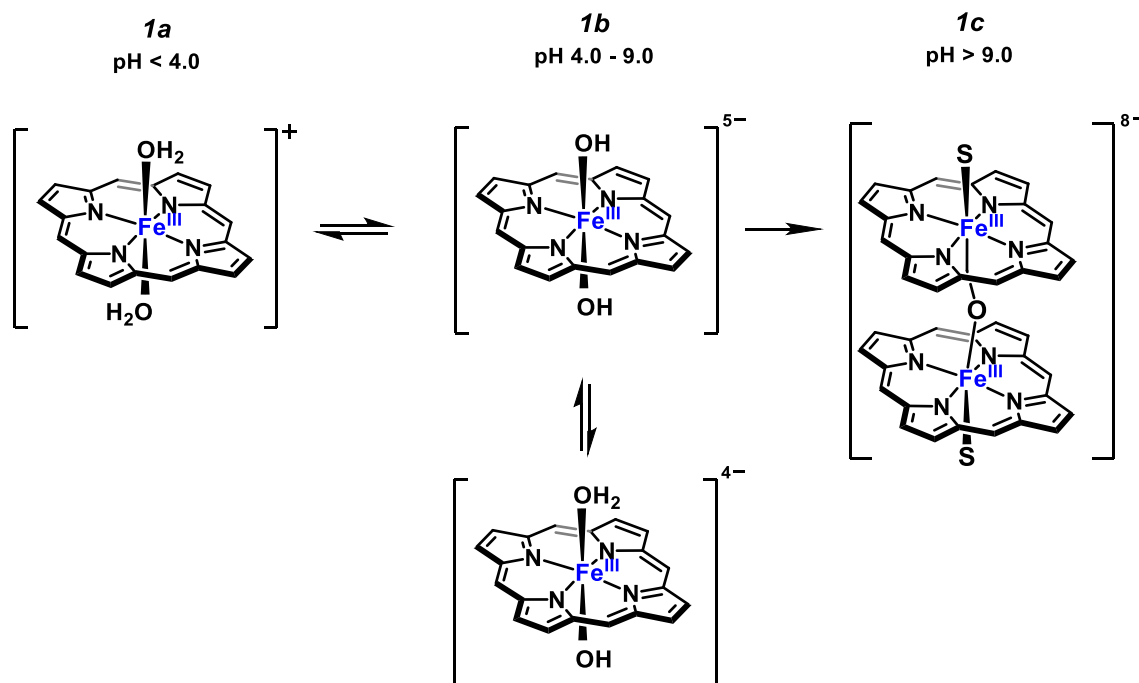
**Table 6.3. Soret and Q-bands wavelength values of [Fe<sup>III</sup>(TPPS)]Cl in aqueous buffered solution as a function of the pH**

<i>pH values</i>	<i>Soret band (nm)</i>	<i>Q-band (nm)</i>
1.92	394	528 and 684
3.89	394	528 and 684
5.72	402	528, 567, 611 and 684
8.51	407	567 and 611
11.77	407	567 and 611

It has been reported by UV-Vis spectroscopy that the iron sulfonatophenyl porphyrin monomer is stable at low pH in aqueous solutions.<sup>11,12</sup> The UV-Vis reported values closely match the experimental results shown in the present text obtained in the BRB at low pH. However, it is proposed that at high pH, a dimer [(Fe<sup>III</sup>(TPPS))<sub>2</sub>O] species is formed, which has two five-coordinated Fe(III) centers linked to an oxygen atom.<sup>11</sup> Wilkins *et al.* have reported a study on the monomer-dimer transition on the [Fe<sup>III</sup>(TPPS)]Cl in aqueous media based on UV-Vis spectroscopy.<sup>13</sup> In this study they concluded that the *pKs* values for the monomer formation, containing two water molecules as axial ligand, is around 6.5-7 ( $\pm 0.2$ ). At pH values higher than 6.5, the deprotonation of the sulphonate substituents at the phenyl group of the porphyrin ring is expected, along with the deprotonation of water ligands to generate hydroxyl groups as axial ligand, modifying the total charge of the complex. The species generated between pH 4.0 to 9.0 are in a transition zone, which is expected to contain several aqua/hydroxo species in equilibrium. Finally, the presence of an intense pre-edge peak observed at higher pH values is in agreement with the reported XANES spectra in the solid state for another iron porphyrin dimer, [Fe<sup>III</sup>(TPP)<sub>2</sub>O].<sup>14</sup> It was proposed that the intense pre-edge peak is observed due to the transition from the *1s* core to the *3d* states of the iron center hybridized with the *p* orbitals of the  $\mu$ -oxo ligand.<sup>14</sup> Therefore, a dimer  $\mu$ -oxo species can be proposed at high pH.

#### • Conclusion

As observed by XANES and UV-Vis spectroscopy, the monomer-dimer equilibrium formation on iron porphyrins is pH dependent in aqueous media. As previously mentioned, at low pH (pH < 4.0) the monomer is favored (scheme 6.3 - **1a**) with the characteristic low and broad pre-edge peak by XANES. In basic conditions, however, the dimer is obtained (scheme 6.3 - **1c**) showing a sharp pre-edge peak. It has also been shown that several species are likely to be in equilibrium between pH 4.0 to 9.0 (scheme 6.3 - **1b**). Likewise, the spectral characteristics of these species are too close to allow the quantification of each of them in solution.



**Scheme 6.3. Proposed species of  $[\text{Fe}^{\text{III}}(\text{TPPS})]\text{Cl}$  as a function of pH in aqueous media.**

*The para-sulfonato-phenyl groups at the porphyrin ring are omitted for clarity.*

*It is suggested that in species 1b and 1c the four para-sulfonato-phenyl groups at the porphyrin ring are deprotonated (four negative charges)*

After comparing the experimental difficulties and requirements of the two different media, water and DMF, for the study of the starting  $\text{Fe}^{\text{III}}$  porphyrin complex, we selected DMF as the solvent for subsequent spectroelectrochemical studies. Indeed, the need for a precise control of the pH value together with the facile formation of  $\mu$ -oxo dimer in aqueous media appeared as a major drawback for conducting a first complete spectroelectrochemical study. In addition to this, cyclic voltammograms of the  $\mu$ -oxo dimer exhibit several anodic and cathodic waves in DMF in argon atmosphere (chapter IV), which makes the electrochemical interpretation of this system rather complicated. In contrast, in DMF, three distinct and reversible waves are observed for iron porphyrin under argon atmosphere and in the absence of protons (chapter II).

Concerning the iron porphyrin selection,  $[\text{Fe}^{\text{III}}(\text{TPP})]\text{Cl}$  was chosen as the porphyrin for further studies mostly for the three following reasons:

- $[\text{Fe}^{\text{III}}(\text{TPP})]\text{Cl}$  is a good catalyst towards the  $\text{CO}_2$  reduction as indicated in chapter II,
- Its kinetic analysis in DMF has been extensively described,
- $[\text{Fe}^{\text{III}}(\text{TPP})]\text{Cl}$  is commercially available and cheap.

Therefore, the remaining part of this chapter and further chapter VII are dedicated to the results obtained during the spectroelectrochemical studies performed on  $[\text{Fe}^{\text{III}}(\text{TPP})]\text{Cl}$  in DMF homogeneous conditions.

## 6.2 *In situ* spectroelectrochemical measurements on reduced species of $[\text{Fe}^{\text{III}}(\text{TPP})]\text{Cl}$ under an inert atmosphere

Figure 6.6 shows the Fe K-edge XANES spectra of the  $[\text{Fe}^{\text{III}}(\text{TPP})]\text{Cl}$  in DMF + 0.1 M TBAPF<sub>6</sub> solution, denoted henceforward as *I*, and is compared with the spectra of the same species in solid state, both in argon atmosphere. As shown, both spectra look essentially the same, with a main edge energy position (taken at a normalized intensity of 0.5, see chapter III) of 7123.0 eV (table 6.4). XANES data suggest that in these conditions, the complex structure is maintained with the chloride axial ligand bounded to the Fe(III) center. Therefore, no important modifications are observed with the presence of DMF at this valence state, allowing to conclude that *I* is in a square planar pyramidal geometry with a spin state of  $S = 5/2$  (high spin) (scheme 6.4) as previously reported.<sup>16</sup>

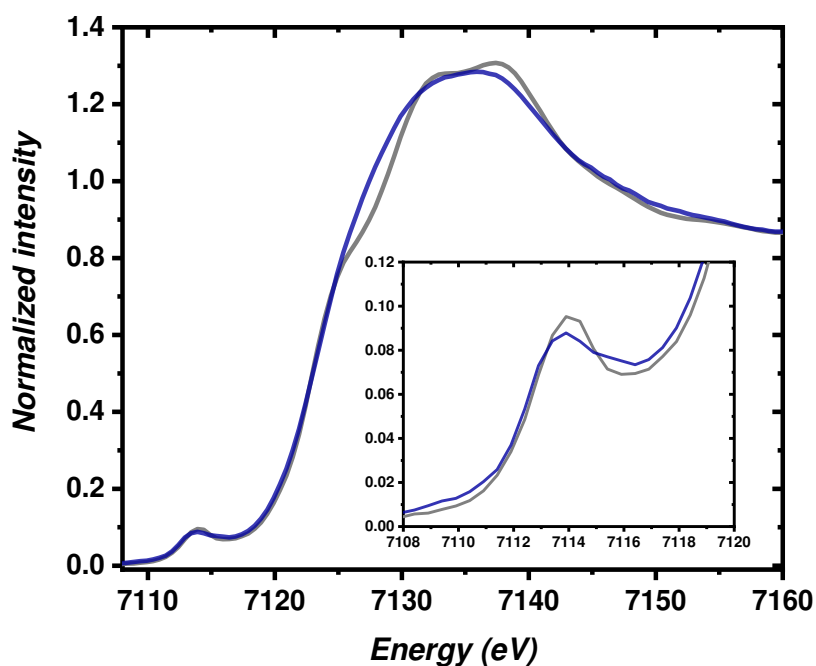


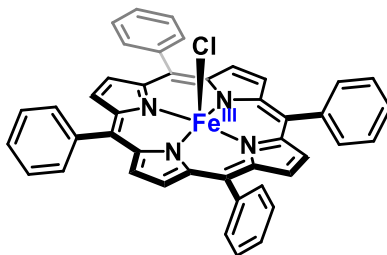
Figure 6.6. Fe K-edge XANES spectra of *I* in solid state (dark grey) and in DMF + 0.1 M TBAPF<sub>6</sub> solution under argon atmosphere (dark blue). Insert: pre-edge region.

Table 6.4. Pre-edge peak and main edge energy position for *I* in different experimental conditions

Conditions	Pre-edge peak energy (eV)*	Main edge energy position (eV)‡	Spin
Solid state	7112.9	7123.0	S = 5/2
DMF + TBAPF <sub>6</sub> solution	7112.6	7123.0	High spin

\* Pre-edge peak energy position measured at the first inflection point of the pre-edge peak

‡ Main edge energy position measured at the half intensity of the normalized spectrum



Scheme 6.4. Structure of the S = 5/2 high spin [Fe<sup>III</sup>(TPP)]Cl expected in DMF+TBAPF<sub>6</sub> (complex *I*).

The cyclic voltammogram of a solution of *I* in DMF + 0.1 M TBAPF<sub>6</sub> recorded in the spectroelectrochemical cell A (chapter V) under argon is shown in figure 6.7. The CV exhibits three well-defined reversible waves, corresponding to the three-electron reduction processes, as shown in chapter II, previously reported for [Fe<sup>III</sup>(TPP)]Cl,<sup>3,17</sup> demonstrating that the cell is electrochemically well adapted for further studies.

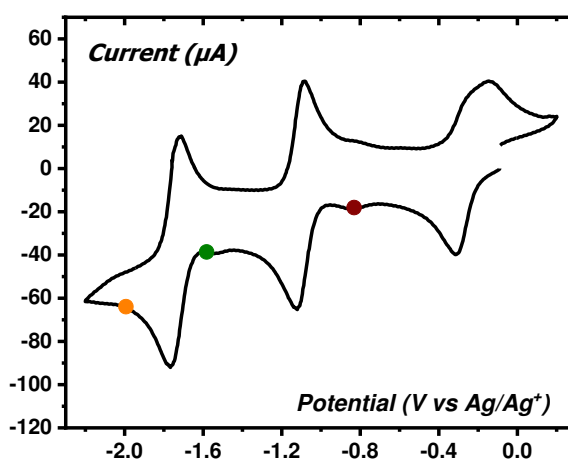


Figure 6.7. Cyclic voltammogram for a 2 mM solution [Fe<sup>III</sup>(TPP)]Cl in DMF + 0.1 M TBAPF<sub>6</sub>, at room temperature (RT) and scan rate  $\nu = 100 \text{ mV s}^{-1}$  recorded in the cell A under a vacuum of  $10^{-2}$  mbar and argon atmosphere on the LUCIA beamline at Synchrotron SOLEIL.

Colored dots indicate the selected potential for control potential electrolysis (CPE) for further spectroelectrochemical measurements. Red: towards Fe<sup>II</sup> generation. Green: towards formally described “Fe<sup>I</sup>” generation. Orange: towards formally described “Fe<sup>0</sup>” generation.

In order to perform spectroelectrochemical measurements for the determination of the different electronic and structural variations of **I** during reduction processes, controlled potential electrolysis (CPE) were performed under argon at the different reduction potentials as indicated in figure 6.7. XANES spectra were recorded when the current reached a plateau in order to interrogate stable species (see appendix C for further description regarding the experimental protocol for CPE).

### 6.2.1 One electron reduction process: $[\text{Fe}^{\text{III}}(\text{TPP})]\text{Cl} + 1\text{e}^-$

Figure 6.8 shows the Fe K-edge spectra of complex **I** and its one electrochemical reduced species (named complex **2a**), obtained by performing CPE at  $E = -0.8 \text{ V vs. Ag/Ag}^+$ . As observed, only slight changes are present in the pre-edge region, while the main edge energy remains at the value at 7123.0 eV.

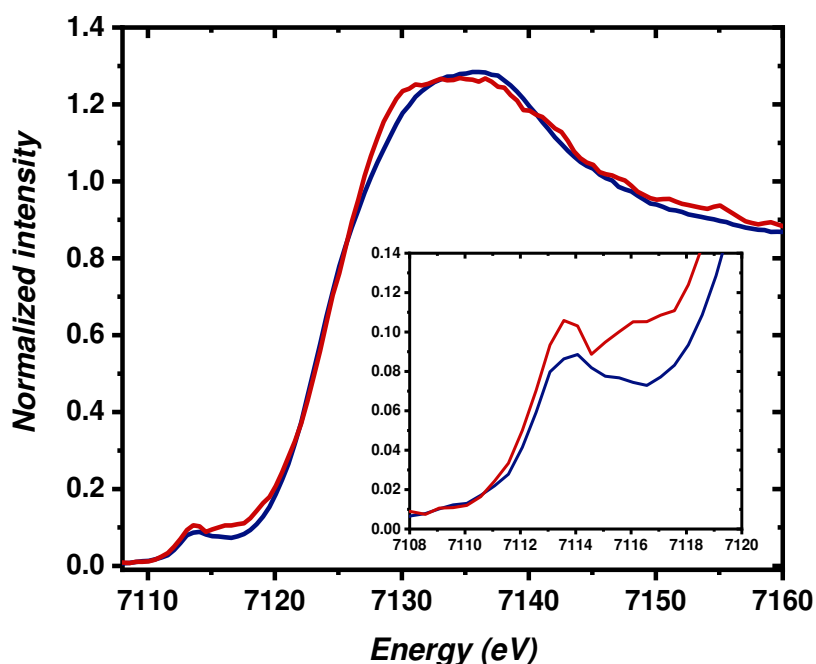
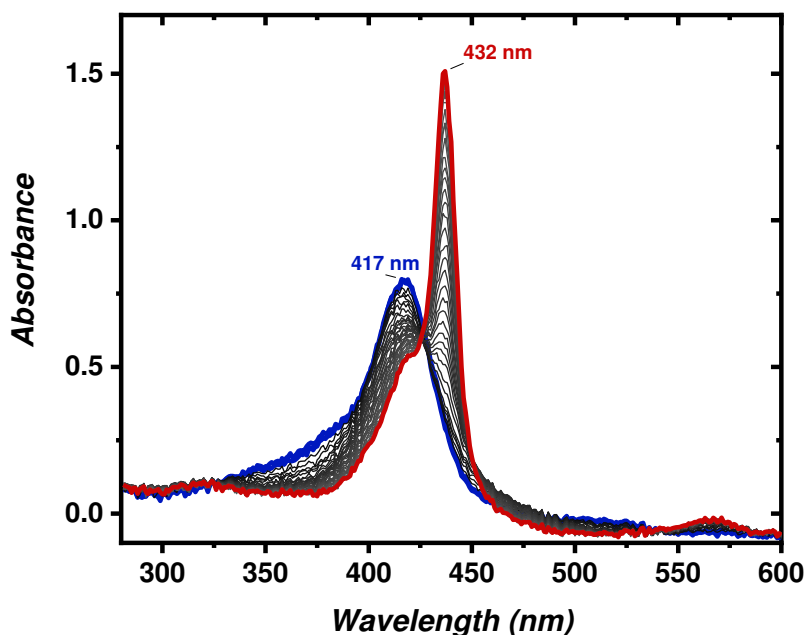


Figure 6.8. Fe K-edge XANES spectra of **I** (blue) and its one-electron reduction species **2a** (red) generated by performing a CPE at  $E = -0.8 \text{ V vs. Ag/Ag}^+$  in DMF + 0.1 M TBAPF<sub>6</sub> under argon atmosphere. Insert: pre-edge region.

Spectroelectrochemical UV-Vis experiments (figure 6.9) were performed under the same conditions than the XANES experiments. The UV-Vis spectra show significant spectroscopic changes. In fact, when the potential is set to  $E = -0.8 \text{ V vs. SCE}$ , a shift of the Soret band is observed from 417 nm for complex **I** to 432 nm for complex **2a**. These values match previously reported data for  $[\text{Fe}^{\text{III}}(\text{TPP})]\text{Cl}$  and its one electron-reduced species under the same conditions.<sup>18</sup>



**Figure 6.9.** UV-Vis spectral evolution obtained from **1** (blue) and its one-electron reduction species **2a** (red), obtained while performing CPE at  $E = -0.8$  V vs SCE in DMF + 0.1M TBAPF<sub>6</sub> in the spectroelectrochemical UV-Vis set-up.

*Dark grey spectra illustrate the transition from 1 to 2a.*

In order to understand the XANES data and the absence of any shift in the main edge energy, we may refer the work of Hodgson *et al.*<sup>19</sup> In this reference, it was reported by *ex-situ* analysis that Fe<sup>II</sup> porphyrins can adopt three different spin states; high spin (HS), low spin (LS) and intermediate spin (IS), which show very different XANES spectra.

To confirm the nature of the electrogenerated species, the [Fe<sup>II</sup>(TPP)] complex was synthesized from the starting [Fe<sup>III</sup>(TPP)]Cl complex by a chemical reduction route, following a reported procedure (see appendix C).<sup>15</sup> Fe K-edge XANES spectra recorded on complex **1** and the chemically reduced synthesized one, **2b**, both in the solid state, are shown in figure 6.10. The XANES spectrum of **2b** shows a 2 eV shift of the main edge towards lower energies (7121.0 eV, see table 6.5) as compared to **1**. The pre-edge peak position (measured as the first inflection point, see chapter III), is located at 7111.3 eV, which is comparable with the one reported by Wilson *et al.* at 7111.5 eV. This spectrum was assigned to the intermediate spin, square planar complex, [Fe<sup>II</sup>(TPP)] (see chapter IV – figure 4.2).<sup>19</sup> The XANES spectrum obtained also shows the presence of a high intensity shoulder at around 7118.0 eV which have been described as the low-lying  $1s$  to  $4p_z$  transition in iron porphyrins and other related molecular catalysts, further supporting the square planar geometry of the synthesized complex.<sup>15,20</sup> These features indicates that **2b** adopts a square planar geometry with an intermediate spin (IS) configuration (scheme 6.5).



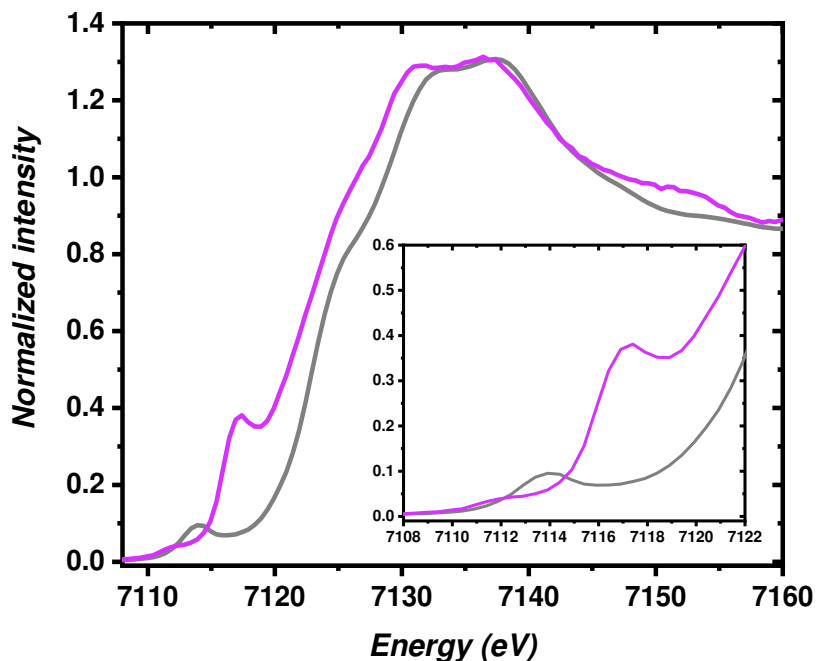


Figure 6.10. Fe K-edge XANES spectra of **1** (grey) and **2b** (purple) - solid state. Insert: pre-edge region.

Nonetheless, the XANES spectrum of the chemically prepared complex **2b** is very different from **2a**, the one obtained by electrochemical reduction of **1** in DMF + TBAPF<sub>6</sub>. It suggests that the two species differ because of the solvent. To get confirmation, the chemically reduced complex **2b** was dissolved in DMF under anaerobic conditions, leading to a complex named **2c**. The XANES spectrum of this solution is compared in figure 6.11 to the ones of **2a** and **2b**. As observed, **2c** shows a spectrum that is very similar to the one for **2a**, with a main edge position of 7123.0 eV (table 6.5), indicating that indeed DMF plays a critical role in the structural changes of the iron porphyrin at this valence state. The disappearance of the feature close to 7118.0 eV is another evidence of the loss of the square planar character, since the  $4p_z$  orbital is shifted towards higher energies due to axial coordination of DMF. Small differences are observed in the pre-edge region of **2a** and **2c**, which we attribute to slightly different conditions in which the two spectra were recorded (presence of chloride anions and supporting electrolyte in the solution of **2a** but not in **2c**).

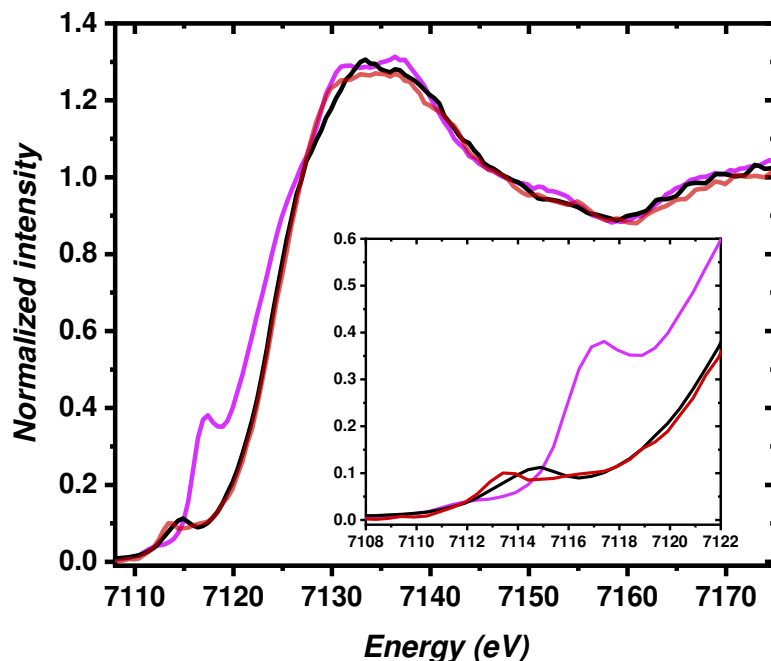


Figure 6.11. Fe K-edge XANES spectra of electrochemical generated species, **2a** (red), chemically generated species in the solid state, **2b** (purple), and obtained from **2b** dissolution in DMF solution, **2c** (black).

Wilson *et al.* also reported an iron porphyrin complex in which the metal center is coordinated by two pyridine moieties, conferring it a low spin configuration.<sup>19</sup> This complex was therefore described as  $[\text{Fe}^{\text{II}}(\text{TPP})(\text{Py})_2]$ , with a pre-edge peak value at 7112.2 eV (see chapter IV – figure 4.2). In our studies, we observed that the pre-edge peak for the **2a** complex is also located at 7112.2 eV. This comparison gives us a further evidence that the electrogenerated complex **2a** indeed corresponds to a Fe(II) state in a low spin configuration, induced by coordination of DMF molecules from the solvent. Although the analogy with the  $[\text{Fe}^{\text{II}}(\text{TPP})(\text{Py})_2]$  from Wilson *et al.* suggests the presence of two coordinating solvent molecules, we do not have experimental evidences to confirm this structure. In particular, the differences observed in the pre-edge region between **2a** and **2c**, indicate that further studies are required to conclude over the axial ligands coordinating the Fe center.

**Table 6.5.** Pre-edge peak and main edge energy position for **2a**, **2b** and **2c** obtained in various experimental conditions.

Complex	Pre-edge peak energy (eV)*	Main edge energy position (eV)‡
<b>2a</b>	7112.2	7123.0
<b>2b</b>	7111.3	7121.0
<b>2c</b>	7113.1	7123.0

\* Pre-edge peak energy position measured at the first inflection point of the pre-edge peak

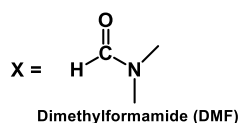
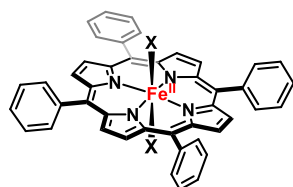
‡ Main absorption edge energy position measured at the half intensity of the normalized spectrum

- Pre-edge values presented by Wilson *et al.*<sup>19</sup>

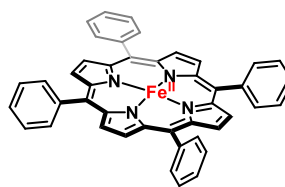
[Fe<sup>II</sup>(TPP)] 7111.5 eV

[Fe<sup>II</sup>(TPP)(Py)<sub>2</sub>] 7112.2 eV

**DMF + 0.1 M TBAPF<sub>6</sub> (2a)**



**Solid state (2b)**



**Scheme 6.5.** Proposed structures for complexes **2a** and **2b**.

- The coordination number of species **2a** has not been determined. Therefore, one or two solvent molecules may be suggested.

### 6.2.2 Two electron reduction process: [Fe<sup>III</sup>TPP(Cl)] + 2e<sup>-</sup>

The second reduction process was followed by XANES, as shown in figure 6.12, upon applying a potential  $E = -1.6$  V vs. Ag/Ag<sup>+</sup>. The electrogenerated species is named **3**. The main edge energy position observed at 7122.3 eV is slightly shifted (0.7 eV) towards lower energy values when compared to the initial sample of [Fe<sup>III</sup>(TPP)]Cl. In addition, the pre-edge peak increases in intensity, presenting a rising shoulder at 7118.0 eV. As previously indicated in this chapter for the chemically reduced **2b** species, the presence of this shoulder indicates a square planar environment around the iron centre, suggesting that under these conditions, the strength of the bond between the Fe center and the axially coordinating ligand(s) is lower.

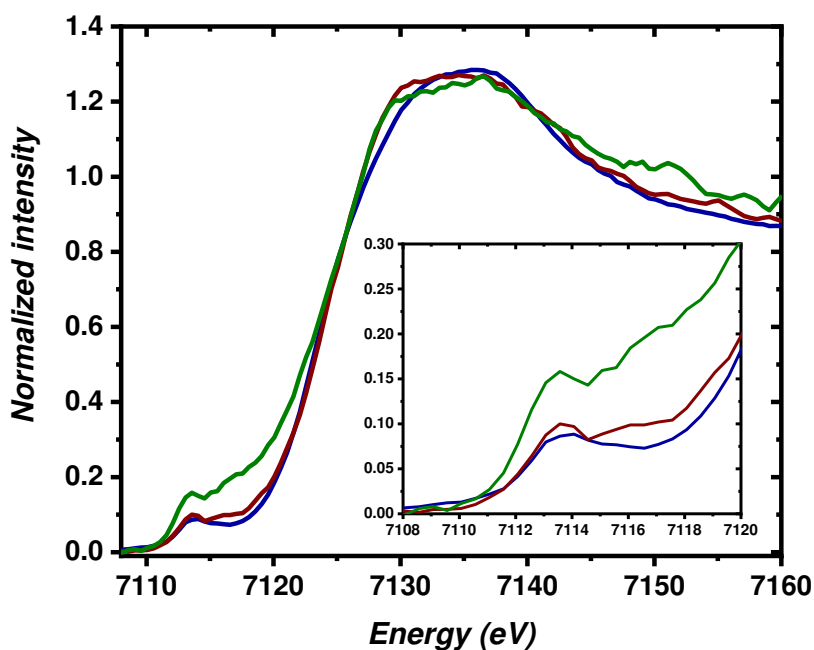


**Figure 6.12.** Fe K-edge XANES spectra of **1** (blue), **2a** (red) and the two-electron reduced species  $[\text{Fe}^{\text{III}}(\text{TPP})]\text{Cl} + 2\text{e}^-$ , **3** (green), generated upon constant potential electrolysis ( $E = -1.6 \text{ V vs Ag/Ag}^+$ ) under Ar. Insert: pre-edge region.

Figure 6.13 shows the spectroelectrochemical UV-Vis spectra while a potential of  $E = -1.6 \text{ V vs. SCE}$  is applied, generating **3**. An important decrease of the Soret band at 432 nm is observed with a split of the band into two signatures at 392 and 427 nm. Another small feature is observed at 332 nm. Meanwhile, Q-bands are also importantly modified with the presence of three bands at 510, 575 and 608 nm (figure 6.17). These UV-Vis signatures are in close agreement with previously reported data of the formal “ $\text{Fe}^{\text{I}}$ ” generated state of  $[\text{Fe}^{\text{III}}(\text{TPP})]\text{Cl}$  in dimethyl sulfoxide (DMSO) + 0.1 M triethylammonium phosphate (TEAP).<sup>21,22</sup>

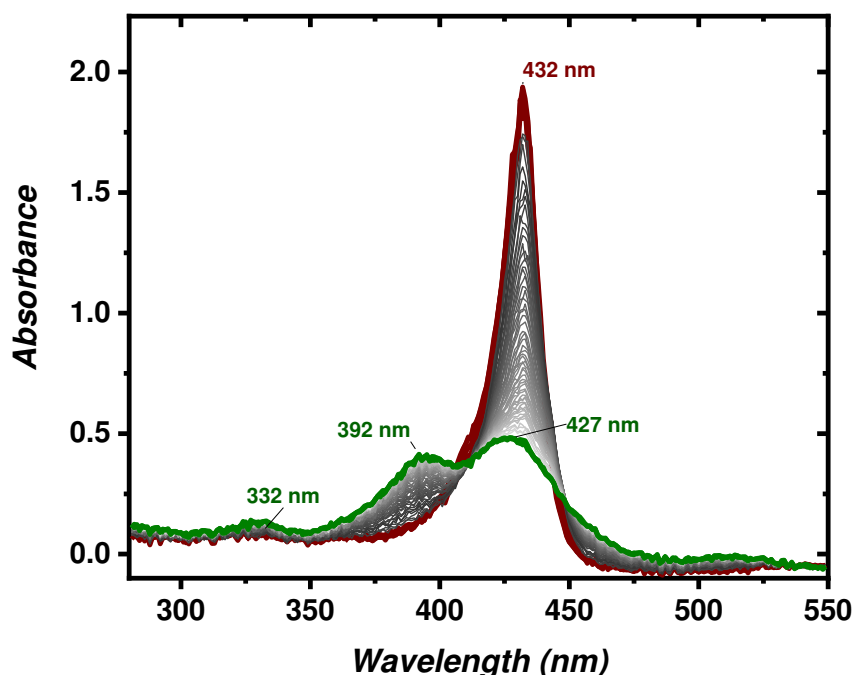


Figure 6.13. UV-Vis spectral variation obtained from **2a** (red) and its one-electron reduction specie **3** (green), obtained while performing CPE at  $E = -1.6$  V vs SCE in DMF + 0.1 M TBAPF<sub>6</sub> in the spectroelectrochemical UV-Vis set-up.

Dark grey spectra illustrate the transition from **2a** to **3**.

### 6.2.3 Three electron reduction process: $[\text{Fe}^{\text{III}}(\text{TPP})]\text{Cl} + 3\text{e}^-$

The third electron transfer process was performed by applying a constant potential  $E = -2.0$  V vs. Ag/Ag<sup>+</sup>, generating the species **4**. Fe K-edge XANES spectra collected on the obtained species, compared with the previous XANES spectra obtained for species **1**, **2a** and **3**, is presented in figure 6.14. A shift of 1 eV of the main edge to lower energies (7122.0 eV – table 6.6), when compared with **1**, can be observed. In addition to this, the intensity of the pre-edge peak decreases, while the shoulder at 7118.0 eV increases when compared the spectra with the one of **3**. As previously evidenced for the chemically reduced complex **2b**, this increased intensity suggests a square planar structure. Such a geometry can be explained by the de-coordination of axial ligands due to an increased electronic density in the three-electron reduced species **4** as compared to **3**.

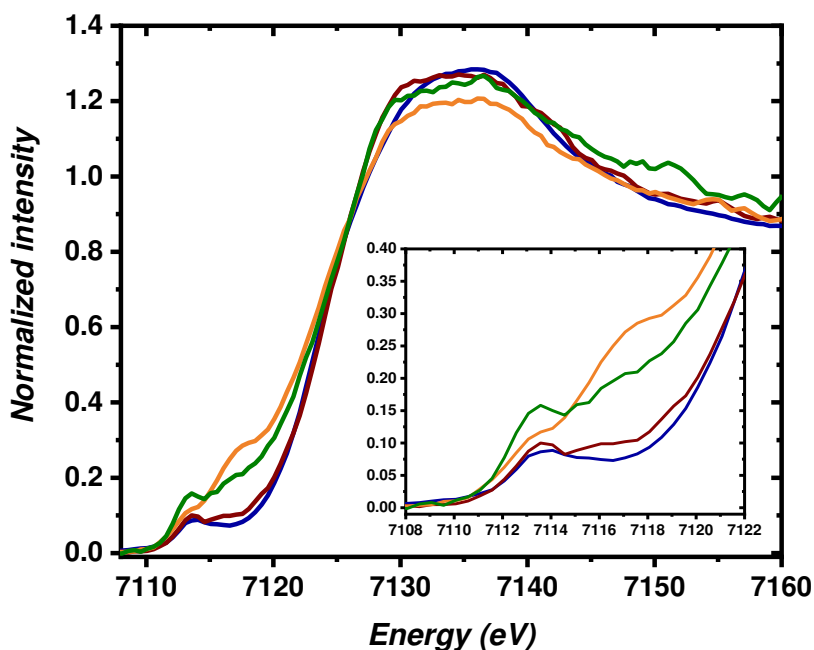
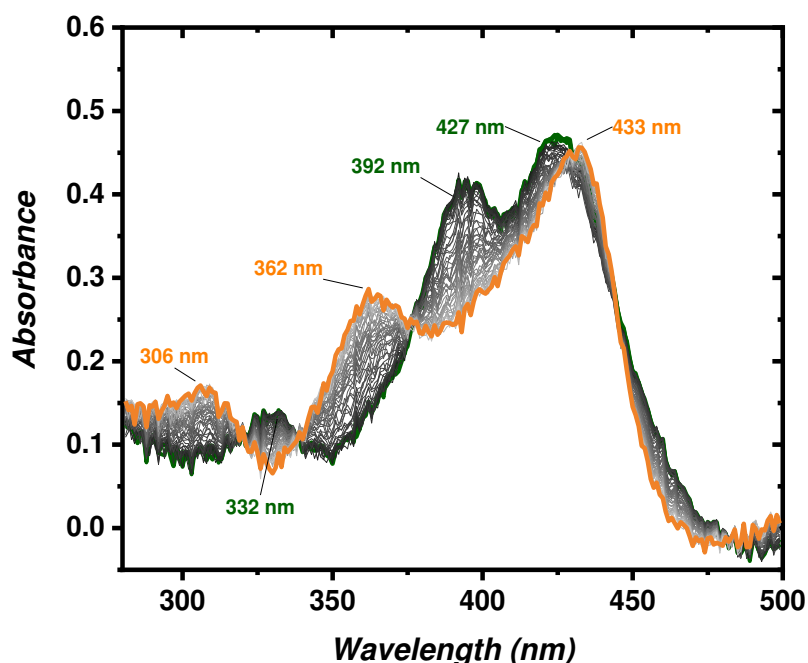


Figure 6.14. Fe K-edge XANES spectra of **1** (blue), **2a** (red), **3** (green) and the three-electron reduced species  $[\text{Fe}^{\text{III}}(\text{TPP})\text{Cl}] + 3\text{e}^-$ , **4** (orange), generated while applying a constant potential  $E = -2.0 \text{ V vs Ag/Ag}^+$ , **4** (orange). Insert: pre-edge region.

Finally, UV-Vis spectroelectrochemistry (figure 6.15) was also performed for this process. The Soret band is slightly modified as compared to the one of **3**, with an increased difference in the split, with values at 362 and 433 nm. In addition to this, a new band appears at 306 nm. Q-bands also varies with the presence of a broader band at 514 nm and a decrease of the band at 608 nm (figure 6.17). These values are approximate with previous reported data both in DMF and in DMSO.<sup>18,21,22</sup>



**Figure 6.15.** UV-Vis spectral variation obtained from **3** (green) and its one-electron reduction species **4** (orange), obtained while performing CPE at  $E = -2.0$  V vs SCE in DMF + 0.1 M TBAPF<sub>6</sub> in the spectroelectrochemical UV-Vis set-up.

*Grey spectra illustrate the transition from 3 to 4.*

Electrogenerated species shown in this manuscript were also compared to other iron species that could be formed due to irradiation, such as metallic particles or oxides. Such degradation has been observed previously for other molecular catalysts due to catalysts degradation<sup>23</sup> or by hydroxyl radical formation due to photolysis of water present in DMF.<sup>24</sup> As illustrated in figure 6.16, the XANES spectra of the metallic iron or iron oxide-hydroxide standard samples do not match the spectra of electrogenerated species. In addition, no species were found on the electrode surface (*ex situ* XANES analysis after electrochemical experiments). These results indicate that, under the experimental conditions presented in this chapter, the molecules of interest do not degrade into metallic or oxide species.

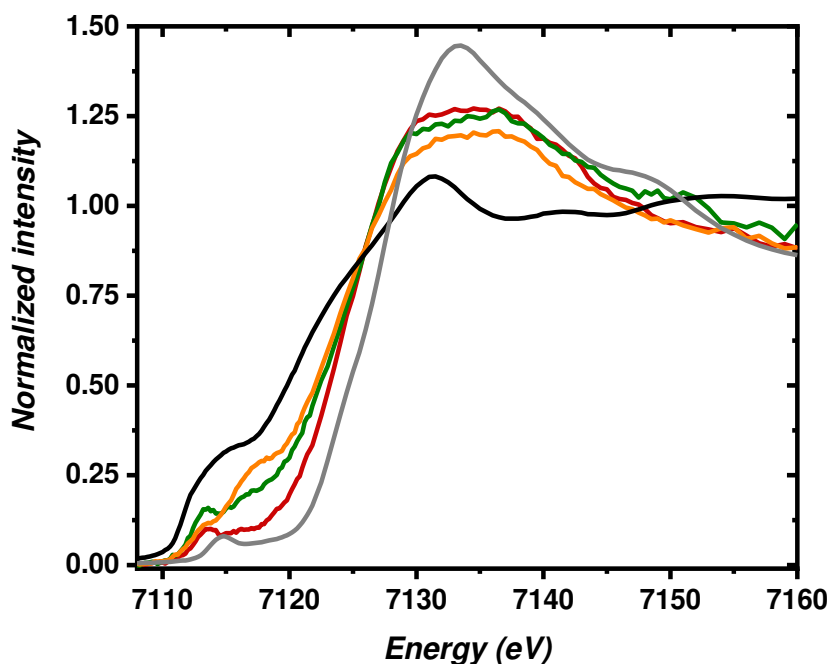


Figure 6.16. Fe K-edge XANES comparative spectra of 2 mM  $[\text{Fe}^{\text{III}}(\text{TPP})]\text{Cl}$  solution in DMF + 0.1 M  $\text{TBAPF}_6$  while performing controlled potential electrolysis at  $E = -0.8$  V (red),  $E = -1.6$  V (green) and  $E = -2$  V (orange) vs.  $\text{Ag}/\text{Ag}^+$  compared to metallic iron sample (black) and  $\text{Fe}^{\text{III}}\text{O}(\text{OH})\cdot n\text{H}_2\text{O}$  in solid state (grey).

#### 6.4. Summary and discussion

The spectra of the initial complex  $[\text{Fe}^{\text{III}}(\text{TPP})]\text{Cl}$  in DMF show almost no differences with respect to the solid state spectra, allowing to conclude that this species retain its spin state and geometry in the presence of DMF. This is no longer the case after a one electron reduction of the complex. Comparison of the XANES spectra between the solid state (chemically generated reduced complex, **2b**) and the electrogenerated complex **2a** shows a 2 eV shift at the main edge position and a difference at the pre-edge peak of 1 eV (table 6.5 and 6.6). This indicates that these complexes are different and point towards an influence of DMF on the metal center. Pre-edge peak values for **2a** and **2b** match literature reports for the low spin  $[\text{Fe}^{\text{II}}(\text{TPP})(\text{Py})_2]$  and intermediate spin  $[\text{Fe}^{\text{II}}(\text{TPP})]$  complex, respectively.<sup>19</sup> Therefore, we can conclude that DMF interacts with the iron center, generating a low spin complex in solution.

Despite the fact that the main edge positions of  $[\text{Fe}^{\text{III}}(\text{TPP})]\text{Cl}$  and its one electron reduced species in solution are identical, several structural and electronic changes influence their edge positions:

- i) A change in oxidation state from (+III) to (+II): shift to lower energies



- ii) A change in the axial coordinating ligands from one Cl<sup>-</sup> to one or two DMF molecules: shift to higher energies
- iii) A spin configuration change from high spin to low spin: shift to higher energies.

These three effects counterbalance each other, so that the final edge position of two different species are identical. This example is a clear demonstration that edge positions should always be considered with care when analyzing a XANES spectrum.

Regarding the analysis of the XANES spectra for the highly reduced species of iron porphyrins, complexes **3** and **4**, the pre-edge peak position does not change when going from **2a** to **4** (table 6.6). This could support the fact that no spin state changes occur at the two and three electron reduction steps starting from the low spin **2a** complex. In addition to this, the appearance of a shoulder at 7118.0 eV, which is associated with a *1s* to *4p<sub>z</sub>* transition, increases as more electrons are injected in the complex (figure 6.14). This peak also appears in the XANES spectra of the [Fe<sup>II</sup>(TPP)] complex in the solid state, **2b** complex, which does not have apical ligands and adopts a square planar structure. This suggest that complexes **3** and **4** have less or no interaction with axial ligands has compared to complexes **2a** and **1** (scheme 6.6). The fact that the shoulder gets more pronounced when three electrons are injected in the system suggests a complete de-coordination of the DMF apical ligands, suggesting a square planar geometry for **4**.

**Table 6.6. Pre-edge peak and main edge energy position values for **1**, the electrogenerated species of [Fe<sup>III</sup>(TPP)]Cl **2a**, **3** and **4**, and **2b** ([Fe<sup>II</sup>(TPP)] – solid state).**

Complex	Pre-edge peak positions* (eV)	Main edge energy positions‡ (eV)
<b>1</b>	7112.6	7123.0
<b>2a</b>	7112.2	7123.0
<b>2b</b>	7111.3	7121.0
<b>3</b>	7112.2	7122.3
<b>4</b>	7112.2	7122.0

\* Pre-edge peak energy position measured at the first inflection point of the pre-edge peak

‡ Main absorption edge energy position measured at the half intensity of the normalized spectrum

The main edge slightly shifts towards lower energies when going from **2a** to **3** (by 0.7 eV) and from **3** to **4** (0.3 eV). These values should be taken with caution, since the increase of the shoulder at 7118.0 eV might artificially displace the main edge position. These shifts are, in any case, quite small and suggest a reduction that is not solely located on the metal centre. It can therefore be suggested that the electronic density in **3** and **4** is distributed between the metal and the ligand.

When analysing the UV-Vis spectra of all the electrogenerated species (figure 6.17), important differences are observed in the Soret and Q-bands positions when going from **1** to **2a** and from **2a** to **3**, however, slight changes in the spectra are observed from **3** to **4**. This observation along with the slight energy shifts observed by XANES, suggest electronic changes that are not as drastic on going from **3** to **4** as from **1** to **2a**. However, at this stage, the exact electronic density distribution on the metal or the ligand cannot be determined. Further spectral fittings and theoretical calculations are needed to achieve this level of understanding.

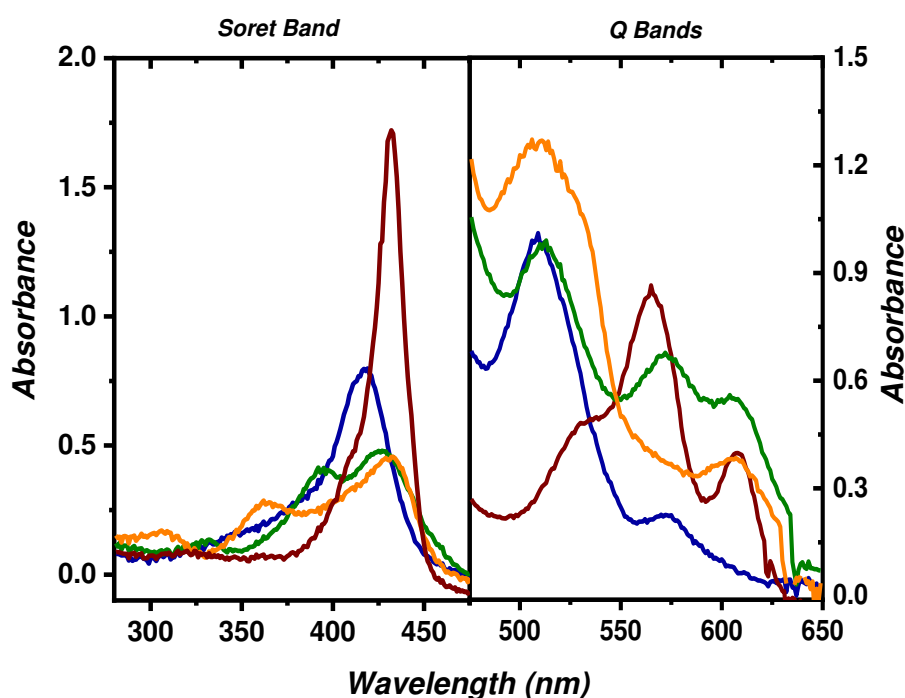
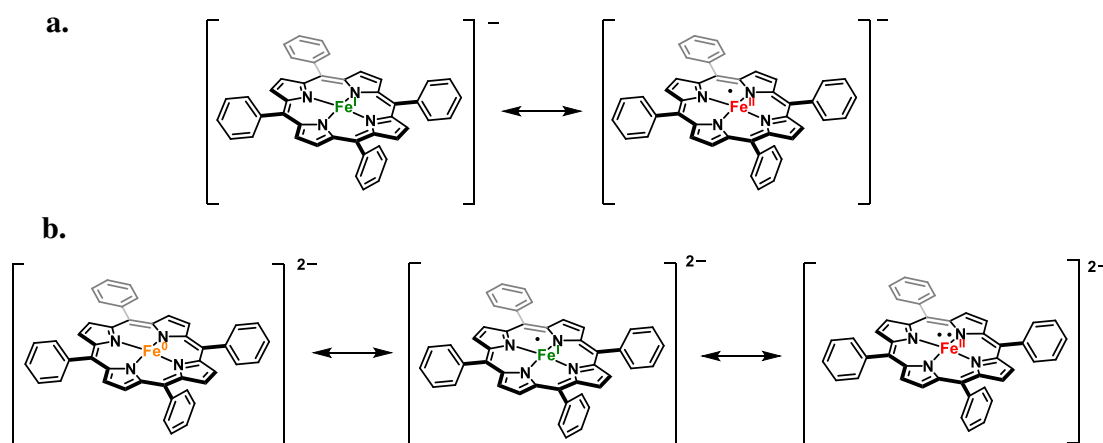


Figure 6.17. UV-Vis profile of **1** (blue), **2a** (red), **3** (green) and **4** (orange) species in DMF + 0.1 M TBAPF<sub>6</sub> under Ar, generated *in situ* by spectroelectrochemistry techniques.

Table 6.7. UV-Vis Soret and Q-band values observed in this work for complex **1** to **4** in DMF-TBAPF<sub>6</sub> solution and reference values reported by Lexa *et al.*<sup>18</sup> and Anxolabéhère *et al.*<sup>21,22</sup>

Complex	Experimental $\lambda$ (nm)		Literature values $\lambda$ (nm)	
	Soret band	Q-bands	Soret band	Q-bands
<b>1</b>	417	509 and 575	416	508 and 572
<b>2a</b>	432	530, 565 and 608	431	563 and 605
<b>3</b>	392 and 425	510, 575 and 608	392 and 426	512, 580, 606, 664
<b>4</b>	362 and 433	514 and 607	360 and 448	515

The analysis of the *in situ* dataset obtained under argon, suggests that the electron density for the highly reduced iron porphyrin species **3** and **4** is not only located on the metal but also partly on the porphyrin ring. These complexes can therefore be described as species in which the metal center is in a Fe(II) state while the ligand holds a radical (scheme 6.6). This description is, however, a formal representation, since it is expected that the electronic density is shared in molecular orbital that involve both the metal and the porphyrin ligand. Theoretical calculations of the UV-Vis and pre-edge features, taking into consideration solvation effect, should complement these experimental data to better describe the electronic structure of these species.



**Scheme 6.6. Formal representation of proposed structures for complexes: a. 3; b. 4.**

In this chapter we have shown the XANES dataset recorded for the iron porphyrin and its electroreduced species in aprotic media in inert atmosphere for the first time. We have not only demonstrated that the developed spectroelectrochemical cell (chapter V) allow to record reproducible data, but also that the signal to noise of this data permits to give insights on the electronic structure of this system based on qualitative analysis and comparison with the few data available in the literature. These data constitute fingerprints which are necessary prior the studies under CO<sub>2</sub>, results that are shown in next chapter VII.

## 6.4 References Chapter VI

- (1) Costentin, C.; Savéant, J.-M.; Tard, C. Ligand “Noninnocence” in Coordination Complexes vs. Kinetic, Mechanistic, and Selectivity Issues in Electrochemical Catalysis. *PNAS* **2018**, *115* (37), 9104–9109.
- (2) Costentin, C.; Drouet, S.; Robert, M.; Savéant, J.-M. A Local Proton Source Enhances CO<sub>2</sub> Electroreduction to CO by a Molecular Fe Catalyst. *Science* **2012**, *338* (6103), 90–94.
- (3) Tatin, A. Electrochemical CO<sub>2</sub> Splitting into CO and O<sub>2</sub> in Neutral Water Using Earth-Abundant Materials. Doctoral Thesis. *Université Paris Diderot*. **2016**.
- (4) Azcarate, I.; Costentin, C.; Robert, M.; Savéant, J.-M. Through-Space Charge Interaction Substituent Effects in Molecular Catalysis Leading to the Design of the Most Efficient Catalyst of CO<sub>2</sub>-to-CO Electrochemical Conversion. *J. Am. Chem. Soc.* **2016**, *138* (51).
- (5) Costentin, C.; Drouet, S.; Passard, G.; Robert, M.; Savéant, J.-M. Proton-Coupled Electron Transfer Cleavage of Heavy-Atom Bonds in Electrocatalytic Processes. Cleavage of a C–O Bond in the Catalyzed Electrochemical Reduction of CO<sub>2</sub>. *J. Am. Chem. Soc.* **2013**, *135*, 24, 9023 - 9031.
- (6) Westre, T. E.; Kennepohl, P.; DeWitt, J. G.; Hedman, B.; Hodgson, K. O.; Solomon, E. I. A Multiplet Analysis of Fe K-Edge 1s → 3d Pre-Edge Features of Iron Complexes. *J. Am. Chem. Soc.* **1997**, *119* (27), 6297–6314.
- (7) Lassalle-Kaiser, B.; Gul, S.; Kern, J.; Yachandra, V. K.; Yano, J. In Situ/Operando Studies of Electrocatalysts Using Hard X-Ray Spectroscopy. *J. Elec. Spec. Rel. Phenom.* **2017**, *221*, 18–27.
- (8) Yamashige, H.; Matsuo, S.; Kurisaki, T.; Perera, R. C. C.; Wakita, H. Electronic Structure Analysis of Iron(III)-Porphyrin Complexes by X-Ray Absorption Spectra at the C, N and Fe K-Edges. *Anal. Sci.* **2005**, *21* (3), 309–314.
- (9) Mongay, C.; Cerdà, V. A Britton-Robinson Buffer of Known Ionic Strength. *Ann. Chim.* **1974**, *64*, 409–412.
- (10) Costentin, C.; Dridi, H.; Savéant, J.-M. Molecular Catalysis of O<sub>2</sub> Reduction by Iron Porphyrins in Water: Heterogeneous versus Homogeneous Pathways. *J. Am. Chem. Soc.* **2015**, *137* (42), 13535–13544.
- (11) Fleischer, E. B.; Palmer, J. M.; Srivastava, T. S.; Chatterjee, A. Thermodynamic and kinetic properties of an iron-porphyrin system. *J. Am. Chem. Soc.* **1971**, *93*, 13, 3162 - 3167.
- (12) Böhm, P.; Gröger, H. Iron(III)-Porphyrin Complex FeTSPP: A Versatile Water-Soluble Catalyst for Oxidations in Organic Syntheses, Biorenewables Degradation and Environmental Applications. *Chem Cat Chem* **2015**, *7* (1), 22–28.
- (13) El-Awady, A. A.; Wilkins, P. C.; Wilkins, R. G. Kinetic Aspects of the Iron(III)-Tetrakis(p-Sulfonatophenyl)Porphine System. *Inorg. Chem.* **1985**, *24* (13), 2053–2057.

- (14) Xu, W.; Dziejczak-Kocurek, K.; Yu, M.; Wu, Z.; Marcelli, A. Spectroscopic Study and Electronic Structure of Prototypical Iron Porphyrins and Their  $\mu$ -Oxo-Dimer Derivatives with Different Functional Configurations. *RSC Adv.* **2014**, *4* (87), 46399–46406.
- (15) Römelt, C.; Song, J.; Tarrago, M.; Rees, J. A.; van Gestel, M.; Weyhermüller, T.; DeBeer, S.; Bill, E.; Neese, F.; Ye, S. Electronic Structure of a Formal Iron(0) Porphyrin Complex Relevant to CO<sub>2</sub> Reduction. *Inorg. Chem.* **2017**, *56* (8), 4745–4750.
- (16) Paulat, F.; Lehnert, N. Detailed Assignment of the Magnetic Circular Dichroism and UV–vis Spectra of Five-Coordinate High-Spin Ferric [Fe(TPP)(Cl)]. *Inorg. Chem.* **2008**, *47* (11), 4963–4976.
- (17) Hammouche, M.; Lexa, D.; Savéant, J.-M.; Momenteau, M. Catalysis of the Electrochemical Reduction of Carbon Dioxide by Iron(“0”) Porphyrins. *J. Electroanal. Chem. Interf. Electrochem.* **1988**, *249* (1), 347–351.
- (18) Lexa, D.; Momenteau, M.; Mispelter, J. Characterization of the Reduction Steps of Fe(III) Porphyrins. *Biochim Biophys Acta.* **1974**, *338* (1), 151–163.
- (19) Wilson, S. A.; Green, E.; Mathews, I. I.; Benfatto, M.; Hodgson, K. O.; Hedman, B.; Sarangi, R. X-Ray Absorption Spectroscopic Investigation of the Electronic Structure Differences in Solution and Crystalline Oxyhemoglobin. *PNAS.* **2013**, *110* (41), 16333–16338.
- (20) Li, N.; Lu, W.; Pei, K.; Chen, W. Interfacial Peroxidase-like Catalytic Activity of Surface-Immobilized Cobalt Phthalocyanine on Multiwall Carbon Nanotubes. *RSC Adv.* **2015**, *5* (13), 9374–9380.
- (21) Anxolabéhère, E.; Chottard, G.; Lexa, D. Highly reduced iron porphyrins: UV-vis and resonance Raman spectroelectrochemical studies of FeTPP and FeTF<sub>5</sub>PP. *New. J. Chem.* **1994**, *18*, 889 - 899.
- (22) Anxolabéhère, E. Influences Supramoléculaires Sur La Reaction Redox Fe(I)/Fe(0) (Ou Fe(0)?) Dans Les Porphyrines de Fer. These de doctorat, *Paris 7*, **1991**.
- (23) Cometto, C.; Chen, L.; Mendoza, D.; Lassalle-Kaiser, B.; Lau, T.-C.; Robert, M. An Iron Quaterpyridine Complex as Precursor for the Electrocatalytic Reduction of CO<sub>2</sub> to Methane. *ChemSusChem* **2019**, *12* (19), 4500–4505.
- (24) King, H. J.; Fournier, M.; Bonke, S. A.; Seeman, E.; Chatti, M.; Jumabekov, A. N.; Johannessen, B.; Kappen, P.; Simonov, A. N.; Hocking, R. K. Photon-Induced, Timescale, and Electrode Effects Critical for the in Situ X-Ray Spectroscopic Analysis of Electrocatalysts: The Water Oxidation Case. *J. Phys. Chem. C* **2019**, *123* (47), 28533–28549.

# Chapter VII

---

## - Results and Discussion -

### Structural and electronic changes in $[\text{Fe}^{\text{III}}(\text{TPP})]\text{Cl}$ and its reduced states under $\text{CO}_2$

#### Content

---

7.1	$[\text{Fe}^{\text{III}}(\text{TPP})]\text{Cl}$ analysis in the presence of $\text{CO}_2$ .....	111
7.2	<i>In situ</i> spectroelectrochemical measurements on reduced species of $[\text{Fe}^{\text{III}}(\text{TPP})]\text{Cl}$ under $\text{CO}_2$ atmosphere .....	114
7.2.1	One electron reduction process: $[\text{Fe}^{\text{III}}\text{TPP}(\text{Cl})] + 1\text{e}^-$ .....	114
7.2.2	Two electron reduction process: $[\text{Fe}^{\text{III}}\text{TPP}(\text{Cl})] + 2\text{e}^-$ .....	116
7.2.3	Three electron reduction process: $[\text{Fe}^{\text{III}}\text{TPP}(\text{Cl})] + 3\text{e}^-$ .....	120
7.3	Identification of the $[\text{Fe}^{\text{II}}(\text{TPP})(\text{CO})]$ adduct .....	123
7.4	Discussion .....	125
7.5	References .....	127



The fundamental understanding of the transformations that a catalyst perform during the reaction is necessary to propose a mechanism. However, as discussed in this text, the isolation of intermediates is challenging due to their short lifetime. In spectroscopic terms, the simultaneous presence of various species in a single spectrum complicates the analysis, if the footprint of each single species is not known. The overall rate of the reaction is conditioned by the rate determining step (rds), which is the slowest step of the reaction.<sup>1,2</sup> Therefore, it is expected that the species that is preceding the rds during the reaction are the ones that can be observed by spectroscopic means. In the CO<sub>2</sub> reduction reaction catalyzed by iron porphyrin, it has been proposed that such step is conditioned by the presence, the nature and the concentration of a proton source. However, no extensive studies based on spectroscopic techniques have been performed along those lines.

This chapter aims to present the data obtained by spectroelectrochemical methods, mainly by XANES and UV-Vis, on the activation of CO<sub>2</sub> by FeTPP. By comparing these data with those obtained under inert conditions (chapter VI), it is possible to observe the influence that the presence of CO<sub>2</sub> has on the Fe reduced species. The spectroscopic observations will allow to describe structural and electronic changes that occurs on iron porphyrins in the presence of the substrate and during its activation.

### 7.1 [Fe<sup>III</sup>(TPP)]Cl analysis in the presence of CO<sub>2</sub>

Figure 7.1 displays the XANES spectra of [Fe<sup>III</sup>(TPP)]Cl in DMF + 0.1 M TBAPF<sub>6</sub> under argon (**I** – blue solid line) and after saturation with CO<sub>2</sub> (**5** – light blue dotted line). As observed on the figure, the two spectra are identical, with a pre-edge peak at 7112.6 eV and a half-edge jump energy at 7123.0 eV (table 7.1). These results allow to conclude that there are no interactions between the CO<sub>2</sub> and the iron center at this oxidation state, therefore the [Fe<sup>III</sup>(TPP)]Cl remains in its square planar pyramidal geometry with a Fe<sup>III</sup> center in high spin (scheme 7.1).



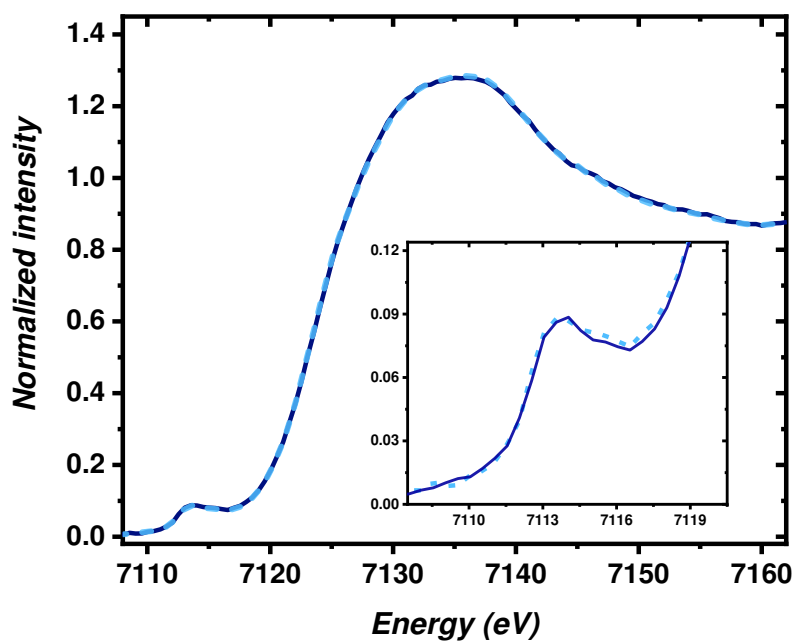


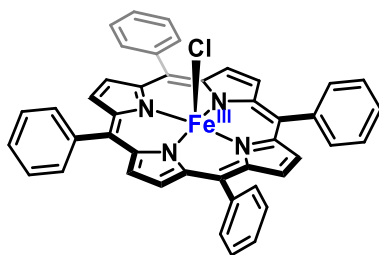
Figure 7.1 Fe K-edge XANES spectra of [Fe<sup>III</sup>(TPP)]Cl in DMF + 0.1 M TBAPF<sub>6</sub> under Ar (*1* - dark blue – solid line) and under CO<sub>2</sub> (*5* - light blue – dashed line) atmosphere. Insert: pre-edge region.

Table 7.1. Pre-edge peak and main edge energy position for *1* and *5*

Complex	Pre-edge peak energy* (eV)	Main edge energy‡ position (eV)	Spin
<i>1</i>	7112.6	7123.0	S = 5/2
<i>5</i>	7112.6	7123.0	High spin

\* Pre-edge peak energy position measured at the first inflection point of the pre-edge peak

‡ Main edge energy position measured at the half intensity of the normalized spectrum



Scheme 7.1. Structure of the S = high spin [Fe<sup>III</sup>(TPP)]Cl expected in DMF + 0.1 M TBAPF<sub>6</sub> under CO<sub>2</sub> atmosphere (complex *5*).

As previously commented, the CV of [Fe<sup>III</sup>(TPP)]Cl in the presence of argon exhibit three defined and reversible waves (Chapter VI). However, when CO<sub>2</sub> is dissolved into the solution, a substantial current increase and a loss of reversibility can be observed on the third reduction wave, as compared with the data observed under argon (figure 7.2).<sup>3,4</sup> As indicated in chapter II, the current increase in the last wave and the changes in its shape have been reported as an evidence of catalytic activity, which requires the presence of an acid source.<sup>4-</sup><sup>6</sup> Despite the precautions taken to avoid the presence of water in the solution (see Appendix C), the presence of protons cannot be completely avoided in these experimental conditions. Additionally, even in the case of extremely low residual proton concentration, CO<sub>2</sub> itself could play the role of an acid (Lewis acid), and provide assistance for C-O bond cleavage leading to the generation of one CO molecule and one CO<sub>3</sub><sup>2-</sup> anion.<sup>7</sup>

In addition to the differences observed at the last wave, slight changes can also be observed on the second wave and the back scan of the first wave. Therefore, having a fingerprint of each electrogenerated species in the presence of CO<sub>2</sub>, as in the case of argon, is necessary to understand its interactions with the iron porphyrin.

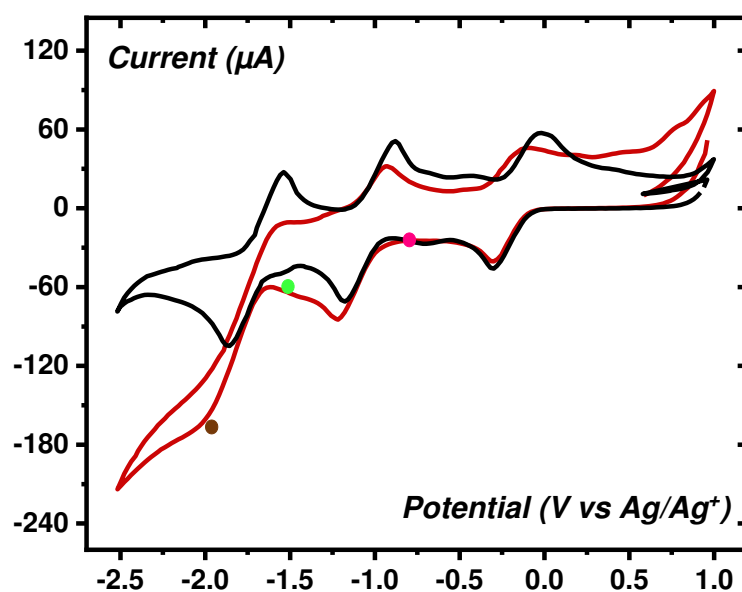


**Figure 7.2.** Cyclic voltammogram of an [Fe<sup>III</sup>(TPP)]Cl 2mM solution in DMF + 0.1 M TBAPF<sub>6</sub>, at room temperature (RT) and scan rate  $\nu = 100 \text{ mVs}^{-1}$  recorded in the cell A under a vacuum of  $10^{-2}$  mbar at the LUCIA beamline at Synchrotron SOLEIL under Ar (black) and CO<sub>2</sub> (red) atmosphere. Colored dots indicate the selected potential for control potential electrolysis (CPE) during spectroelectrochemical measurements.

## 7.2 *In situ* spectroelectrochemical measurements on reduced species of [Fe<sup>III</sup>(TPP)]Cl under CO<sub>2</sub> atmosphere

### 7.2.1 One electron reduction of the porphyrin: [Fe<sup>III</sup>(TPP)]Cl + 1e<sup>-</sup>

As discussed in chapter VI, in the presence of argon, the first electroreduction of [Fe<sup>III</sup>(TPP)]Cl in DMF + 0.1 M TBAPF<sub>6</sub> yields a complex in which DMF interacts with the Fe(II) center. It was suggested that this effect results in a change of spin state of this structure (from a high spin in [Fe<sup>III</sup>(TPP)]Cl to a low spin configuration).

Figure 7.3 shows the XANES spectrum of the species (**6**) generated by applying a potential  $E = -0.8$  V vs. Ag/Ag<sup>+</sup> under CO<sub>2</sub> atmosphere. When compared with the same solution in the presence of argon, complex **2a**, no significant changes are observed, with the half-edge energy position maintained at 7123.0 eV and the pre-edge peak at 7112.1 eV (table 7.2). The presence of CO<sub>2</sub> in the one-electron reduced species in solution therefore seems to have no influence on the structure of the Fe(II) state. This species can thus be considered, as in the argon case (scheme 7.2).

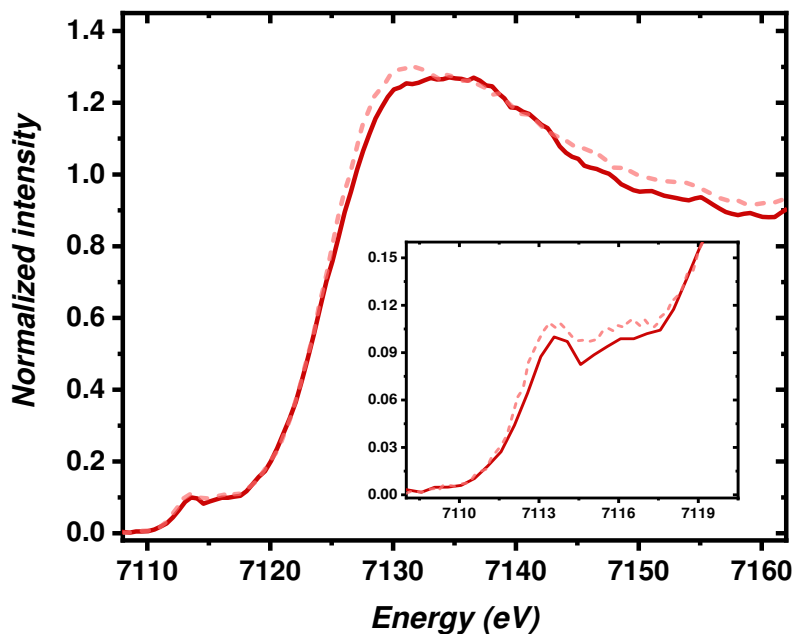


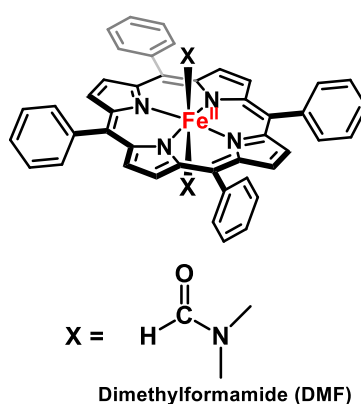
Figure 7.3. Fe K-edge XANES spectra of [Fe<sup>III</sup>(TPP)]Cl + 1e<sup>-</sup> in DMF + 0.1 M TBAPF<sub>6</sub> under Ar, **2a**, (red – solid line) and under CO<sub>2</sub>, **6**, (pink – dashed line) atmosphere. Insert: pre-edge region.

Table 7.2. Pre-edge peak and main edge energy position for 2a and 6.

Complex	Pre-edge peak energy* (eV)	Main edge energy position <sup>‡</sup> (eV)
2a	7112.2	7123.0
6	7112.1	7123.0

\* Pre-edge peak energy position measured at the first inflection point of the pre-edge peak

<sup>‡</sup> Main edge energy position measured at the half intensity of the normalized spectrum



#### Scheme 7.2. Proposed structure for complex 6

- As for complex 2a, the coordination number of species 6 has not been determined. Therefore, one or two solvent molecules can be suggested.

UV-Vis spectroelectrochemistry was also performed in the presence of CO<sub>2</sub> which was compared with the argon case (figure 7.4). Firstly, the UV-Vis spectrum of the [Fe<sup>III</sup>(TPP)]Cl in CO<sub>2</sub> possesses a Soret band at 417 nm and a significantly intense Q-band at 508 nm that match with the reported bands in the presence of argon (chapter VI – table 6.7). These UV-Vis results are in concordance with XANES conclusion detailed above supporting the fact that CO<sub>2</sub> does not interact with [Fe<sup>III</sup>(TPP)]Cl. When the [Fe<sup>III</sup>(TPP)]Cl is electroreduced by one electron (controlled potential electrolysis at  $E = -0.8$  V vs SCE), the Soret band is red-shifted, with a new intense peak at 430 nm and the appearance of new Q-bands, an intense one at 567 nm and two others at 535 and 609 nm. The Soret and Q-band wavelength values are very similar to the ones reported for the argon case (chapter VI - figure 6.9) and support the fact that no interaction between CO<sub>2</sub> and the iron center occurs at this oxidation state.

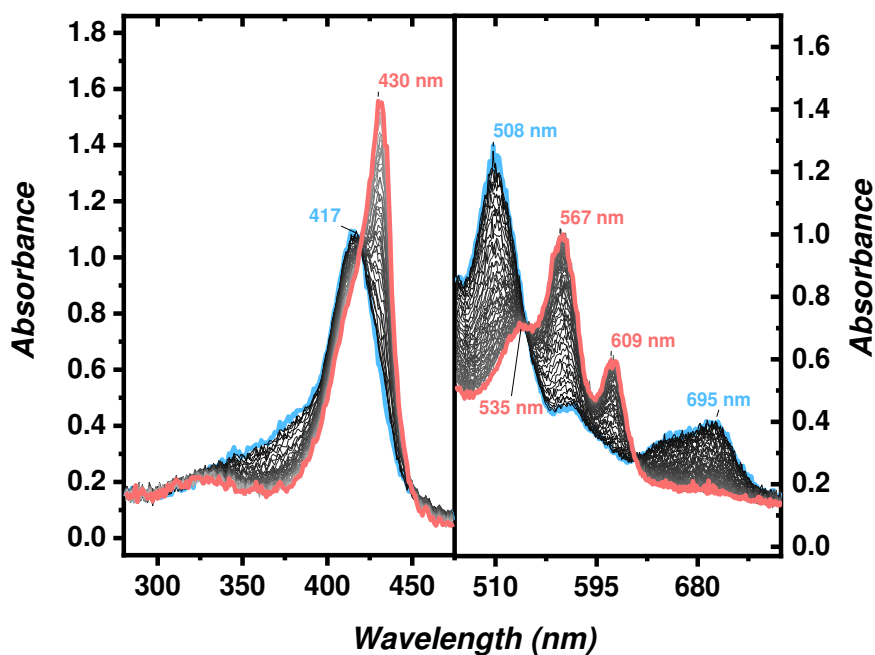


Figure 7.4. UV-Vis spectra obtained for **5** (blue) and the one-electron reduced species **6** (pink) obtained during CPE at  $E = -0.8$  V vs SCE in DMF + 0.1 M TBAPF<sub>6</sub> solution in the presence of CO<sub>2</sub>. Dark grey spectra illustrate the transition from **5** to **6**.

### 7.2.2 Two electron reduction of the porphyrin: [Fe<sup>III</sup>TPP(Cl)] + 2e<sup>-</sup>

Figure 7.5 shows the XANES spectrum of [Fe<sup>III</sup>(TPP)]Cl under CO<sub>2</sub> (**5**, light blue) and reduced by one (**6**, pink) and two electrons, named **7** (light green). As observed, the spectra of **7** is very similar to the one of **6**. Indeed, the half-edge energy is observed at 7123.0 eV, while the pre-edge peak position is located at 7112.1 eV, with just slight differences in the shape of the peak when compared with the spectrum of **1** and **2a**.

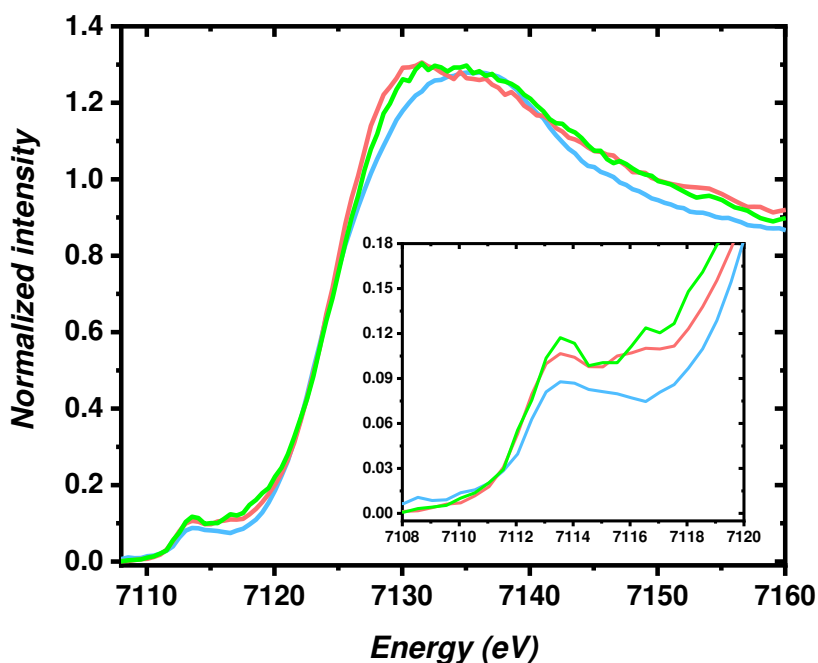


Figure 7.5. Fe K-edge XANES spectra of [Fe<sup>III</sup>TPP]Cl + n e<sup>-</sup> in DMF + 0.1 M TBAPF<sub>6</sub> under CO<sub>2</sub>: 5 (n = 0, light blue), 6 (n = 1, pink) and 7 (n = 2, light green). Insert: pre-edge region.

However, 7 presents significant differences when compared with the same species generated under inert conditions (figure 7.6). Indeed, the shoulder close to 7118.0 eV present in 3 is absent in 7. This supports a first conclusion indicating that the square planar structure of the complex, postulated in the presence of argon, is different in the presence of CO<sub>2</sub>. It is likely that CO<sub>2</sub> is responsible for this geometry change and is therefore interacting with the metal center. In addition, there is a slight shift of 0.7 eV in the main edge position towards higher energies, indicating that the Fe center donates some electronic density to the CO<sub>2</sub>. Such interaction between CO<sub>2</sub> and the iron center was recently reported for [Fe<sup>I</sup>(TPP)]<sup>-</sup> in acetonitrile,<sup>9</sup> which illustrates the possible interaction between CO<sub>2</sub> and a formally Fe(I) species.

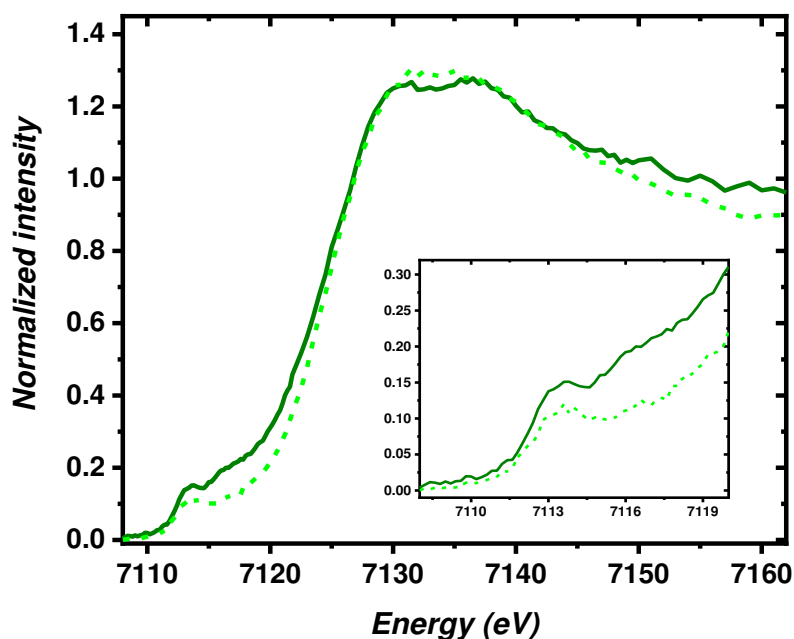


Figure 7.6. Fe K-edge XANES spectra of [Fe<sup>III</sup>TPP]Cl + 2e<sup>-</sup> in DMF + 0.1 M TBAPF<sub>6</sub> solution in argon, **3**, (green) and in CO<sub>2</sub>, **7**, atmosphere (dashed light green). Insert: pre-edge region.

Spectroelectrochemical UV-Vis measurements were performed during the conversion of **6** to **7**, in the same conditions as for the XANES experiment (figure 7.7). A split of the Soret band is observed going from a single intense band at 430 nm to two lower intensity bands at 392 and 427 nm. These values, along with the Q-bands observed, are in line with what has been observed for the two-electron reduction process in the presence of argon (chapter VI – figure 6.13 and figure 6.17), suggesting no significant changes in the presence of CO<sub>2</sub> when compare to inert conditions for this doubly reduced species, as it is illustrated in figure 7.8.

Taken together these spectroscopic data, we therefore suggest a loose interaction between CO<sub>2</sub> and the Fe center in **7** (scheme 8.2), which can be detected by XANES due to its sensitivity to the local geometry, while it cannot be seen by UV-Vis.

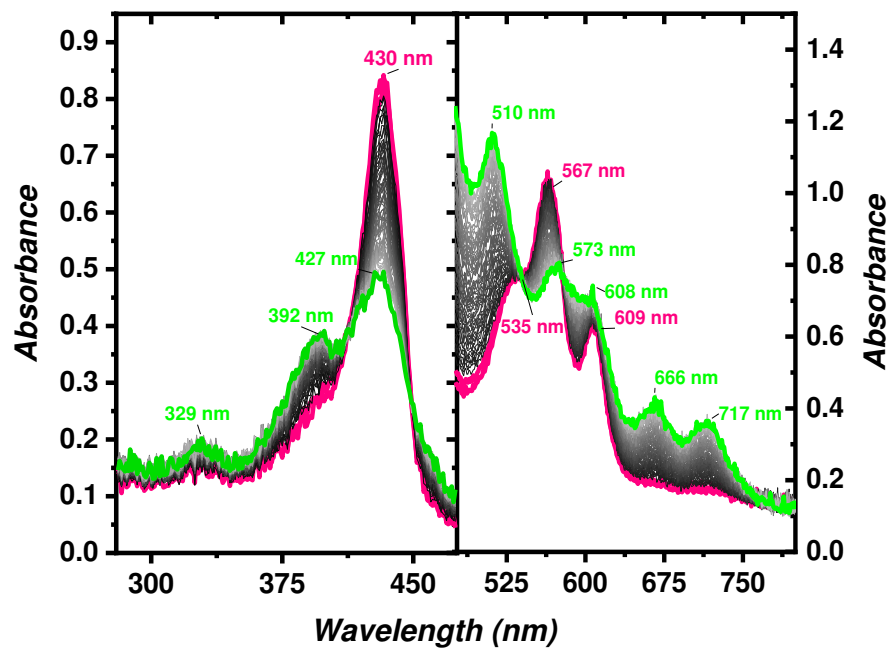


Figure 7.7. UV-Vis spectra obtained upon conversion of 6 (pink) to 7 (light green) during CPE at  $E = -1.6$  V vs SCE in DMF + 0.1 M TBAPF<sub>6</sub> under CO<sub>2</sub>. Dark grey spectra illustrate the transition from 6 to 7.

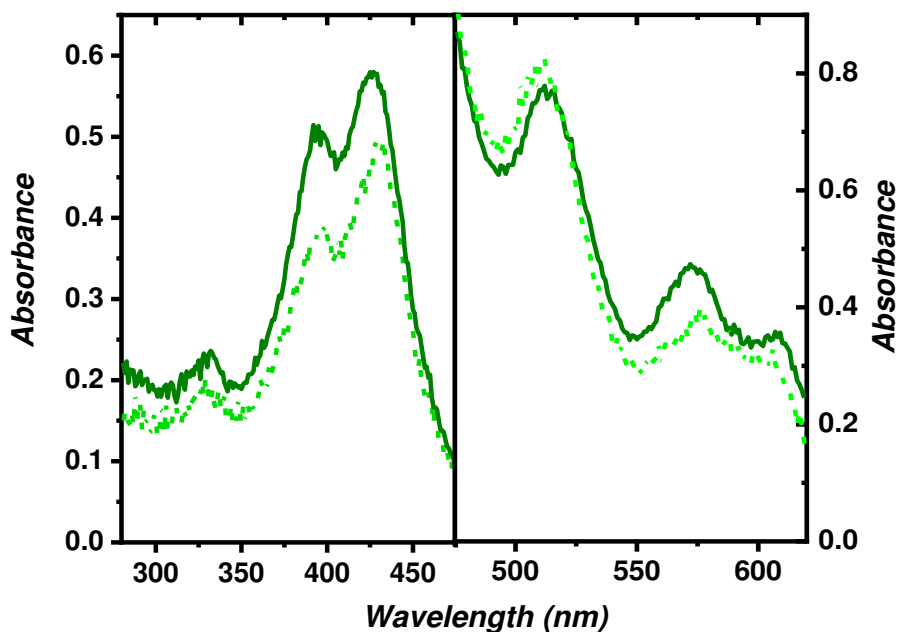


Figure 7.8. UV-Vis comparison between the two-electron reduced species 3 (under Ar, green) and 7 (under CO<sub>2</sub>, dashed - light green).



### 7.2.3 Three electron reduction of the porphyrin: [Fe<sup>III</sup>TPP(Cl)] + 3e<sup>-</sup>

Figure 7.9 shows the XANES spectrum [Fe<sup>III</sup>(TPP)]Cl under CO<sub>2</sub> recorded at the potential corresponding to the catalytic wave ( $E = -2.0$  V vs Ag/Ag<sup>+</sup>) (species **8**), compared with the same species in the presence of argon, complex **4**. The pre-edge peak is lowered in intensity and the shoulder at around 7118.0 eV is no more observable (figure 7.9). Such changes suggest an important interaction between the CO<sub>2</sub> and the iron center, yielding a complex with a different structure than in the argon case, *i.e.* not square planar.

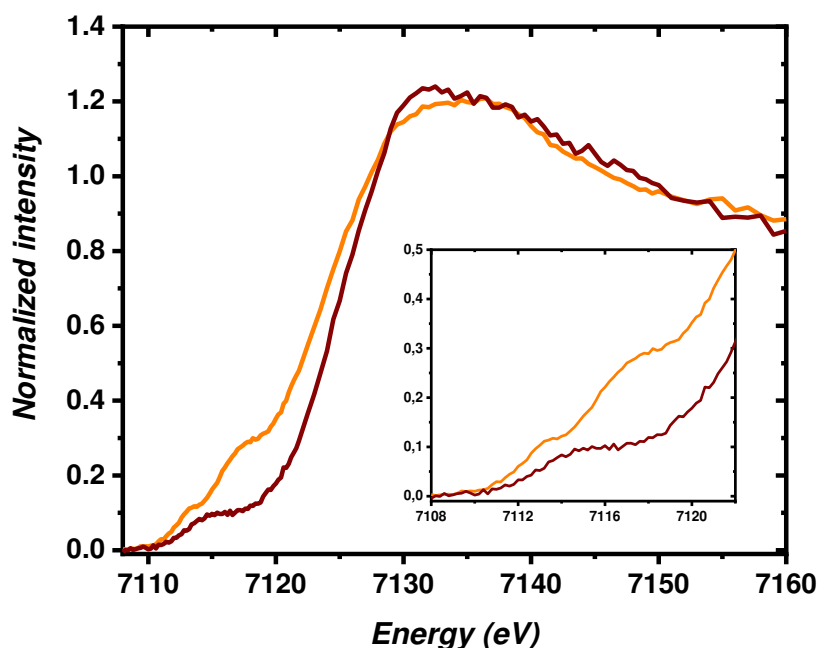


Figure 7.9. Fe K-edge XANES spectra of [Fe<sup>III</sup>TPP]Cl + 3e<sup>-</sup> in DMF-TBAPF<sub>6</sub> solution in argon, **4**, (orange) and in CO<sub>2</sub> atmosphere, **8**, (brown). Insert: pre-edge region.

The pre-edge peak observed on the spectrum of the complex **8** is significantly different than the one observed on the spectra of [Fe<sup>III</sup>(TPP)]Cl and its one and two electroreduced species in the presence of CO<sub>2</sub> (figure 7.10 and table 7.3). Along with this, the edge position is shifted towards higher energies by 0.7 eV when compared with the two-electron reduced species obtained in CO<sub>2</sub>, suggesting an electronic structure change for **8**. This shift is even more pronounced (+1.7 eV) when compared with the spectrum of the three-electron reduced species under argon, indicating an important interaction of CO<sub>2</sub> with the iron center in **8**. Indeed, this shift is in agreement with the Fe center donating part of its electronic density to the CO<sub>2</sub> molecule. This observation further supports a coordination of CO<sub>2</sub> to the iron center with a proposed structure that is presented on scheme 8.2 in chapter VIII.

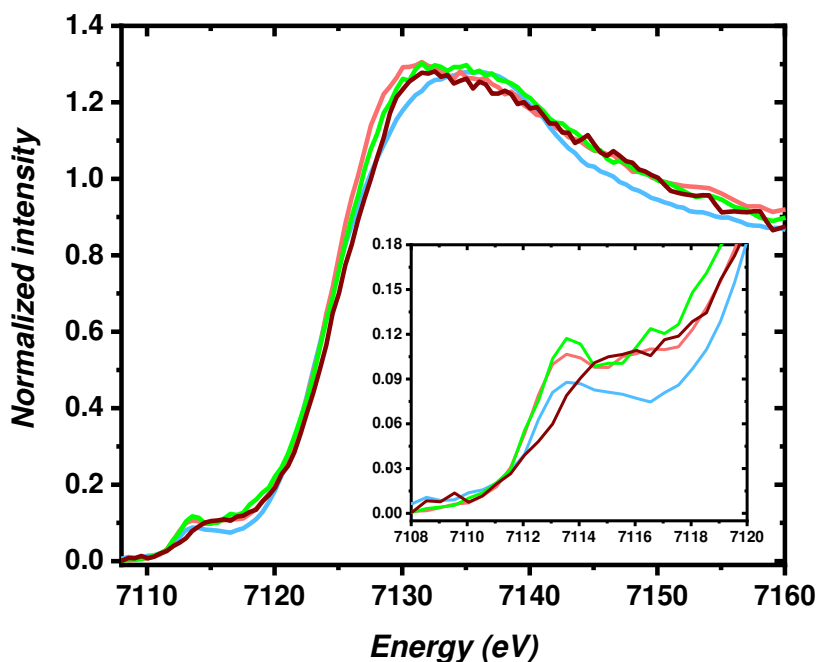


Figure 7.10. Fe K-edge XANES spectra of [Fe<sup>III</sup>TPP]Cl + ne<sup>-</sup> (n = 0, 1, 2, 3) in DMF + 0.1 M TBAPF<sub>6</sub> under CO<sub>2</sub>: 5 (n = 0, light blue), 6 (n = 1, pink), 7 (n = 2, light green) and 8 (n = 3, brown). Insert: pre-edge region.

Table 7.3. Summary of the pre-edge peak and main edge energy position values for 1 to 8.

<i>Complex</i>	<i>Pre-edge peak position* (eV)</i>	<i>Main edge energy position‡ (eV)</i>
<i>Argon</i>		
<i>1</i>	7112.6	7123.0
<i>2a</i>	7112.2	7123.0
<i>3</i>	7112.2	7122.3
<i>4</i>	7112.2	7122.0
<i>CO<sub>2</sub></i>		
<i>5</i>	7112.6	7123.0
<i>6</i>	7112.1	7123.0
<i>7</i>	7112.1	7123.0
<i>8</i>	7113.1	7123.7

\* Pre-edge peak energy position measured at the first inflection point of the pre-edge peak

‡ Main edge energy position measured at the half intensity of the normalized spectrum

Concerning the UV-Vis spectra, when a third electron is transferred to the porphyrin in the presence of CO<sub>2</sub>, no significant changes are observed at the Soret and Q-bands when compared with the two-electrons reduced species, as evidenced in figure 7.11. However, when the CO<sub>2</sub> data is compared with the one obtained under argon, important differences are observed in the Soret and in the Q-bands (figure 7.12). These results are in line with those obtained from XANES, indicating that the three-electrons reduced species has a significant different structure under CO<sub>2</sub> than under Ar.

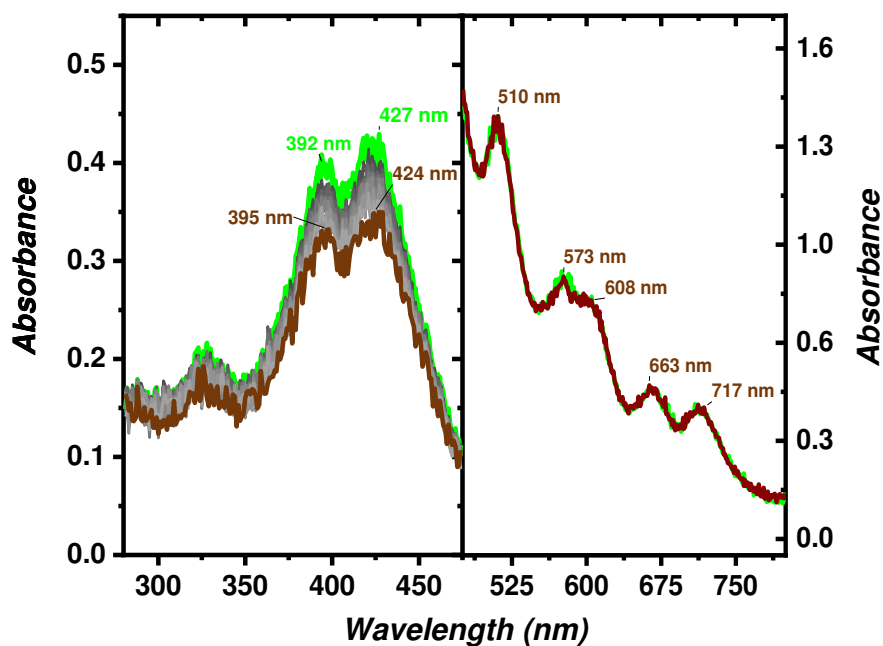


**Figure 7.11.** UV-Vis spectra obtained upon conversion of 7 (light green) to 8 (brown) while performing CPE at  $E = -2.0$  V vs SCE in DMF 0.1 M TBAPF<sub>6</sub> under CO<sub>2</sub>.

*Dark grey spectra illustrate the transition from 7 to 8.*

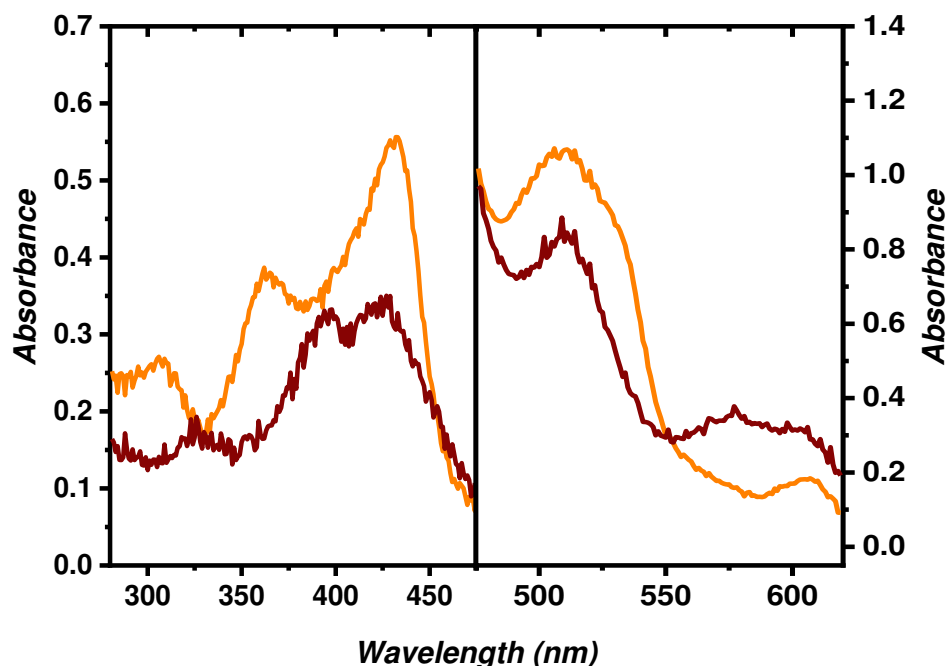


Figure 7.12. UV-Vis difference of CPE at  $E = -2.0$  V vs SCE under Ar, complex **4** (orange) and under CO<sub>2</sub>, complex **8** in DMF-TBAPF<sub>6</sub> solution in the spectroelectrochemical UV-Vis set-up.

### 7.3 Identification of [Fe<sup>II</sup>(TPP)(CO)] adduct

#### 7.3.1 UV-Vis Spectroelectrochemistry

[Fe<sup>III</sup>(TPP)]Cl in DMF + 0.1 M TBAPF<sub>6</sub> was reduced in the presence of CO<sub>2</sub> by applying a constant potential at  $E = -2.0$  V vs SCE, as previously indicated, obtaining complex **8** (figure 7.13 – brown). After approximately 20 minutes of CPE at  $E = -2.0$  V vs SCE and while keeping the setup tightly closed, the potential was set back to  $E = -1.0$  V vs SCE for an extra 10 minutes while simultaneously recording UV-Vis spectra. The following changes are observed: a new intense Soret band rises at 420 nm while a single Q-band appears at 540 nm, evidencing the generation of a new species, hereafter named **9**. A similar spectrum was previously reported in acetonitrile in the presence of CO with UV-Vis characteristic values at  $\lambda = 420$  nm (Soret band) and  $\lambda = 535$  nm (Q-band) (see chapter IV – figure 4.9).<sup>10</sup> Similarly, features at 420 and 540 nm have been reported for other Fe(II) porphyrin complexes under CO atmosphere.<sup>11,12</sup> The literature data therefore strongly support the identification of complex **9** as [Fe<sup>II</sup>(TPP)(CO)], which would result from the reaction of CO generated at  $E = -2.0$  V vs SCE with [Fe<sup>II</sup>(TPP)] generated at  $E = -1.0$  V. This identification confirms the catalytic formation of CO when a solution of [Fe<sup>III</sup>(TPP)]Cl in DMF + 0.1 M TBAPF<sub>6</sub> is set to an applied potential of  $E = -2.0$  V vs SCE. This catalytic activity, as previously proposed, is due to both the presence of residual water in the DMF solution and to the CO<sub>2</sub> itself being a weak Lewis acid.

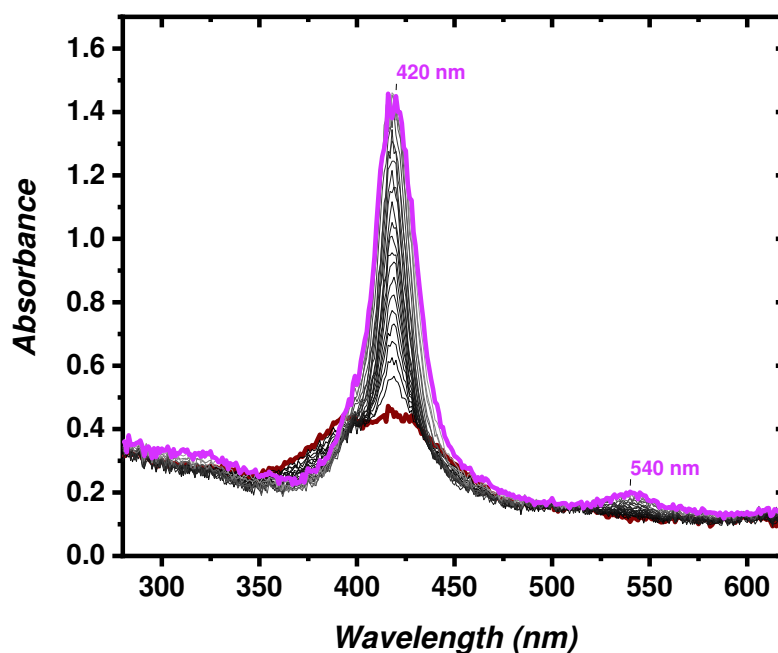


Figure 7.13. UV-Vis spectra of **8** (brown) and **9** (purple) which was obtained after generation of CO at  $E = -2.0$  V vs SCE and after setting back the potential at  $E = -1.0$  V vs SCE while keeping the solution tightly closed in the same setup.

- Dark grey lines show the gradual formation of **9**

### 7.3.2 IR Spectroelectrochemistry

In order to complement this data, preliminary measurements were performed by *in situ* middle-infrared (mid-IR) spectroelectrochemistry on [Fe<sup>III</sup>(TPP)]Cl in DMF and its electroreduced species. Experimental conditions and data acquisition mode were similar to the ones required to collect UV-Vis spectroelectrochemical data, however, measurements were performed at the AILES beamline of synchrotron SOLEIL. The description of this beamline as well as experimental details are given in appendix B. The setup developed in collaboration with the AILES beamline scientists is described in appendix D.

Figure 7.14 shows the IR spectra collected on a DMF solution of [Fe<sup>III</sup>(TPP)]Cl poised at  $E = -2.2$  V vs Ag/Ag<sup>+</sup> under a CO<sub>2</sub> atmosphere (figure 7.14 - brown). A signature is present around 2325 cm<sup>-1</sup>, which has been previously attributed to the presence of CO<sub>2</sub> in solution.<sup>13</sup> In addition to this, two bands at 1881 cm<sup>-1</sup> and at 1915 cm<sup>-1</sup> are present. While keeping the solution in the same experimental setup, the potential was set back to  $E = -0.8$  V vs Ag/Ag<sup>+</sup> (corresponding to the formation of the [Fe<sup>I</sup>(TPP)] species). Under these conditions, a new band appears at 1953 cm<sup>-1</sup>, while the bands at 1881 cm<sup>-1</sup> and 1915 cm<sup>-1</sup> disappear (figure 7.14 - purple). Croisy *et al.* performed IR measurements on a solution of an iron porphyrin complex in benzonitrile + 0.24 M 1-methylimidazole, poised at  $E = -0.6$  V vs SCE under CO.

They observed a band at 1966 cm<sup>-1</sup>, which they assigned to the formation of an Fe(II)-CO complex.<sup>12</sup> This supports the attribution of the band observed at 1953 cm<sup>-1</sup> to an [Fe<sup>II</sup>(TPP)(CO)], which is also corroborated by the UV-Vis spectroelectrochemical measurements presented above. In these preliminary studies we have not addressed yet the nature of the bands at 1881 cm<sup>-1</sup> and 1915 cm<sup>-1</sup>. However, these results show the relevance of IR spectroelectrochemical methods to describe the structure of iron porphyrins during the catalytic reduction of CO<sub>2</sub>.

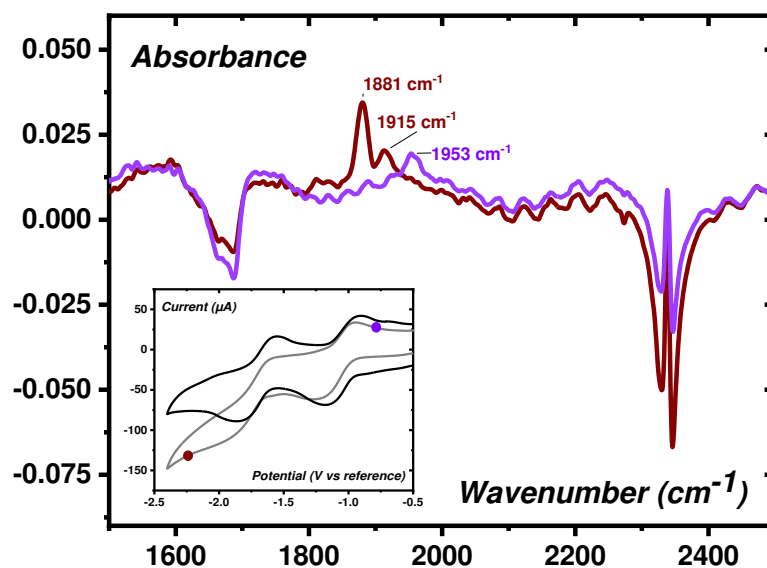


**Figure 7.14** *In situ* mid-IR spectroelectrochemical measurements performed on [Fe<sup>III</sup>(TPP)]Cl in DMF + 0.1M TBAPF<sub>6</sub> under CO<sub>2</sub>. The data were recorded at the AILES beamline of synchrotron SOLEIL, while performing controlled potential electrolysis (CPE) at  $E = -2.2$  V vs Ag/Ag<sup>+</sup> (brown) and subsequently at  $-0.8$  V vs Ag/Ag<sup>+</sup> on the same sample solution. **Insert:** CV recorded under argon (black) and CO<sub>2</sub> (grey) in the spectroelectrochemical cell.

- Dots indicate the potential in which CPE was performed to obtain the corresponding spectra.

- Only the last two waves of the iron porphyrin are shown in the inserted CV.

## 7.4. Discussion

Given the results presented in this chapter, we can conclude that at the Fe<sup>III</sup> and Fe<sup>II</sup> oxidation states, no significant structural or electronic changes are observed due to the presence of CO<sub>2</sub>. This is not true for more reduced species. The two-electron reduced species presents a XANES spectrum that is different from the one under argon, with a pre-edge region that misses the shoulder at 7118.0 eV, attributed to a deviation from the square planar geometry and suggesting an interaction of the metal center with the CO<sub>2</sub>. The UV-Vis spectrum obtained under these conditions is, however, almost identical to the one obtained under argon suggesting that such interaction with CO<sub>2</sub> is loose and that no bond is formed.

When reduced with a third electron, more prominent differences can be observed for the porphyrin, both in XANES and UV-Visible spectra, when compared to the argon atmosphere conditions. The pre-edge region of the XANES spectrum is clearly different, not only by the disappearance of the shoulder at 7118.0 eV, but also by the shift of the pre-edge peak present at 7112.2 eV under argon and at 7113.1 eV under CO<sub>2</sub>. Moreover, the main edge position lies 1.7 eV higher in energy than for the data under argon, which suggests that the iron center donates some of the electronic density to the CO<sub>2</sub>, supporting its coordination. The UV-Visible data is also very different from the one obtained under argon. These results suggest that, under these conditions, CO<sub>2</sub> is binding to the iron center. The disappearance of the peak at 7118.0 eV in the pre-edge region of the XANES spectrum supports a deviation from the square-planar geometry, consistent with a square pyramidal geometry with CO<sub>2</sub> bound to iron and sitting on top of the porphyrin plane.

Finally, UV-Vis and IR spectroelectrochemical measurements performed by setting back the potential from a value where catalysis occurs ( $E = -2.2$  V vs. Ag/Ag<sup>+</sup>) to a value where Fe(II) species is stable ( $E = -0.8$  V vs. Ag/Ag<sup>+</sup>) evidencing the formation of the [Fe<sup>II</sup>(TPP)(CO)] adduct. This was possible since (i) CO<sub>2</sub> reduction initially occurs at negative potentials, generating CO and (ii) the solution was maintained in the same sample compartment, allowing for the direct reoxidation of the Fe species. A similar experiment is envisaged to obtain the signature of the [Fe<sup>II</sup>(TPP)(CO)] by XANES, as further discussed in next chapter, in order to enlarge the dataset of reference XANES spectra.

Considering all the results presented in chapter VI (related to the spectroelectrochemical reduction of iron porphyrins under inert conditions) and in the present chapter, we will provide a discussion on the reaction mechanism and perspectives of this project in the next chapter.

## 7.5 References chapter VII

- (1) Roy, L.; Mondal, B.; Neese, F.; Ye, S. Chapter 5: Theoretical Approach to Homogeneous Catalytic Reduction of CO<sub>2</sub>: Mechanistic Understanding to Build New Catalysts. In *Carbon Dioxide Electrochemistry*; **2020**; pp 197–225.
- (2) Lamberti, C.; van Bokhoven, J. A. X-Ray Absorption and Emission Spectroscopy for Catalysis. In *X-Ray Absorption and X-Ray Emission Spectroscopy*; John Wiley & Sons, Ltd, **2016**; pp 351–383.
- (3) Hammouche, M.; Lexa, D.; Savéant, J.-M.; Momenteau, M. Catalysis of the Electrochemical Reduction of Carbon Dioxide by Iron(“0”) Porphyrins. *J. Electroanal. Chem. Interfac. Electrochem.* **1988**, *249* (1), 347–351.
- (4) Bhugun, I.; Lexa, D.; Savéant, J.-M. Catalysis of the Electrochemical Reduction of Carbon Dioxide by Iron(0) Porphyrins: Synergistic Effect of Weak Brönsted Acids. *J. Am. Chem. Soc.* **1996**, *118* (7), 1769–1776.
- (5) Hammouche, M.; Lexa, D.; Momenteau, M.; Savéant, J.-M. Chemical Catalysis of Electrochemical Reactions. Homogeneous Catalysis of the Electrochemical Reduction of Carbon Dioxide by Iron(“0”) Porphyrins. Role of the Addition of Magnesium Cations. *J. Am. Chem. Soc.* **1991**, *113* (22), 8455–8466.
- (6) Bhugun, I.; Lexa, D.; Savéant, J.-M. Ultraefficient Selective Homogeneous Catalysis of the Electrochemical Reduction of Carbon Dioxide by an Iron(0) Porphyrin Associated with a Weak Brönsted Acid Cocatalyst. *J. Am. Chem. Soc.* **1994**, *116* (11), 5015–5016.
- (7) Hammouche, M.; Lexa, D.; Momenteau, M.; Savéant, J.-M. Chemical Catalysis of Electrochemical Reactions. Homogeneous Catalysis of the Electrochemical Reduction of Carbon Dioxide by Iron(“0”) Porphyrins. Role of the Addition of Magnesium Cations. *J. Am. Chem. Soc.* **1991**, *113* (22), 8455–8466.
- (8) Lu, X.; Ahsaine, H. A.; Dereli, B.; Garcia-Esparza, A. T.; Reinhard, M.; Shinagawa, T.; Li, D.; Adil, K.; Tchalala, M. R.; Kroll, T.; Eddaoudi, M.; Sokaras, D.; Cavallo, L.; Takanabe, K. Operando Elucidation on the Working State of Immobilized Fluorinated Iron Porphyrin for Selective Aqueous Electroreduction of CO<sub>2</sub> to CO. *ACS Catal.* **2021**, *11* (11), 6499–6509.
- (9) Masaoka, S.; Kosugi, K.; Kondo, M. Quick and Easy Method for Dramatic Improvement of the Electrochemical CO<sub>2</sub> Reduction Activity of an Iron Porphyrin Complex. *Angew. Chem. Int. Ed.* **2021**, *60*, 22070–22074.
- (10) Bonin, J.; Chaussemier, M.; Robert, M.; Routier, M. Homogeneous Photocatalytic Reduction of CO<sub>2</sub> to CO Using Iron(0) Porphyrin Catalysts: Mechanism and Intrinsic Limitations. *ChemCatChem* **2014**, *6* (11), 3200–3207.
- (11) Balducci, G.; Chottard, G.; Gueutin, C.; Lexa, D.; Savéant, J.-M. Electrochemistry of Iron(I) Porphyrins in the Presence of Carbon Monoxide. Comparison with Zinc Porphyrins. *Inorg. Chem.* **1994**, *33* (9), 1972–1978.





- (12) Croisy, Alain.; Lexa, Doris.; Momenteau, Michel.; Savéant, J.-M. Integrated Molecular Systems. Fixation of Carbon Monoxide on Iron(I) in Simple and Superstructured Porphyrins. *Organometallics* **1985**, 4 (9), 1574–1579.
- (13) Bunea, S.; Urakawa, A. Chapter 9: In Situ Spectroscopic Methods to Study Electrochemical CO<sub>2</sub> Reduction. In *Carbon Dioxide Electrochemistry*; **2020**; pp 347–407.

# Chapter VIII

---

## Conclusions and Perspectives

### Content

---

8.1	Key findings .....	131
8.2	Perspectives .....	138
8.3	Final outlook.....	140
8.4	References .....	142



## 8.1 Key findings

### *- Development of an X-Ray spectroelectrochemical cell*

In the present project, we have developed and optimized a custom-made X-Ray spectroelectrochemical cell, which has been used for acquiring XANES data under vacuum conditions in low concentrated solutions, minimizing any effect from radiation damage. We have shown in chapter V, that in order to achieve an optimal measurement, various parameters must be simultaneously fulfilled. In particular, a thin layer configuration was used to favor an excellent conversion rate of 96 %.

### *- Spectroelectrochemical studies on the [Fe<sup>III</sup>(TPP)]Cl system and its electroreduced species under argon.*

With our custom-made cell, we collected *in situ* XANES spectra of the [Fe<sup>III</sup>(TPP)]Cl complex in DMF, together with its one, two and three electroreduced species, both under argon and CO<sub>2</sub> atmospheres. Under argon atmosphere, these results provide information on the electronic structure of the generated species (table 8.1) based on a qualitative analysis of the XANES data, leading to the following conclusions:

- [Fe<sup>III</sup>(TPP)]Cl in DMF, complex **1**, has the same electronic configuration that in its solid state, *i.e.* a high spin square pyramidal complex with a chloride coordinating the iron center as axial ligand.<sup>1</sup>

- When one electron is transferred to [Fe<sup>III</sup>(TPP)]Cl in DMF to generate complex **2a**, few changes were observed as compared to the initial species. Analyzing the XANES data and the literature, we concluded that, while the chemically generated solid sample has an intermediate spin state,<sup>2,3</sup> in DMF complex **2a** is in a low spin configuration due to the coordination of DMF to the iron center. Although the comparison with the low spin iron(II) porphyrin reported by Wilson *et al.*<sup>3</sup> (which bears two pyridine moieties as axial ligands) supports the presence of two DMF molecules in **2a**, there is no final evidence at this point for the number of DMF molecules coordinated. Therefore, two or one DMF ligands can be expected.

- Reduction with two and three electrons leads to complexes **3** and **4**, respectively, and is accompanied by slight shifts of the main edge position towards lower energies. These shifts are, however, very small (0.7 eV for complex **3** and 0.3 eV for complex **4**), indicating that the additional electrons are not solely localized on the metal center, but partly distributed on the aromatic system of the porphyrin ligand. Owing to these data, species **3** and **4** can be represented by a superimposition of several mesomeric forms as presented in table 8.1. The feature observed in the spectra of these species at 7118 eV, can be attributed to a *1s* to *4p<sub>z</sub>* transition and is indicative of a square planar geometry. The appearance of this transition for

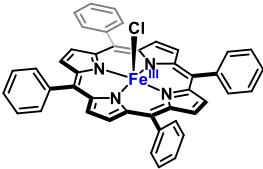
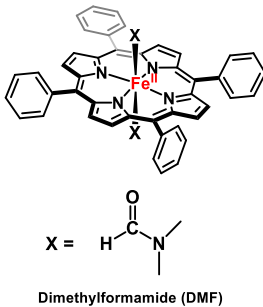
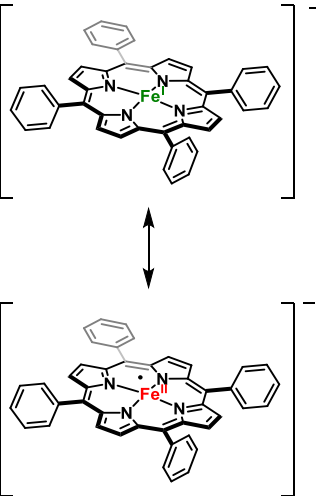
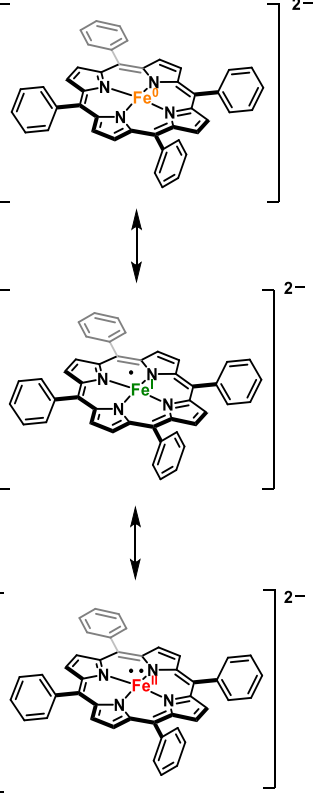


complexes **3** and **4** indicates that these two species are in a square planar geometry. It implies the absence of any DMF coordinating the metal center which can be explained by the increasingly negative charge of the complexes as they are reduced.

- The results shown in this thesis highlight the importance of considering the solvent to precisely describe the structure of reduced iron porphyrin species in solution. Spectroscopic analysis performed in the solid state cannot adequately describe the structures in homogeneous conditions and could not be taken as final proof of the complex electronic structures. DFT calculations, if used to describe such structures, should also include explicit solvent molecules.

- Our complete set of data for the reduced complexes indicates that the electronic density is likely shared between the metal and the ligand for the doubly and triply reduced species, contrary to recent claims that describe a reduction occurring rather at the ligand only.<sup>2</sup>

**Table 8.1.** [Fe<sup>III</sup>(TPP)]Cl – complex *1*, and its successive one electron (complex *2a*), two electron (complex *3*) and three electron (complex *4*) reduced species proposed structures, with their XANES (main edge and pre-edge energy position) and UV-Vis data ( $\lambda_{\max}$  of the Soret and Q-bands) in DMF + 0.1 M TBAPF<sub>6</sub> under argon atmosphere.

Complex	<i>1</i> [Fe <sup>III</sup> (TPP)]Cl	<i>2a</i> [Fe <sup>III</sup> (TPP)]Cl + 1e <sup>-</sup>	<i>3</i> [Fe <sup>III</sup> (TPP)]Cl + 2e <sup>-</sup>	<i>4</i> [Fe <sup>III</sup> (TPP)]Cl + 3e <sup>-</sup>
Proposed structures				
Pre-edge peak energy position (eV)*	7112.6	7112.2	7112.2	7112.2
Main edge energy position (eV)‡	7123.0	7123.0	7122.3	7122.0
$\lambda_{\max}$ Soret band (nm)	417	432	392 and 425	362 and 433
$\lambda_{\max}$ Q-bands (nm)	509 and 575	530, 565 and 608	510, 575 and 608	514 and 607

- Complex *2a* is represented with the coordination of two DMF solvent molecules in comparison with XANES reported data.<sup>3</sup> However, the coordination number of species *2a* has not been determined. Therefore, one or two solvent molecules may be present.

\* Pre-edge peak energy position measured at the 1<sup>st</sup> inflection point of the pre-edge peak

‡ Main absorption edge energy position measured at the half the intensity of the normalized spectrum

**- Spectroelectrochemical studies on the  $[\text{Fe}^{\text{III}}(\text{TPP})]\text{Cl}$  and its electroreduced species in the presence of  $\text{CO}_2$**

In the presence of  $\text{CO}_2$ , the XAS, UV-Vis and IR spectra collected *in situ* allow to conclude on the following points:

- The XANES and UV-Vis spectroelectrochemical data collected on the initial complex in DMF and in the presence of  $\text{CO}_2$ ,  $[\text{Fe}^{\text{III}}(\text{TPP})]\text{Cl}$ , named **5**, and its one electron reduced species, complex **6**, do not show any changes as compared to the data collected under argon atmosphere. There are no interactions between  $[\text{Fe}^{\text{III}}(\text{TPP})]\text{Cl}$  and its one electron reduction species and  $\text{CO}_2$ .

- However, when the  $[\text{Fe}^{\text{III}}(\text{TPP})]\text{Cl}$  is reduced by two electrons in the presence of  $\text{CO}_2$  to generate complex **7**, the shoulder at 7118 eV, which is indicative of a square planar geometry, disappears, suggesting a possible interaction between  $\text{CO}_2$  and the iron centre. Since almost no differences are detected by UV-Vis between the argon and the  $\text{CO}_2$  data, we proposed that this interaction is weak.

- When  $[\text{Fe}^{\text{III}}(\text{TPP})]\text{Cl}$  is reduced with 3 electrons under  $\text{CO}_2$  atmosphere to yield complex **8**, significant differences are observed in the XANES data. A decrease of the pre-edge intensity as well as the disappearance of the shoulder at 7118 eV suggest a deviation from the square-planar geometry. In addition to this, a shift of the main edge towards higher energies (0.7 eV when compared with **5**) was also observed. This is consistent with  $\text{CO}_2$  binding to the Fe center, and concomitant electronic density donation from the metal to the  $\text{CO}_2$ . We conclude that  $\text{CO}_2$  is coordinated to the metal center. Overall, our data point toward the description of the bound  $\text{CO}_2$  complex by the combination of the mesomeric electronic structures  $[\text{Fe}^{\text{II}}(\text{TPP})(\text{CO}_2^{\bullet-})]^{2-} \leftrightarrow [\text{Fe}^{\text{I}}(\text{TPP})(\text{CO}_2^{\bullet-})]^{2-}$ , as shown in table 8.2.

- After performing control potential electrolysis in a solution of  $[\text{Fe}^{\text{III}}(\text{TPP})]\text{Cl}$  at  $E = -2.0$  V vs SCE in the presence of  $\text{CO}_2$ , the potential was switched to  $E = -1.0$  V vs SCE while maintaining the setup tightly closed. A newly formed species, named **9**, features Soret and Q-bands similar to those reported for Fe(II) porphyrin adduct with CO.<sup>4,5</sup> These results were further confirmed by *in situ* IR spectroelectrochemistry, with the appearance of bands at 1953  $\text{cm}^{-1}$ , closely matching previous reports for other iron porphyrin complex.<sup>5</sup> This set of data provides useful fingerprint for future identification of CO adducts with iron porphyrins by XANES, and it also confirms that CO was formed during electrolysis at  $E = -2$  V vs SCE.

**Table 8.2.**  $[\text{Fe}^{\text{III}}(\text{TPP})]\text{Cl}$  – complex **5**, and its successive one electron (complex **6**), two electron (complex **7**) and three electron (complex **8**) reduced species proposed structures, with their XANES (main edge and pre-edge energy position) and UV-Vis data ( $\lambda_{\text{max}}$  of the Soret and Q-bands) in DMF + 0.1 M TBAPF<sub>6</sub> under CO<sub>2</sub> atmosphere. The *in situ* generated species **9** is also included for comparison.

Complex	<b>5</b> $[\text{Fe}^{\text{III}}(\text{TPP})]\text{Cl}$	<b>6</b> $[\text{Fe}^{\text{III}}(\text{TPP})]\text{Cl} + 1\text{e}^-$	<b>7</b> $[\text{Fe}^{\text{III}}(\text{TPP})]\text{Cl} + 2\text{e}^-$	<b>8</b> $[\text{Fe}^{\text{III}}(\text{TPP})]\text{Cl} + 3\text{e}^-$	<b>9</b>
Proposed structures					
Pre-edge peak energy position (eV)*	7112.6	7112.1	7112.1	7113.1	-
Main edge energy position (eV)‡	7123.0	7123.0	7123.0	7123.7	-
$\lambda_{\text{max}}$ Soret band (nm)	417	430	392 and 427	395 and 424	420
$\lambda_{\text{max}}$ Q-bands (nm)	508 and 575	535, 567 and 609	510, 573 and 608	510, 575 and 608	540
IR band (cm <sup>-1</sup> )	-	-	-	-	1953

- Complex **6** is represented as for **2a** with the coordination of two DMF solvent molecules in comparison with XANES reported data.<sup>3</sup> However, the coordination number of species **6** has not been determined. Therefore, one or two solvent molecules may be suggested.

\* Pre-edge peak energy position measured at the 1<sup>st</sup> inflection point of the pre-edge peak

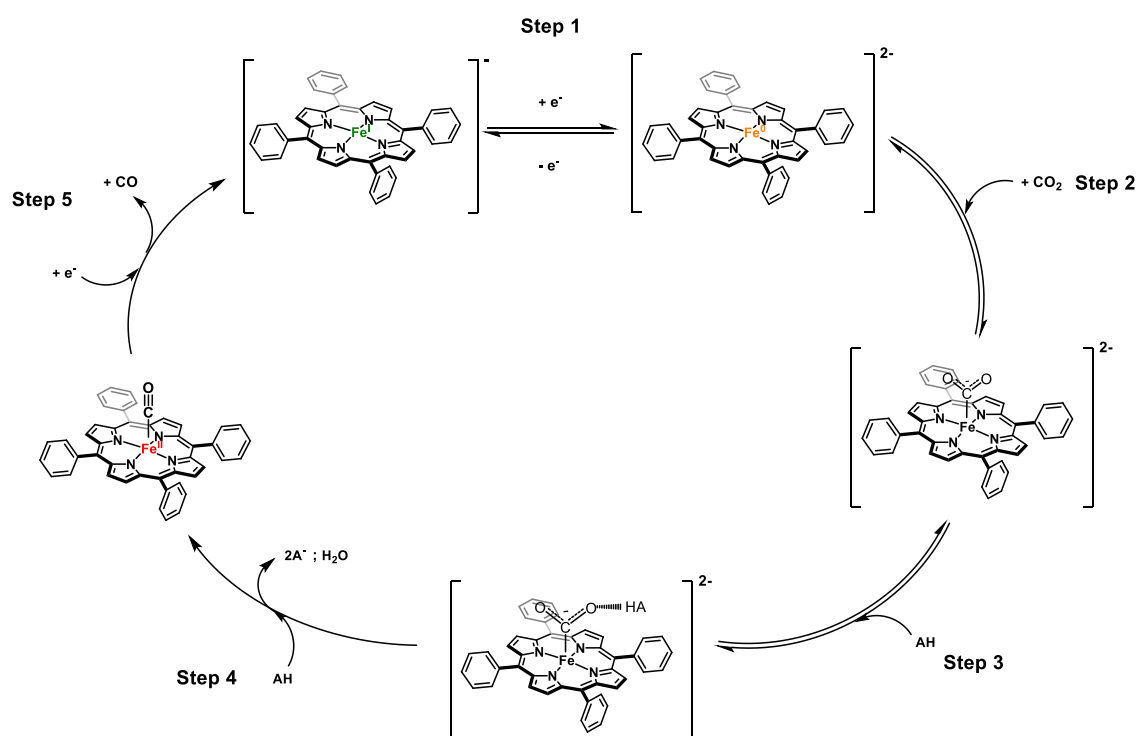
‡ Main absorption edge energy position measured at the half the intensity of the normalized spectrum





- *CO<sub>2</sub> reduction into CO by iron tetraphenyl porphyrin – Discussion on the mechanism*

As commented in chapter II, many kinetic parameters have been determined for the electrocatalytic reduction of CO<sub>2</sub> into CO by [Fe<sup>III</sup>(TPP)]Cl in homogeneous conditions by J.-M. Savéant and his colleagues,<sup>6-8</sup> leading to the following mechanism (scheme 8.1), described in chapter II.



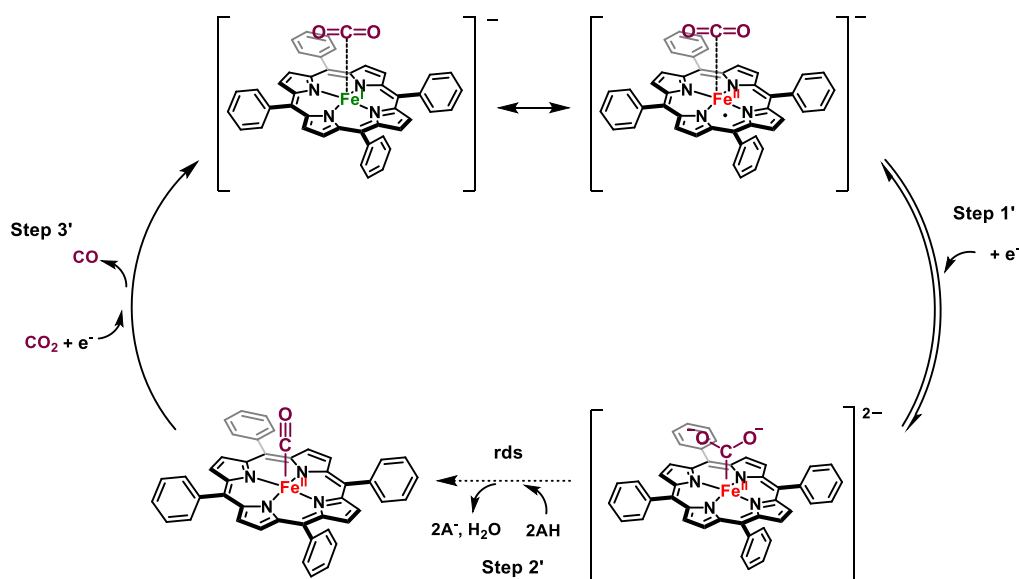
**Scheme 8.1. Proposed mechanism for electrocatalytic reduction of CO<sub>2</sub> into CO by iron tetraphenyl porphyrin chloride in aprotic media in the presence of an acid.**

*Adapted from A. Tatin's thesis – Université Paris-Diderot.<sup>7</sup>*

The acid concentration is pivotal in driving the reaction. It has been shown that, at low concentration of acid, the rate determining step (rds) of the process is the breaking of the C-O bond in step 4, while CO<sub>2</sub> binding and adduct stabilization through H-bonding act as pre-equilibrium (overall, the reaction is second order towards the acid).<sup>9</sup> At high acid concentration (e.g phenol 3 M), cleavage becomes so fast that the coordination of CO<sub>2</sub> in step 2 becomes the rds.<sup>9,11,12</sup> In our work, spectroscopic data were collected on complex **8** at -2.0 V vs. SCE with a low concentration of acid (no proton source added and only residual water present (*ca.* 20-30 mM in DMF)).<sup>10</sup> In such conditions, we also need to consider the Lewis acidity of the CO<sub>2</sub> itself, which is highly concentrated (0.2 M).<sup>13,14</sup> In these conditions, the rate-limiting step in the CO<sub>2</sub> reduction reaction is considered to be the C-O bond breaking. Hence, the experimental observation of the [Fe<sup>II</sup>(TPP)(CO<sub>2</sub><sup>2-</sup>)]<sup>2-</sup> ↔ [Fe<sup>I</sup>(TPP)(CO<sub>2</sub><sup>•-</sup>)]<sup>2-</sup> species obtained at highly negative potentials and in the presence of CO<sub>2</sub> is consistent with

such kinetic conditions. Our observations provide direct evidence for the coordination of CO<sub>2</sub> to the Fe ion in the triply reduced form of [Fe<sup>III</sup>(TPP)]Cl and demonstrate that, despite an electronic density partly localized on the porphyrin ligand ([Fe<sup>0</sup>(TPP)]<sup>2-</sup> ↔ [Fe<sup>I</sup>(TPP<sup>\*</sup>)]<sup>2-</sup> ↔ [Fe<sup>II</sup>(TPP<sup>\*\*</sup>)]<sup>2-</sup>), CO<sub>2</sub> binding and reduction occurs at the metallic center. It additionally suggests that the electronic density is reallocated at the metal upon CO<sub>2</sub> coordination.

Based on the different observations reported in this document, a simplified mechanism, relying on spectroelectrochemical data, is proposed in scheme 8.2.



**Scheme 8.2. Simplified mechanism for the electrocatalytic reduction of CO<sub>2</sub> into CO by iron tetraphenyl porphyrin in the presence of a low amount of protons based on the spectroelectrochemical evidences presented in this manuscript.**

- Considering that a low amount of protons is available in these conditions (residual water – AH), the role of CO<sub>2</sub> as Lewis acid cannot be excluded. Indeed, the reaction of CO<sub>2</sub> from the solution with a CO<sub>2</sub> molecule bound to a reduced Fe center is known to produce CO and CO<sub>3</sub><sup>2-</sup>.<sup>8,15</sup>

The mechanism can be summarized in the following steps:

- **Step 1'**

The doubly reduced porphyrin ([Fe<sup>I</sup>(TPP)]<sup>-</sup> ↔ [Fe<sup>II</sup>(TPP<sup>\*</sup>)]<sup>-</sup>) weakly interacts with CO<sub>2</sub>. One electron reduction of this species furnishes **8** whose mesomeric forms include a Fe(I) complex bound to an asymmetric CO<sub>2</sub> radical and a Fe(II) complex coordinated to a symmetric, doubly charged CO<sub>2</sub>. XANES data suggest that the later structure is more probable, at least under the conditions in which the *in situ* experiments were performed. *In situ* spectroelectrochemical measurements presented in this manuscript also suggest that CO<sub>2</sub> activation occurs at the metal center with reallocation of the electronic density at the metal upon CO<sub>2</sub> coordination.

- **Step 2'**

Weakening of the C-O bond due to the presence of acid (residual water, or CO<sub>2</sub> acting as Lewis acid) leads to bond breaking, and this is the rate determining step of the process, since Fe-CO<sub>2</sub> adduct can be accumulated and spectroscopically characterized. We do not exclude the possibility that the generated spectra are due to mixed species obtained during catalytic reduction. However, we suggest that the major fraction of species observed in our experimental conditions is the Fe-CO<sub>2</sub> adduct.

- **Step 3'**

CO formation during electrolysis of [Fe<sup>III</sup>(TPP)]Cl at  $E = -2.0$  V vs SCE was confirmed by *in situ* spectroelectrochemical methods. UV-Vis and IR experiments allowed to observe the adduct formed between CO and Fe(II) porphyrin, which was generated upon increasing the potential at a value of  $E = -1.0$  V vs SCE after electrolysis.

These findings provide complementary evidence, based on spectroscopic data, for the electrocatalytic mechanism of CO<sub>2</sub>-reducing molecular electrocatalysts by iron porphyrins. It also offers a XANES library of species obtained during electroreduction but also in the presence of CO<sub>2</sub>. These unprecedented data are precious and open a path for further experimental studies, as described below.

## 8.2 Perspectives

- ***In situ* determination of the [Fe<sup>II</sup>(TPP)(CO)] adduct by XANES spectroelectrochemistry**

During this project, we firstly envisioned to obtain a reference spectrum for the [Fe<sup>II</sup>(TPP)(CO)] species, by electrogenerating [Fe<sup>II</sup>(TPP)] in the presence of CO. In order to do that, a complete setup was developed to control the dissolution of CO in DMF. The description of this setup is presented in appendix D (cell B). First trials were performed on the SAMBA beamline in the synchrotron SOLEIL. Cyclic voltammogram (appendix D – figure D.4) indicates the presence of CO in interaction with iron porphyrin in solution with the shift of the reversible Fe<sup>II</sup>/Fe<sup>I</sup> wave, as described in chapter II.<sup>10,11</sup> Due to the design of the cell used on SAMBA, the XANES spectrum of the [Fe<sup>II</sup>(TPP)(CO)] obtained does not represent a pure species, but likely a mixture.

We therefore plan a future experiment on the LUCIA beamline using the same cell as the one produced the data shown in this manuscript. In this experiment, the [Fe<sup>III</sup>(TPP)]Cl will first be electroreduced by three electrons under CO<sub>2</sub> in the cell A at LUCIA beamline (under vacuum). After approximately 20 minutes of electrolysis, the same time that was required by UV-Vis and IR spectroelectrochemical measurements, the potential will be set at  $E = -1.0$  V

vs SCE while XANES spectra will be recorded. Based on previous results obtained by UV-Vis and IR spectroelectrochemistry, the obtained spectra should correspond to  $[\text{Fe}^{\text{II}}(\text{TPP})(\text{CO})]$ , issued from the coordination of the Fe(II) generated species with the CO produced *during* electroreduction of  $\text{CO}_2$ .

Direct acquisition of the Fe-CO adduct spectrum upon reacting CO with electrogenerated Fe(II) would be useful to complete the spectroscopic library of species involved in the  $\text{CO}_2$  reduction reaction. It will serve as signature for future *operando* measurements and for linear combination fitting analysis.

-  **$\text{CO}_2$  binding mode determination by IR spectroelectrochemistry**

Infrared spectroscopy has been widely used to study the  $\text{CO}_2$  reduction reaction mechanism by different molecular catalysts as briefly discussed in chapter III and more extensively in references 16 and 17.<sup>16,17</sup> However, fewer studies have been performed on iron porphyrins so far, as briefly discussed in chapter IV.

As presented in chapter VII and discussed in the present chapter, preliminary *in situ/operando* IR spectroelectrochemical measurements on iron porphyrins were performed in this project. A signature for the triply reduced  $[\text{Fe}^{\text{III}}(\text{TPP})]\text{Cl}$  in the presence of  $\text{CO}_2$  was obtained. Further experiments showed that CO was formed under catalytic potentials, since the *in situ* formation of the  $[\text{Fe}^{\text{II}}(\text{TPP})(\text{CO})]$  adduct, was observed at a potential  $E = -1.0 \text{ V vs SCE}$ . These experiments open the path to further studies:

1. *In situ* IR spectroelectrochemistry can be used to study the interaction between the  $[\text{Fe}^{\text{III}}(\text{TPP})]\text{Cl} + 2e^-$  and the  $\text{CO}_2$ , complementing the *in situ* UV-Vis and XANES data already collected.
2. The exploration of how the  $\text{CO}_2$  binds the metal center may also be addressed by IR spectroelectrochemistry. We have considered so far that  $\text{CO}_2$  binds in the  $\eta^1\text{-C}$  coordination mode to the iron center (see chapter IV). IR spectroscopy will help deciphering the exact coordination modes.
3. This technique can also be used to follow the formation of carbonates.  $\text{CO}_2$  is a Lewis acid, generating CO and  $\text{CO}_3^{2-}$  as products in the absence of additional proton source. IR spectroelectrochemistry has already been used to describe the metal-carbonate species with signatures between  $1300 - 1600 \text{ cm}^{-1}$ .<sup>17</sup> Therefore, it can be used in iron porphyrin solutions to follow the formation of related species.
4. Far-IR studies can ultimately be used to probe the direct bonding between Fe and the  $\text{CO}_2$ .

#### - Extended X-Ray Absorption fine structure (EXAFS) measurements

As discussed in chapter III, EXAFS can be used to follow structural changes at the element of interest, such as ligand binding. Therefore, performing *in situ* or *operando* EXAFS measurements on iron porphyrins in aprotic solutions could give further insights on the interactions of CO<sub>2</sub> with the metal center, complementing the XANES data. The arrival or departure of ligands (such as CO<sub>2</sub>) could be probed, as well as the determination of bond distances between the metal and the substrate or products. Modifications within the porphyrin structure (contraction, bending, metal position in the plane, etc) could also be tracked. However, due to the longer recording times required by EXAFS, radiation-induced damage must be carefully controlled and limited. For this reason, further optimization of the set-up and data recording procedure must be performed in order to allow for the acquisition of relevant data.

#### - Density functional theory (DFT) calculations

Quantum chemistry can be used as a complementary technique.<sup>12,19</sup> Neese and his team have recently shown examples in which theoretical calculations were used to support experimental data obtained on iron porphyrins in the solid state through XANES, Mössbauer and Raman spectroscopy.<sup>2,20</sup> Pre-edge analysis is also gaining more attention in the late years through density functional theory with the development of new data analysis softwares.<sup>21,22</sup> However, after showing in this manuscript the role that the solvent plays in the spectroscopic data and the species associated to it, the use of explicit solvent molecules should be systematically considered when performing theoretical calculations.

### 8.3. Final outlook

One important aspect to address by *in situ/operando* techniques is the comparison of the data presented in this manuscript for the FeTPP model system, with those obtained for more efficient catalysts, such as the ones described in chapter II (section 2.2.3). This comparison will, ultimately, improve our knowledge of the catalysts' efficiency and provide guidelines for their improvement.

By using, for instance the CAT catalyst (scheme 2.5), we could probe the changes occurring by IR spectroelectrochemistry, in order to have a spectroscopic evidence of the proposed Fe-CO<sub>2</sub> adduct, such as the one described in scheme 2.4, and compare these results with the one obtained for FeTPP. This could confirm the ability of substituents to influence the coordination of CO<sub>2</sub> (and its reduction products) to iron. EXAFS could also be used to determine bond distances (particularly the one between CO<sub>2</sub> and the iron) in catalytic intermediates with and without substituents.



Another catalyst with high efficiency and long-term stability bearing trimethylanilinium groups in meso positions of the porphyrin (Fe-o-TMA, see scheme 2.6) could benefit from such studies, to distinguish the geometric and electronic effects of the substituents. Other macrocycles bearing abundant metals, such as cobalt phthalocyanines, which has shown recently interesting results towards the production of methanol<sup>23</sup> or high CO rates,<sup>24</sup> could also benefit from spectroelectrochemical measurements. This catalyst, however, has shown high efficiency by being immobilized on carbon materials. Therefore, the understanding of the surfaces modifications and catalytic film characterization is an interesting point to consider.

Ultimately, performing experiments in water is an important targeted towards applicability of these catalysts. Therefore, determining which are the mechanistic modifications occurring in the presence of this solvent and the pH effect are necessary. A starting point on this topic was address at the beginning of chapter VI. However, more efficient catalyst under aqueous solutions, such as Fe-o-TMA or Fe-p-TMA (chapter II) should be used.

The contribution of spectroscopic techniques to improve the understanding of electrochemical reactions should be emphasized. This complementarity could ultimately provide relationships between the structural changes and the catalyst activity for many electrocatalysts and thus help in the design of molecular catalysts with high performances.

Finally, the combination of spectroscopic techniques with product detection methods, such as *in situ* gas chromatography (GC) or gas chromatography/mass spectrometry (GC/MS), could be of great interest. For instance, the development and optimization of a setup that could address concomitantly electronic structures changes and CO<sub>2</sub>/CO (de)-coordination while determining *in situ* the product generation would allow correlating the formation of a given product with a specific catalytic intermediate.

## 8.4 References Chapter VIII

- (1) Paulat, F.; Lehnert, N. Detailed Assignment of the Magnetic Circular Dichroism and UV–vis Spectra of Five-Coordinate High-Spin Ferric [Fe(TPP)(Cl)]. *Inorg. Chem.* **2008**, *47* (11), 4963–4976.
- (2) Römelt, C.; Song, J.; Tarrago, M.; Rees, J. A.; van Gestel, M.; Weyhermüller, T.; DeBeer, S.; Bill, E.; Neese, F.; Ye, S. Electronic Structure of a Formal Iron(0) Porphyrin Complex Relevant to CO<sub>2</sub> Reduction. *Inorg. Chem.* **2017**, *56* (8), 4745–4750.
- (3) Wilson, S. A.; Green, E.; Mathews, I. I.; Benfatto, M.; Hodgson, K. O.; Hedman, B.; Sarangi, R. X-Ray Absorption Spectroscopic Investigation of the Electronic Structure Differences in Solution and Crystalline Oxyhemoglobin. *PNAS* **2013**, *110* (41), 16333–16338.
- (4) Bonin, J.; Chaussemier, M.; Robert, M.; Routier, M. Homogeneous Photocatalytic Reduction of CO<sub>2</sub> to CO Using Iron(0) Porphyrin Catalysts: Mechanism and Intrinsic Limitations. *ChemCatChem* **2014**, *6* (11), 3200–3207.
- (5) Croisy, Alain.; Lexa, Doris.; Momenteau, Michel.; Savéant, J.M. Integrated Molecular Systems. Fixation of Carbon Monoxide on Iron(I) in Simple and Superstructured Porphyrins. *Organometallics* **1985**, *4* (9), 1574–1579.
- (6) Costentin, C.; Drouet, S.; Passard, G.; Robert, M.; Savéant, J.M. Proton-Coupled Electron Transfer Cleavage of Heavy-Atom Bonds in Electrocatalytic Processes. Cleavage of a C–O Bond in the Catalyzed Electrochemical Reduction of CO<sub>2</sub>. *J. Am. Chem. Soc.* **2013**, *135*, 24, 9023–9031.
- (7) Tatin, A. Electrochemical CO<sub>2</sub> Splitting into CO and O<sub>2</sub> in Neutral Water Using Earth-Abundant Materials. Doctoral thesis. Université Paris Diderot. **2016**.
- (8) Bhugun, I.; Lexa, D.; Savéant, J.M. Catalysis of the Electrochemical Reduction of Carbon Dioxide by Iron(0) Porphyrins: Synergistic Effect of Weak Brönsted Acids. *J. Am. Chem. Soc.* **1996**, *118* (7), 1769–1776.
- (9) Francke, R.; Schille, B.; Roemelt, M. Homogeneously Catalyzed Electroreduction of Carbon Dioxide-Methods, Mechanisms, and Catalysts. *Chem Rev* **2018**, *118* (9), 4631–4701.
- (10) Brezny, A. C.; Johnson, S. I.; Raugei, S.; Mayer, J.M. Selectivity-Determining Steps in O<sub>2</sub> Reduction Catalyzed by Iron(Tetramesitylporphyrin). *J. Am. Chem. Soc.* **2020**, *142* (9), 4108–4113.
- (11) Lamy, E.; Nadjo, L.; Savéant, J.M. Standard Potential and Kinetic Parameters of the Electrochemical Reduction of Carbon Dioxide in Dimethylformamide. *J. Electroanal. Chem. Interf. Electrochem.* **1977**, *78* (2), 403–407.
- (12) Costentin, C.; Drouet, S.; Robert, M.; Savéant, J.M. A Local Proton Source Enhances CO<sub>2</sub> Electroreduction to CO by a Molecular Fe Catalyst. *Science* **2012**, *338* (6103), 90–94.
- (13) Hammouche, M.; Lexa, D.; Momenteau, M.; Savéant, J.M. Chemical Catalysis of Electrochemical Reactions. Homogeneous Catalysis of the Electrochemical Reduction of Carbon Dioxide by Iron(“0”) Porphyrins. Role of the Addition of Magnesium Cations. *J. Am. Chem. Soc.* **1991**, *113* (22), 8455–8466.



- (14) Bhugun, I.; Lexa, D.; Savéant, J.-M. Catalysis of the Electrochemical Reduction of Carbon Dioxide by Iron(0) Porphyrins. Synergistic Effect of Lewis Acid Cations. *J. Phys. Chem.* **1996**, *100* (51), 19981–19985.
- (15) Best, S. P.; Borg, S. J.; Vincent, K. A. Chapter 1: Infrared Spectroelectrochemistry. In *Spectroelectrochemistry*; **2008**; pp 1–30.
- (16) Bunea, S.; Urakawa, A. Chapter 9: In Situ Spectroscopic Methods to Study Electrochemical CO<sub>2</sub> Reduction. In *Carbon Dioxide Electrochemistry*; **2020**; pp 347–407.
- (17) Roy, L.; Mondal, B.; Neese, F.; Ye, S. Chapter 5: Theoretical Approach to Homogeneous Catalytic Reduction of CO<sub>2</sub>: Mechanistic Understanding to Build New Catalysts. In *Carbon Dioxide Electrochemistry*; **2020**; pp 197–225.
- (18) Römel, C.; Ye, S.; Bill, E.; Weyhermüller, T.; van Gestel, M.; Neese, F. Electronic Structure and Spin Multiplicity of Iron Tetraphenylporphyrins in Their Reduced States as Determined by a Combination of Resonance Raman Spectroscopy and Quantum Chemistry. *Inorg. Chem.* **2018**, *57* (4), 2141–2148.
- (19) Cabaret, D.; Bordage, A.; Juhin, A.; Arfaoui, M.; Gaudry, E. First-Principles Calculations of X-Ray Absorption Spectra at the K -Edge of 3d Transition Metals: An Electronic Structure Analysis of the Pre-Edge. *Physical Chemistry Chemical Physics* **2010**, *12* (21), 5619–5633.
- (20) Timoshenko, J.; Roldan Cuenya, B. In Situ/Operando Electrocatalyst Characterization by X-Ray Absorption Spectroscopy. *Chem. Rev.* **2021**, *121* (2), 882–961.
- (21) Boutin, E.; Wang, M.; Lin, J. C.; Mesnage, M.; Mendoza, D.; Lassalle-Kaiser, B.; Hahn, C.; Jaramillo, T. F.; Robert, M. Aqueous Electrochemical Reduction of Carbon Dioxide and Carbon Monoxide into Methanol with Cobalt Phthalocyanine. *Angewandte Chemie International Edition* **2019**, *58* (45), 16172–16176.
- (22) Ren, S.; Joulié, D.; Salvatore, D.; Torbensen, K.; Wang, M.; Robert, M.; Berlinguette, C. P. Molecular Electrocatalysts Can Mediate Fast, Selective CO<sub>2</sub> Reduction in a Flow Cell. *Science* **2019**, *365* (6451), 367–369.





# Appendix A

---

## Electrochemical experiments

### Content

---

A.1 Cyclic voltammetry .....	147
A.2 Controlled potential electrolysis .....	147
A.3 Setting up an experiment .....	148
A.3.1 Electrodes .....	148
A.3.2 Solvent .....	148
A.3.3 Supporting electrolyte .....	149
A.4 Accessing to kinetic information .....	149
A.5 References .....	153



In terms of electrochemical techniques, two different methods were employed throughout this project depending on what was required. Cyclic voltammetry has been used to provide thermodynamic or kinetic information on the species of interest, while bulk electrolysis was used during spectroelectrochemical experiments, to convert species into a reduced or oxidized counterpart. In this appendix, the electrochemical procedures for setting up these types of experiments are described.

### A.1 Cyclic Voltammetry (CV)

Cyclic voltammetry is a non-destructive technique used to assess kinetic information of a given reaction. For doing so, reduction and oxidation processes are analyzed on a plot known as cyclic voltammogram. These traces can be interpreted by analyzing the electrical response of a species in solution (y-axis – the current in amperes) as a function of the applied potential (x-axis – in volts).<sup>1</sup> Over the course of this thesis, all the cyclic voltammogram representation follow the IUPAC convention (positive potentials to the right and positive currents upwards), otherwise is noticed if US convention is used.

Cyclic voltammetry is used to describe the equilibrium of species expressed by the Nerst equation. With this non-destructive technique, useful information can be extracted, with almost no perturbation of the system. Electrodes of *ca.* 3 mm in diameter are used, usually in a volume of 5 – 10 mL, while the solution is kept still to ensure that the transport of matter is only controlled by diffusion. Details regarding on how to access kinetic information with this technique are further developed in this appendix.

### A.2 Controlled potential electrolysis (CPE)

A controlled potential electrolysis allows to convert the species into one of its reduced or oxidized counterparts. For doing so, a specific potential is constantly applied during the experiment and the current is measured over time. In contrast with CV experiments, surface electrodes (*e.g.* 1 – 3 cm<sup>2</sup>) are immersed in a minimal volume, while the solution is stirred. This allows the whole solution to be in contact with the electrode and yield a complete conversion.

Two reactions occur simultaneously during a CPE experiment, a reduction at the cathode and an oxidation at the anode. Depending on the reaction of interest, the other one is isolated by using a fritted glass, to avoid contamination of the species generated at the electrodes. This technique can be used to quantify the products formed during an electrocatalytic experiments, thus determining the selectivity of the reaction. When run over long periods of times, it also allows to determine the stability of a catalyst. When coupled to spectroscopic techniques, it allows isolating related species in their reduced or oxidized states. Analyzing these species

by spectroscopic or electrochemical techniques can provide information pertaining to a catalytic reaction.

### A.3 Setting up an experiment

When setting up electrochemical experiments many considerations are required. In this section, these aspects are further extended.

#### A.3.1 Electrodes

The setups shown throughout this thesis always involved a three-electrode configuration. The electrodes that constitute the setup are as follow:

**a. Working electrode (WE) :** in all experiments presented in this manuscript, the WE was a glassy carbon film, or a carbon paper. This material was chosen because it is known to have a lower hydrogen evolution activity than platinum and does not interfere with porphyrins like gold electrodes. As mentioned before, for CPE experiments the WE must possess a surface area large enough to convert a maximum of species in a short period of time. The applied potential on the working electrode is always referred versus the reference electrode (RE).

**b. Reference electrode (RE) :** it is used to define the potential of the working electrode. Consequently, it must possess a stable and known potential. For the electrochemical experiments performed in the Laboratoire d'Electrochimie Moléculaire and presented in this thesis, a saturated calomel electrode (SCE) was employed. In the case of spectroelectrochemical measurements, pseudo-reference electrodes were used (such a silver wire, in the case of XAS and IR experiments, or carbon fibers immersed in the solvent-electrolyte solution was used for UV-Vis spectroelectrochemical measurements).

**c. Counter electrode (CE) :** it allows collecting the current that circulates through the WE and the solution. The reactions that occur at the CE are not well controlled and can sometimes lead to corrosion. For this reason, the material needs to be inert and resist high potentials and currents. All experiments presented in this thesis therefore use a CE made of platinum. The surface area of the CE must be large enough to ensure the potential stability of the cell. Because of this, grids or mesh electrodes were used to provide a large surface area.

#### A.3.2 Solvent

In the present manuscript, we have used both water and dimethylformamide (DMF) as solvents for electrochemical experiments. DMF of high purity was used directly from commercial flasks (Aldrich) stored under nitrogen and containing molecular sieves. Aliquots of solvents were collected with syringes flushed with argon and a constant stream of argon

was circulated in the DMF flask while sampling it. At all times, special care was taken to avoid the presence of oxygen or water, which can interact with iron porphyrins during electrochemical experiments.

### A.3.3 Supporting electrolyte

When electron transfer occurs, the presence of ions it is required in the solution to allow the movement of the charged particles. Tetrabutylammonium hexafluorophosphate (TBAPF<sub>6</sub>) at a concentration of 0.1 M was used as electrolyte in DMF because it is inert (both chemically and electrochemically) in the potential range of study.

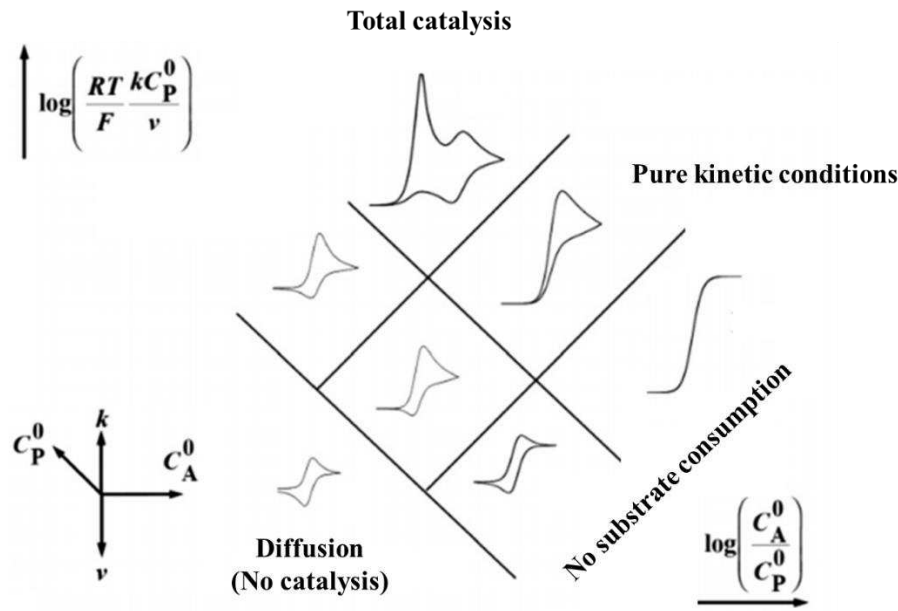
### A.4 Accessing kinetic information

The use of electrochemistry to understand CO<sub>2</sub> reduction catalytic processes by molecular systems have become instrumental in the last decades. Many references offer a first approach to this analysis based on electrochemical experiments, essentially cyclic voltammetry.<sup>2-5</sup> Here, we summarize, in the most comprehensive way, some of the key aspect for extracting kinetic information from a cyclic voltammogram. Information regarding this aspect for the CO<sub>2</sub>RR by iron porphyrins are summarized in chapter II.

Cyclic voltammetry is a technique that provides information based on the intensity, shape and position of the waves in the voltammogram (current vs potential plot). In simple terms, this plot indicates that a signal (current) is obtained when a potential of an electrode, in contact with the species of interest, varies with time. In these voltammograms, one can get the potential at which the redox reaction occurs, which can be translated to the oxidative or reductive evidence of species. In addition, the intensity of the current is proportional to the concentration of the active species. Finally, the shape of the waves provides kinetic information on the reaction(s) occurring as a response to an electrochemical stimulus.<sup>1,6</sup>

As described in chapter II, the active site of the catalyst (Q) reacts with the substrate (A) to generate the products (B or subsequent reactions). The reaction is catalytic when the catalysts can be regenerated many times, without suffering from decomposition. The reaction occurs close to the electrode, which donates the electron to the catalysts to be reduced.<sup>7</sup>

The general behavior of the system can be summarized in what Prof. Jean-Michel Savéant described as the zone diagram (scheme A.1).<sup>7-9</sup>



**Scheme A.1. Kinetic zone diagram with simulated CV forms.**

*Adapted from reference 7.*

In there, two dimensionless parameters can be set out, one that establishes a concentration relation between the substrate and the catalysts as in equation A.1 and a kinetic parameter which relates the time scale of the reaction and the diffusion parameter as in equation A.2.

$$\gamma = \frac{C_A^{\circ}}{C_P^{\circ}} \quad \text{A.1}$$

$$\lambda = \frac{RT k_{cat} C_P^{\circ}}{F v} \quad \text{A.2}$$

Where  $R$  is the ideal gas constant ( $J/mol.K$ ),  $T$  is the temperature in Kelvin ( $K$ ),  $F$  is the Faradaic constant ( $C/mol$ ),  $k_{cat}$  the kinetic rate constant,  $C_P^{\circ}$  and  $C_A^{\circ}$  as the concentration of the catalysts and the substrate in ( $mol/cm^3$ ) respectively and  $v$  the scan rate ( $V/s$ ).

The corresponding analysis can be separated in three main cases that can be described as follow.

**Case 1: Pure diffusion with low  $\gamma$  and  $\lambda$  and with  $k_{cat} = 0$**

Considering P as the catalyst initial form, and Q its activated species, therefore, when P receives an electron from the electrode to be reduced to Q, a reversible profile is generated that gives the diffusion coefficient of species P/Q without providing further kinetic information (no catalysis). The peak current ( $i_p^{\circ}$ ) can be easily measured allowing the direct obtention of the diffusion coefficient ( $D_p$ ) by using the Randles-Sevcik reaction (A.3)

knowing the parameters described in equation A.2 and the working electrode surface (S) in  $\text{cm}^2$ .<sup>7</sup>

$$i_p^\circ = 0.4463FSC_P^\circ\sqrt{D_P}\sqrt{\frac{Fv}{RT}} \quad \text{A.3}$$

**Case 2: Pure kinetic conditions with large  $\gamma$ ,  $\lambda$  and  $k_{cat}$**

In this case, the *substrate A is in excess and the catalysts concentration Q is low*. This brings to the case where kinetics are fast, which can be observed by the presence of a plateau shape current. A new parameter can be described in which a relation between the kinetic rate constant  $k_{cat}$  and the plateau current  $i_{pl}$  can be obtained independently of the scan rate (equation A.4).<sup>7</sup>

$$i_{pl} = FSC_P^\circ\sqrt{D_P}\sqrt{k_{cat}C_A^\circ} \quad \text{A.4}$$

**Case 3: Total catalysis**

When the *concentration of the substrate A is low* a total catalysis regime is obtained. In this case, the substrate is easily consumed at the reaction-diffusion layer, the region close to the electrode where the reaction occurs. This can be observed in CV by the absence of a plateau but the evidence of two waves due to the consumption of substrate and limitation of diffusion of it to the electrode surface. For this reason, the current exclusively depends on substrate diffusion and not on kinetic parameter, and it can be determined by using equation A.5.

$$i_p = 0.609FSC_A^\circ\sqrt{D_A}\sqrt{\frac{Fv}{RT}} \quad \text{A.5}$$

In case 2 (pure kinetic conditions) the current plateau can be reached by increasing the scan rate and directly determine the kinetic rate constant by using equation A.4 or its derivative equation by applying  $\frac{i_{pl}}{i_p^\circ}$ . However, if no plateau can be obtained, the analysis of the slope can be achieved by resolving equation A.6.<sup>10</sup>

$$\frac{i}{i_p^\circ} = - \frac{2.24\sqrt{\frac{RT}{Fv}}\sqrt{k_e C_A^\circ}}{1 + e^{\frac{F}{RT}(E-E^\circ)}} \quad \text{A.6}$$



The plot of  $\frac{i}{i_p^\circ}$  vs.  $\frac{1}{1 + e^{\frac{F}{RT}(E-E^\circ)}}$  results in a straight line. Further the kinetic rate constant can be determined from the slope  $2.24 \sqrt{\frac{RT}{Fv}} \sqrt{k_e C_A^\circ}$ .

In the case of CO<sub>2</sub> reduction by iron porphyrins (at least to the CO generation), two electrons are necessary, as described in chapter II. In this case, it has been proposed that if a large amount of substrate A is present, the step  $Q + A \xrightarrow{k} B + P$  is described firstly as  $Q + A \xrightarrow{k} Q'$  in which an intermediate is generated during the reaction. This step is dependent on the amount of protons available for the reaction to proceed. In these case, different procedures must be selected to achieve the determination of the kinetic rate constants. Firstly, the current can be deduced as in equation A.7

$$i = \frac{FS\sqrt{D}\sqrt{2kC_A^\circ C_P^\circ}}{1 + e^{\frac{F}{RT}(E-E^\circ)}} \quad \text{A.7}$$

Subsequently, different analysis can be performed depending on the experimental conditions:

- **Pure kinetic conditions (substrate A (CO<sub>2</sub>) is in excess and the catalysts concentration Q is low)**

The kinetic rate constant can be obtained by a slope analysis knowing that

$$\frac{i_{pl}}{i_p^\circ} = 2.24 \sqrt{\frac{2k_{cat} RT}{vF}} \quad \text{A.8}$$

From where  $k_{cat}$  parameter can be subtracted. A plot of  $k_{cat}$  vs the concentration of substrate (CO<sub>2</sub>), give a straight line which slope is the kinetic rate constant  $k$ , following equation A.9

$$k_{cat} = k[\text{CO}_2] \quad \text{A.9}$$

In the presence of low amount of co-substrate (protons), no plateau is obtained from the CV. Since not enough protons are added, and they are known for being required for catalysis to occur, the process is expected to proceed in a rather low rate. In this case, it is not possible to obtain  $k_{cat}$  based on a  $\frac{i_{pl}}{i_p^\circ}$  analysis. Rather a required simulation of a plot of  $\frac{i_p}{i_p^\circ}$  (in which  $i_p$  represents the peak current in the presence of the catalysts) vs.  $\log \lambda$  is necessary. On the other hand, when protons are in excess there is a possibility of inhibition of the reaction due to an excess of products (such as carbonates) at the electrode. One alternative in this case is to increase the scan rate in order to reduce the charge passed and secondary effects associated.

### A.5. References Appendix A

- (1) Elgrishi, N.; Rountree, K.J.; McCarthy, B.D.; Rountree, E.S.; Eisenhart, T.T.; Dempsey, J.L. A Practical Beginner's Guide to Cyclic Voltammetry *J. Chem. Educ.* **2018**, 95, 197-206.
- (2) Costentin, C.; Robert, M.; Savéant, J.-M. Catalysis of the Electrochemical Reduction of Carbon Dioxide. *Chem. Soc. Rev.* **2013**, 42 (6), 2423–2436.
- (3) Francke, R.; Schille, B.; Roemelt, M. Homogeneously Catalyzed Electroreduction of Carbon Dioxide-Methods, Mechanisms, and Catalysts. *Chem Rev.* **2018**, 118 (9), 4631–4701.
- (4) Hammouche, M.; Lexa, D.; Savéant, J.-M.; Mometeau, M. Catalysis of the Electrochemical Reduction of Carbon Dioxide by Iron(“0”) Porphyrins. *J. Electroanal. Chem. Interf. Electrochem.* **1988**, 249 (1), 347–351.
- (5) Bhugun, I.; Lexa, D.; Savéant, J.-M. Ultraefficient Selective Homogeneous Catalysis of the Electrochemical Reduction of Carbon Dioxide by an Iron(0) Porphyrin Associated with a Weak Broensted Acid Cocatalyst. *J. Am. Chem. Soc.* **1994**, 116 (11), 5015–5016.
- (6) Tatin, A. Electrochemical CO<sub>2</sub> Splitting into CO and O<sub>2</sub> in Neutral Water Using Earth-Abundant Materials. Doctoral Thesis. *Université Paris Diderot.* **2016**.
- (7) Boutin, E.; Merakeb, L.; Ma, B.; Boudy, B.; Wang, M.; Bonin, J.; Anxolabéhère-Mallart, E.; Robert, M. Molecular Catalysis of CO<sub>2</sub> Reduction: Recent Advances and Perspectives in Electrochemical and Light-Driven Processes with Selected Fe, Ni and Co Aza Macrocyclic and Polypyridine Complexes. *Chem. Soc. Rev.* **2020**, 49 (16), 5772–5809.
- (8) Savéant, J.-M. Molecular Catalysis of Electrochemical Reactions. Mechanistic Aspects. *Chem. Rev.* **2008**, 108, 2348-2378.
- (9) Savéant, J.-M. *Elements of Molecular and Biomolecular Electrochemistry: An Electrochemical Approach to Electron Transfer Chemistry*, John Wiley & Sons. **2006**, pp. 78 - 181.
- (10) Costentin, C.; Robert, M.; Savéant, J.-M. Catalysis of the electrochemical reduction of carbon dioxide. *Chem. Soc. Rev.* **2013**. 42, 2423-2436.



# Appendix B

---

## X-Ray Absorption Spectroscopy

### Content

---

<b>B.1</b> XAS physical principles.....	157
<b>B.2</b> Synchrotron radiation sources.....	160
<b>B.2.1</b> Beamlines components .....	160
<b>B.3</b> Synchrotron SOLEIL .....	163
<b>B.3.1</b> General descriptions of the beamlines of SOLEIL used for this thesis.....	164
<b>B.4</b> How to start a synchrotron-based experiment? .....	167
<b>B.5</b> References.....	169



## B.1 XAS physical principles

The Lambert-Beer law, represented by equation B.1, describes the absorption of light by a sample being excited in a specific section of the electromagnetic spectrum:<sup>1</sup>

$$I_T = I_0 e^{-\mu d} \quad (\text{B.1})$$

This law states that the intensity of the sample after irradiation ( $I_T$ ) decreases exponentially, in comparison with the intensity of the incident radiation ( $I_0$ ), as the thickness of the sample ( $d$ ) and the linear absorption coefficient ( $\mu$ ) increases. This latest parameter ( $\mu$ ) is important in XAS experiments, which depend on the energy of the incident radiation ( $E$ ) and is described by Fermi's Golden rule (equation B.2):<sup>1,2</sup>

$$\mu(E) \approx \sum_f |\langle f | \hat{T} | i \rangle|^2 \delta(\epsilon_f - \epsilon_i - E) \quad (\text{B.2})$$

This rule states that the linear absorption coefficient can be correlated to the sum of states going from an initial or ground state ( $i$ ) to a final state ( $f$ ). Indeed, at specific values, the energy of the incident photon equals the binding energy of the core electron (initial state). The latter is ejected into the LUMO or the continuum (final state), which gives rise to a sharp increase of the absorption, known as an *edge*. This absorption interruption is known as the K-edge when the electron is excited from a core level  $1s$  and has an energy that is characteristic of each element. This rule also indicates the conservation of energy of the system, in which the mathematical expression  $\delta(\epsilon_f - \epsilon_i - E)$ , also known as Dirac function, specifies that the transition can only be possible for energies that are well defined. Finally, the operator  $\hat{T}$ , known as the Hamiltonian of interactions between the initial and the final state, describes the core electron and the X-ray photon.<sup>1</sup>

The most important contribution to the K-edge spectrum is determined by the  $1s \rightarrow np$  transition, with  $np$  corresponding to the lowest unoccupied  $p$  orbital of the absorbing atom. The intensity and shape of the edge is correlated to the density of the states and the selection rules of a specific transition. The region of an X-ray absorption spectrum around the edge is known as X-ray Absorption Near Edge Structure (XANES).

In transition metal complexes, another transition can be observed before the rising edge, which is due to a  $1s$  to  $(n-1)d$  transition in disrupted center of symmetry (for instance in the case of tetrahedral complexes) or due to hybridization effect, in which  $d$ -orbitals can mix with  $p$ -type ones, resulting in a dipole-allowed effect and a transition. This signature is usually weaker than the main edge and it is known as the *pre-edge*.

Finally, a last transition occurs when the core electron is excited towards the continuum. The different interactions between this photoelectron and the neighbor's atoms in the system give rise to an oscillatory signature known as Extended X-ray Absorption Fine Structure (EXAFS), which is described by the EXAFS component  $x(E)$  given by the equation B.3:<sup>3,4</sup>

$$x(E) = \frac{\mu(E) - \mu_0(E)}{\Delta\mu_0(E_0)} \quad (\text{B.3})$$

The EXAFS component  $x(E)$  describes the difference between the absorption coefficient  $\mu(E)$  and the free atom absorption probability  $\mu_0(E)$ . This parameter is further divided by the difference between the two functions that describe the pre-edge (function before the rising edge) and the post edge region, taking the minimal energy necessary to excite the photoelectron ( $E_0$ ) as reference parameter. This equation gives rise to a signature observed in the spectrum that goes from right after the absorption edge to around 1keV after the edge.

However, when EXAFS data is shown, its representation is converted to two parameters. Firstly, the EXAFS signal is transformed to what is known as k-space (figure B.1 – a), given by the equation B.4:

$$k = \sqrt{\frac{2m_e}{h^2}(E - E_0)} \quad (\text{B.4})$$

Where  $h$  corresponds to the Planck's constant while  $m_e$  is the mass of the electron.

Due to the different interactions that the photoelectron possesses with the other atoms, a backscattered effect occurs. Taking into consideration the scattering formalism, the EXAFS component can be formulated as indicated in equation B.5, as a sum of all the possible contributions of the photoelectron interactions:<sup>1</sup>

$$x(k) = \sum_p x_p(k) \quad (\text{B.5})$$

However, the representation of equation B.5 is more extended, and it can be represented in terms of a sinusoidal function. This is due to the different interferences obtained by the photoelectron while interacting with the neighbor atoms. At a specific energy, the backscattered waves are in phase, forming a constructive interference and increasing the absorption coefficient. At another energy, the waves are out-of-phase, producing a destructive interference and decreasing the absorption coefficient (figure B.1 – b). For this reason, a representation of  $x_p(k)$  is better described as indicated in equation B.6:<sup>3</sup>



$$x_p(k) = S_0^2 \int_0^{+\infty} g_p(R) F_p(k, R) e^{-2R/\lambda(k)} \sin(2kR + \phi_p(k, R)) \frac{dR}{kR^2} \quad (\text{B.6})$$

In which  $g_p(R)$  is known as the partial radial distribution form. This parameter is of relevance in EXAFS since it represents the probability to find an atom interacting with the photoelectron at a specific distance (R). EXAFS provides radial information between the absorbing atom and its neighbor in a range that limits with precision, and depending on the k-space, up to  $8 \text{ \AA}^{-1}$ .<sup>1,5</sup> In addition to this, parameters such as  $F_p(k, R)$  and  $\phi_p(k, R)$  indicates the variations in terms of amplitude and phase respectively of the photoelectron while interacting with the other atoms in the system. Furthermore, these parameters give information related to the sensitivity of the measurement. The terms  $\frac{-2R}{\lambda(k)}$ ,  $\frac{1}{kR^2}$  and  $S_0^2$  contribute to making the EXAFS measurement a local technique, since they decrease the farther distances and concentrate specifically on atoms that are in a close shell to the absorbing atom. Due to the sinusoidal nature of equation B.6, the EXAFS component can finally be rewritten as a Fourier transform (FT) (figure B.10 - c) which is the most common representation of an EXAFS spectrum.

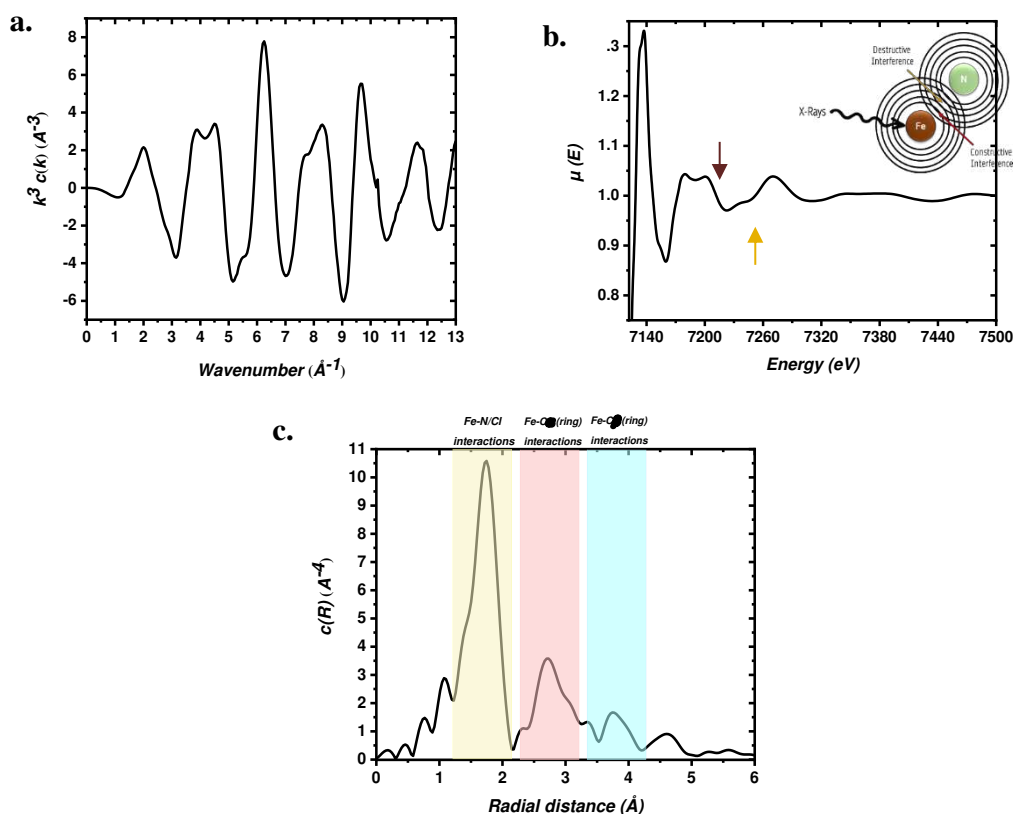


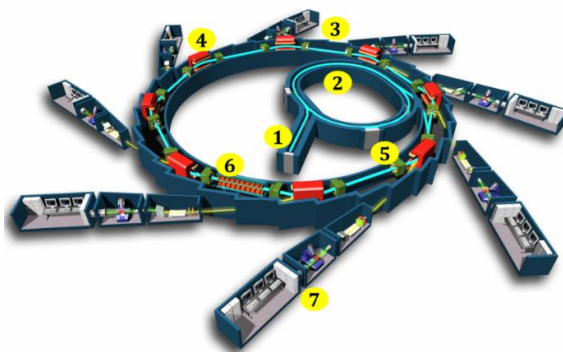
**Figure B.1.** a.  $k$ -space representation for  $[\text{Fe}^{\text{III}}(\text{TPP})]\text{Cl}$  in the solid state recorded in transmission mode on the LUCIA beamline at Synchrotron SOLEIL. b. In-phase constructive (red arrows) and out-of-phase destructive (yellow arrows) interferences obtained for the same system. c. Fourier transform signal of the  $k$ -space EXAFS.

The colored bars indicate the expected radial interaction peaks.



## B.2 Synchrotron radiation sources

A synchrotron radiation source is a large instrument in which electrons are accelerated to relativistic velocities. The operation of a synchrotron, scheme B.1, starts by the generation of a thin electron beam emitted from an electron gun and directed towards a long linear accelerator called LINAC in where electrons reach the speed of light. The electron beam is then oriented towards a second accelerator, this time a circular one called the booster. It is there where the electrons reach their operating energy. When this occurs, the electrons are directed towards a larger circular ring, called the storage ring, where they continuously circulate. Bending magnets and undulators inserted inside this ring allow controlling the direction and oscillation of the electrons. This phenomenon makes the electrons lose some energy which is converted into a beam of light, known as the *synchrotron radiation*. This beam is oriented towards experimental stations called *beamlines*, where a variety of samples can be analyzed under many forms and types of experiments.<sup>6,7</sup>



**Scheme B.1. Synchrotron scheme: 1. LINAC. 2. Booster. 3. Storage ring. 4. Dipoles. 5. Radiofrequencies cavities. 6. Undulators. 7. Beamlines.**

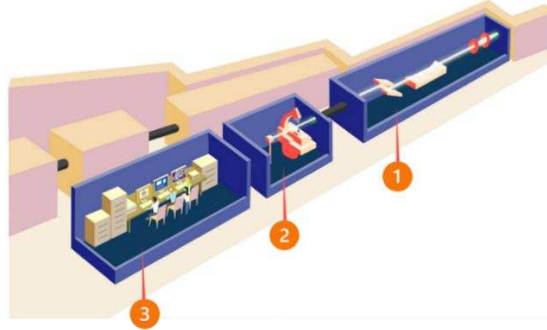
*Adapted from reference 6.*

By generating an extremely brilliant source of light in a wide range of energies, this large instrument is indeed very powerful. The beam of light produced at synchrotrons allow the study of samples with several techniques using a variety of photon energies, a high energy resolution and intensity. Even though there has been some development in the recent years in laboratory based XAS, still the vast majority of XAS experiments are performed inside a synchrotron radiation source. This is even more important in the case of *in situ* and/or *operando* or time-resolved experiments, which require a large number of photons.

### B.2.1 Beamlines components

The experimental chambers inside the synchrotron are called beamlines, scheme B.2. Each beamline is equipped with optical systems that select the energy of the beam, focus and direct it towards the experimental station where the measurements occur.<sup>8</sup> The experimental station

is characteristic of each beamline and is equipped with different conditions and/or techniques for a specific analysis. At the end of the beamline a working station is found, where the experiment is controlled, and the data analysis is performed.



**Scheme B.2. Beamline scheme indicating its sections: 1. Optical hutch. 2. Experimental station. 3. Working station.**

*Figure adapted from reference 9.*

Before going further in the description of each beamline used for the purpose of this thesis project, important consideration in the optical section as well as detection should be described.

In general terms, the goal of an XAS experiment is to measure the absorption coefficient ( $\mu$ ) as a function of the energy ( $E$ ) of the incident X-rays:

$$\mu = f(E) \tag{B.7}$$

Such an experiment relies on two experimental parts:

- 1) The monochromator, which allows selecting the working energy ( $E$ )
- 2) The detection of  $\mu$  by direct or indirect modes.

### 1) Monochromator

The monochromator is constituted by two parallel crystals which are cut along a determined plane, for instance (111), (220) or (311). The rotation of these crystals with an incident angle  $\theta$  allows the selection of a wavelength ( $\lambda$ ) following the Bragg law (equation B.8).

$$n\lambda = 2d \sin \theta \tag{B.8}$$

Where  $n$  is the diffraction order and  $d$  is the spacing between the layer of atoms. The wavelength can be further transformed into energy as shown in equation B.9

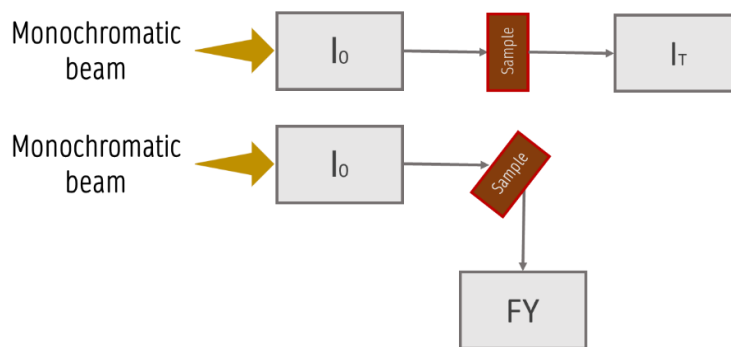
$$\lambda = hcE \tag{B.9}$$

Where  $h$  is the Plank constant and  $c$  the speed of light.

Therefore, the energy resolution of the experimental spectra is conditioned by the monochromator's crystals resolution.

## 2) Detection

After the beam has been monochromatized, it interacts with the sample and a detector is used to record the signature of this interaction. Two main types of detections are usually used in hard XAS, as shown on scheme B.3.



**Scheme B.3. Representation of the two different detection modes usually used in hard XAS. Top: transmission mode. Bottom: fluorescence mode.**

$I_0$  = intensity of the incident radiation;  $I_T$  = intensity of the signal after transmission detection;  $FY$  = fluorescence yield

### - *Transmission:*

For transmission experiments two detectors are located before and after the sample, so as to monitor the difference in absorption. If the detection is direct, the absorption coefficient ( $\mu$ ) is expressed following the B.1 equation (also expressed as in equation B.10)

$$\mu d = \ln \frac{I_0}{I_1} \quad (\text{B.10})$$

in which  $I_0$  and  $I_1$  are the intensities of the beam before and after the sample, respectively. These intensities are usually measured in ionization chambers containing an inert gas, which is ionized when the X-rays passes through it. A current is then generated, which is proportional to the intensity of the X-Ray beam.

- **Fluorescence:**

In fluorescence detection, a detector monitors the photons that are re-emitted by a sample during the relaxation process that follow the ejection of a core-hole electron. In this case, the absorption coefficient is expressed as equation B.11

$$\mu \approx \frac{I_1}{I_0} \quad (\text{B.11})$$

Fluorescence detectors are based on semiconducting materials (usually Ge or Si), which convert X-ray photons into electrical current. They are usually placed in a backscattering position with respect to the sample, if possible, at 90° to the X-Ray beam and 45° from the sample, to minimize the presence of the elastic peak (X-rays reflected by the sample without interacting with it). The detector is also located as close as possible to the sample.

The selection of the detection mode depends on the experimental parameters, such as concentration, energy range, sample state or geometry. Generally, transmission mode generates data with better signal to noise. For this reason, it is the preferred mode to be used in fast acquisition experiment such as *operando* or time-resolved. However, the main limitation of this mode is the sample quality and concentration, since it requires a highly concentrated sample in order to ensure absorption but not too thick or non-homogeneous that does not allow penetration and proper detection of  $I_1$ .

### B.3 Synchrotron SOLEIL

SOLEIL, which means “optimized light source of intermediate energy of LURE”, from its acronym in French, is a synchrotron source facility located in Gif-sur-Yvette, just outside Paris - France. LURE was a pioneering synchrotron radiation laboratory located close to SOLEIL facilities. After closing LURE in 2003, it was converted into SOLEIL, one of the main synchrotron facilities of Europe.



**Figure B.2. Aerial and internal views of the synchrotron SOLEIL.**

*Credits for the aerial photography to communication team - Synchrotron SOLEIL.*



The beam produced at SOLEIL possesses remarkable properties such as being extremely brilliant, around 10000 times brighter than the sunlight.<sup>6</sup> For this reason, a broad range of studies can be performed there due to the wide spectral range that goes from the  $\mu\text{eV}$  (at the infrared range) to 100 keV (at the hard X-rays level).

Inside the synchrotron SOLEIL the LINAC accelerates the electrons reaching a first energy level of 100 MeV. Further injection of the electrons into the booster increases their energy as high as 2.75 GeV, which is the energy operating value at SOLEIL. Finally, electrons travel within the storage ring which possess a circumference of 157 m.<sup>6</sup>

### B.3.1 General description of the beamlines of SOLEIL used for this thesis

29 beamlines are found inside the synchrotron SOLEIL. They are classified depending on their energy range on figure B.3. During this thesis project, several proposals applications were submitted and beamtime allocation was obtained on three beamlines, going from infrared at AILES beamline, tender X-Rays at LUCIA beamline and hard X-Rays at SAMBA beamline. General aspects of each of these beamlines, used to obtain the results presented in this thesis, are summarized below.

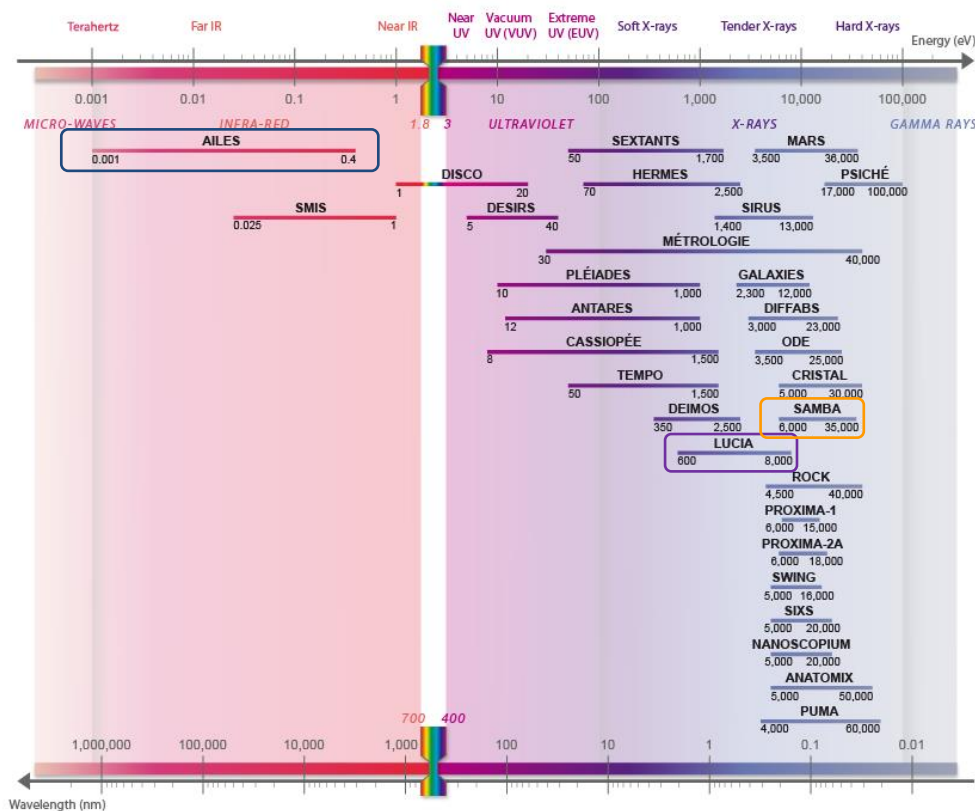


Figure B.3. Beamlines at the Synchrotron SOLEIL classified by energy range.

Source: [synchrotron-soleil.fr](http://synchrotron-soleil.fr).<sup>6</sup>

- *AILES Beamline (Infrared)*

AILES (Advanced Infrared Line Exploited for Spectroscopy) beamline is exclusively dedicated to studies in the infrared (IR) region. It covers an energy range that goes from 0.001 eV ( $4\text{ cm}^{-1}$ ) to 0.4 eV ( $5000\text{ cm}^{-1}$ ), including the spectral range of the far-infrared and terahertz (THz) region, to the near (NIR) and mid-infrared (MIR).<sup>6</sup> The main advantage of performing IR experiments at this beamline in contrast with a standard source, lies in the high flux of the synchrotron beam, especially in the FIR region, which is not available in a conventional IR benchtop equipment. In addition to this, mechanical stability is increased, which is translated to data acquisition with lower background and an improved signal to noise. This is reached by performing the experiments under vacuum, minimizing in this way any atmospheric or acoustic perturbation. Due to this, experiments performed at AILES reach exceptional resolutions, which is not possible with tabletop sources. This allows the range of experiments to be extended to all types of samples (solid, liquid or gas phase), with the possibility to detect even the smallest rotational and vibrational variations.<sup>10,11</sup>

Figure B.4 shows a scheme of the AILES beamline. It has three different workstations depending on the interferometer used. AILES A, allows achieving the highest resolution, usually dedicated to rovibrational studies in the gas phase. AILES B allows reaching a resolution of  $0.007\text{ cm}^{-1}$ , comparable with benchtop sources, and is dedicated to studies in condensed matter and molecular systems. AILES C is equipped with an attenuated total reflectance (ATR) system and a conventional detector, as well as an equipment for low temperature experiments. AILES C station was use in the present project for the convenience of its experimental chamber.

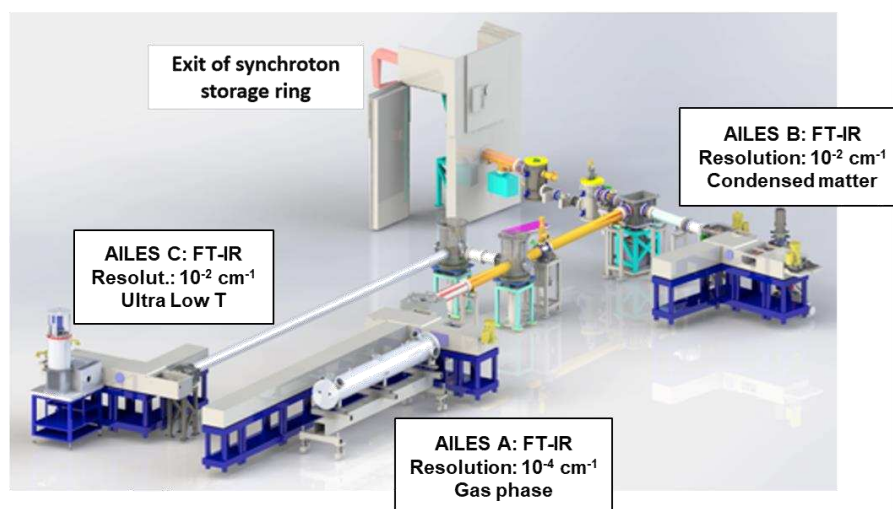


**Figure B.4.** AILES Beamline scheme.

*Credit: scheme courtesy of Dr. J.B. Brubach AILES beamline scientist.*





The experimental setup used during the beamtime session consisted of a vacuum compatible flow cell. The specifications of this set-up are shown in Appendix D.

- *LUCIA Beamline (Tender X-Rays)*

LUCIA (Line for Ultimate Characterization by Imaging and Absorption) beamline allow detection between 800 and 8000 eV, in the tender X-Rays region.<sup>6</sup> The main application of this beamline is the study of heterogeneous samples by X-ray micro-fluorescence and X-ray micro-XAS due to the micron size of the focused beam (3x3µm). X-Ray absorption studies in this energy region are also performed with a non-focused beam (2x2mm). Besides its focused beam, the energy range offered by the LUCIA beamline also offers opportunities for the study of earlier transition metals, halides, alkalines and earth-alkalines.

A scheme of the LUCIA beamline is shown in figure B.5. The beam passes through a double-crystal monochromator, which allows selecting the energy of the beam. In micro-focused mode, the beam passes through a set a curvable (so-called Kirkpatrick-Baez) mirrors, that can focus it down to *ca.* 3x3µm. Finally, the beam reaches the sample in which three detection modes are possible: transmission, total electron yield, and fluorescence. The data collected at LUCIA in the frame of this thesis were measured with a silicon drift diode (SDD) fluorescence detector. The experiments were performed in an experimental chamber under primary vacuum (10<sup>-2</sup> mbars).<sup>12</sup>

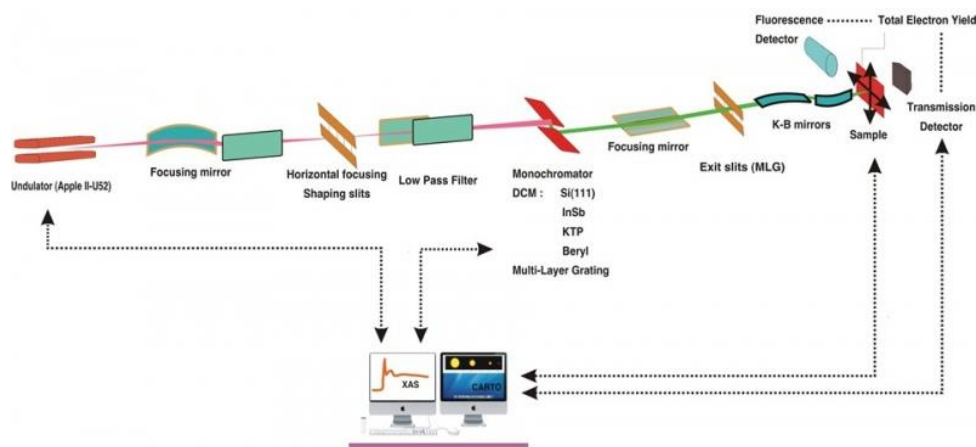


Figure B.5. LUCIA Beamline general scheme.

Source: [synchrotron-soleil.fr](http://synchrotron-soleil.fr).

LUCIA beamline was extensively used during this project since access to *in house* experiments was also available. As mentioned in chapter V and further in appendix D, optimization of the spectroelectrochemical set-up to obtain reproducible data under *in situ / operando* conditions were performed on this beamline.

- *SAMBA Beamline (Hard X-Rays)*

SAMBA (Spectroscopy Applied to Material Based on Absorption) is a hard X-Rays beamline, which broad energy range goes from 6000 to 35000 eV.<sup>13</sup> The high flux and beam stability on this beamtime makes it ideal for a wide range of experiments. The large space available at the sample/beam interaction point makes it appropriate for complex experimental setups.

A scheme of the SAMBA beamline optical section as well as a picture of the detector is shown in figure B.6. The monochromator used during the experiments presented in this project is a sagittal double crystal monochromator, which contains a cylindrical Si(220) mirror and a sagittally bent crystal giving a resolution of  $6 \times 10^{-5}$  at 15 keV. A 35-elements pixel array germanium fluorescence detector placed at  $90^\circ$  from the incident beam and  $45^\circ$  from the sample was used for measurements.<sup>13,14</sup> The experiments were performed at ambient pressure in the experimental hutch.

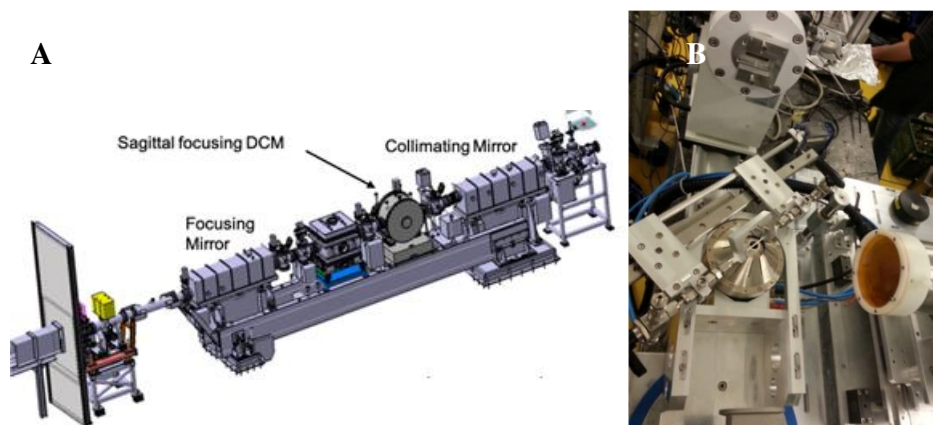


**Figure B.6. SAMBA Beamline A. optical layout. B. Sample environment.**

Source: *synchrotron-soleil.fr*.<sup>6</sup>

#### **B.4. How to start a synchrotron-based experiment?**

A synchrotron experiment differs from a common laboratory experiment in many aspects.<sup>8</sup> Due to the demanding application procedure, the limited access and time, the pressure of achieving the results in the short experimental sessions and the difficulty for repetitions, synchrotron experiments require a high level of organization and a detail long-term planning.

The first step for starting a synchrotron-based experiment is the submission of the application proposal, which is a short document, in which the objectives, the experimental plan, the expected results and the shifts requested must be described in a detailed manner. A required question when planning a synchrotron-based experiment is to know if indeed the synchrotron





radiation is essential to answer the scientific question of interest. Knowing the advantages of its use as well as the kind of information that can be subtracted from a spectrum is mandatory. However, considering the limitations of the techniques available is also critical. For instance, the consideration of radiation damages that can be generated by a high photon flux on fragile samples is necessary. Possibilities to reduce this damage and how they can be applied to the experimental conditions needs to be considered. The concentration of the sample is also another major parameter to consider, since detectors have detection limits (especially in transmission mode). If the experiment requires the development of new instrumentation, extensive optimization of the setups must be performed prior to the synchrotron session.

When all of these conditions have been considered and evaluated, a proposal can be written and submitted. The proposals firstly pass a feasibility analysis and another one related to safety concerns. It is then analyzed by a peer review panel who examines it and allocate beamtime depending on several aspects, such as the importance of the scientific question addressed, the proposal quality and the availability of the beamline requested.

Finally, if the application is successful, the allocation time will be granted between the next 6 months. The experimental conditions must be organized for the allocated time. The experiment must be performed as planned but keeping in mind to be innovative, problem-solving, ingenious and flexible if unexpected problems occur.

Data acquisition as well as calibration, signal optimization parameters and sample preparation performed during beamtime allocation are presented in appendix C. In addition, the setup and optimizations requirements were shown in chapter V and and in appendix D.

## B.5 References Appendix B

- (1) Timoshenko, J.; Roldan Cuenya, B. In Situ/Operando Electrocatalyst Characterization by X-Ray Absorption Spectroscopy. *Chem. Rev.* **2021**, *121* (2), 882–961.
- (2) Rehr, J. J.; Kas, J. J.; Prange, M. P.; Sorini, A. P.; Takimoto, Y.; Vila, F. Ab Initio Theory and Calculations of X-Ray Spectra. *Comptes Rendus Physique* **2009**, *10* (6), 548–559.
- (3) Yano, J.; Yachandra, V. K. X-Ray Absorption Spectroscopy. *Photosynth Res* **2009**, *102* (2–3), 241–254.
- (4) Bianconi, A., Incoccia, L., Stipcich, S., Eds.; Goldanskii, V. I., Gomer, R., Schäfer, F. P., Toennies, J. P., *EXAFS and Near Edge Structure: Proceedings of the International Conference Frascati, Italy, September 13–17, 1982*; Series Eds.; Springer Series in Chemical Physics; Springer Berlin Heidelberg: Berlin, Heidelberg, **1983**; Vol. 27.
- (5) Kuzmin, A.; Timoshenko, J.; Kalinko, A.; Jonane, I.; Anspoks, A. Treatment of Disorder Effects in X-Ray Absorption Spectra beyond the Conventional Approach. *Rad. Phys. Chem.* **2020**, *175*.
- (6) Synchrotron SOLEIL. *SOLEIL en 3 questions*. **2021**. Source: <https://www.synchrotron-soleil.fr/fr>
- (7) Mitchell, E.; Kuhn, P.; Garman, E. Demystifying the Synchrotron Trip: A First Time User's Guide. *Structure*. **1999**, *7* (5), R111–R121.
- (8) Gianolio, D. How to Start an XAS Experiment. In *X-Ray Absorption and X-Ray Emission Spectroscopy*; John Wiley & Sons, Ltd, **2016**; pp 99–124.
- (9) European Synchrotron Radiation Facility (ESRF). **2021**. Source: <https://www.esrf.fr/home.html>
- (10) Roy, P.; Rouzières, M.; Qi, Z.; Chubar, O. The AILES Infrared Beamline on the third generation Synchrotron Radiation Facility SOLEIL. *Infrared Physics and technology*. **2006**. *49*, 1-2, 139-146.
- (11) Roy, P.; Brubach, J.B.; Manceron, L.; Rouzies, M.; Pirali, O.; Creff, G.; Peng, W.; Kwabiatachana, F. The AILES beamline for THz and IR spectroscopy. *IRMMW-THz* **2010**: 35th International Conference on Infrared, Millimeter, and Terahertz Waves.
- (12) Vantelon, D.; Trcera, N.; Roy, D.; Moreno, T.; Mailly, D.; Guilet, S.; Metchalkov, E.; Delmotte, F.; Lassalle, B.; Lagarde, P.; Flank, A.-M. The LUCIA Beamline at SOLEIL. *J Synchrotron Rad* **2016**, *23* (2), 635–640.
- (13) Belin, S.; Briois, V.; Traverse, A.; Idir, M.; Moreno, T.; Ribbens, M. SAMBA a New Beamline at SOLEIL for X-Ray Absorption Spectroscopy in the 4–40 KeV Energy Range. *Phys. Scr.* **2005**, *2005* (T115), 980.
- (14) Briois, V.; Fonda, E.; Belin, S.; Barthe, L.; Fontaine, C. L.; Langlois, F.; Ribbens, M.; Villain, F. SAMBA: The 4–40 KeV X-Ray Absorption Spectroscopy Beamline at SOLEIL. In *UVX 2010 - 10e Colloque sur les Sources Cohérentes et Incohérentes UV, VUV et X; Applications et Développements Récents*; EDP Sciences, **2011**; pp 41–47.



# Appendix C

---

## Instrumentation and Materials

### Content

---

C.1 Materials .....	173
C.2 Instrumentation and experimental details.....	174
C.2.1 Electrochemical measurements .....	174
C.2.2 X-Ray absorption spectroscopy measurements .....	175
C.2.3 UV-Vis spectroscopy .....	177
C.2.4 Infrared spectroscopy .....	178
C.3 Sample preparation.....	179
C.3.1 Spectro(electro)chemical catalysts samples .....	179
C.3.2 Other samples .....	179
C.3.3 Synthesis .....	180
C.3.3.1 Catalyst's preparation .....	180
C.3.3.2 Chemical reduction .....	181
C.4 References .....	184





## C.1 Materials

### - Gases

Gases were purchased from Air Liquide. The grade and specifications are indicated below:

- Argon (Ar) Alphagaz 1. Impurities:  $\text{H}_2\text{O}$  and  $\text{O}_2 \leq 2$  ppm  
 $\text{CO}_2$  and  $\text{CO} \leq 1$  ppm
- Carbon Dioxide Arcal ( $\text{CO}_2$ ). Impurities:  $\text{H}_2\text{O} \leq 40$  ppm
- Carbon Monoxide N18 Bundle ( $\text{CO} \geq 98\%$ ).

### - Solids

**Catalysts.** Iron tetraphenyl porphyrin chloride [ $\text{Fe}^{\text{III}}(\text{TPP})\text{Cl}$ ] and iron sulphonatophenyl porphyrin chloride [ $\text{Fe}^{\text{III}}(\text{TPPS})\text{Cl}$ ] were purchased from Porphyrchem and Porphyrin-laboratories GmbH, respectively. Iron 5,10,15,20-tetra(N,N,N-trimethyl-4-anilinium) porphyrin tetrachloride [ $\text{Fe}^{\text{III}}(-\text{p-TMA})\text{Cl}$ ] synthesis, which is explained in detail later on this appendix, required 5,10,15,20-tetra(N,N,N-trimethyl-4-anilinium)porphyrin tetrachloride (free porphyrin ligand) was purchased from Frontier Scientific. Iron(II) ammonium sulphate hexahydrate [ $(\text{NH}_4)_2\text{Fe}(\text{SO}_4)_2 \cdot 6\text{H}_2\text{O}$ ], used as iron precursor, was purchased from Sigma Aldrich. Ammonium hexafluorophosphate ( $\text{NH}_4\text{PF}_6$ ) was purchased from Acros Organics.

**Electrolyte.** Tetrabutylammonium chloride ( $\text{TBAPF}_6 \geq 99.0\%$ ) was purchased from Sigma Aldrich. For aqueous conditions experiments, as indicated in the text, Britton-Robinson buffer was used.<sup>1</sup> It is prepared by mixing 0.04 M of each of the following acids in 1.0 L of deionized water: acetic acid ( $\text{CH}_3\text{COOH}$ ), phosphoric acid ( $\text{H}_3\text{PO}_4$ ) and boric acid ( $\text{H}_3\text{BO}_3$ ). All acids were purchased from Sigma Aldrich. Initial pH of the buffer was 2.54. The pH value was measured by using a pH-meter FiveEasy F20 from Mettler Toledo, with a precision of  $\pm 0.01$  pH.

### Chemicals.

*Required for chemical reduction:* sodium (Na 99.9%) cubes contained in mineral oil were obtained from Sigma Aldrich. Anthracene (~98% powder) was purchased from technical chemical laboratories (TCL).

*Required for pellet preparation:* graphite powder  $< 20 \mu\text{m}$  and boron nitride powder  $\sim 1 \mu\text{m}$  98% both from Sigma Aldrich.

*Required for cell optimization:* Iron(III) chloride hexahydrate [ $\text{Fe}^{\text{III}}\text{Cl}_3 \cdot 6\text{H}_2\text{O}$ ] (ACS reagent, crystalized) and iron(II) chloride [ $\text{Fe}^{\text{II}}\text{Cl}_2$ ] (98%) were purchased from Sigma Aldrich.

### - Liquids

**Solvent for spectro(electro)chemical sample preparation** N,N-dimethylformamide (DMF) was purchased from Acros Organics ( $\geq 99.8\%$ ) electrochemical grade, over

molecular sieves, and stored and manipulated under Argon atmosphere inside of a fume hood since it is classified as a health dangerous compound. Ultra-pure water (TKA MicroPure  $0.055\mu\text{Scm}^{-1}$ ) was used.

**Required for catalysts preparation [Fe<sup>III</sup>-p-TMA(Cl)]** acetone ( $\geq 99.8\%$ ), chloroform ( $\geq 99.9\%$ ), methanol ( $\geq 99.8\%$ ), ethyl acetate ( $\geq 99.5\%$ ), hydrochloric acid (37%) were obtained from VWR Chemicals.

**Required for chemical reduction** tetrahydrofuran (THF ACS grade), n-Hexane ( $\geq 97\%$ ) were obtained from VWR Chemicals. They were used after drying standard procedure (distillation on sodium) as reported.<sup>2</sup>

## C.2 Instrumentation and experimental details

### C.2.1 Electrochemical measurements

Routine electrochemical measurements were performed at the Laboratoire d'Electrochimie Moleculaire (LEM) by using a Metrohm Autolab potentiostat interfaced with the software Nova 2.1. For routine cyclic voltammetry (CV) experiments, a heart shaped cell (figure C.1), was used. Generally, these experiments were performed to confirm the purity of iron porphyrins synthesized in the laboratory or their catalytic behavior. As previously mentioned in appendix A, a three electrodes setup was used. The working electrode (WE) was a home-made glassy carbon electrode of 3 mm diameter. The WE was carefully polished before each voltammogram on a rotating polishing cloth with a  $1\mu\text{m}$  diamond paste, sonicated and washed in acetone. The counter electrode (CE) was a platinum wire directly immersed in the sample solution. Finally, a commercial saturated calomel electrode (SCE) purchased from Bio-logic was used as reference, otherwise is indicated another reference. This reference electrode is placed inside of a bridge filled with the solvent-electrolyte solution to avoid electrode contamination. Its potential, at 21 °C, is known to be 240 mV vs. SHE (standard hydrogen electrode).<sup>3</sup>

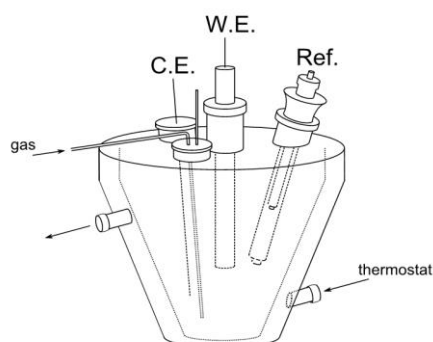


**Figure C.1.** Representation of a heart-shaped electrochemical cell used for cyclic voltammetry experiments. WE stands for Working Electrode, Ref stands for Reference Electrode and CE stands for Counter Electrode.

Since water serves as a proton source, before starting any spectro(electro)chemical experiment, it was firstly required to remove water content on the catalysts and electrolyte. This was achieved by drying both compounds at 40 °C under vacuum for at least 2 hours prior to the measurement. The effect of water/moisture presence was clearly detectable by cyclic voltammetry, (figure C.2). An important increase of the catalytic current in the presence of CO<sub>2</sub> when the samples are not dry is observed. In addition to this, there is the evidence of an anodic wave at -1.2 V vs SCE, indicating the formation of the Fe-CO adduct as previously discussed, even if no external proton source is added. When the drying procedure is followed, an important diminution on the current is observed. This indicates an important improvement on the water/moisture removal by performing this procedure.

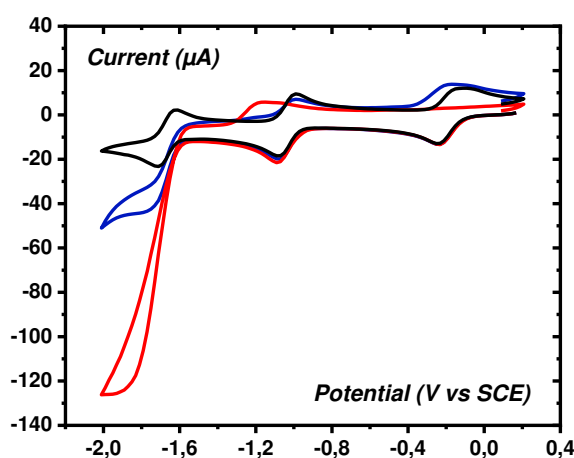


**Figure C.2.** Cyclic voltammogram of a solution [Fe<sup>III</sup>(TPP)]Cl in DMF + TBAPF<sub>6</sub> 0.1 M under Ar (black), CO<sub>2</sub> (red) and in CO<sub>2</sub> after drying the catalyst and the electrolyte (blue).

All gases used (Ar and CO<sub>2</sub>) were passed through a glass tube filled with CaCl<sub>2</sub>. Having hygroscopic properties, the calcium chloride salt is used to remove any remaining water in the gas itself or in the tubings it goes through. For the same reason, DMF was always sampled from a fresh flask (with molecular sieves) and the sample preparation was always performed under anaerobic conditions.<sup>4</sup> Ar or CO<sub>2</sub> was bubbled during all CV experiments, just removing it from the sample solution while recording the CV in order to avoid convection. For spectroelectrochemical experiments gases were continuously degassed and flown in the solution.

### C.2.2 X-Ray Absorption spectroscopy

Fe K-edge XAS data was recorded on the LUCIA beamline (otherwise is noted), operating with an electron beam energy of 2.7 GeV and beam current of 500 mA at the Synchrotron SOLEIL. The incident photons were monochromatized by using a Si(111) double crystal monochromator. The beam size was reduced to 1(v) x 2(h) mm using slits. Data was collected in fluorescence mode using a silicon drift diode (SDD) detector from Bruker. Internal energy



calibration was performed by measurement of the absorption of an iron foil, which first inflection point was fixed at 7112 eV.<sup>5</sup> The spectroelectrochemical cell was set on the XYZ monitor aligned 45° to the detector. All data were collected at room temperature and under a primary vacuum chamber ( $10^{-2}$  mbars).

Collection of a single spectrum in the XANES region required between 5 and 15 minutes. Samples were monitored for radiation damage by collecting several spectra on the same spot and checking for an evolution. Therefore, the solid state XANES samples (pellet) were collected by recording data at multiple spots. Liquid samples XANES were recorded by measuring a first spectrum in a set position, flowing the sample ( $100\mu\text{L}\cdot\text{min}^{-1}$ ) and recording a next spectrum. Consecutive spectra were identical. Average of *ca.* 4 spectra were sufficient to obtain an optimal signal to noise. *In situ* spectroelectrochemical XANES measurements were performed without any flow of the sample. Measurements were performed 2 minutes after the starting of the controlled potential electrolysis, time in which the current stabilizes. When performing spectroelectrochemical experiments, a Bio-logic potentiostat interfaced with the EC-Lab software was used. The raw data collected by XANES was processed (normalization, pre-edge and post-edge analysis) by using the Athena software.<sup>6</sup>

In order to obtain the pre-edge peak, two possibilities can be considered as described in chapter III. In this manuscript, the 1st inflection point was considered. For doing this, the 1st derivative was required. Figure C.3 shows the 1st derivative of a single spectrum obtained for the 2 mM solution of  $[\text{Fe}^{\text{III}}(\text{TPP})]\text{Cl} + 1e^-$  in DMF + 0.1 M TBAPF<sub>6</sub> under argon (grey – dottle line). As observed, the data is noisy due to the low concentration, for XANES measurements of the probed element, making difficult the determination of the experimental parameters. By using the smooth data tool of the software Athena, a smoothed signature for the same species is obtained (black - solid line).

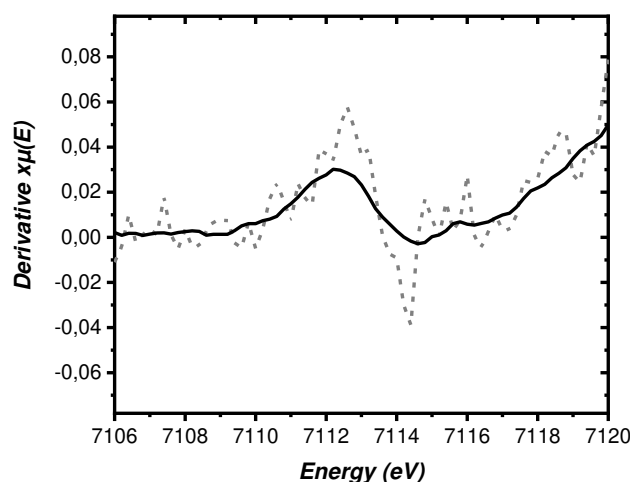


**Figure C.3.** Comparison of the first derivative spectra of a 2 mM solution of  $[\text{Fe}^{\text{III}}(\text{TPP})]\text{Cl}$  in DMF + 0.1 M TBAPF<sub>6</sub> under argon before (grey – dottle line) and after smoothing (black – solid line).

Considering the smoothed data, a comparison between the raw spectrum and the first derivative can be performed. Figure C.4 shows the different spectral points that allow the determination of the pre-edge peak:

- 1) The O-crossing line of the 1<sup>st</sup> derivative giving the position of the peak top of the raw spectrum
- 2) The peak top of the 1<sup>st</sup> derivative giving the 1<sup>st</sup> inflection point in the raw spectrum (method used to determine the pre-edge peak energy positions in this manuscript)

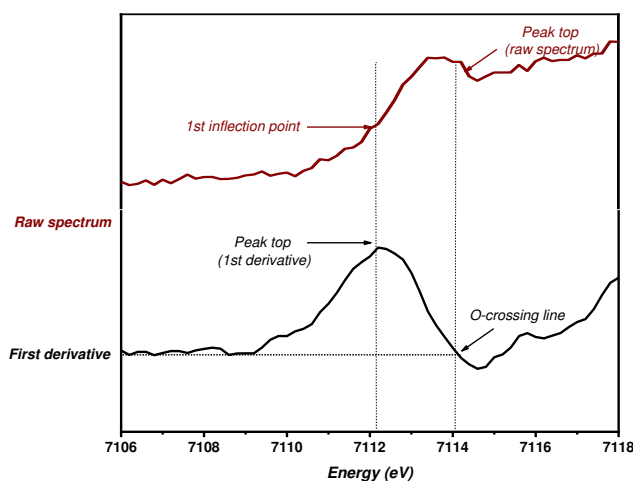


**Figure C.4. Determination of the pre-edge peak energy position.**

The main edge energy position was determined, as discussed in chapter III, by considering the half-edge jump position (i.e. 0.5) of the normalized spectrum.

Details on the synchrotron as well as the beamline and its components are summarized in appendix B. The cells as well as experimental setup to carry these experiments are described in appendix D.

The energy resolution of the Si(111) monochromator of the LUCIA beamline is of 1 eV at 7200 eV. The energy stepsize used during XANES spectra collection were 0.2 eV. In the pre-edge and main edge regions.

### C.2.3 UV-Vis spectroscopy

UV-Vis absorption measurements were performed on a Cary 60 spectrophotometer from Agilent Technologies. For routine UV-Vis characterization experiments a conventional quartz cell (1 cm length) was used. The experimental conditions were set at a normal mode. Data were collected and analyzed by using the software CaryWin Scan Application. For spectroelectrochemical UV-Vis experiments a thin layer cell (described in appendix D) was

used. The scan control was selected in fast mode, with 0.1 counts meaning of a number of 100 spectra for 10 minutes of measurement. In both cases, the spectral region was set from 280 to 800 nm. UV-Vis spectroelectrochemical measurements started after setting a linear scan voltammogram and starting a controlled potential electrolysis to the specific reduction potential.

#### C.2.4 Infrared spectroscopy

Infrared measurements were recorded on the AILES beamline in SOLEIL. IR spectra were measured at  $4\text{ cm}^{-1}$  resolution using a vacuum evacuated ( $10^{-5}$  mbar) Bruker IFS125 spectrometer of the beamline AILES connected to the synchrotron source. The spectrometer is outfitted with  $6\text{ }\mu\text{m}$  mylar beam splitter and Si bolometer detectors. Each single spectrum resulted from averaging approximately 50 scans. Mid-IR region between  $850\text{ cm}^{-1}$  to  $3500\text{ cm}^{-1}$  was considered. Spectra were recorded at room temperature. IR spectroelectrochemical experiments were performed at a concentration of 2 mM for the catalyst.

In order to maximize the signal from the species formed at the surface of the electrode, a reflectance configuration was chosen, with incident an outgoing angle of  $60^\circ$  with respect to the working electrode plane. The reflectance mode provides a signal twice as good as transmission, since the beam probes the sample on the way in and on the way back (see figure C5 for a scheme of the optical path). The dimensions of the cell therefore need to be optimized to provide a layer of liquid thick enough to obtain sufficient signal, and yet not too thick to avoid absorption of the beam. The thickness of the liquid layer was tuned from  $25$  to  $200\text{ }\mu\text{m}$  by using Kapton spacers of  $25\text{ }\mu\text{m}$  each. In addition to this, differential spectroscopy is used for data analysis, in order to remove the background signal from the solvent, electrolyte, and optical path (diamond window). Further experimental specifications and cell required for these experiences is further described in appendix D.

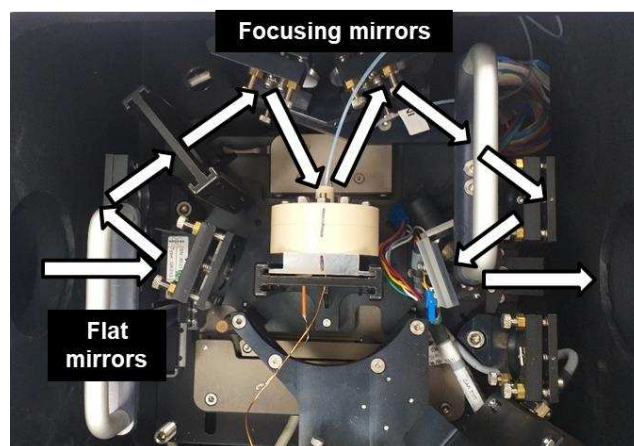


Figure C.5. Photograph of the top view of the IR spectroelectrochemical cell in the AILES beamline station showing the beam path of the reflectance configuration.



## C.3 Sample preparation

### C.3.1 Spectro(Electro)chemical catalysts samples

Generally, in all the electrochemical and XAS spectroelectrochemical experiments summarized in this manuscript the catalysts concentration was set at 2 mM. However, as discussed in chapter VI, some experiments performed in aqueous solution required the concentration increase to 20 mM. When these requirements were necessary, it is indicated in the manuscript.

Concerning UV-Vis spectroelectrochemical experiments, sample concentration varies depending on the range of study (analysis of Soret or Q-bands). Soret bands are usually high in absorbance between the 300-400 nm region, and require low concentrations, which was kept at 0.02 mM for these experiments. Q-bands are usually low in intensity; therefore, the concentration was kept at a higher range at 2 mM (like in XAS spectro(electro)chemical conditions as mentioned above). Finally, for all cases, electrolyte (TBAPF<sub>6</sub>) concentration was maintained at 100 mM whereas solvent volume was set at 6 mL since at this range all the cell was filled, and electrodes were immersed in the solution.

**Table C.1. Concentrations required for sample preparation**

<i>Component</i>	<i>Concentration (mM)*</i>	<i>Molecular weight (g/mol)</i>
[Fe <sup>III</sup> (TPP)]Cl	2	704.03
[Fe <sup>III</sup> (TPPS)]Cl	2	1024.30
[Fe <sup>III</sup> (-p-TMA)]Cl	2	1078.26
TBAPF <sub>6</sub>	100	387.43

\* Concentration was kept in 2 mM unless it is mentioned differently in the text.

### C.3.2 Other samples

#### - Iron chloride

Iron(III) chloride (Fe<sup>III</sup>Cl<sub>3</sub>).6H<sub>2</sub>O solution (2.0 mM – 3.2 mg) was prepared in the presence of TBAPF<sub>6</sub> (0.1 M - 232.5 g) as electrolyte in 6 mL DMF. Iron(II) chloride (Fe<sup>II</sup>Cl<sub>2</sub>) solution was prepared following same concentrations than for the previous case (2.0 mM – 1.5 mg). However, this sample was always prepared inside of a glove box (H<sub>2</sub>O and O<sub>2</sub> content ≤ 2.5 ppm) in order to avoid oxidation of the iron center which easily occurs for this salt in the presence of O<sub>2</sub>. The sample was then transferred under inert atmosphere to the beamline.



### *- Pellets preparation for XAS studies*

In order to analyze solid samples by XAS, pellets must be prepared. Pellets are usually prepared by mixing a specific amount of the sample of study with a supported that must not interfere with the analyte. Usually, supporting materials such as graphite or boron nitrite are used. In the present case, pellets were prepared with a proportion of 1:10 (w/w, analyte/support). Both powders are weighted, crushed and mixed together in a mortar and transferred into a pellet pressing tool. The powder is then pressed by using a manually operated hydraulic press. In these conditions, homogeneous and smooth pellets were obtained.

## **C.3.3 Synthesis**

### **C.3.3.1 Catalyst's preparation**

The procedure was adapted from the thesis of Dr. Arnaud Tatin.<sup>7</sup>

The only catalyst that was chemically prepared was the [Fe-(p-TMA)]Cl<sub>5</sub>. Its metalation was performed from the commercial free-base porphyrin and iron(II) ammonium sulphate hexahydrate [(NH<sub>4</sub>)<sub>2</sub>Fe(SO<sub>4</sub>)<sub>2</sub>].6H<sub>2</sub>O (Mohr's salt). It has been reported that this salt is more stable than other iron precursor such as iron(II) bromide.

5,10,15,20-tetra(N,N,N-trimethyl-4-anilinium)porphyrin tetrachloride (124.5 mg, 0.13 mmol) was dissolved in H<sub>2</sub>O (50 mL) in a double neck Schlenck flask and degassed under Argon. Mohr's salt (394.9 mg, 1.0 mmol) was added into the free-base solution under Argon and degassed for another 20 minutes. The solution was heated up to 85 °C during 3 hours under Ar atmosphere. After this time, heating was stopped, and the solution was cooled down. NH<sub>4</sub>PF<sub>6</sub> (205.4 mg, 1.3 mmol) was dissolved in H<sub>2</sub>O (50 mL). This solution was slowly added into the metalated iron porphyrin solution, in which a precipitate was observed. The solution was centrifugated at 20000 rpm for 20 minutes and washed two times with more NH<sub>4</sub>PF<sub>6</sub> solution. The last wash is performed with H<sub>2</sub>O at 0 °C. It was left to dry overnight under vacuum. The yield obtained is 87.3%.

The dry powder obtained is dissolved in 5 mL of an acetone: chloroform (1:1) mixture and centrifuged at 20000 rpm for 10 minutes. The supernatant is taken and 25 mL of acetone are added. This procedure eliminates traces of free-base that did not react during metalation. The solution is further transferred to a round-bottom flask and left under stirring in an ice bath. HCl (37%) is slowly added until a precipitate is observed (approximately 2.5 mL of HCl are sufficient to precipitate the iron porphyrin containing anilinium counter-ions). The resulting suspension is sonicated for 10 minutes and further centrifuged at 20000 rpm during 10 more minutes. The final product is washed with acetone (25 mL), to remove any unreacted PF<sub>6</sub><sup>-</sup> salts. The product is finally dissolved in the lowest amount of methanol as possible (~2 mL)

and an excess of ethyl acetate is added until a dark red precipitate is observed. Finally, a last centrifugation is performed. The product is dried overnight in vacuum. Yield: 89.9 %. UV-Vis (DMF): Soret band – 418 nm; Q-bands: 507, 570, 644, 684 nm. CV (0.5 mM iron porphyrin in DMF): three reversible waves are reported at -0.14 V (1<sup>st</sup> wave), -0.95 V (2<sup>nd</sup> wave) and -1.52 V (3<sup>rd</sup> wave) vs SCE. XANES: as reported in chapter VI.

### C.3.3.2 Synthesis of $[Fe^{II}TPP]$

All procedures were performed inside a glove box. All the liquids and powders were dried as indicated above. The procedure follows those reported in previous publications.<sup>8,9</sup>

#### - *Reducing agent preparation (Sodium anthracenide)*

Anthracene (610 mg –  $3.4 \times 10^{-3}$  mol) and solid sodium (76 mg –  $3.4 \times 10^{-3}$  mol) were mixed in a conical flask with dry/distilled THF (15 mL). The dark blue solution was left stirring for 24 hours, until all the sodium was dissolved. Sodium anthracenide (0.2 M) was obtained, without requiring further purification.

#### - *Reduction reaction*

$[Fe^{III}(TPP)]Cl$  (50 mg – 0.071 mmol) was dissolved in dry/distilled THF (6 mL). The brown solution was left under agitation for 30 minutes at -35 °C. Sodium anthracenide (0.2M - 0.355 mL) was added slowly with a syringe while stirring at -35 °C. The solution was kept at this temperature for 2 days.

#### - *Crystallization*

The solution was transferred to a larger volume flask (20 mL capacity). Dry hexane was added (20 mL) slowly on top of the solution, without perturbation, in order to create two separate phases. The solution was left at -35°C in the glove box during approximately 12 days. After this period crystals were observed at the bottom of the vial, while the solution at the top was yellowish. The solution was discarded and the solid was washed several times with hexane. The shining dark purple powder/crystals were dried in vacuum. When dissolved in DMF, the solution was of an intense red color.

### *Characterization*

#### - *UV-Vis*

Solutions of  $[Fe^{II}(TPP)]$  (2.0 mM –  $4.0 \times 10^{-3}$  mmol) in DMF (2 mL) were prepared in the glove box. They were added to a dry and sealed quartz cuvette (1.0 cm optical path). Measurements were performed in the UV-Vis spectrometer described above, outside of the glove box. Q-bands (see figure C.6) present features at 534, 564 and 606 nm and match those observed for the species generated by electrochemical reduction of  $[Fe^{III}(TPP)]Cl$  in DMF



previously reported in this manuscript (chapter VI). This indicates the formation of  $[\text{Fe}^{\text{II}}(\text{TPP})]$ , as further confirmed by XAS spectroscopy.

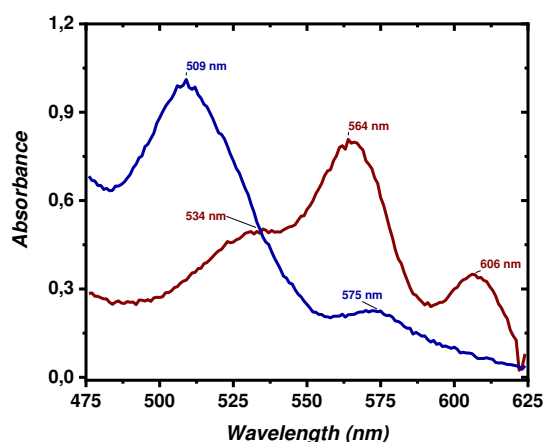
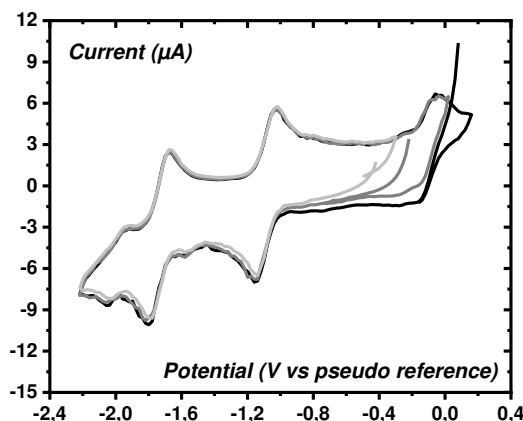


Figure C.6. UV-Vis Q-bands of a 2 mM solution of  $[\text{Fe}^{\text{III}}(\text{TPP})]\text{Cl}$  (blue) and chemically generated  $[\text{Fe}^{\text{II}}(\text{TPP})]$  in DMF under Ar.

#### - Cyclic voltammetry (CV)

The chemically prepared  $[\text{Fe}^{\text{II}}\text{TPP}]$  was analyzed by CV inside the glove box where it was synthesized.  $\text{TBAPF}_6$  (0.1 M – 0.310 g) was dissolved in DMF (6 mL).  $[\text{Fe}^{\text{II}}(\text{TPP})]$  (0.5 mM – 2.0 mg) was added to the electrolyte-solvent solution. The cell setup was constituted as above described, by a glassy carbon working electrode (3 mm diameter), a platinum wire as counter electrode and a carbon foam reference electrode prepared as previously reported.<sup>10</sup> Figure C.7 shows the CV obtained for the chemically reduced  $[\text{Fe}^{\text{II}}(\text{TPP})]$  species. Starting from a potential between 0 V and -0.3 V vs pseudo reference, two reversible waves are observed, which can be attributed to the reduction of  $[\text{Fe}^{\text{II}}(\text{TPP})]$  by one and two electrons respectively. At the back scan the appearance of a cathodic wave is presented, which can be attributed to the generation of Fe(III) species at the electrode surface. A reversible wave at -2.0 V vs pseudo reference can be attributed to a residual anthracene in the media.<sup>11</sup>





**Figure C.7. Cyclic voltammetry of a 0.5 mM solution of [Fe<sup>II</sup>(TPP)] in DMF + 0.1 M TBAPF<sub>6</sub> under Ar at different starting potentials: 0 V (black), -0.2 (dark grey) and -0.4 V (light grey) vs pseudo reference in a conventional electrochemical cell.**

**- XAS (solid state)**

The [Fe<sup>II</sup>(TPP)] sample was transported in anaerobic conditions to the Synchrotron SOLEIL and store in a glove box. [Fe<sup>II</sup>(TPP)] (2.0 mg – 3.0 x 10<sup>-3</sup> mmol) was placed as a powder inside the dry X-ray spectroelectrochemical cell A in the glove box. The cell was closed with the glassy carbon WE and sealed with a cap and screws. The cell was transported to the LUCIA beamline chamber under anaerobic conditions and connected to the liquid circulation system. After installation in the experimental chamber, the system was pumped under vacuum. The XAS spectra collected on the resulting dry, solid sample are presented in chapter VI.

**- XAS (solution).**

[Fe<sup>II</sup>(TPP)] (2.0 mM – 4.0 x 10<sup>-3</sup> mmol) powder was incorporated in the spectroelectrochemical cell (A) and transported to the beamline station as detailed above. TBAPF<sub>6</sub> (0.1 M – 0.2 mmol) in DMF (2 mL) solution was flown inside the cell chamber under vacuum. XANES spectra were recorded immediately after dissolving the powder in the electrolyte-solvent solution. XAS spectra of the resulting solution are shown in chapter VI.



**C.4. References Appendix C**

- (1) Mongay, C.; Cerdà, V. A Britton-Robinson Buffer of Known Ionic Strength. *Ann. Chim.* **1974**, *64*, 409–412.
- (2) Armarego, W. L. F. Chapter 3 - Purification of Organic Chemicals. In *Purification of Laboratory Chemicals (Eighth Edition)*; Armarego, W. L. F., Ed.; Butterworth-Heinemann, **2017**; pp 95–634.
- (3) Scott, R. A.; Lukehart, C. M. *Applications of Physical Methods to Inorganic and Bioinorganic Chemistry*; John Wiley & Sons, **2007**.
- (4) Burfield, D. R.; Smithers, R. H. Desiccant Efficiency in Solvent Drying. 3. Dipolar Aprotic Solvents. *J. Org. Chem.* **1978**, *43* (20), 3966–3968.
- (5) Center for X-ray Optics and Advanced Light Source. Lawrence Berkeley National Laboratory. *X-Ray Data Booklet*. **2009**.
- (6) Ravel, B.; Newville, M. Athena, Artemis, Hephaestus: Data Analysis for X-Ray Absorption Spectroscopy Using IFEFFIT. *J. Synchrotron Rad* **2005**, *12* (4), 537–541.
- (7) Tatin, A. Electrochemical CO<sub>2</sub> Splitting into CO and O<sub>2</sub> in Neutral Water Using Earth-Abundant Materials. *Université Paris-Diderot*. Doctoral Thesis. **2016**.
- (8) Römelt, C.; Song, J.; Tarrago, M.; Rees, J. A.; van Gastel, M.; Weyhermüller, T.; DeBeer, S.; Bill, E.; Neese, F.; Ye, S. Electronic Structure of a Formal Iron(0) Porphyrin Complex Relevant to CO<sub>2</sub> Reduction. *Inorg. Chem.* **2017**, *56* (8), 4745–4750.
- (9) Mashiko, T.; Reed, C. A.; Haller, K. J.; Scheidt, W. R. Nature of Iron(I) and Iron(0) Tetraphenylporphyrin Complexes. Synthesis and Molecular Structure of (Dibenzo-18-Crown-6) Bis(Tetrahydrofuran)Sodium (Meso-Tetraphenylporphinato) Ferrate and Bis [Tris(Tetrahydrofuran)Sodium] (Meso-Tetraphenylporphinato)Ferrate. *Inorg. Chem.* **1984**, *23* (20), 3192–3196.
- (10) Weingarth, D.; Foelske-Schmitz, A.; Wokaun, A.; Kötz, R. PTFE Bound Activated Carbon—A Quasi-Reference Electrode for Ionic Liquids. *Electrochemistry Comm.* **2012**, *18*, 116-118.
- (11) Connelly, N.G.; Geiger, W.E. Chemical Redox Agents for Organometallic Chemistry. *Chem. Rev.* **1996**, *96*, 2, 877-910.

# Appendix D

---

## Spectroelectrochemical cells

### Content

---

<b>D.1</b>	X-Ray Absorption (XAS) .....	187
<b>D.1.1</b>	Cell A .....	187
<b>D.1.2</b>	Cell B .....	191
<b>D.2</b>	Ultraviolet-Visible (UV-Vis) .....	195
<b>D.3</b>	Reflectance infrared (IR).....	196
<b>D.3.1</b>	Constraints .....	196
<b>D.3.1</b>	Vacuum-chamber compatible cell.....	197
<b>D.4</b>	References .....	200



As described in chapter V, spectroelectrochemical experiments demands the development of instrumentation, that allows not only the recording spectra with good signal-to-noise, but also an optimal electrochemical correlation and maximum conversion of species in the shortest period of time. This appendix is entirely devoted to the description of instrumentation, classifying them by the spectroscopic method used throughout this thesis.

## D.1 X-Ray absorption (XAS)

Several XAS spectroelectrochemical cells have been designed and used by the team of B. Lassalle-Kaiser at SOLEIL in the last decade.<sup>1-4</sup> One of these cells was further optimized to suit the requirements of homogeneous electrochemistry in organic solvents (cell A), while another one was optimized for time-resolved spectroelectrochemical XAS experiments (cell B). These two cells are described below.

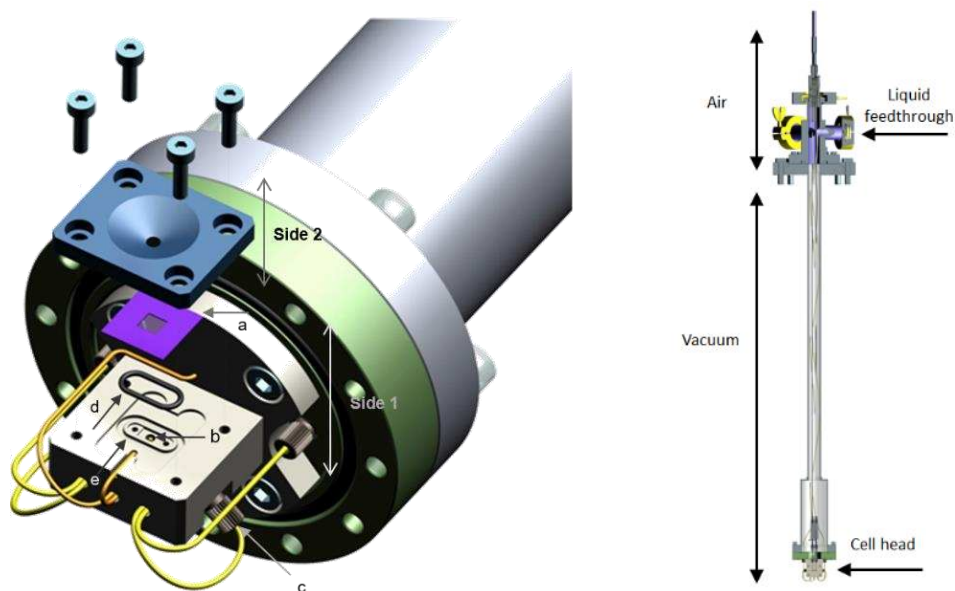
### D.1.1 Cell A

This XAS spectroelectrochemical cell was first built to analyze solutions, including under electrochemical conditions, with tender X-rays, while withstanding the low pressure of the LUCIA beamline experimental chamber. It is inspired from a cell developed at the Advanced Light Source at the Lawrence Berkeley National Laboratory and by a gas cell developed at MAX IV.<sup>5</sup>

The design of this cell was performed in close collaboration with M. Victor Pinty from the mechanical engineering group of Synchrotron SOLEIL. The cell consists in three main parts, as shown on scheme D.1. Side 1 constitutes the body of the cell, built in polyether-ether ketone (PEEK). This polymer is chemically resistant, does not degas under vacuum, and offers good mechanical machining properties. Moreover it does not contain significant amounts of impurities that could perturb the XAS signal. The liquid compartment is a rectangle of 2(v) x 6(h) x 0.2(d) mm. A platinum grid placed at the bottom of this compartment is used as counter electrode. It is electrically contacted by silver epoxy glue to a copper wire, which are never in contact with the solution. A silver wire is inserted, on the side of the main body, to serve as a pseudoreference electrode. The iron porphyrin second wave ( $\text{Fe}^{\text{II}}/\text{Fe}^{\text{III}}$ ) was used as internal standard, to monitor any potential shifts from the reference. The working electrode is a glassy carbon (GC) film from HTW GmbH under the name SIGRADUR® and of dimensions 10 x 10 x 0.06 mm. Being X-Ray transparent, it serves as a cell window, separating the sample solution and the X-Ray chamber. The window cap (side 2) is built in PEEK and has a hole for incoming and outgoing X-rays of 4 mm in diameter. The liquid compartment has a volume of 200  $\mu\text{L}$ , which allows a fast (2-5 min) electrochemical conversion of the solution when a constant potential is applied.



The liquid to be studied is circulated in the cell with either a peristaltic (Ismatec) or a syringe pump (KFTechnology®). Teflon tubings are connected from the cell directly to the outside of the chamber by a feedthrough flange on top of the cell holder (side 3). The cell is attached vertically to this holder, as shown in scheme D.1. The holder is inserted in the experimental chamber on an XYZ stage, which is required for cell alignment. All the parts mentioned above as well as some schemes and pictures of cell A are shown in scheme D.1 and figure D1.



**Scheme D.1. Vacuum compatible XAS spectroelectrochemical cell A. Left: Part 1: PEEK cell body. Components: a. Glassy carbon film electrode; b. Pt grid electrode; c. Ag wire pseudoreference electrode; d. o-ring; e. Liquid feedthrough. Part 2: PEEK cap. Right: Part 3: Stainless-steel liquid feedthrough tube and connection with the cell head.**

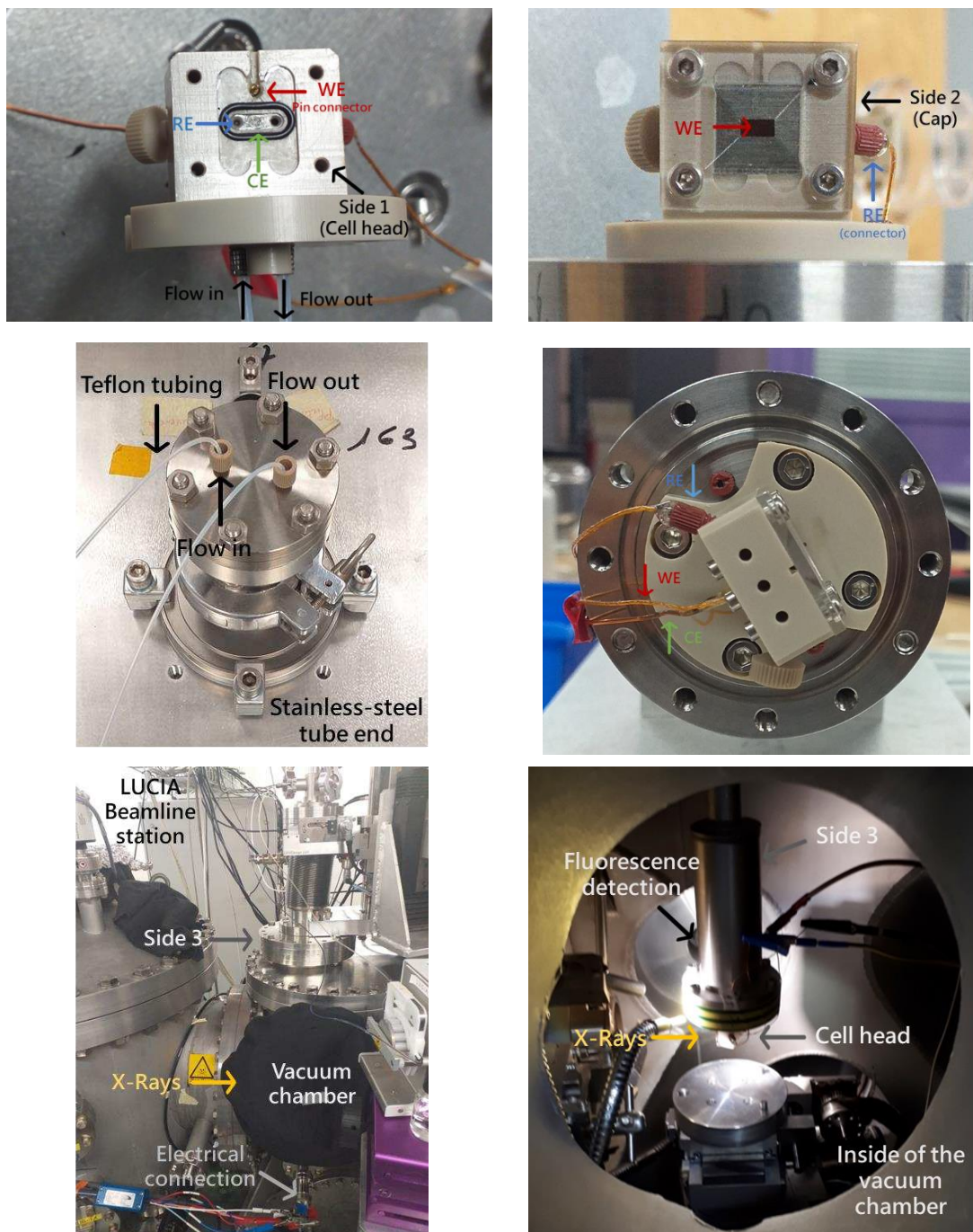


**Figure D.1.** Photographs of cell A installed on the LUCIA Beamline. Top – left : front view of the open cell head. Top – right: front view of the closed cell head showing part 2. Central – left: stainless steel tube (part 3) showing the liquid feedthrough and connections. Central – right: cell head assembly with part 3, with indications of the electrical connections. Bottom – left: LUCIA Beamline station with the cell installed in the vacuum chamber. Bottom – right: inside of the vacuum chamber with the cell oriented at 45° degrees with respect to the incident beam and fluorescence detector. Abbreviations: CE: counter electrode – Platinum mesh. RE: reference electrode – silver wire. WE: working electrode – glassy carbon film.



An important consideration when switching from aqueous to organic solvents is to find the right material for the o-ring used to ensure liquid and gas tightness. DMF is an excellent solvent for electrochemical reactions due to its large electrochemical range and stability. However, it penetrates almost all polymers and make them swell. Therefore, several o-ring materials (from the Sephat® company) were initially tested in DMF, as shown in table D.1. All the materials showed relatively good resistance towards DMF except for fluorocarbon (FPM), which swelled in a matter of minutes. Perfluoroelastomer (FFKM) and Silicon (MVQ) did not show any evolution for several minutes but did not withstand longer tests (>2h). Polytetrafluoroethylene (PTFE) o-ring showed extremely high solvent resistance, but its stiffness prevented from using it as a sealing material. Finally, ethylene propylene diene monomer (EPDM) was the only material that showed excellent DMF, X-Rays and vacuum resistance during long term experiments required for beamtime sessions. Therefore, EPDM o-rings were used for all the following experiences.

**Table D.1. O-ring material resistance on DMF and vacuum**

Material	Resistance		
	1	2	3
Fluorocarbon (FPM)	X		
Ethylene propylene diene monomer (EPDM)			X
Polytetrafluoroethylene (PTFE)			X
Perfluoroelastomer (FFKM)		X	
Silicon (MVQ)		X	

1 Poorly resistant (it breaks, degrades and/or swells after a few minutes)

2 Resistant (it breaks, degrades and/or swell after a few hours)

3 Highly resistant (it does not break, degrade and/or swell after many hours of continuous use)

Another important consideration while determining the parameters for the XAS experiments by using cell A was the determination of the concentration range and the detection mode. In order to do, we recorded the Fe K-edge XANES spectrum of a 20 mM aqueous solution of iron(III)-tetrakis(p-sulfonatophenyl) porphyrin chloride, abbreviated as  $[\text{Fe}^{\text{III}}(\text{TPPS})]\text{Cl}$ , in transmission and fluorescence mode. This porphyrin was selected for this cell test experiments, since it is soluble in water, even at high concentrations in the porphyrin range, for instance 20 mM, which are required for transmission mode experiments. This, however, is not the case for  $[\text{Fe}^{\text{III}}(\text{TPP})]\text{Cl}$ , since it is not soluble in water and in DMF the maximum concentration that allows its solubility is of approximately 5 mM. For this reason, it is important to remember that common electrochemical experiments are performed in around 0.5 to 2 mM porphyrin concentrations. Figure D.2 shows the  $[\text{Fe}^{\text{III}}(\text{TPPS})]\text{Cl}$  recorded in transmission mode (red), which evidence the presence of glitches at *ca.* 7140 eV being a



demonstration of the sub-optimal normalization of the transmitted beam ( $I_1$ ) by the incoming beam ( $I_0$ ), as a result of a high concentration. Although the S/N ratio of the fluorescence signal (figure D.2 – black trace) is not as good as the transmission one, the glitches are essentially suppressed. All experiments performed during this project were therefore collected in fluorescence mode. In order to find a balance between good S/N, acquisition time and electrochemical relevance, we used a 2mM concentration as a standard for all solution experiments.

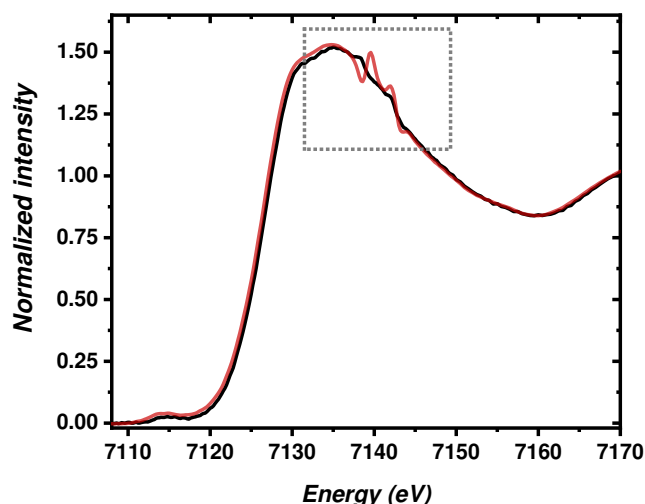
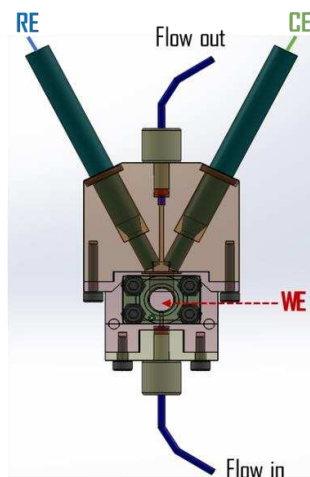


**Figure D.2.** Fe K-edge XANES spectra comparison of a aqueous solution 20 mM  $[\text{Fe}^{\text{III}}(\text{TPPS})]\text{Cl}$  + 0.1 M KCl recorded in cell A by using transmission mode (red) and fluorescence mode (black). Glitches are indicated on the grey dotted square.

### D.1.2 Cell B

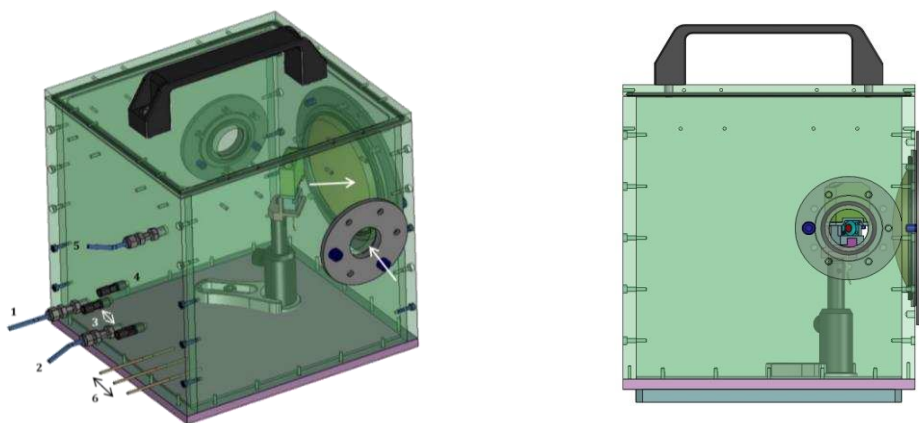
Cell B was designed and built in close collaboration with the microfluid laboratory (M. B. Maurice and M. S. Lefrançois) of the synchrotron SOLEIL. Scheme D.2 shows a figure of the cell. It consists of three main parts. The main body, built in PEEK for organic solvent resistance, hosts the analysis compartment and the liquid inlet (from the bottom). The second compartment is fixed on top of the first one and holds the liquid outlet (at the top). Two glass frits are inserted on top of this compartment, sealed with EPDM o-rings to ensure liquid and gas tightness. The two glass frits are filled with solvent-electrolyte solutions and host a CE (Pt mesh) and an RE (leakless Ag/AgCl). All the parts in this main body were fixed by mean of screws. The third part is a cap, also built in PEEK that allows incoming and outgoing X-Rays to and from the sample. A glassy carbon film was also used as working electrode.





**Scheme D.2.** XAS spectroelectrochemical cell B. Components: WE: Glassy carbon film electrode; CE: counter platinum mesh electrode inside of a glass frit container, RE: Ag/AgCl microelectrode inside of a glass frit container. Liquid feedthrough as indicated in the scheme.

When toxic gases are used, a secured gas delivery and extraction system must be setup. For this reason, a specific setup was required when CO, a lethal gas, was used in our experiments. A scheme of this “CO box”, developed by M. S. Lefrançois and G. Alizon, is shown in scheme D.3. Three windows were created in the box: the ones facing each other for transmission experiments, and the one at 90° from the two others for fluorescence experiments. These windows were sealed with thin (25µm) Kapton® foils. Gas and liquid feedthroughs were arranged on one of the walls of the box.

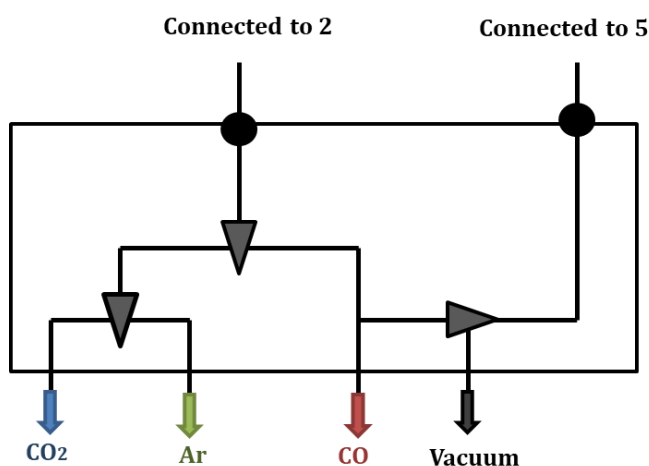


**Scheme D.3.** Left: “CO box” components. 1. Gas inlet to fill the box, 2. Gas inlet to saturate the liquid sample, 3. Liquid feedthroughs in and out, 4. Gas feedthrough for *in situ* gas chromatography detection (not used so far), 5. Gas exit (from the sample and the box) connected to a vacuum extraction system, 6. Electrical connectors. White arrows: indicate the incident beam and outgoing photons towards fluorescence detector. Right: front view of the box “sitting” on top of the X-Ray beam.

Further explanation of the different gas, liquid and electrical connections are described below.

#### - Gas system (Scheme D.4)

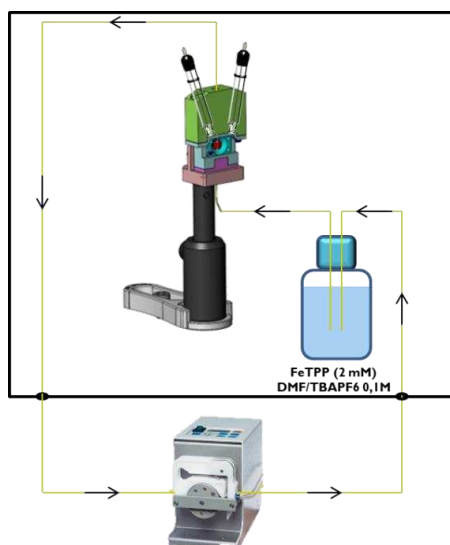
- **Part 1** allows the inlet of an inert gases such as argon or helium or can be adapted to a vacuum system to get the entire box under vacuum.
- **Part 2** allows the gas saturation of the solution inside of the box (Ar, O<sub>2</sub>, CO<sub>2</sub> or CO as requested). Since the gas bubbles out of the sample solution, the box gets filled with it. The box was therefore kept under vacuum to avoid any accumulation of CO.
- **Part 5** is the gas outlet that is connected to a pump and to an evacuation system to remove any trace of dangerous gas outside the beamline chamber.
- Another feedthrough was inserted, indicated as part 4, to allow the future analysis by *in situ* gas chromatography detection.
- Finally, gas detection was ensured by placing a CO detector inside the box. Support from the safety team of Synchrotron SOLEIL also guaranteed a maximal safety.



Scheme D.4. Gas flowing system.

#### - Liquid system (Scheme D.5)

To allow the circulation of liquids, two feedthroughs are placed in the wall of the box, indicated as 3 in scheme D.3. The circulation was ensured by a syringe pump or a peristaltic pump as shown in scheme D.5.



Scheme D.5. Liquid circulation system

**- Electrical connections**

Electrical connections, indicated in scheme D.3 as 6, were ensured by three copper rods inserted and glued in the wall of the box.

Some schemes and pictures of the designed cell B and the “CO box” in the SAMBA beamline end-station are shown in figure D3.

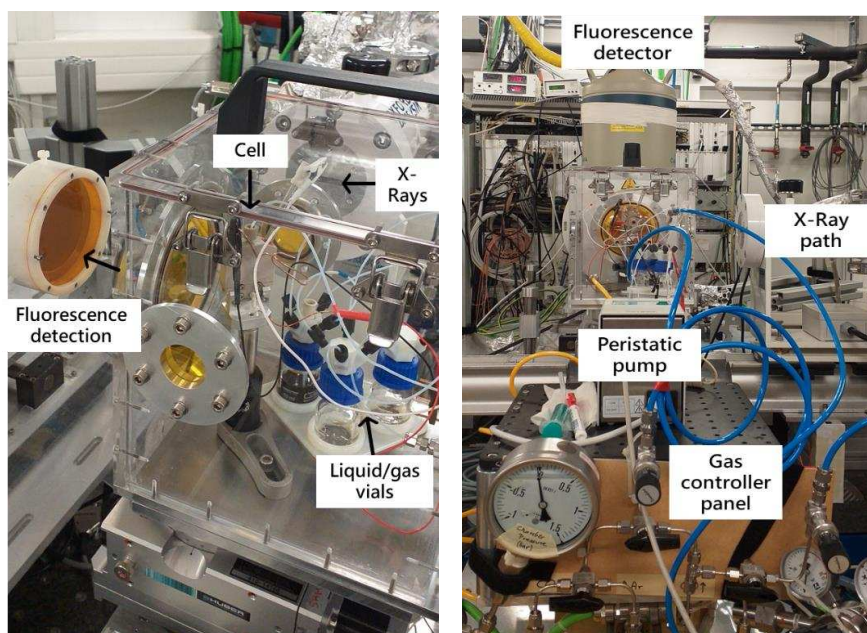
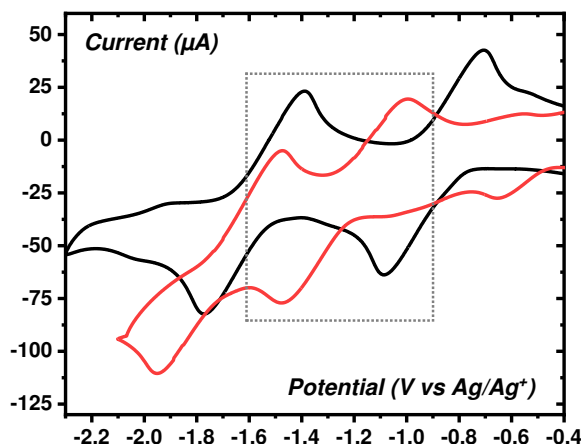


Figure D.4. Photograph of cell B and the associated setup on the SAMBA Beamline. Top – left: zoom of the box with the cell and liquid/gas vials inside. Top – right: side view with indication of the fluorescence detector, gas controller panel and peristaltic pump. Bottom: complete view of the set-up during operation.

First trial on spectroelectrochemical measurements on iron porphyrins in the presence of CO was performed in SAMBA beamline in the synchrotron SOLEIL. All the instrumentation was properly set for measurements ensuring security and proper detection of CO. Cyclic voltammogram performed in a solution of  $[\text{Fe}^{\text{III}}(\text{TPP})]\text{Cl}$  in DMF + 0.1 M TBAPF<sub>6</sub> saturated with CO, indicates the presence of CO in interaction with iron porphyrin in solution (figure D.4), with the shift of the reversible wave at the  $\text{Fe}^{\text{II}}$ /formally “ $\text{Fe}^{\text{I}}$ ”, as described in chapter II.



**Figure D.5.** Cyclic voltammogram  $[\text{Fe}^{\text{III}}(\text{TPP})]\text{Cl}$  in DMF 0.1 M TBAPF<sub>6</sub> under argon (black) and CO (red) atmosphere, recorded in the spectroelectrochemical cell B.

*Only second and third (last wave) are shown in the presence of argon.*

*Dotted grey square indicates the CV modifications in the presence of CO.*

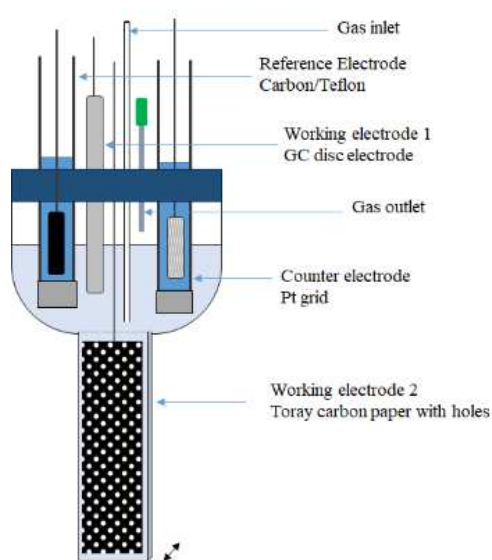
Nonetheless, further XANES spectroelectrochemical experiments requires setup optimization.

## D.2 Ultraviolet-Visible spectroscopy (UV-Vis)

UV-Vis spectroelectrochemistry consists of measuring the absorbance of electrogenerated species which are produced or consumed close to an optically transparent electrode. Electrodes must therefore be built in a material that allows the transmission of UV-Visible photons. In order to fulfill these requirements a cell have been developed by the LEM team,<sup>6</sup> with an optimized version shown in scheme D.6. It consists of a quartz UV-Vis cell, with an optical path of 1 mm, which have been modified with a glass compartment in which the bulk solution and electrodes are located. The counter electrode is a platinum grid, which is inserted in a glass frit to avoid side reactions in the bulk. The reference electrode is either  $\text{Ag}/\text{AgNO}_3$  in acetonitrile or an activated carbon pseudoreference electrode.<sup>7</sup> A small glassy carbon (1.6 mm, Bio-logic – named 1) is inserted in the cell to record cyclic voltammograms, while controlled potential electrolysis are performed with a high surface working electrode (named 2). A carbon paper (Toray Alfa Aesar TGP-H-60) with holes made with a needle is used as



working electrode. This electrode avoids the generation of hydrogen as sometimes occurs with Pt grids and is more economical. For electrical connection, a gold (Au) thread is passed through the top holes and covered with Teflon tape to avoid contact with the solution. Finally, the cell is closed with a screw cap and a large silicon/PTFE septum which contains specific holes for all the required components.



**Scheme D.6.** UV-Vis spectroelectrochemical cell used during the experiments described in this manuscript.

*Credits for the scheme to: Dr. Nikolaos Kostopoulos. First version of the cell is described in reference 5.*

The system was always kept under inert atmosphere (Ar) or CO<sub>2</sub> when required. The sample was transferred from its original vial to the spectroelectrochemical cell with a cannula. In order to avoid water from the gas bottle or tubing, a CaCl<sub>2</sub> trap, similarly used in electrochemical experiments, was also connected to the gas tubing. All cell components were cleaned and dried in an oven at 100 °C. The spectroelectrochemical cell was set in a transparent support which was positioned in the spectrophotometer. In this manner, vibrations and movements were avoided which could interfere in the measurement.

### D.3 Reflectance infrared *in situ* spectroelectrochemical cell (IR)

#### D.3.1 Constraints

*Vacuum.* In order to reduce interferences due to air absorption, the *in situ* setup will be placed inside a vacuum chamber, therefore the cell must be built to withstand a primary vacuum.

*Materials.* In order to manipulate organic solvent, PEEK was chosen as material for the body of the cell, while EPDM o-rings were used for liquid and gas tightness (see part D1.1 for o-ring choice). In order to achieve good transmission in the far infrared region and resist the vacuum conditions, a diamond window (1° wedged CVD 300 μm thickness) was used. The



working electrode used was a glassy carbon film, which is appropriate for electrochemical measurements and a good mirror for reflectance IR measurements. A platinum wire was used as counter electrode and a silver wire was used as pseudo-reference electrode.

*Sample flow.* Inlet and outlet ports were placed on the front side (holding the diamond window) of the cell. PTFE tubings were used and connected to a feedthrough flange to a syringe pump outside of the vacuum chamber (Figure D5)

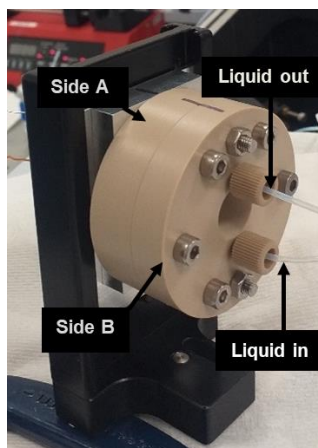


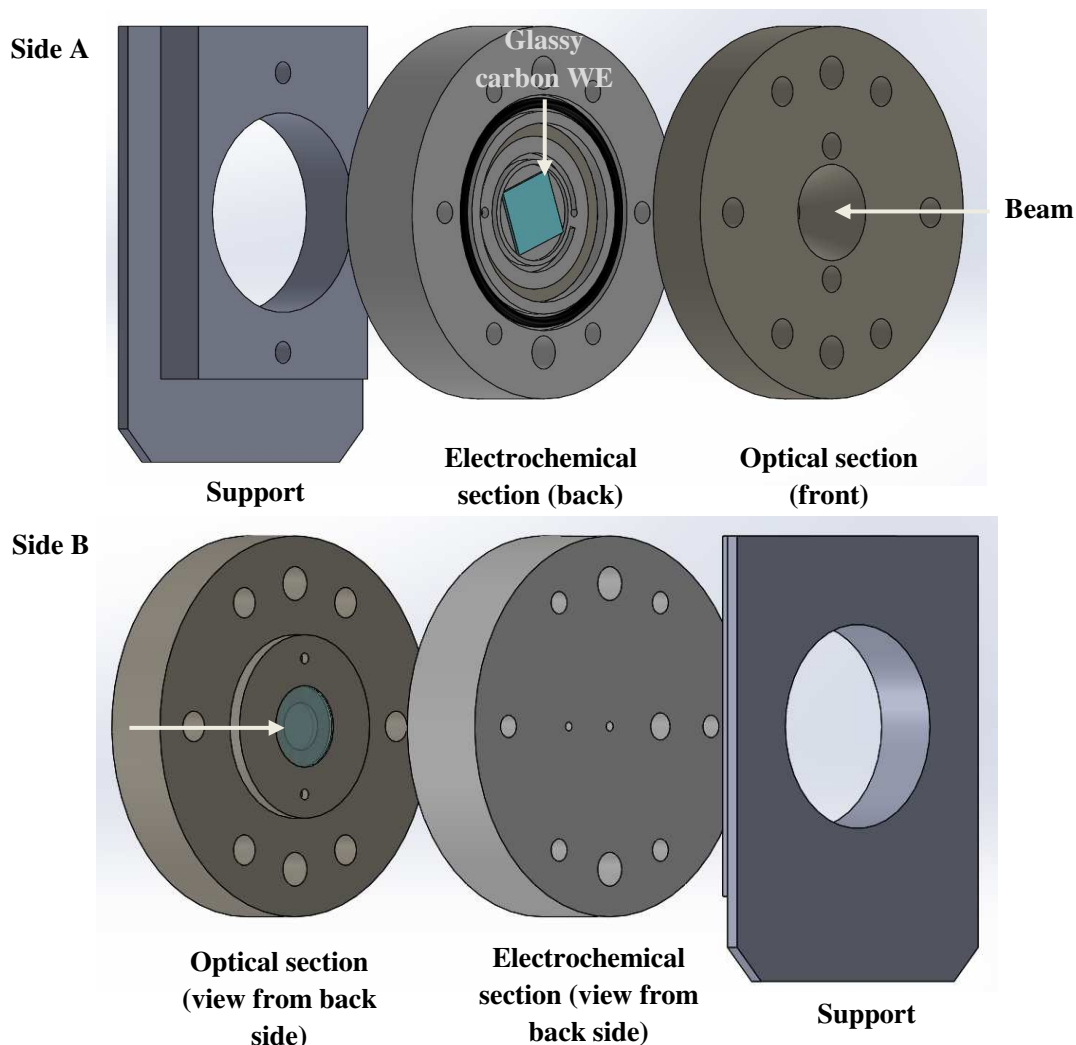
**Figure D.5.** Photograph of the IR cell installed on the AILES-C Beamline showing the flowing system indications.

### D.3.2 A vacuum-chamber compatible cell

In order to perform homogeneous CO<sub>2</sub> reduction by iron porphyrins at low concentration by differential IR spectroelectrochemistry, a new setup was developed. This was possible thanks to a close collaboration with the AILES beamline team (M. K. Rader and M. J.-B. Brubach). This design allows differential reflectivity measurements, and the thin layer configuration provides a fast electrochemical conversion of species.

The general scheme of the cell is shown in scheme D.7. Part A (top) shows the back side that holds the WE, CE and RE, whereas part B (bottom) shows the front side with the diamond window allowing the beam to go in and out of the cell.



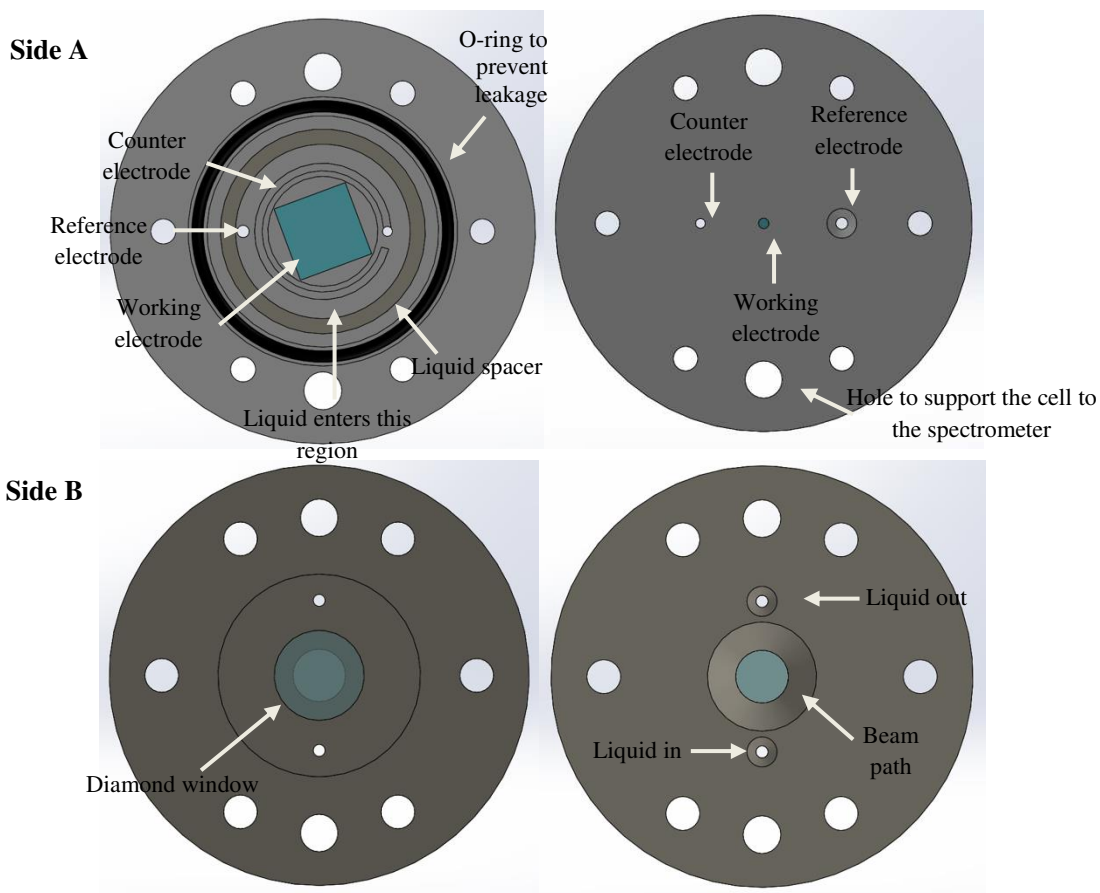


**Scheme D.7. Infrared spectroelectrochemical cell for reflectance measurements. Side A: Optical front part. Side B: Electrochemical part. Arrows indicate the beam path, the glassy carbon electrode and the diamond IR window.**

Scheme D.8 shows the front and back section of each part A and B with indications of each component of the cell. As previously indicated, part A (so-called electrochemical part) contain all the electrodes and electrical components, while part B (so-called optical part) contains the windows for IR measurements. As mentioned above, the WE is the same glassy carbon film as used for XAS-EC experiments, with surface area of 10 x 10 mm. The WE was electrically connected by means of a Cu wire that was glued with a conductive epoxy paste as for the XAS-EC cell A. The CE was a Pt wire (thickness = 0.8 mm), which was rolled in the compartment, as indicated in scheme D.8, and glued with epoxy at the back side of part A to prevent liquid leaks. Finally, a pseudo-reference Ag electrode was used as in XAS studies. The circulation of the liquid was performed by means of a peristaltic pump REGLO Digital from Ismatec®. Teflon tubings and liquid connectors were inserted into part B, as indicated on scheme D.8. The thickness of the liquid circulation area was adapted to provide



good electrochemical and spectroscopic signals. EPDM O-ring were used in the cell to prevent leakage. Finally, as observed in scheme D.8, part B contained a diamond window (1° wedged CVD 300 μm width) allowing the path of the beam towards the surface of the electrode.



**Scheme D.8. Parts of the IR spectroelectrochemical cell. Part A: Electrochemical. Part B: Optical. Arrows indicate the components of each parts.**





#### D.4 References Appendix D

- (1) Lassalle-Kaiser, B.; Zitolo, A.; Fonda, E.; Robert, M.; Anxolabéhère-Mallart, E. In Situ Observation of the Formation and Structure of Hydrogen-Evolving Amorphous Cobalt Electrocatalysts. *ACS Energy Lett.* **2017**, 2 (11), 2545–2551.
- (2) Lassalle-Kaiser, B.; Gul, S.; Kern, J.; Yachandra, V. K.; Yano, J. In Situ/Operando Studies of Electrocatalysts Using Hard X-Ray Spectroscopy. *J. Elect. Spect. Rel. Phenom.* **2017**, 221, 18–27.
- (3) Larquet, C.; Nguyen, A.-M.; Ávila-Gutiérrez, M.; Tinat, L.; Lassalle-Kaiser, B.; Gallet, J.-J.; Bournel, F.; Gauzzi, A.; Sanchez, C.; Carencio, S. Synthesis of Ce<sub>2</sub>O<sub>2</sub>S and Gd<sub>2</sub>(1-y)Ce<sub>2</sub>yO<sub>2</sub>S Nanoparticles and Reactivity from in Situ X-Ray Absorption Spectroscopy and X-Ray Photoelectron Spectroscopy. *Inorg. Chem.* **2017**, 56 (22), 14227–14236.
- (4) Cheaib, K.; Maurice, B.; Mateo, T.; Halime, Z.; Lassalle-Kaiser, B. Time-Resolved X-Ray Absorption Spectroelectrochemistry of Redox Active Species in Solution. *J Synchrotron Rad* **2019**, 26 (6), 1980–1985.
- (5) Bora, D. K.; Glans, P.-A.; Pepper, J.; Liu, Y.-S.; Du, C.; Wang, D.; Guo, J.-H. An Ultra-High Vacuum Electrochemical Flow Cell for in Situ/Operando Soft X-Ray Spectroscopy Study. *Rev. Sci. Inst.* **2014**, 85 (4), 043106.
- (6) Gueutin, C.; Lexa, D. Low Temperature Spectroelectrochemistry for the Characterization of Highly Reduced  $\sigma$ -Alkyl Iron Halogenated Porphyrins. *Electroanalysis* **1996**, 8 (11), 1029–1033.
- (7) Weingarh, D.; Foelske-Schmitz, A.; Wokaun, A.; Kötz, R. PTFE Bound Activated Carbon—A Quasi-Reference Electrode for Ionic Liquids. *Electrochemistry Comm.* **2012**, 18, 116–118.

## Université Paris Cité

Ecole doctorale chimie physique et chimie analytique de Paris Centre ED 388

Laboratoire d'Electrochimie Moléculaire

---

### *Résumé détaillé en français*

## **Etudes de porphyrines de fer pour la réduction électrochimique du CO<sub>2</sub> par spectroscopie d'absorption des rayons X**

---

**Par Daniela MENDOZA-FRANZESE**

**Thèse de doctorat en électrochimie moléculaire et biologique**

*Directrice de thèse :*

Dr. Elodie ANXOLABEHERE-MALLART

*Co-directeur de thèse :*

Prof. Marc ROBERT

Laboratoire d'Electrochimie Moléculaire UMR CNRS 7591

*Co-encadrant:*

Dr. Benedikt LASSALLE-KAISER

Synchrotron SOLEIL

## Chapitre I - Introduction Générale

Le dioxyde de carbone ( $\text{CO}_2$ ) est essentiel pour rendre la vie sur Terre hospitalière. Cependant, depuis le début de la révolution industrielle, au milieu du 18<sup>e</sup> siècle, le niveau de  $\text{CO}_2$  a considérablement augmenté en raison de l'activité anthropique, perturbant l'équilibre du cycle naturel du carbone, le climat et l'environnement terrestres. Malgré les alertes continues de la communauté scientifique et les accords sur le climat, seule une petite fraction, environ 0,6 %, du  $\text{CO}_2$  généré, est recyclée et les combustibles fossiles dominent toujours la consommation d'énergie mondiale.<sup>1</sup> L'une des solutions proposées pour résoudre le problème du  $\text{CO}_2$  est de stocker et de convertir l'énergie à l'aide de sources renouvelables, par exemple en utilisant le rayonnement solaire. S'inspirant de la nature, la photosynthèse artificielle vise à convertir l'eau et le  $\text{CO}_2$  en molécules dérivées de l'oxygène et du carbone en stockant l'énergie solaire dans des liaisons chimiques. Par conséquent, l'électrochimie peut être utilisée afin de réduire le  $\text{CO}_2$  en molécules utiles telles que le monoxyde de carbone (CO), qui peut être utilisé comme précurseur de carburant ou pour la synthèse de produits chimiques de plus haute valeur ajoutée. Cependant, la réaction de réduction du  $\text{CO}_2$  est un processus difficile et exigeant énergétiquement en raison de la grande stabilité et de l'inertie de cette molécule, ce qui nécessite l'utilisation de catalyseurs.

Le développement de catalyseurs, qui permet de surmonter les barrières énergétiques et de rendre les réactions plus sélectives pour la formation d'un produit spécifique, a connu une progression accélérée ces dernières années. Les catalyseurs moléculaires, tels que les macrocycles basés sur des métaux non-nobles, ont été décrits comme des catalyseurs efficaces, économiques et sélectifs pour la réduction du  $\text{CO}_2$  à deux électrons.<sup>2,3</sup> L'un de leurs principaux avantages est la possibilité d'ajuster et de contrôler précisément leurs structures, et donc leur activité catalytique. Cette possibilité de modifications structurales ouvre la voie à des études mécanistiques permettant de corrélérer l'activité des catalyseurs à leurs structures moléculaires.

En ce qui concerne les catalyseurs moléculaires, la compréhension de la réaction de réduction du  $\text{CO}_2$  nécessite l'observation d'espèces intermédiaires réactionnelles afin de formuler un mécanisme. Par conséquent, la caractérisation d'un catalyseur doit inclure l'utilisation de techniques spectroscopiques, idéalement en conditions *in situ*. Le projet de ce travail de thèse consiste à caractériser par spectroélectrochimie *in situ* une famille de catalyseurs moléculaires réducteurs de  $\text{CO}_2$  les plus actifs connus à ce jour, les porphyrines de fer. La spectroscopie d'absorption des rayons X (son acronyme en anglais est XAS) a été couplée à l'électrochimie, afin de fournir des informations spectroscopiques sur les formes réduites de ce catalyseur moléculaire, qui ont été décrites comme étant les plus actives.<sup>4,5</sup> Les données XAS et Ultraviolet-Visible (UV-Vis) ont été collectées sous atmosphère inerte et  $\text{CO}_2$  pour comprendre la nature de l'interaction entre le  $\text{CO}_2$  et les espèces réduites de la porphyrine de fer. Ces données sont discutées dans le but de contribuer à la compréhension du mécanisme de la réduction électrochimique du  $\text{CO}_2$  par ces catalyseurs.

La thèse est organisée en huit chapitres et quatre annexes, où les aspects expérimentaux et théoriques des techniques utilisées tout au long du manuscrit sont décrits. Le chapitre 1 constitue une introduction générale et le plan de la thèse tel que décrit ici. Le chapitre 2 est consacré aux études électrochimiques précédentes réalisées sur les porphyrines de fer pour l'activation du CO<sub>2</sub>. Cependant, comme l'électrochimie seule ne suffit pas à décrire complètement le mécanisme de réaction, le chapitre 3 présente le couplage de cette technique avec des méthodes spectroscopiques, en accordant une attention particulière au XAS. Le chapitre 4 décrit les études spectroscopiques précédentes portant spécifiquement sur les porphyrines de fer, y compris les mesures initiales *ex situ* mais aussi les résultats récents obtenus par spectroélectrochimie *in situ* et *operando*. Cependant, la réalisation de mesures spectroélectrochimiques nécessite le développement d'une instrumentation spécifique. Ainsi, le chapitre 5 décrit la cellule spectroélectrochimique qui a été développée au cours de ce projet, ainsi que les paramètres qui doivent être contrôlés pour éviter les artefacts expérimentaux. Les deux chapitres suivants résument les résultats obtenus par les méthodes spectroélectrochimiques sur la tétraphénylène porphyrine de fer [Fe<sup>III</sup>(TPP)]Cl en solution. Le chapitre 6 est consacré à l'analyse *in situ* de la structure électronique des espèces de porphyrines de fer électro-réduites dans une atmosphère inerte tandis que le chapitre 7 explore les informations spectroscopiques obtenues sur le même système en présence de CO<sub>2</sub>. En comparant les données recueillies en conditions inertes et sous atmosphère de CO<sub>2</sub>, les interactions métal-substrat sont décrites et utilisées pour contribuer aux hypothèses mécanistiques proposées précédemment. Ces réflexions sont décrites dans le chapitre 8, ainsi que les perspectives à venir pour ce projet.

## **Chapitre II - Activation électrochimique du CO<sub>2</sub> par les porphyrines de fer**

Même si la réduction du CO<sub>2</sub> par des méthodes électrochimiques est connue depuis les années 50, ce domaine de recherche s'est développé au cours des dernières décennies en raison de la nécessité de trouver des alternatives énergétiques à l'utilisation de combustibles fossiles afin de réduire les effets du réchauffement climatique. Les complexes métalliques, basés, par exemple, sur le fer, ont été choisis comme la meilleure alternative de catalyseur, en raison de leur abondance, permettant de réduire leur coût de fabrication. Parmi eux, la tétraphénylène porphyrine de fer [Fe<sup>III</sup>(TPP)]Cl (figure 1.a) a été décrite comme un catalyseur potentiel pour la réduction du CO<sub>2</sub> en CO.<sup>4</sup> Le voltammogramme cyclique de [Fe<sup>III</sup>(TPP)(Cl)] dans un solvant sec et aprotique, tel que le diméthylformamide, DMF, en présence d'un électrolyte, par exemple l'hexafluorophosphate de tétrabutylammonium (TBAPF<sub>6</sub>) et sous une atmosphère inerte (Ar), montre trois vagues réversibles et bien définies. Chacune de ces vagues a été proposée comme une transition électronique centrée sur le métal. Par exemple, la réduction de Fe<sup>III</sup> en Fe<sup>II</sup> a lieu à -0.13 V vs. électrode de référence au calomel saturé (ECS), celle de Fe<sup>II</sup> en "Fe<sup>I</sup>" à -1.00 V vs ECS, et enfin celle de "Fe<sup>I</sup>" en "Fe<sup>0</sup>" au potentiel de la dernière vague à -1.67 V vs ECS (figure 1.b). Notons que les termes "Fe<sup>I</sup>" et "Fe<sup>0</sup>" sont formels puisque la localisation de l'électron injecté dans le système n'est pas clairement établie.

Ces processus de transfert d'électron sont réversibles : lorsque le potentiel est inversé lors du scan de retour, les espèces sont régénérées jusqu'à revenir à l'espèce  $\text{Fe}^{\text{III}}$  initiale. Comme ces processus de réduction sont contrôlés par des lois de diffusion, chaque vague présente le même courant de pic, lequel correspond à des processus impliquant un unique électron. Par conséquent, aucune réaction chimique ou processus catalytique n'a lieu dans ces conditions. Ce n'est pas le cas lorsque du  $\text{CO}_2$  est dissout dans la solution, puisqu'une augmentation du courant ainsi qu'une perte de réversibilité sont observées au niveau de la dernière vague (figure 1.c). Il a donc été proposé que la catalyse se produise au niveau de cette vague, appelée vague catalytique, dans laquelle l'espèce " $\text{Fe}^{\text{I}}$ " est réduite en " $\text{Fe}^{\text{0}}$ ". Par conséquent, cet état réduit à trois électrons est considéré comme la forme active du catalyseur.<sup>4-6</sup>

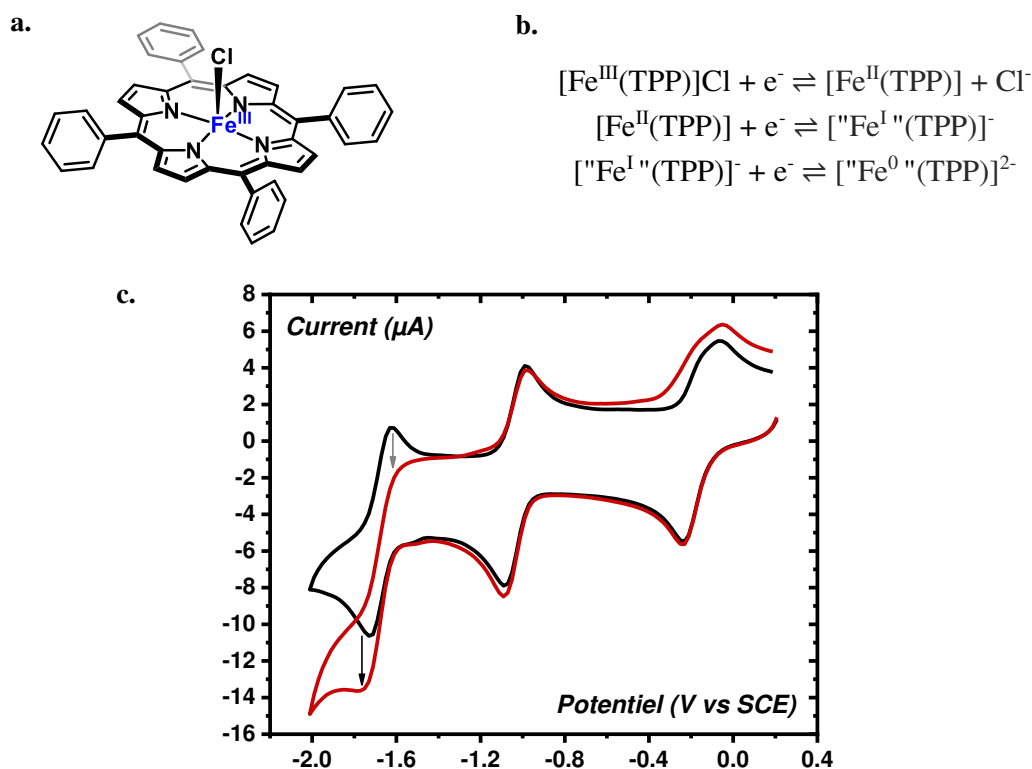


**Figure 1.** a. Structure de la tétraphénylène porphyrine de fer  $[\text{Fe}^{\text{III}}(\text{TPP})(\text{Cl})]$ . b. Demi-équations des réactions de réduction attendues à chaque vague sous Argon. c : Voltammogrammes cycliques d'une solution 2 mM de  $[\text{Fe}^{\text{III}}(\text{TPP})(\text{Cl})]$  dans du DMF + 0.1 M TBAPF<sub>6</sub> sous atmosphère d'Argon (noire) et  $\text{CO}_2$  (rouge) à température ambiante (RT). La vitesse de balayage est de 100 mV.s<sup>-1</sup>.

Sur la base de données électrochimiques, un mécanisme de réduction du  $\text{CO}_2$  en CO par  $[\text{Fe}^{\text{III}}(\text{TPP})]\text{Cl}$  en présence d'un acide faible, par exemple l'eau, a été proposé. On s'attend à ce que le centre métallique riche en électrons généré à bas potentiel subisse une attaque nucléophile du carbone électrophile de la molécule de  $\text{CO}_2$ , formant un adduit de type  $[\text{Fe}^{\text{II}}(\text{TPP})(\text{CO})]$ . Cette réaction est favorisée par l'effet push-pull induit par la présence de protons, lesquels affaiblissent la liaison C-O et contribuent à son clivage. La réduction de l'adduit  $[\text{Fe}^{\text{II}}(\text{TPP})(\text{CO})]$  le rend instable et conduit à la libération de CO et à la régénération du site actif.<sup>5,7,8</sup>

A ce jour, même si de nombreuses études expérimentales et quelques études théoriques ont été réalisées permettant de proposer ce mécanisme, des informations structurales sur les intermédiaires impliqués sont encore manquantes. Pour cette raison, le couplage de l'électrochimie avec des techniques spectroscopiques est envisagé, dans le but de permettre une compréhension plus complète des changements structurels et électroniques des catalyseurs pendant leur fonctionnement.

### Chapitre III – Spectroélectrochimie d'absorption des rayons X

L'électrochimie ne peut seule fournir une sonde directe sur les changements structurels et électroniques ayant lieu au sein de l'espèce d'intérêt. Par conséquent, la combinaison de l'électrochimie avec la spectroscopie, technique connue sous le nom de spectroélectrochimie (SEC), peut fournir des informations liées aux processus redox tout en offrant des détails sur la configuration électronique des espèces étudiées.<sup>9</sup> Cette technique devient encore plus intéressante pour les études mécanistiques si les deux mesures sont effectuées simultanément à la même électrode (conditions *in situ*) et dans des conditions de catalyse (conditions *operando*).

Même si les mesures spectroélectrochimiques UV-Vis, IR et Raman ont été utilisées pour caractériser la réaction électrochimique de réduction du CO<sub>2</sub>, les exemples sont rares et ces techniques manquent de sensibilité pour décrire la structure électronique des échantillons de manière complète. C'est pourquoi la spectroscopie d'absorption des rayons-X est apparue comme idéale, puisque c'est une technique non destructive et spécifique à un élément, qui n'est pas non plus limitée à l'état de l'échantillon et qui fournit une grande quantité d'informations en une seule expérience.<sup>10</sup> Avec cette technique, un électron est excité depuis le niveau de cœur vers une orbitale inoccupée au-delà du niveau de Fermi. Lorsque l'énergie incidente correspond à l'énergie de liaison de l'électron de cœur, une augmentation du signal est observée dans le spectre XAS, connue sous le nom de *seuil d'absorption*. Lorsque l'électron qui est promu est situé dans la couche la plus interne, le niveau *1s*, l'absorption qui se produit est définie comme le *seuil K*.<sup>11</sup>

La *X-ray Absorption Near Edge Spectroscopie* (XANES est son acronyme en anglais) est la région qui va de quelques eV avant à environ 50 eV après le seuil. La principale caractéristique observable dans cette région est due à une transition de l'orbitale *1s* à l'orbitale inoccupée la plus basse, *np*. Sa position est généralement utilisée pour évaluer l'état d'oxydation de l'atome absorbant. La région du pré-seuil est placée juste avant le seuil principal, et regroupe des pics de faible intensité. Dans les complexes de métaux de transition, ces pics sont présents en raison de transitions de l'orbitale *1s* vers les orbitales  $(n-1)d$ , combinées à des orbitales de type *4p*. La présence d'un caractère *p* dans les orbitales finales est ce qui explique l'intensité de ces transitions qui seraient sinon interdites d'après les règles de transition de Laporte ( $\Delta l = \pm 1$ ). En général, tout changement dans l'organisation des niveaux de valence qui conduit à un réarrangement du mélange *p-d* entraînera des changements dans les transitions de pré-seuil. Par conséquent, cette région est extrêmement utile pour déterminer la *symétrie du site*, les états de

*spin, l'échange de ligands* ou tout autre changement géométrique.<sup>11-13</sup> Nous avons concentré nos études sur l'analyse qualitative des régions XANES et du pré-seuil au seuil K du fer.

## Chapitre IV – Etat de l'art des observations spectroscopiques liées au mécanisme de réduction du CO<sub>2</sub> par des porphyrines de fer.

### - Structure électronique de porphyrines de fer

La compréhension de la structure électronique des porphyrines de fer est un sujet d'intérêt depuis plusieurs décennies. Même si la description des orbitales moléculaires (MO) est généralement très complexe, l'analyse des orbitales *d* peut toujours offrir de nombreuses informations sur la configuration électronique.<sup>14</sup> Dans ces complexes, le centre métallique est chélaté par quatre atomes d'azote provenant de groupes pyrrole, ce qui lui confère une géométrie plan carré. Cette structure est caractérisée par une élévation de l'orbitale  $d_{x^2-y^2}$ . En outre, dans certains cas, le fer peut être coordonné par un ou deux autres ligands axiaux, ce qui donne des structures pyramidales carrées ou octaédriques déformées. Dans ces cas, l'orbitale  $d_{z^2}$  est fortement déstabilisée, comme pour [Fe<sup>III</sup>(TPP)]Cl, dans lequel un anion chlorure agit comme un ligand axial qui coordonne le fer, donnant un complexe pyramidal carré en configuration haut spin.<sup>15</sup>

En ce qui concerne les espèces réduites des porphyrines de fer, les Fe<sup>II</sup> ont été les plus étudiées en raison de leur importance dans la nature. Des mesures électrochimiques ont montré que, pendant la réduction à un électron de [Fe<sup>III</sup>(TPP)]Cl, l'anion chlorure décoordonne le centre du fer, ce qui conduit à une structure plan carré de spin intermédiaire.<sup>16</sup> Cependant, des mesures XAS récentes ont également montré que les molécules de solvant, telles que le tétrahydrofurane (THF), peuvent se coordonner au centre du Fe<sup>II</sup> et affecter l'état de spin de ces structures. Nous avons donc concentré nos études sur la structure de cet intermédiaire en présence de DMF.<sup>17</sup>

Il y a peu de rapports sur la spectroscopie des porphyrines ferriques hautement réduites, car il est difficile de les réduire chimiquement et de stabiliser des espèces monomériques. Néanmoins, Scheidt *et al.* ont pu isoler l'espèce [Fe<sup>I</sup>(TPP)]<sup>-</sup> à bas spin et le composé dianionique, [Fe<sup>0</sup>(TPP)]<sup>2-</sup>, après avoir effectué une réduction chimique avec de l'anthracène de sodium dans des conditions anaérobiques.<sup>18</sup> Ces structures ont également été récemment analysées par XANES à l'état solide.<sup>19</sup>

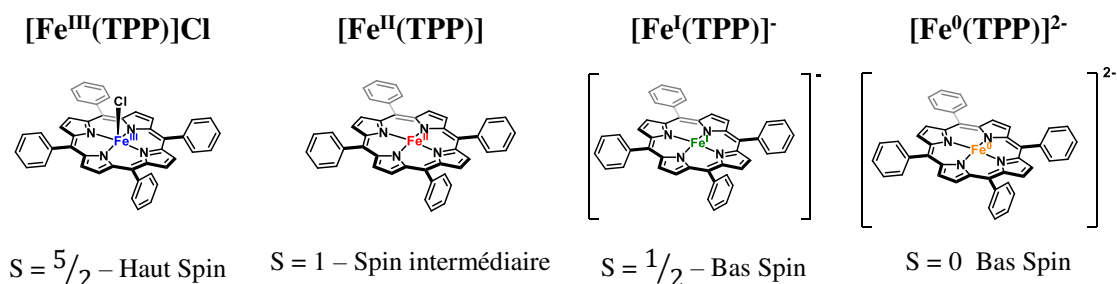


Schéma 1. Représentation de [Fe<sup>III</sup>(TPP)]Cl et de ses espèces réduites avec leur états de spin à l'état solide.

Malgré les efforts de la communauté scientifique, la description des états d'oxydation des espèces de porphyrines de fer hautement réduites, qui peuvent être formulées comme des espèces réduites au niveau du métal ou du ligand, suscite toujours la controverse. Par conséquent, les mesures XAS *in situ* et de spectroélectrochimie UV-Vis présentées au chapitre VI visent à donner un nouvel éclairage sur cette question.

#### **- Interaction du CO<sub>2</sub> et du CO généré avec le fer**

En raison de la polarisation des liaisons dans la molécule de CO<sub>2</sub> ainsi que dans les produits de réduction attendus, la spectroscopie vibrationnelle a été traditionnellement utilisée pour la détection d'intermédiaires de réaction. Par exemple, Dey *et al.* ont utilisé la spectroscopie Raman *ex situ* pour étudier les espèces de porphyrine de fer chimiquement réduites en présence de CO<sub>2</sub>. A la lumière de leurs résultats, ils ont suggéré la réaction de l'espèce hautement réduite "Fe<sup>0</sup>" avec le CO<sub>2</sub> qui génère la formation d'un intermédiaire de courte durée, le [Fe<sup>II</sup>(CO<sub>2</sub>)]<sup>2-</sup>, lequel est facilement protoné, et génère l'espèce [Fe<sup>II</sup>(COOH)]<sup>-</sup>.<sup>20</sup> Lexa *et al.* ont confirmé par spectroscopie IR *ex situ* la formation de l'autre adduit attendu, l'espèce [Fe<sup>II</sup>(TPP)(CO)] en faisant barboter du CO dans une solution de l'espèce Fe<sup>II</sup> générée électrochimiquement.<sup>21</sup>

Malgré ces quelques observations d'espèces discrètes, la caractérisation spectroélectrochimique en conditions *operando* de la réduction du CO<sub>2</sub> par les porphyrines de fer n'a été décrite que dans de rares exemples. Ce n'est que récemment que Takanabe *et al.* ont pu réaliser une caractérisation spectroélectrochimique *operando* UV-Vis et XAS d'une porphyrine de fer immobilisée sur des matériaux de carbone à haute surface dans une solution aqueuse contenant du bicarbonate de sodium (NaHCO<sub>3</sub>). Ils concluent, sur la base des données collectées et de calculs théoriques, que l'espèce Fe<sup>II</sup> constitue le site actif de la catalyse, capable de réduire le CO<sub>2</sub> en CO, pour former l'adduit stable de type [Fe<sup>II</sup>(Porphyrine)(CO)].<sup>22</sup> Cependant, en raison des divergences de leurs résultats avec ce qui a été proposé pour le mécanisme de réduction du CO<sub>2</sub>, il est plus pertinent d'étudier des échantillons homogènes, dans lesquels l'analyse cinétique a été largement décrite, par des méthodes spectroélectrochimiques *in situ*.

## **Chapitre V - Développement de l'instrumentation XAS**

Les mesures spectroélectrochimiques XAS nécessitent le développement de cellules spécifiques puisque chaque expérience doit être adaptée à la ligne de lumière et à des objectifs expérimentaux spécifiques. Afin de satisfaire aux exigences d'une expérience de spectroélectrochimie des rayons-X en conditions homogènes et en présence d'un solvant organique, l'optimisation d'une cellule spécifique (figure 2) a été la première tâche à accomplir au cours de ce projet de thèse.

Comme pour les montages électrochimiques classiques, cette cellule comporte trois électrodes. Un film fin (60 µm) de carbone vitreux (*glassy carbon*, GC) est utilisé comme électrode de travail. L'utilisation de ces électrodes, qui font également office de fenêtre de cellule, permet une bonne pénétration des rayons X, tout en offrant des performances électrochimiques



similaires à celles utilisées dans les montages conventionnels. Une grille de platine à haute surface est utilisée comme contre-électrode, tandis qu'un fil d'argent est utilisé comme électrode de pseudo-référence. Cette cellule permet l'enregistrement simultané de données électrochimiques pendant que des spectres XAS sont collectés. La géométrie en couche mince de 200  $\mu\text{m}$  d'épaisseur, permet une conversion presque totale des espèces (96%). Cette configuration permet également la détection par fluorescence des rayons-X des espèces même à faible concentration (2 mM). Cette cellule a été construite en polyétheréthercétone (PEEK), permettant un bon usinage mécanique et l'utilisation de solvants organiques, tels que le DMF, requis dans l'étude électrochimique de la réaction de réduction du  $\text{CO}_2$  par les porphyrines de fer. De plus, cette cellule permet également de faire circuler la solution à analyser, ce qui réduit les dommages possibles à l'échantillon tout en permettant le changement d'échantillon sans démontage. Enfin, cette cellule a permis des études à l'intérieur d'une chambre à vide, réduisant drastiquement la présence d'oxygène, lequel est connu pour réagir avec les formes réduites des porphyrines de fer.

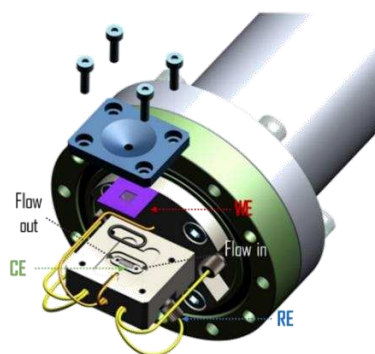


**Figure 2.** Schéma général de la cellule conçue et optimisée au cours du projet.

*WE : électrode de travail, CE : contre-électrode, RE : électrode de référence.*

## Chapitre VI – Analyse de la structure électronique des porphyrines de fer par des méthodes spectroélectrochimiques sous atmosphère d'argon.

Comme décrit dans le chapitre IV, différentes techniques spectroscopiques ont été utilisées afin de déterminer les structures électroniques de porphyrines de fer, en particulier pour les espèces réduites qui sont encore sujettes à controverse. Pour compléter les données disponibles et contribuer à lever cette controverse, nous avons donc utilisé des méthodes spectroélectrochimiques *in situ* XANES pour analyser la  $[\text{Fe}^{\text{III}}(\text{TPP})]\text{Cl}$  et ses espèces électroréduites en solution dans le DMF.

En étudiant une solution de  $[\text{Fe}^{\text{III}}(\text{TPP})]\text{Cl}$  dans le DMF avec électrolyte ( $\text{TBAPF}_6$ ), nommée **I** (schéma 2), nous avons pu observer par XANES et UV-Vis que la structure électronique de cette espèce en solution correspond à celle d'une porphyrine à haut spin précédemment décrite (chapitre IV). Le voltammogramme cyclique de cette solution enregistrée dans la cellule spectroélectrochimique sous argon présente trois vagues réversibles bien définies, correspondant aux processus de réduction à trois électrons, démontrant que la cellule est électrochimiquement optimale pour des études ultérieures (figure 3.a).

La première réaction de réduction à un électron a été réalisée en appliquant un potentiel de  $E = -0,8 \text{ V vs Ag/Ag}^+$ , dont le produit est nommé **2a**. Le spectre XANES a été enregistré lorsque le courant a atteint un plateau afin d'observer les espèces stables, cependant, seuls de légers changements ont été observés par XANES même si les mesures électrochimiques et spectroélectrochimiques UV-Vis indiquent une conversion totale de l'espèce de départ. Afin de confirmer la nature de l'espèce électrogénérée, le complexe  $[\text{Fe}^{\text{II}}(\text{TPP})]$  a été synthétisé à partir du complexe de départ  $[\text{Fe}^{\text{III}}(\text{TPP})]\text{Cl}$  par une voie de réduction chimique, suivant une procédure connue.<sup>19</sup> Le spectre XANES au seuil K du fer de l'échantillon solide réduit chimiquement montre un décalage de 2 eV vers des énergies plus basses. Il montre également la présence d'un épaulement à environ 7118 eV qui a été décrit comme une transition  $1s$  vers  $4p_z$  dans les porphyrines de fer et autres complexes moléculaires.<sup>19,23</sup> Toutes ces caractéristiques indiquent que le complexe synthétisé est, à l'état solide, dans une géométrie plan carrée, comme précédemment rapporté dans la littérature. Cependant, la dissolution dans du DMF de cet échantillon généré chimiquement génère un spectre XANES qui ressemble à celui de **2a**, indiquant qu'effectivement le DMF joue un rôle critique dans les changements structuraux de la porphyrine de fer dans cet état de valence. La disparition du pic à 7118 eV est une preuve claire de la perte du caractère plan carré, puisque l'orbitale  $4p_z$  est déplacée vers des énergies plus élevées en raison de la coordination axiale par le DMF. Par conséquent, l'échantillon électrogénéré peut être décrit comme un complexe bas spin avec une (ou deux) molécules de DMF agissant comme ligand axial.

Le deuxième processus de réduction a été suivi par XANES, tout en appliquant un potentiel à  $E = -1,6 \text{ V vs Ag/Ag}^+$ . L'échantillon généré, nommé **3**, montre un spectre XANES avec un épaulement s'élevant à 7118 eV suggérant un environnement plan carré autour du centre du fer, comme discuté au chapitre II. Un léger déplacement du seuil vers les basses énergies a été observé, ce qui ne caractérise pas une réduction à un électron centrée sur le métal. Enfin, un troisième transfert d'électrons a été effectué en appliquant un potentiel au niveau de la dernière vague, à  $E = -2,0 \text{ V vs Ag/Ag}^+$ , générant l'espèce **4**. Les spectres XANES au seuil K du fer collectés sur **4** sont présentés dans la figure 3 et comparés aux spectres XANES obtenus pour les autres espèces. Un déplacement de la position du seuil de 1 eV vers les basses énergies, en comparaison avec **1**, peut être observé pour l'espèce **4**, bien que ces valeurs doivent être prises avec précaution, car l'augmentation de l'épaulement à 7118.0 eV pourrait déplacer artificiellement la position du seuil principal. Cependant, la modification la plus importante est observée dans la région du pré-seuil. En effet, l'intensité du pic de pré-seuil diminue, tandis que l'épaulement à 7118 eV augmente, suggérant une géométrie plane carré qui peut être expliquée par la répulsion des ligands axiaux due à une densité électronique accrue dans l'espèce réduite à trois électrons.

L'analyse de l'ensemble des données *in situ* obtenues sous argon, en particulier l'absence de déplacement significatif du seuil vers les basses énergies lors des étapes de réduction, suggère que la densité électronique pour les espèces de porphyrine de fer réduites **3** et **4** n'est pas seulement localisée sur le métal mais aussi partiellement sur la porphyrine. Ces complexes peuvent donc être décrits comme des formes mésomères (schéma 2).

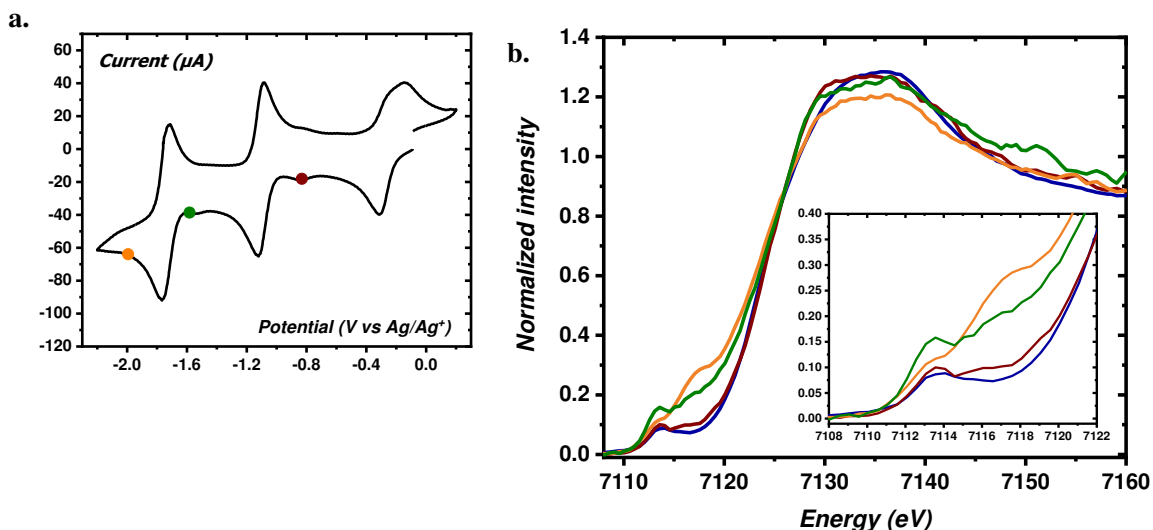


Figure 3. a. Voltammogramme cyclique d'une solution 2 mM de  $[\text{Fe}^{\text{III}}(\text{TPP})(\text{Cl})]$  dans du DMF + 0.1 M TBAPF<sub>6</sub> sous atmosphère d'argon à température ambiante, enregistré dans la cellule spectroélectrochimique, avec une vitesse de balayage de 100 mV.s<sup>-1</sup>. Les points colorés indiquent le potentiel sélectionné pour l'électrolyse à potentiel constant pour les mesures spectroélectrochimiques. b. Spectres XANES au seuil K du fer de *1* (bleu), *2a* (rouge), *3* (vert) et *4* (orange) en solution DMF-TBAPF<sub>6</sub> sous atmosphère d'argon. Encart: région du pré-seuil.

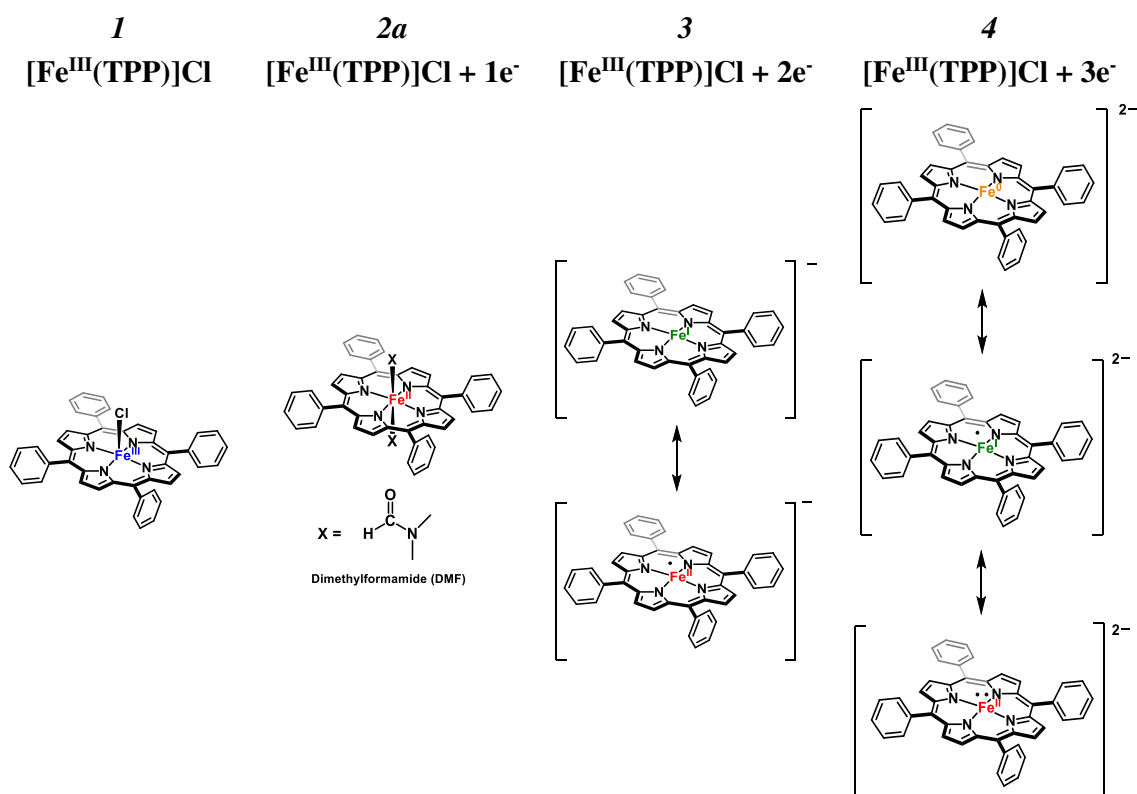


Schéma 2. Structures proposées pour le complexe *1* de  $[\text{Fe}^{\text{III}}(\text{TPP})]\text{Cl}$ , et ses espèces associées réduites à un électron (complexe *2a*), deux électrons (complexe *3*) et trois électrons (complexe *4*) dans le DMF + 0.1 M TBAPF<sub>6</sub> sous atmosphère d'argon.

## Chapitre VII – Analyse de la structure électronique des porphyrines de fer par des méthodes spectroélectrochimiques en présence de CO<sub>2</sub>.

Comme commenté précédemment, le CV de [Fe<sup>III</sup>(TPP)]Cl en présence d'argon présente trois vagues définies et réversibles. Cependant, lorsque du CO<sub>2</sub> est dissous dans la solution, une augmentation substantielle du courant et une perte de réversibilité sont observées sur la troisième vague de réduction, par rapport aux données observées sous argon, indiquant une activité catalytique (figure 4.a). Malgré les précautions prises pour éviter la présence d'eau dans la solution, la présence de protons, qui sont nécessaires pour que la catalyse ait lieu,<sup>5,24,25</sup> ne peut être complètement évitée dans ces conditions expérimentales. De plus, même dans le cas d'une concentration résiduelle de protons extrêmement faible, le CO<sub>2</sub> lui-même peut jouer le rôle d'un acide (acide de Lewis), et fournir une assistance pour le clivage de la liaison C-O conduisant à la formation d'une molécule de CO et d'un anion CO<sub>3</sub><sup>2-</sup>.<sup>26</sup>

Outre les différences observées sur la dernière vague, de légers changements peuvent également être observés sur la deuxième vague et sur le scan retour de la première vague. Par conséquent, il est nécessaire d'avoir une empreinte de chaque espèce électrogénérée en présence de CO<sub>2</sub>, comme dans le cas de l'argon, pour comprendre ses interactions avec la porphyrine de fer. Les données spectroélectrochimiques XANES et UV-Vis recueillies sur le complexe initial dans le DMF et en présence de CO<sub>2</sub>, nommé **5**, et son espèce réduite à un électron en appliquant un potentiel de  $E = -0.8 \text{ V vs Ag/Ag}^+$ , le complexe **6**, ne montrent aucun changement par rapport aux données recueillies sous atmosphère d'argon. Il n'y a donc aucune interaction entre le [Fe<sup>III</sup>(TPP)]Cl et son espèce réduite à un électron et le CO<sub>2</sub>.

Cependant, lorsque [Fe<sup>III</sup>(TPP)]Cl est réduit par deux électrons avec un potentiel de  $E = -1.6 \text{ V vs Ag/Ag}^+$ , en présence de CO<sub>2</sub> pour générer le complexe **7**, l'épaule à 7118 eV, qui indique une géométrie plan carré, disparaît, ce qui suggère une interaction entre le CO<sub>2</sub> et le centre métallique. Puisque presque aucune différence n'est détectée par UV-Vis entre les données de l'argon et du CO<sub>2</sub>, nous proposons que cette interaction soit faible (schéma 3). Lorsque [Fe<sup>III</sup>(TPP)]Cl est réduit avec 3 électrons sous atmosphère de CO<sub>2</sub> en appliquant un potentiel de  $E = -2.0 \text{ V vs Ag/Ag}^+$ , pour donner le complexe **8**, des différences significatives sont observées dans les données XANES par rapport aux autres espèces réduites en présence de CO<sub>2</sub> mais de manière encore plus significative sous argon. Une diminution de l'intensité du pré-seuil ainsi que la disparition de l'épaule à 7118 eV suggèrent une déviation de la géométrie plan carré. En plus de cela, un déplacement du seuil principal vers des énergies plus élevées (0.7 eV par rapport à **5**) a également été observé. Ceci est cohérent avec la liaison du CO<sub>2</sub> au centre Fe, et le déplacement concomitant de densité électronique du métal vers le CO<sub>2</sub>. Nous en concluons que le CO<sub>2</sub> est coordonné au centre métallique dans ces conditions. Globalement, nos données pointent, pour les composés **7** et **8**, vers des structures électroniques impliquant le CO<sub>2</sub> et le centre métallique, ainsi que le ligand porphyrinique, comme représenté par les structures mésomères du schéma 3.

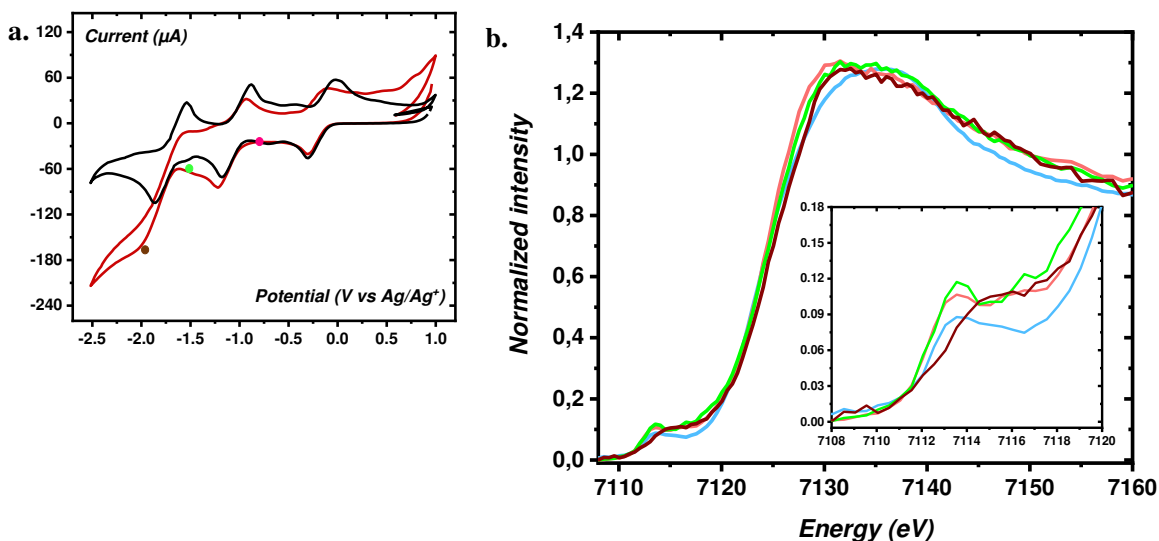


Figure 4. a. Voltammogramme cyclique d'une solution 2 mM de  $[\text{Fe}^{\text{III}}(\text{TPP})(\text{Cl})]$  dans du DMF + 0.1 M  $\text{TBAPF}_6$  sous atmosphère d'argon (noir) et de  $\text{CO}_2$  (rouge), enregistré dans la cellule spectroélectrochimique, avec une vitesse de balayage de  $100 \text{ mV}\cdot\text{s}^{-1}$ . Les points colorés indiquent le potentiel sélectionné pour l'électrolyse à potentiel de contrôle pour les mesures spectroélectrochimiques ultérieures. b. Spectres XANES au seuil K du fer de 5 (bleu clair), 6 (rose), 7 (vert clair) et 8 (marron) pour  $[\text{Fe}^{\text{III}}(\text{TPP})]\text{Cl}$  en solution dans DMF + 0.1 M  $\text{TBAPF}_6$  sous atmosphère de  $\text{CO}_2$ . Encart: région du pré-seuil.

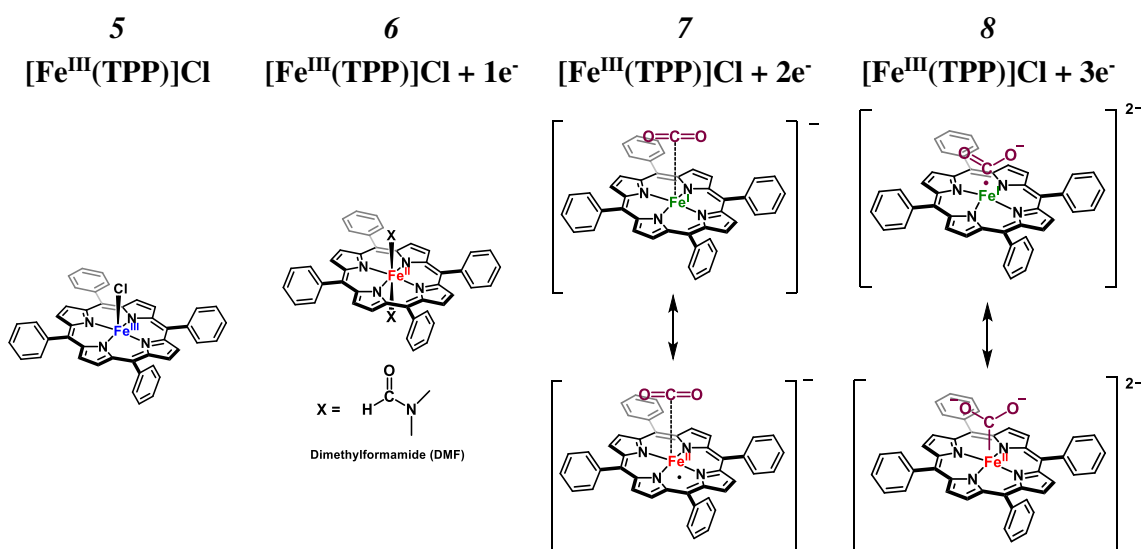


Schéma 3. Complexe 5 de  $[\text{Fe}^{\text{III}}(\text{TPP})]\text{Cl}$  sous atmosphère de  $\text{CO}_2$ , et ses structures associées réduites à un électron (complexe 6), deux électrons (complexe 7) et trois électrons (complexe 8) dans le DMF + 0.1 M  $\text{TBAPF}_6$  sous atmosphère de  $\text{CO}_2$ .

Après avoir effectué une électrolyse à potentiel constant dans une solution de  $[\text{Fe}^{\text{III}}(\text{TPP})]\text{Cl}$  à  $E = -2.0 \text{ V vs SCE}$  en présence de  $\text{CO}_2$ , le potentiel a été modifié à  $E = -1.0 \text{ V vs SCE}$  tout en maintenant le dispositif hermétiquement fermé. Une nouvelle espèce est formée, nommée **9**, laquelle présente des bandes de Soret et Q similaires à celles décrites pour l'adduit de la porphyrine de  $\text{Fe}(\text{II})$  avec le  $\text{CO}$ .<sup>21,27</sup> Ces résultats ont été confirmés par spectroélectrochimie

IR *in situ*, avec l'apparition de bandes à  $1953\text{ cm}^{-1}$ , correspondant étroitement aux rapports précédents pour d'autres complexes de porphyrine de fer.<sup>21</sup> Cet ensemble de données fournit une empreinte utile pour l'identification future des adduits de CO avec les porphyrines de fer par XANES, et confirme également que du CO a été formé pendant l'électrolyse à  $E = -2.0\text{ V}$  vs SCE.

## Chapitre VIII – Discussion sur le mécanisme et perspectives

En comparant les données obtenues sous  $\text{CO}_2$  avec celles obtenues sous conditions inertes (chapitre VI), nous avons pu observer l'influence que la présence de  $\text{CO}_2$  a sur les espèces réduites de Fe. Les observations spectroscopiques permettent de décrire les changements structuraux et électroniques qui se produisent sur les porphyrines de fer en présence du substrat et pendant son activation. Sur la base de méthodes spectroélectrochimiques, un mécanisme simplifié pour la réduction électrocatalytique du  $\text{CO}_2$  en CO par le  $[\text{Fe}^{\text{III}}(\text{TPP})]\text{Cl}$  dans des conditions homogènes est proposé dans le schéma 4.

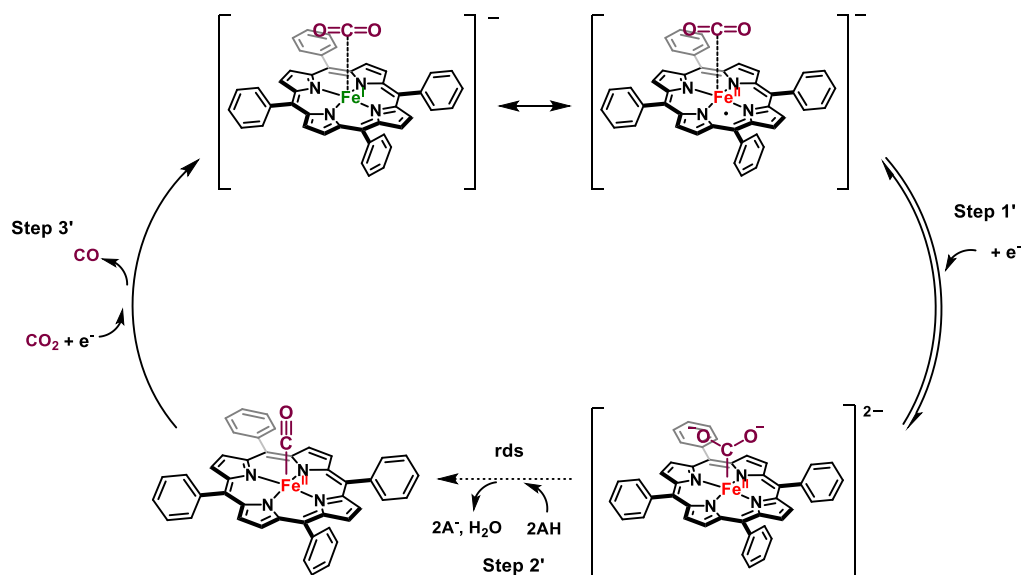


**Schéma 4. Mécanisme simplifié pour la réduction électrocatalytique du  $\text{CO}_2$  en CO par la tétraphénylporphyrine de fer en présence d'une faible quantité de protons, basé sur les données spectroélectrochimiques présentées dans le manuscrit.**

*Une faible quantité de protons est disponible dans les conditions décrites ci-dessus (eau résiduelle - AH).*

Le mécanisme peut être résumé par les étapes suivantes :

### Étape 1'

La porphyrine doublement réduite ( $[\text{Fe}^{\text{I}}(\text{TPP})]^{-} \leftrightarrow [\text{Fe}^{\text{II}}(\text{TPP}')^{-}]$ ) interagit faiblement avec le  $\text{CO}_2$ . La réduction à un électron de cette espèce fournit **8**, qui peut être décrit par des formes mésomères comprenant un complexe de Fe(I) lié à un radical  $\text{CO}_2$  asymétrique et un complexe de Fe(II) coordonné à une molécule de  $\text{CO}_2$  symétrique, doublement chargé. Les données XANES suggèrent que la dernière structure est plus probable, au moins dans les conditions

dans lesquelles les expériences *in situ* ont été effectuées. Les mesures spectroélectrochimiques *in situ* présentées suggèrent également que l'activation du CO<sub>2</sub> se produit au niveau du centre métallique avec une relocalisation de la densité électronique au niveau du métal lors de la coordination du CO<sub>2</sub>.

### Étape 2'

La concentration d'acide joue un rôle central dans la conduite de la réaction. Il a été démontré qu'à faible concentration d'acide, l'étape déterminante du processus est la rupture de la liaison C-O.<sup>25</sup> À forte concentration d'acide (par exemple, phénol 3 M), le clivage devient si rapide que la coordination du CO<sub>2</sub> devient l'étape déterminante du processus.<sup>5,25</sup> Dans notre travail, les données spectroscopiques ont été recueillies sur le complexe **8** à  $E = -2.0$  V vs SCE avec une faible concentration d'acide (aucune source de protons ajoutée et seulement de l'eau résiduelle présente, soit environ 20-30 mM dans le DMF). Dans ces conditions, nous devons également tenir compte de l'acidité de Lewis du CO<sub>2</sub> lui-même, qui est très concentré (0,2 M).<sup>28,29</sup> Dans ces conditions, l'étape limitant de la réaction de réduction du CO<sub>2</sub> est considérée comme étant la rupture de la liaison C-O puisque l'adduit Fe-CO<sub>2</sub> peut être accumulé et caractérisé spectroscopiquement. Nous n'excluons pas la possibilité que les spectres obtenus soient dus à des mélanges d'espèces obtenus pendant la réduction catalytique. Cependant, nous suggérons que la fraction majeure des espèces observées dans nos conditions expérimentales est l'adduit Fe-CO<sub>2</sub>.

### Étape 3'

La formation de CO pendant l'électrolyse de [Fe<sup>III</sup>(TPP)]Cl à  $E = -2.0$  V vs SCE a été confirmée par des méthodes spectroélectrochimiques *in situ*. Les expériences UV-Vis et IR ont permis d'observer l'adduit formé entre le CO et la porphyrine Fe(II), qui a été généré lors de l'augmentation du potentiel à une valeur de  $E = -1.0$  V vs SCE après l'électrolyse.

Ces résultats fournissent des preuves complémentaires, basées sur des données spectroscopiques, pour le mécanisme électrocatalytique des électrocatalyseurs moléculaires de réduction du CO<sub>2</sub> par les porphyrines de fer. En particulier, ils donnent un aperçu supplémentaire de la structure électronique des porphyrines de fer, notamment dans l'état controversé des espèces réduites. En outre, elles complètent les premières études électrochimiques montrant les interactions entre le CO<sub>2</sub> et le centre du fer, soulignant l'importance de comprendre les changements structuraux et électroniques pendant l'activation du CO<sub>2</sub>. Finalement, ils offrent également une bibliothèque XANES d'espèces obtenues lors de l'électroréduction de porphyrines de fer en solution sous conditions inertes mais aussi en présence de CO<sub>2</sub>. Ces données sans précédent sont précieuses et ouvrent une voie pour de nouvelles études expérimentales, comme les suivants :

- Détermination *in situ* de l'adduit [Fe<sup>II</sup>(TPP)(CO)] par spectroélectrochimie XANES dans les mêmes conditions expérimentales que celles utilisées pour la spectroélectrochimie *in situ* UV-



Vis et IR. Ces données serviront de signature pour les futures mesures *operando* et l'analyse des données obtenues par combinaisons linéaires.

- Détermination du mode de liaison du CO<sub>2</sub> au fer dans les espèces réduites de [Fe<sup>III</sup>(TPP)]Cl, par spectroélectrochimie IR en complément des données UV-Vis et XANES collectées *in situ* au cours de ce projet.

- Mesures *in situ* et *operando* de la structure locale des intermédiaires étudiés dans ce projet par EXAFS, afin de mieux comprendre les interactions du CO<sub>2</sub> avec le centre métallique, en complément des données XANES. Par conséquent, l'arrivée ou le départ de ligands (tels que le CO<sub>2</sub>) pourrait être sondé, ainsi que la détermination des distances de liaison entre le métal et le substrat ou les produits.

- La simulation des spectres XANES obtenus par des calculs de théoriques (DFT) en considérant des molécules de solvant explicites pourraient également servir de support aux données expérimentales.

- Un aspect important à aborder par les techniques *in situ/operando* est la comparaison des données présentées pour le système modèle FeTPP, avec celles obtenues pour des catalyseurs plus efficaces, tels que la porphyrine de fer portant des groupes triméthylanilinium en positions méso de la porphyrine (Fe-o-TMA). Cette comparaison permettra, à terme, d'améliorer notre connaissance de l'efficacité des catalyseurs et de fournir des lignes directrices pour leur amélioration.

- Enfin, la combinaison des techniques spectroscopiques avec des méthodes de détection des produits, telles que la chromatographie en phase gazeuse (GC) *in situ* ou la chromatographie en phase gazeuse/spectrométrie de masse (GC/MS), pourrait être d'un grand intérêt. Par exemple, le développement d'une expérience qui pourrait traiter simultanément les changements de structures électroniques et la (dé)-coordination CO<sub>2</sub>/CO tout en déterminant *in situ* la génération de produits permettrait de corrélérer la formation d'un produit donné avec un intermédiaire catalytique spécifique.



## References

- (1) Robert, M. Running the Clock: CO<sub>2</sub> Catalysis in the Age of Anthropocene. *ACS Energy Lett.* **2016**, *1* (1), 281–282.
- (2) Boutin, E.; Merakeb, L.; Ma, B.; Boudy, B.; Wang, M.; Bonin, J.; Anxolabéhère-Mallart, E.; Robert, M. Molecular Catalysis of CO<sub>2</sub> Reduction: Recent Advances and Perspectives in Electrochemical and Light-Driven Processes with Selected Fe, Ni and Co Aza Macrocylic and Polypyridine Complexes. *Chem. Soc. Rev.* **2020**, *49* (16), 5772–5809.
- (3) Kinzel, N. W.; Werlé, C.; Leitner, W. Transition Metal Complexes as Catalysts for the Electroconversion of CO<sub>2</sub>: An Organometallic Perspective. *Angew. Chem. Int. Ed.* **2021**, *60* (21), 11628–11686.
- (4) Hammouche, M.; Lexa, D.; Savéant, J.-M.; Momenteau, M. Catalysis of the Electrochemical Reduction of Carbon Dioxide by Iron(“0”) Porphyrins. *J. Electroanal. Chem. Interfac. Electrochem.* **1988**, *249* (1), 347–351.
- (5) Bhugun, I.; Lexa, D.; Savéant, J.-M. Catalysis of the Electrochemical Reduction of Carbon Dioxide by Iron(0) Porphyrins: Synergistic Effect of Weak Brönsted Acids. *J. Am. Chem. Soc.* **1996**, *118* (7), 1769–1776.
- (6) Bhugun, I.; Lexa, D.; Savéant, J.-M. Catalysis of the Electrochemical Reduction of Carbon Dioxide by Iron(0) Porphyrins. Synergistic Effect of Lewis Acid Cations. *J. Phys. Chem.* **1996**, *100* (51), 19981–19985.
- (7) Hammouche, M.; Lexa, D.; Momenteau, M.; Savéant, J.-M. Chemical Catalysis of Electrochemical Reactions. Homogeneous Catalysis of the Electrochemical Reduction of Carbon Dioxide by Iron(“0”) Porphyrins. Role of the Addition of Magnesium Cations. *J. Am. Chem. Soc.* **1991**, *113* (22), 8455–8466.
- (8) Costentin, C.; Robert, M.; Savéant, J.-M. Catalysis of the Electrochemical Reduction of Carbon Dioxide. *Chem. Soc. Rev.* **2013**, *42* (6), 2423–2436.
- (9) Kaim, W.; Fiedler, J. Spectroelectrochemistry: The Best of Two Worlds. *Chem. Soc. Rev.* **2009**, *38* (12), 3373–3382.
- (10) Yano, J.; Yachandra, V. K. X-Ray Absorption Spectroscopy. *Photosynth Res.* **2009**, *102* (2), 241–254.
- (11) Timoshenko, J.; Roldan Cuenya, B. In Situ/Operando Electrocatalyst Characterization by X-Ray Absorption Spectroscopy. *Chem. Rev.* **2021**, *121* (2), 882–961.
- (12) Lassalle-Kaiser, B.; Gul, S.; Kern, J.; Yachandra, V. K.; Yano, J. In Situ/Operando Studies of Electrocatalysts Using Hard X-Ray Spectroscopy. *J. Electr. Spectr. Rel. Phenomen* **2017**, *221*, 18–27.
- (13) Kowalska, J.; DeBeer, S. The Role of X-Ray Spectroscopy in Understanding the Geometric and Electronic Structure of Nitrogenase. *Biochim. Biophys Act.* **2015**, *1853* (6), 1406–1415.
- (14) Walker, F.A.; Simonis, U. Iron Porphyrin Chemistry. *Encyclopedia of Inorganic Chemistry*. Volume IV. John Wiley & Sons. 2<sup>nd</sup> edition. **2006**. pp: 2390-2521.
- (15) Paulat, F.; Lehnert, N. Detailed Assignment of the Magnetic Circular Dichroism and UV–vis Spectra of Five-Coordinate High-Spin Ferric [Fe(TPP)(Cl)]. *Inorg. Chem.* **2008**, *47* (11), 4963–4976.

- (16) Lexa, D.; Rentien, P.; Savéant, J. M.; Xu, F. Methods for Investigating the Mechanistic and Kinetic Role of Ligand Exchange Reactions in Coordination Electrochemistry: Cyclic Voltammetry of Chloroiron(III)Tetraphenylporphyrin in Dimethylformamide. *J. Electroanal. Chem. Interfac. Electrochem.* **1985**, *191* (2), 253–279.
- (17) Wilson, S. A.; Green, E.; Mathews, I. I.; Benfatto, M.; Hodgson, K. O.; Hedman, B.; Sarangi, R. X-Ray Absorption Spectroscopic Investigation of the Electronic Structure Differences in Solution and Crystalline Oxyhemoglobin. *PNAS* **2013**, *110* (41), 16333–16338.
- (18) Mashiko, T.; Reed, C. A.; Haller, K. J.; Scheidt, W. R. Nature of Iron(I) and Iron(0) Tetraphenylporphyrin Complexes. Synthesis and Molecular Structure of (Dibenzo-18-Crown-6) Bis(Tetrahydrofuran)Sodium (Meso-Tetraphenylporphinato) Ferrate and Bis[Tris(Tetrahydrofuran)Sodium] (Meso-Tetraphenylporphinato) Ferrate. *Inorg. Chem.* **1984**, *23* (20), 3192–3196.
- (19) Römelt, C.; Song, J.; Tarrago, M.; Rees, J. A.; van Gestel, M.; Weyhermüller, T.; DeBeer, S.; Bill, E.; Neese, F.; Ye, S. Electronic Structure of a Formal Iron(0) Porphyrin Complex Relevant to CO<sub>2</sub> Reduction. *Inorg. Chem.* **2017**, *56* (8), 4745–4750.
- (20) Mondal, B.; Rana, A.; Sen, P.; Dey, A. Intermediates Involved in the 2e<sup>-</sup>/2H<sup>+</sup> Reduction of CO<sub>2</sub> to CO by Iron(0) Porphyrin. *J. Am. Chem. Soc.* **2015**, *137* (35), 11214–11217.
- (21) Croisy, A.; Lexa, D.; Momenteau, M.; Savéant, J.-M. Integrated Molecular Systems. Fixation of Carbon Monoxide on Iron(I) in Simple and Superstructured Porphyrins. *Organometallics* **1985**, *4* (9), 1574–1579.
- (22) Lu, X.; Ahsaine, H. A.; Dereli, B.; Garcia-Esparza, A. T.; Reinhard, M.; Shinagawa, T.; Li, D.; Adil, K.; Tchalala, M. R.; Kroll, T.; Eddaoudi, M.; Sokaras, D.; Cavallo, L.; Takanebe, K. Operando Elucidation on the Working State of Immobilized Fluorinated Iron Porphyrin for Selective Aqueous Electroreduction of CO<sub>2</sub> to CO. *ACS Catal.* **2021**, *11* (11), 6499–6509.
- (23) Li, N.; Lu, W.; Pei, K.; Chen, W. Interfacial Peroxidase-like Catalytic Activity of Surface-Immobilized Cobalt Phthalocyanine on Multiwall Carbon Nanotubes. *RSC Adv.* **2015**, *5* (13), 9374–9380.
- (24) Costentin, C.; Drouet, S.; Robert, M.; Savéant, J.-M. A Local Proton Source Enhances CO<sub>2</sub> Electroreduction to CO by a Molecular Fe Catalyst. *Science* **2012**, *338* (6103), 90–94.
- (25) Costentin, C.; Drouet, S.; Passard, G.; Robert, M.; Savéant, J.-M. Proton-Coupled Electron Transfer Cleavage of Heavy-Atom Bonds in Electrocatalytic Processes. Cleavage of a C–O Bond in the Catalyzed Electrochemical Reduction of CO<sub>2</sub>. *J. Am. Chem. Soc.* **2013**, *135*, 24, 9023–9031.
- (26) Hammouche, M.; Lexa, D.; Momenteau, M.; Savéant, J.-M. Chemical Catalysis of Electrochemical Reactions. Homogeneous Catalysis of the Electrochemical Reduction of Carbon Dioxide by Iron(“0”) Porphyrins. Role of the Addition of Magnesium Cations. *J. Am. Chem. Soc.* **1991**, *113* (22), 8455–8466.
- (27) Bonin, J.; Chaussemier, M.; Robert, M.; Routier, M. Homogeneous Photocatalytic Reduction of CO<sub>2</sub> to CO Using Iron(0) Porphyrin Catalysts: Mechanism and Intrinsic Limitations. *ChemCatChem* **2014**, *6* (11), 3200–3207.

- (28) Lamy, E.; Nadjo, L.; Savéant, J.-M. Standard Potential and Kinetic Parameters of the Electrochemical Reduction of Carbon Dioxide in Dimethylformamide. *J. Electroanal. Chem. Interfac. Electrochem.* **1977**, 78 (2), 403–407.
- (29) Costentin, C.; Drouet, S.; Robert, M.; Savéant, J.-M. A Local Proton Source Enhances CO<sub>2</sub> Electroreduction to CO by a Molecular Fe Catalyst. *Science* **2012**, 338 (6103), 90–94.

---

# Publications

---

ARTICLE

<https://doi.org/10.1038/s41467-019-11542-w>

OPEN

# CO<sub>2</sub> electrochemical catalytic reduction with a highly active cobalt phthalocyanine

Min Wang<sup>1</sup>, Kristian Torbensen<sup>1</sup>, Danielle Salvatore<sup>2</sup>, Shaoxuan Ren<sup>3</sup>, Dorian Joulié<sup>1,3</sup>, Fabienne Dumoulin<sup>4</sup>, Daniela Mendoza<sup>1,6</sup>, Benedikt Lassalle-Kaiser<sup>6</sup>, Umit Işci<sup>4</sup>, Curtis P. Berlinguette<sup>2,3,5</sup> & Marc Robert<sup>1</sup>

Molecular catalysts that combine high product selectivity and high current density for CO<sub>2</sub> electrochemical reduction to CO or other chemical feedstocks are urgently needed. While earth-abundant metal-based molecular electrocatalysts with high selectivity for CO<sub>2</sub> to CO conversion are known, they are characterized by current densities that are significantly lower than those obtained with solid-state metal materials. Here, we report that a cobalt phthalocyanine bearing a trimethyl ammonium group appended to the phthalocyanine macrocycle is capable of reducing CO<sub>2</sub> to CO in water with high activity over a broad pH range from 4 to 14. In a flow cell configuration operating in basic conditions, CO production occurs with excellent selectivity (ca. 95%), and good stability with a maximum partial current density of 165 mA cm<sup>-2</sup> (at -0.92 V vs. RHE), matching the most active noble metal-based nanocatalysts. These results represent state-of-the-art performance for electrolytic carbon dioxide reduction by a molecular catalyst.

<sup>1</sup>Université de Paris, Laboratoire d'Electrochimie Moléculaire, CNRS, F-75013 Paris, France. <sup>2</sup>Department of Chemical and Biological Engineering, The University of British Columbia, 2360 East Mall, Vancouver, BC V6Y 1Z3, Canada. <sup>3</sup>Department of Chemistry, The University of British Columbia, 2036 Main Mall, Vancouver, BC V6T 1Z1, Canada. <sup>4</sup>Gebze Technical University, Department of Chemistry, 41400 Gebze, Kocaeli, Turkey. <sup>5</sup>Stewart Blusson Quantum Matter Institute, The University of British Columbia, 2355 East Mall, Vancouver, BC V6T 1Z4, Canada. <sup>6</sup>Synchrotron SOLEIL, L'Orme des Merisiers, Saint-Aubin, 91192 Gif-sur-Yvette, France. Correspondence and requests for materials should be addressed to U.I. (email: [u.isci@gtu.edu.tr](mailto:u.isci@gtu.edu.tr)) or to C.P.B. (email: [cberling@chem.ubc.ca](mailto:cberling@chem.ubc.ca)) or to M.R. (email: [robert@univ-paris-diderot.fr](mailto:robert@univ-paris-diderot.fr))

CO<sub>2</sub> can potentially be used as a renewable feedstock in electrochemical devices for sustainable energy storage in the form of synthetic fuels or fuel precursors (such as CO, CH<sub>3</sub>OH, and CH<sub>4</sub>), or for commodity chemicals. Hence, electrochemical reduction of CO<sub>2</sub> is an attractive way for industry to exploit surplus sustainable electricity in periods of low demand and it may contribute to mitigating the environmental impact caused by the massive release of CO<sub>2</sub><sup>1–3</sup>. However, the efficient and robust electrolytically driven reduction of CO<sub>2</sub> remains a formidable challenge for the scientific community. Fundamentally new approaches are needed to realize the selective transformation of CO<sub>2</sub> into desired products in an industrial setting.

There are several approaches available to catalyze the carbon dioxide reduction reaction (CO<sub>2</sub>RR), including molecular catalysts<sup>4–7</sup>. Molecular transition metal catalysts offer the distinct advantage of allowing for the fine-tuning of the primary and secondary coordination spheres by manipulating the chelating environment and the steric and electronic effects of the ligands. The ability to improve catalytic efficiency and product selectivity through the rational optimization of the ligand structure is a feature not accessible to the solid-state catalysts common to pilot-scale electrolyzer units<sup>8,9</sup>.

There now exist a range of known molecular catalysts, including those based on noble (e.g., Ru, Ir, and Re) and earth-abundant metals (e.g., Co, Ni, Fe, Mn, and Cu)<sup>4–12</sup>. These catalysts typically mediate a two electron reduction of CO<sub>2</sub> to either CO or formate with reasonable efficiencies, but in organic solvents. (there are also rare reports demonstrating molecules to catalyze highly reduced products such as light hydrocarbons)<sup>13–15</sup>. Integrating molecules with thin porous carbon films, such as carbon powder, carbon nanotubes, or graphene to form hybrid catalytic materials has proven to be a promising strategy to selectively achieve CO production in pure aqueous conditions. Importantly, these systems used earth-abundant metal catalysts such as Fe and Co porphyrins<sup>16–23</sup>, Mn bipyridine complexes<sup>24,25</sup>, Co quaterpyridines<sup>26</sup>, and Co phthalocyanines<sup>27–32</sup>. Good performances have been obtained in close to neutral conditions (pH 7–7.5) with excellent selectivity. The state-of-the-art system is a Co quaterpyridine adsorbed onto multiwalled carbon nanotubes, which shows exceptional selectivity (99%) at a current density up to 20 mA cm<sup>-2</sup> at a 440 mV overpotential<sup>26</sup>. An octacyano-substituted Co phthalocyanine complex deposited onto a gas diffusion electrode (GDE) and tested in a flow cell has been reported to achieve a current density of ~30 mA cm<sup>-2</sup> at an overpotential of ~550 mV with 96% selectivity for 10 h<sup>31</sup>.

While these values represent important advances for molecular CO<sub>2</sub>RR catalysts, much higher current densities are needed for commercial operation. Moreover, these current densities remain far below those obtained with state-of-the-art solid-state Ag<sup>33,34</sup> or Au<sup>35</sup> nanomaterials that have been reported to reach >150 mA cm<sup>-2</sup>.

In this work, we design a new Co phthalocyanine (**CoPc2**) bearing one trimethyl ammonium moiety and three *tert*-butyl groups appended on the phthalocyanine macrocycle. The cobalt complex is obtained and used as a mixture of the different regioisomers, which exhibit identical electronic and steric properties<sup>36,37</sup>, and **CoPc2** thus gives a unique electrochemical signature (Supplementary Fig. 1) with three reversible Faradaic waves that could be assigned to the Co<sup>II</sup>/Co<sup>I</sup> redox couple and to ligand reduction peaks<sup>38,39</sup>. With relatively low catalyst loadings of **CoPc2** dispersed into porous films of carbon black powder or carbon nanotubes on a carbon paper cathode, the modified electrode functions as highly effective CO<sub>2</sub>RR electrocatalysts in acidic (pH 4), neutral (pH 7.3), and basic conditions (pH 14). Importantly, the conversion of CO<sub>2</sub> to CO with very high

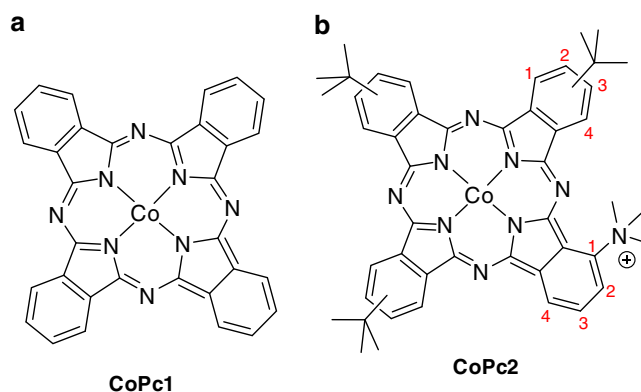


**Fig. 1** Cobalt phthalocyanine catalysts **CoPc1** and **CoPc2** investigated in this study. **a** **CoPc1** bears no substituents. **b** **CoPc2** bears one trimethyl ammonium group at position 1 of the isoindole subunits, and three *tert*-butyl groups (positions 2 or 3) of the other subunits

selectivities and current densities (up to 165 mA cm<sup>-2</sup> at pH 14) closely matches the performances of the most active noble metal-based catalysts.

## Results

**Preparation and electrochemical characterization of the catalytic inks.** Cobalt complexes **CoPc1** (Fig. 1a) and **CoPc2** (Fig. 1b) were deposited onto carbon electrodes from prepared colloidal inks.

Briefly, multiwalled carbon nanotubes (MWCNTs) or carbon black were dispersed in 1:1 mixtures of EG and ethanol by sonication. The catalyst was then added to the suspension, and after sonication and addition of a small amount of Nafion<sup>®</sup>, the catalytic material was drop casted on a glassy carbon electrode ( $d = 3$  mm) for cyclic voltammetry (CV) characterization, or onto carbon paper (1 or 0.5 cm<sup>2</sup>) for preparative scale electrolysis. Typical CVs recorded in a 0.5 M NaHCO<sub>3</sub> aqueous solution (pH 7.3) are shown in Fig. 2. The reversible wave centered at ca. -0.1 V vs. RHE could be assigned to the surface confined Co<sup>II</sup>/Co<sup>I</sup> redox couple, as shown by the linear increase of the peak current as a function of the scan rate (Fig. 2b, e).

The electroactive amount of catalyst within the film was 1.3–1.5 nmol cm<sup>-2</sup>, corresponding to about 9% of the total loaded concentration (Fig. 2e, f). Upon CO<sub>2</sub> saturation of the solution, the Co<sup>II</sup>/Co<sup>I</sup> wave remained unchanged, while a large catalytic increase of the current occurs at potentials more negative than -0.4 V vs. RHE (Fig. 2a, d). Repetitive CV shows good stability of the current response, indicative of a stable catalytic film (Supplementary Fig. 2). Remarkably, **CoPc2** gives a larger catalytic current at potentials very close from **CoPc1**, indicative of a better activity on kinetic grounds. We conjecture that the enhanced reactivity of **CoPc2** for CO<sub>2</sub> to CO conversion may be attributed to the through-space interactions between the positive charge of the trimethyl ammonium substituent and the partial negative charge borne by the O atoms in CO<sub>2</sub>, which facilitate the reductive coordination of the CO<sub>2</sub> molecule to the Co metal center. This mechanism has been reported for a tetraphenyl Fe porphyrins substituted with same functional groups on the phenyl rings for CO<sub>2</sub> to CO conversion<sup>8</sup>. These interactions may also favor the subsequent C–O bond cleavage leading to CO formation, thus illustrating how simple tuning of the phthalocyanine substituents can accelerate the catalytic reaction. Further mechanistic studies are in preparation.

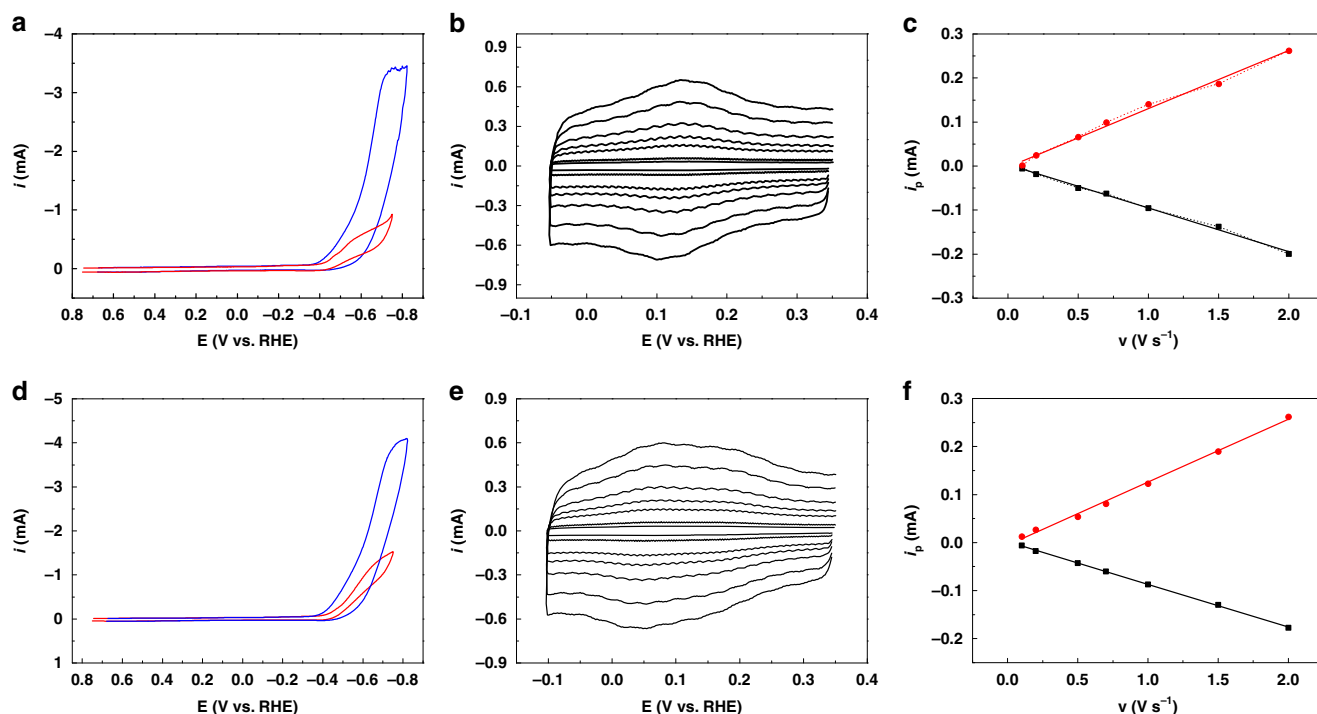


**Fig. 2** Cyclic voltammetry of cobalt phthalocyanine catalytic films. Top **a–c** **CoPc1@MWCNTs**, bottom **d–f** **CoPc2@MWCNTs**. **a, d** CV of a cobalt phthalocyanine catalytic film deposited onto a glassy carbon electrode ( $d = 3$  mm) in  $0.5$  M  $\text{NaHCO}_3$  at  $v = 0.1$  V  $\text{s}^{-1}$  under argon (red, pH 8.5) and  $\text{CO}_2$  (blue, pH 7.3). **b, e** CV at various scan rates of the  $\text{Co}^{\text{II}}/\text{Co}^{\text{I}}$  wave under argon atmosphere. **c, f** Variation of the peak current vs. scan rate for the  $\text{Co}^{\text{II}}/\text{Co}^{\text{I}}$  redox wave. A redox active catalyst concentration of  $\Gamma = 1.45 \pm 0.12$  nmol  $\text{cm}^{-2}$  was obtained from  $i_p = n^2 F^2 v \Gamma / 4RT$  for both catalysts

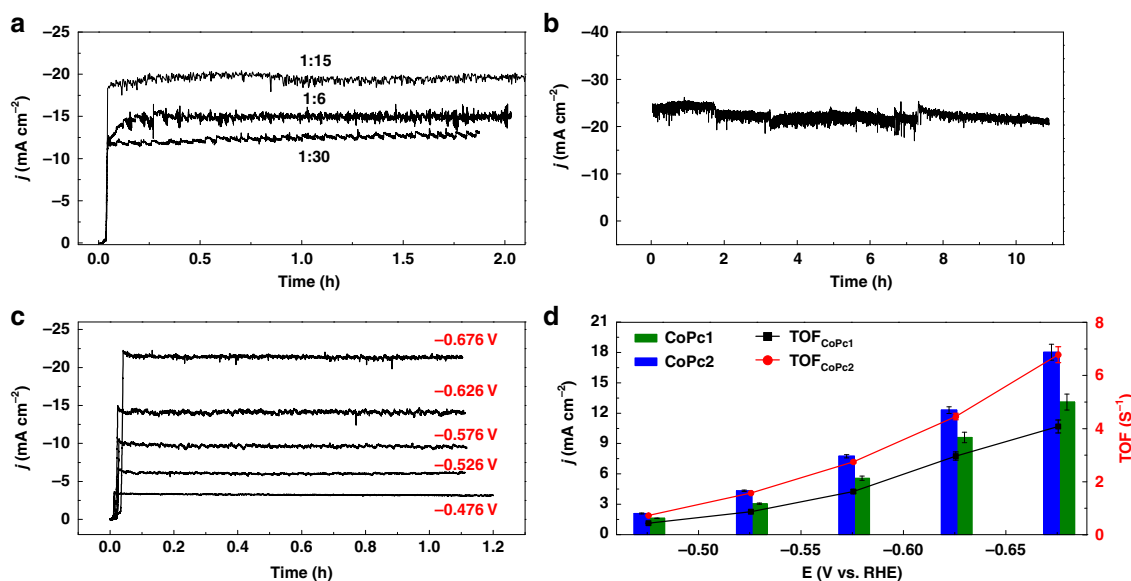


**Fig. 3** Controlled potential electrolysis of  $\text{CO}_2$  reduction. **a** Electrolysis current densities ( $E = -0.676$  V vs. RHE) for a **CoPc2@MWCNTs** film at various catalyst mass ratio. **b** Long-term electrolysis ( $E = -0.676$  V vs. RHE) at optimized mass ratio. **c** Variation of the current as a function of the electrolysis potential at optimized mass ratio (see text). **d** Current density and rate constant (TOF) for **CoPc1@MWCNTs** and **CoPc2@MWCNTs** for CO production in a  $\text{CO}_2$  saturated solution containing  $0.5$  M  $\text{NaHCO}_3$  (pH 7.3). The uncertainties represent standard errors obtained from four measurements

**Electrolysis experiments at neutral and acidic pH.** After the catalytic ink was deposited on a carbon paper electrode (see Methods and Supplementary Fig. 3 for a scanning electron microscopy (SEM) image of the porous catalytic film), bulk electrolysis was performed at pH neutral conditions with **CoPc2** for various loadings of the molecular catalyst. An optimal loading ratio of 1:15 (catalyst:MWCNTs weight ratio) shows reasonably good stability over the course of the 2 h experiments (Fig. 3a).

The CO selectivity was typically 92–93% in repeated runs, with  $\text{H}_2$  being identified as a minor gas phase by-product (7–8%). No other product was detected in the liquid phase upon nuclear magnetic resonance (NMR) analysis. The electrolysis performed in the absence of catalyst or with **CoPc2@MWCNTs** (1:15) under Ar atmosphere only furnished  $\text{H}_2$  (Supplementary Fig. 4). The TON and TOF values in Tables 1 and 2 and in the text were calculated using the total



**Table 1 Comparative data for CoPc1@MWCNTs and CoPc2@MWCNTs catalytic materials during a 1 h electrolysis as a function of the potential in CO<sub>2</sub>-saturated aqueous solution containing 0.5 M NaHCO<sub>3</sub> (pH 7.3)**

E (V vs. RHE)	Entry	overpotential (mV) <sup>a</sup>	Catalyst <sup>b</sup>	$j_{\text{CO}}$ (mA cm <sup>-2</sup> ) <sup>c</sup>	TOF (CO, s <sup>-1</sup> ) <sup>c</sup>	Selectivity (CO, ±0.5%)
-0.676	1	546	<b>CoPc1</b>	13.10 ± 0.79	4.08 ± 0.25	92
	2	539	<b>CoPc2</b>	18.10 ± 0.80	6.81 ± 0.30	93
-0.626	3	502	<b>CoPc1</b>	9.61 ± 0.51	2.97 ± 0.16	92
	4	498	<b>CoPc2</b>	12.3 ± 0.34	4.46 ± 0.12	92
-0.576	5	458	<b>CoPc1</b>	5.57 ± 0.21	1.63 ± 0.06	86
	6	454	<b>CoPc2</b>	7.75 ± 0.16	2.75 ± 0.06	84
-0.526	7	411	<b>CoPc1</b>	3.10 ± 0.07	0.87 ± 0.02	80
	8	410	<b>CoPc2</b>	4.33 ± 0.08	1.57 ± 0.03	73
-0.476	9	364	<b>CoPc1</b>	1.62 ± 0.01	0.44 ± 0.01	76
	10	363	<b>CoPc2</b>	2.09 ± 0.04	0.74 ± 0.01	65

<sup>a</sup>Corrected from ohmic drop (uncompensated solution resistance of ca. 3 Ω, electrode surface 0.5 cm<sup>2</sup>)

<sup>b</sup> $\Gamma(\text{CoPc1}) = 23.3 \text{ nmol cm}^{-2}$ ,  $\Gamma(\text{CoPc2}) = 14.4 \text{ nmol cm}^{-2}$  (total added catalysts)

<sup>c</sup>The uncertainties represent standard errors obtained from four measurements

**Table 2 Comparison of electrolysis performances between CoPc2@carbon powder hybrid catalyst and previously reported state-of-the-art immobilized molecular Co catalysts and Ag nanomaterial**

Entry	Catalyst	E (V vs. RHE) [overpotential (mV)]	Electrolyte	$j_{\text{CO}}$ (mA cm <sup>-2</sup> )	TOF (s <sup>-1</sup> )	CO sel. (%)	Cell type	Ref.
<b>1</b>	<b>CoPc2</b>	-0.97 [836] <sup>a</sup>	0.5 M KCl	16.3	6.1	92	H cell	this work
<b>2</b>	<b>CoPc2</b>	-0.676 [539] <sup>a</sup>	0.5 M NaHCO <sub>3</sub>	18.1	6.8	93	H cell	this work
<b>3</b>	<b>CoPc</b>	-0.676 [546] <sup>a</sup>	0.5 M NaHCO <sub>3</sub>	13.1	4.1	92	H cell	this work
<b>4</b>	CoPc-CN	-0.63 [520]	0.1 M KHCO <sub>3</sub>	14.7	4.1	98	H cell	28
<b>5</b>	CoPpc	-0.61 [500]	0.5 M NaHCO <sub>3</sub>	18	1.4	ca. 90	H cell	29
<b>6</b>	Coqpy	-0.55 [440]	0.5 M NaHCO <sub>3</sub>	19.9	12	99	H cell	26
<b>7</b>	<b>CoPc2</b>	-0.31 [200] <sup>b</sup>	1 M KOH	22.2	0.54	93	Flow cell	this work
<b>8</b>	<b>CoPc2</b>	-0.65 [540] <sup>b</sup>	1 M KOH	70.5	1.67	94	Flow cell	this work
<b>9</b>	<b>CoPc2</b>	-0.72 [610] <sup>b</sup>	1 M KOH	111.6	2.7	96	Flow cell	this work
<b>10</b>	<b>CoPc2</b>	-0.92 [810] <sup>b</sup>	1 M KOH	165	3.9	94	Flow cell	this work
<b>11</b>	CoPc-CN	-0.66 [550]	1 M KOH	31	/	94	Flow cell	31
<b>12</b>	Ag <sup>c</sup>	-0.81 [700]	1 M KOH	156.5	/	92	Flow cell	34

Entry 1:  $\Gamma = 14.4 \text{ nmol cm}^{-2}$  (pH 4, 2 h electrolysis), entry 2:  $\Gamma = 14.4 \text{ nmol cm}^{-2}$  (pH 7.3, 1 h electrolysis), entry 3:  $\Gamma = 23.3 \text{ nmol cm}^{-2}$  (pH 7.3, 1 h electrolysis), entries 7-10:  $\Gamma = 0.216 \text{ } \mu\text{mol cm}^{-2}$  (pH 14, for 0.5, 10, 3, and 0.3 h electrolysis, respectively).

<sup>a</sup>Corrected from ohmic drop (uncompensated solution resistance of ca. 3 Ω, electrode surface 0.5 cm<sup>2</sup>)

<sup>b</sup>Uncorrected from ohmic drop

<sup>c</sup>Carbonate-derived Ag nano-catalyst (500 nm thickness), see Ref. 34 for details

amount of catalyst added in the films, hence these values are underestimated.

Using this 1:15 catalyst loading weight ratio, the effect of the applied potential on efficiency and selectivity was investigated for both the cobalt catalysts at pH neutral conditions (Fig. 3c and Supplementary Fig. 5). As shown in Fig. 3d, the current density was systematically larger for **CoPc2** as compared to **CoPc1** (ca. 25% increase). Concomitantly, the CO selectivity increases at more negative electrolysis potentials, with a relative higher increase for **CoPc2** (Table 1). This shows that, at more negative potentials, the catalytic CO<sub>2</sub> reduction reaction outruns the H<sub>2</sub> evolution reaction. At -0.676 V vs. RHE which corresponds to an overpotential  $\eta = 546 \text{ mV}$  and in neutral pH conditions, **CoPc1** gave 92% CO with an average partial current density of 13.1 mA cm<sup>-2</sup> (Table 1, entry 1). At the same potential ( $\eta = 539 \text{ mV}$ ), a 1 h electrolysis with **CoPc2** led to a TON of 24516 for CO (TOF = 6.8 s<sup>-1</sup>) with 93% selectivity. The partial current density for CO production reaches 18.1 mA cm<sup>-2</sup> (Table 1, entry 2).

Longer term electrolysis at pH 7.3 further demonstrates the excellent stability of the catalytic system, since no decrease in either the current density or the selectivity for CO production were observed upon a 10.5 h experiment. An average selectivity of

91% for CO production along with  $j_{\text{CO}}$  close to 20 mA cm<sup>-2</sup> (Fig. 3b) were measured. XPS analysis of the cathode material before and after electrolysis does not reveal major changes of the Co 2p and N 1s peaks, suggesting integrity of the molecular catalyst during the entire course of the electrolysis (Supplementary Fig. 6). Remarkably, an electrolysis (2 h) at  $E = -0.971 \text{ V vs. RHE}$  in a CO<sub>2</sub> saturated 0.5 M KCl solution (pH 4) led to equally good results, with a selectivity of 92% and  $j_{\text{CO}} = 17 \text{ mA cm}^{-2}$  (Supplementary Fig. 7). When the cobalt phthalocyanine bearing four t-butyl groups (**4-Co**) was used as catalyst in an electrolysis experiment (1:15 catalyst loading weight ratio,  $E = -0.676 \text{ V vs. RHE}$ ) in neutral pH conditions, a Faradaic efficiency of 92% for CO was obtained with an average CO partial current density of 15.8 mA cm<sup>-2</sup> (Supplementary Fig. 8). This reference complex is thus less active than **CoPc2**, further illustrating that the enhanced activity of **CoPc2** may arise from the trimethyl ammonium substituent on the ligand via through-space effects.

**Electrolysis experiments in basic solutions using a flow cell.** Encouraged by these results, we included **CoPc2** into a flow cell setup comprising **CoPc2** supported on a GDE as the cathode, in order to realize CO<sub>2</sub> to CO conversion in industrial setting.



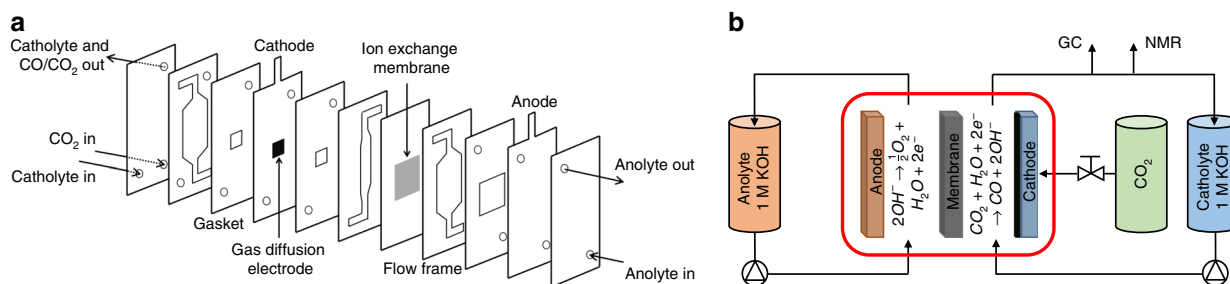


**Fig. 4** Graphic illustration of the CO<sub>2</sub> electrolyzer flow cell. **a** Cross-sectional view of the cell and **b** general scheme of the entire experimental set-up

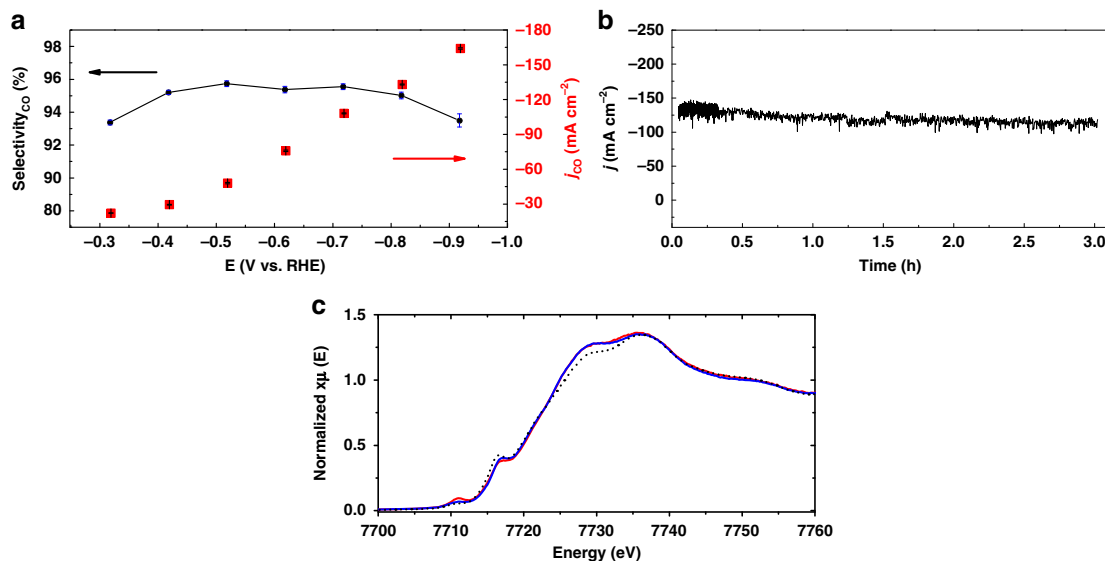


**Fig. 5** Controlled potential electrolysis and **CoPc2** film characterization. **a** Current density and selectivity for CO production as a function of the potential and **b** bulk electrolysis at fixed potential ( $E = -0.72$  V vs. RHE) for **CoPc2**@carbon black deposited onto a carbon paper as cathodic material, in 1 M KOH. **c** Co K-edge XANES profiles of **CoPc2** (black dots) and **CoPc2**@carbon black before (blue) and after electrolysis ( $E = -0.72$  V vs. RHE) (red) in 1 M KOH solution

Details of the setup are provided in the methods. Briefly, the electrolyzer consists of a sandwich of flow frames, electrodes, gaskets and an ion exchange membrane, which were assembled as schematically illustrated in Fig. 4a. A gas flow of CO<sub>2</sub> is delivered from the back side of the cathodic compartment and flows through the GDE, while the catholyte solution is circulated in between the GDE and the anion exchange membrane (AEM). On the other side of the AEM, the anolyte is directed between the AEM and the Pt/Ti alloy anode, Fig. 4b. **CoPc2** was dispersed in a colloidal ink with carbon black and subsequently deposited on the carbon fiber paper, composing the cathode.

At  $-0.3$  V vs. RHE, which corresponds to a low 200 mV overpotential, a high current density with  $j_{\text{CO}} = 22.2$  mA cm<sup>-2</sup> was achieved. The dependence of the current density for CO production is reported in Fig. 5a (see also Supplementary Fig. 9). Upon setting the electrolysis potential at  $-0.72$  V vs. RHE,  $j_{\text{CO}}$  raised to 111.6 mA cm<sup>-2</sup> with 96% selectivity, while excellent stability over the course of the 3 h electrolysis was obtained (Fig. 5b). The only additional gas phase by-product was H<sub>2</sub> (4% selectivity) and the catholyte solution was carefully checked by <sup>1</sup>H NMR. Formate or methanol were not detected while the absence of any **CoPc2** trace further indicate that the molecular catalyst is not leaching out of the supporting film. The obtained  $j_{\text{CO}}$  corresponds to a turnover frequency (TOF) of 2.7 s<sup>-1</sup> and a turnover number (TON) of 29,008. A maximum current density

of 165 mA cm<sup>-2</sup> for CO generation was obtained at  $-0.92$  V vs. RHE. Long-term stability of the catalytic material was further illustrated upon applying a constant current density of 75 mA cm<sup>-2</sup> for 10 h, which led to a cathodic potential of  $-0.65$  V vs. RHE ( $\eta = 540$  mV) with 94% selectivity of CO ( $j_{\text{CO}} = 70.5$  mA cm<sup>-2</sup>) (Supplementary Fig. 10). All the collected data are compiled in Table 2, along with a comparison of previously reported catalysts. The type of cell used (H cell vs. flow cell) is also indicated to ease comparison between data. The Co K-edge XANES spectra of **CoPc2**@carbon black were recorded before and after electrocatalysis at  $E = -0.72$  V vs. RHE. Figure 5c shows these spectra together with that of the starting **CoPc2** complex. All these spectra present the typical features expected for a cobalt (II) phthalocyanine complex, i.e., a low intensity pre-edge peak at 7711 eV (corresponding to a 1s to 3d/4p transition) and a shoulder at 7717 eV (corresponding to a 1s to 4p<sub>z</sub> transition)<sup>29,40,41</sup>. The intensity of these two transitions were shown by Li et al.<sup>41</sup> to depend on the attachment to a surface, i.e., the pre-edge intensity increases and the shoulder decreases upon adsorption onto nanotubes, respectively.

The same trend is observed in the **CoPc2**@carbon black system, with decreased pre-edge and increased shoulder intensities on going from the starting complex to the adsorbed species. This trend retains after catalysis, suggesting an even closer interaction with the surface while maintaining the overall

structure of the molecular catalyst after the experiment. This conservation of structure is further confirmed by the EXAFS spectra (Supplementary Fig. 11), which also present the typical features of a cobalt phthalocyanine complex<sup>41</sup>. In addition, comparison of the spectrum of **CoPc2**@carbon black recorded after catalysis with those of reference cobalt samples (Supplementary Fig. 11) clearly shows that the changes observed on the spectrum after catalysis are insignificant as far as the overall structure is concerned.

## Discussion

Remarkably, **CoPc2** remains highly selective for the CO<sub>2</sub>-to-CO conversion across 10 pH units, extending from acidic (pH 4) to basic solutions (pH 14). An averaged 92% selectivity for CO<sub>2</sub> reduction with partial current densities of ca. 20 mA cm<sup>-2</sup> were routinely obtained in the whole domain of pH values with excellent stability over time. In close to neutral solutions (pH 7.3), **CoPc2** is a significantly better catalyst than the unsubstituted phthalocyanine **CoPc1** (see Table 2, entries 2 and 3) with a ca. 25% increase in current density at similar overpotential, but it also surpasses state-of-the-art tetra-cyano substituted phthalocyanine (CoPc-CN, Table 2, entry 4) and unsubstituted Co phthalocyanine polymerized around carbon nanotubes (CoPpc, Table 2, entry 5), both in terms of current density and TOF. Similarly to the previously reported cobalt phthalocyanines mentioned above, **CoPc2** exhibits excellent stability over time, as illustrated in Fig. 3b, showing a 10.5 h electrolysis experiment, with no loss of performance. A TOF up to 6.8 s<sup>-1</sup> was reached and, generally, only a very small loading of the catalysts was necessary to obtain high *j*<sub>CO</sub> (see for example Table 2, entries 1–2). In a 1 M KOH electrolyte solution (pH 14), ca. 20 mA cm<sup>-2</sup> could be obtained at a very low overpotential of 200 mV, once the hybrid catalyst mixed with carbon support was included in a gas flow cell (Table 2, entry 7). Long-term electrolysis (10 h) in basic conditions (pH 14) at -0.65 V vs. RHE led to an average *j*<sub>CO</sub> close to 70.5 mA cm<sup>-2</sup>. The ability to implement **CoPc2** in various pH conditions is also a key feature that may allow for combining the Co catalyst to various types of anodic materials in order to decrease the overall cell potential. In particular, the excellent performance obtained at pH 14 could permit pairing of the **CoPc2** loaded cathode with the most efficient oxygen evolving metal oxide anode materials. At this pH, at -0.92 V vs. RHE, this hybrid catalyst can form CO with 94% selectivity at a partial current density of 165 mA cm<sup>-2</sup>, matching the state-of-the-art Ag based catalyst sputtered onto a PTFE membrane, both in terms of selectivity and current density (Table 2, compare entries 10 and 12).

In conclusion, upon introducing a positively charged trimethyl ammonium group and three tert-butyl groups on the parent cobalt phthalocyanine, a highly efficient and versatile catalyst for the CO<sub>2</sub>-to-CO electrochemical conversion in water has been obtained. This study highlights that rational tuning of the structure of simple metal complexes may allow for high CO<sub>2</sub> electroreduction performances, and it is likely that further improvement is yet to come. This work opens up new perspectives for the development of low-cost catalytic materials to be included in CO<sub>2</sub> electrolyzers that will hopefully soon emerge at an industrial scale.

## Methods

**Chemicals.** Chemicals and materials were purchased from Sigma-Aldrich, Fluka, TCI America, ABCR or Alfa Aesar, and used as received. All aqueous solutions were prepared with Millipore water (18.2 MΩ cm). The MWCNTs were purchased from Sigma-Aldrich (O.D. × L 6–9 nm × 5 μm, >95%). The cobalt (II) phthalocyanine (**CoPc1**) (β-form, dye content 97%) was purchased from Sigma-Aldrich. Toray Carbon Paper (CAS number: 7782-42-5), TGP-H-60, 19 × 19 cm was purchased from Alfa Aesar and used for preparation of the cathodes for the

electrochemical cell. The cathodes (GDEs) used in the flow cell were prepared using Freudenberg C24H5 carbon paper (21 × 29.7 cm, product code F5GDL). VUL-CAN® XC72R Speciality Carbon Black was purchased from Cabot Corporation. 4-Tert-butylphthalonitrile was obtained from TCI America. 3-Nitrophthalonitrile was purchased from ABCR. All solvents were of synthetic grade. Supplementary Fig. 13 describes the synthesis and characterization of **CoPc2**, and supplementary Figs. 14–27 provide characterization of reaction intermediates and final compound.

**Preparation of the hybrid materials.** For CV experiments and electrolysis in the closed electrolysis cell, 3 mg of MWCNTs were dispersed in 2 mL ethylene glycol (EG)/ethanol (EtOH) 1:1 (v/v) mixture followed by 30 min of sonication. Totally, 1 mg of the cobalt catalyst (**CoPc1**, **CoPc2**) was dissolved in 1 mL EG/EtOH mixture. Various volumes of this solution were added to the MWCNTs suspension in a total volume of 3 mL, so as to get mass ratio (1:6, 1:15 and 1:30) of the catalyst. The suspension was further sonicated for 30 min. Finally, Nafion® was added (2.9%, 30 μL) and the complete mixture was sonicated for 30 min to obtain the final catalytic ink.

For the flow cell set-up, 3 mg of carbon black were dispersed in 3 mL EtOH followed by 30 min of sonication. Totally, 0.2 mg of **CoPc2** was dissolved in 1 mL EtOH so as to get a mass ratio (1:15) of the catalyst. The suspension was further sonicated for 30 min. Finally, Nafion® was added (2.9%, 30 μL) and the complete mixture was sonicated for 30 min to obtain the final catalytic ink. The ink was drop casted on carbon paper masked with a Teflon frame to obtain an electrode area of 1 × 1 cm<sup>2</sup>.

**Electrochemical studies.** CV experiments were performed using an AUTOLAB PGSTAT128N potentiostat (Metrohm). Controlled potential electrolysis were performed using a PARSTAT 4000A potentiostat (Princeton Applied Research).

**CV:** The three-electrode setup consisted of a glassy carbon working electrode (custom made, 0.071 cm<sup>2</sup>), a Pt wire counter electrode, and a SCE reference electrode (-0.241 V vs. NHE). The working electrode was polished with diamond paste (15, 6, 3, and 1 μm successively, 60 s per polishing cycle), thoroughly rinsed and sonicated in ethanol, and dried. Totally, 10 μL of the hybrid materials suspension were dropped on the surface of the electrode, and allowed to dry under 100 °C ambient conditions. Ohmic drop was compensated using the positive feedback compensation implemented in the instrument.

**Preparative scale electrolysis:** In the closed cell, experiments were carried out in a cell using a Toray carbon paper as working electrode, and a SCE reference electrode closely positioned one from the other. The Pt grid counter electrode was separated from the cathodic compartment with a glass frit. The catalytic ink was dropped on one face of the Toray carbon paper cathode (100 μL for a 0.5 cm<sup>2</sup> electrode), and allowed to dry under 100 °C ambient conditions prior to use. The full cell setup was identical to the one used previously<sup>26</sup>.

The flow cell electrolyzer (Micro Flow Cell® purchased by Electrocell) is composed by a sandwich of flow frames, electrodes, gaskets, and a membrane, which, when assembled as illustrated in Fig. 3, constitute a three-compartment flow cell. One compartment delivers the CO<sub>2</sub> (at 16.7 sccm) from the back side and through the GDE (1 × 1 cm<sup>2</sup>, fixated in a Ti frame), while another directs the catholyte solution (1 M KOH, flow rate of 16 sccm) in between the GDE and the AEM (Sustainion™ X37-50). On the other side of the latter, the anolyte (1 M KOH, flow rate of 16 sccm) is directed between the AEM and the Pt/Ti alloy anode. The flow frames are made of PTFE, and the gaskets of peroxide cured EDPM. Catholyte and anolyte were recycled using peristaltic pumps. All tubings were made of PTFE and connected to the cell with PEEK ferrules and fittings. The whole setup is schematically shown Supplementary Fig. 12.

**Gas detection.** Gas chromatography analyses of gas sampled from the headspace during the electrolysis were performed with an Agilent Technologies 7820A GC system equipped with a thermal conductivity detector. CO and H<sub>2</sub> production was quantitatively detected using a CP-CarboPlot P7 capillary column (27.46 m in length and 25 μm internal diameter). Temperature was held at 150 °C for the detector and 34 °C for the oven. The carrier gas was argon flowing at 9.5 mL/min at constant pressure of 0.4 bars. Injection was performed via a 250-μL gas-tight (Hamilton) syringe previously degassed with CO<sub>2</sub>. Conditions allowed detection of both H<sub>2</sub>, O<sub>2</sub>, N<sub>2</sub>, CO, and CO<sub>2</sub>. Calibration curves for H<sub>2</sub> and CO were determined separately by injecting known quantities of pure gas.

**Material characterizations.** An X-Ray Photoelectron Spectrometer THERMO-VG ESCALAB 250 (RX source K Al (1486.6 eV)) was used. X-ray absorption spectra were collected at the LUCIA beamline of SOLEIL with a ring energy of 2.75 GeV and a current of 490 mA. The energy was monochromatized by means of a Si (111) double crystal monochromator. Data were collected in a primary vacuum chamber as fluorescence spectra with an outgoing angle of 5° using a Bruker silicon drift detector. The data were normalized to the intensity of the incoming incident energy and processed with the Athena software from the IFFEFIT package. For the EXAFS analysis, an E<sub>0</sub> value of 7715.4 eV was used for the cobalt K-edge jump energy. SEM using a field emission gun was performed using a Zeiss Supra 40. Infrared spectra (IR) were recorded on a Bio-Rad FTS 175 C Fourier transform infrared spectrometer spectrophotometer. Ultraviolet (UV)-visible absorption

spectra were obtained using a Shimadzu 2001 UV spectrophotometer. High resolution mass spectra were measured on an Agilent 6530 Accurate-Mass Q-TOF LC/MS spectrometer equipped with electrospray ionization source. NMR spectra were recorded in deuterated chloroform ( $\text{CDCl}_3$ ) and THF- $d_6$  on a Varian 500 MHz spectrometer. Melting points were recorded on a Stuart SMP apparatus.

### Data availability

Data supporting the findings of this study are available within the Article and its Supplementary Information, or from the corresponding authors upon reasonable request.

Received: 22 February 2019 Accepted: 19 July 2019

Published online: 09 August 2019

### References

1. Aresta, M., Dibenedetto, A. & Angelini, A. Catalysis for the valorization of exhaust carbon: from  $\text{CO}_2$  to chemicals, materials, and fuels. *technological use of  $\text{CO}_2$* . *Chem. Rev.* **114**, 1709–1742 (2014).
2. Jhong, H.-R. M., Ma, S. & Kenis, P. J. A. Electrochemical conversion of  $\text{CO}_2$  to useful chemicals: current status, remaining challenges, and future opportunities. *Curr. Opin. Chem. Eng.* **2**, 191–199 (2013).
3. Seh, Z. W. et al. Combining theory and experiment in electrocatalysis: Insights into materials design. *Science* **355**, eaad4998 (2017).
4. Costentin, C., Robert, M. & Savéant, J.-M. Catalysis of the electrochemical reduction of carbon dioxide. *Chem. Soc. Rev.* **42**, 2423–2436 (2013).
5. Qiao, J., Liu, Y., Hong, F. & Zhang, J. A review of catalysts for the electroreduction of carbon dioxide to produce low-carbon fuels. *Chem. Soc. Rev.* **43**, 631–675 (2014).
6. Elgrishi, N., Chambers, M. B., Wang, X. & Fontecave, M. Molecular polypyridine-based metal complexes as catalysts for the reduction of  $\text{CO}_2$ . *Chem. Soc. Rev.* **46**, 761–796 (2017).
7. Grice, K. A. Carbon dioxide reduction with homogenous early transition metal complexes: opportunities and challenges for developing  $\text{CO}_2$  catalysis. *Coord. Chem. Rev.* **336**, 78–95 (2017).
8. Azcarate, I., Costentin, C., Robert, M. & Savéant, J.-M. Through-space charge interaction substituent effects in molecular catalysis leading to the design of the most efficient catalyst of  $\text{CO}_2$ -to-CO electrochemical conversion. *J. Am. Chem. Soc.* **138**, 16639–16644 (2016).
9. Francke, R., Schille, B. & Roemelt, M. Homogeneously catalyzed electroreduction of carbon dioxide—methods, mechanisms, and catalysts. *Chem. Rev.* **116**, 4631–4701 (2018).
10. Grills, D. C., Ertem, M. Z., McKinnon, M., Ngo, K. T. & Rochford, J. Mechanistic aspects of  $\text{CO}_2$  reduction catalysis with manganese-based molecular catalysts. *Coord. Chem. Rev.* **374**, 173–217 (2018).
11. Loewen, N. D., Neelakantan, T. V. & Berben, L. A. Renewable formate from C–H bond formation with  $\text{CO}_2$ : using iron carbonyl clusters as electrocatalysts. *Acc. Chem. Res.* **50**, 2362–2370 (2017).
12. Takeda, H., Cometto, C., Ishitani, O. & Robert, M. Electrons, photons, protons and earth abundant metal complexes for molecular catalysis of  $\text{CO}_2$  reduction. *ACS Catal.* **7**, 70–88 (2017).
13. Shen, J. et al. Electrocatalytic reduction of carbon dioxide to carbon monoxide and methane at an immobilized cobalt protoporphyrin. *Nat. Commun.* **6**, 8177 (2015).
14. Rao, H., Schmidt, L. C., Bonin, J. & Robert, M. Visible-light-driven methane formation from  $\text{CO}_2$  with an iron complex. *Nature* **548**, 74–77 (2017).
15. Rao, H., Lim, C.-H., Bonin, J., Miyake, G. M. & Robert, M. Visible-light-driven conversion of  $\text{CO}_2$  to  $\text{CH}_4$  with an organic sensitizer and an iron porphyrin catalyst. *J. Am. Chem. Soc.* **140**, 17830–17834 (2018).
16. Tatin, A. et al. Efficient electrolyser for  $\text{CO}_2$  splitting in neutral water using earth abundant materials. *Proc. Natl Acad. Sci. USA* **113**, 5526–5529 (2016).
17. Maurin, A. & Robert, M. Noncovalent immobilization of a molecular iron based electrocatalyst on carbon electrodes for selective, efficient  $\text{CO}_2$ -to-CO conversion in water. *J. Am. Chem. Soc.* **138**, 2492–2495 (2016).
18. Mohamed, E. A., Zahran, Z. N. & Naruta, Y. Efficient heterogeneous  $\text{CO}_2$  to CO conversion with a phosphonic acid fabricated cofacial iron porphyrin dimer. *Chem. Mater.* **29**, 7140–7150 (2017).
19. Choi, J. et al. A porphyrin/graphene framework: a highly efficient and robust electrocatalyst for carbon dioxide reduction. *Adv. Energy Mater.* **8**, 1801280 (2018).
20. Choi, J. et al. Energy efficient electrochemical reduction of  $\text{CO}_2$  to CO using a three-dimensional porphyrin/graphene hydrogel. *Energy Environ. Sci.* **12**, 747–755 (2019).
21. Sonoyama, N., Kirii, M. & Sakata, T. Electrochemical reduction of  $\text{CO}_2$  at metal-porphyrin supported gas diffusion electrodes under high pressure  $\text{CO}_2$ . *Electrochem. Commun.* **1**, 213–216 (1999).
22. Aoi, S., Mase, K., Ohkubo, K. & Fukuzumi, S. Selective electrochemical reduction of  $\text{CO}_2$  to CO with a cobalt chlorin complex adsorbed on multi-walled carbon nanotubes in water. *Chem. Commun.* **50**, 10226–10228 (2015).
23. Hu, X.-M., Ronne, M. H., Pedersen, S. U., Skrydstrup, T. & Daasbjerg, K. Enhanced catalytic activity of cobalt porphyrin in  $\text{CO}_2$  electroreduction upon immobilization on carbon materials. *Angew. Chem. Int. Ed.* **56**, 6468–6472 (2017).
24. Rotundo, L. et al. Electrochemical  $\text{CO}_2$  reduction in water at carbon cloth electrodes functionalized with a fac-Mn (apbpy)( $\text{CO}_3$ )Br complex. *Chem. Commun.* **55**, 775–777 (2019).
25. Walsh, J. J., Neri, G., Smith, C. L. & Cowan, A. J. Electrocatalytic  $\text{CO}_2$  reduction with a membrane supported manganese catalyst in aqueous solution. *Chem. Commun.* **50**, 12698–12701 (2014).
26. Wang, M., Chen, L., Lau, T.-C. & Robert, M. Hybrid Co quaterpyridine complex/carbon nanotube catalytic material for  $\text{CO}_2$  reduction in water. *Angew. Chem. Int. Ed.* **57**, 7769–7773 (2018).
27. Morlanes, N., Takanabe, K. & Rodionov, V. Simultaneous reduction of  $\text{CO}_2$  and splitting of  $\text{H}_2\text{O}$  by a single immobilized cobalt phthalocyanine electrocatalyst. *ACS Catal.* **6**, 3092–3095 (2016).
28. Zhang, X. et al. Highly selective and active  $\text{CO}_2$  reduction electrocatalysts based on cobalt phthalocyanine/carbon nanotube hybrid structures. *Nat. Commun.* **8**, 14675 (2017).
29. Han, N. et al. Supported cobalt phthalocyanine for high-performance electrocatalytic  $\text{CO}_2$  reduction. *Chem* **3**, 652–664 (2017).
30. Chen, C. et al. Enhanced  $\text{CO}_2$  electroreduction via interaction of dangling S bonds and Co sites in cobalt phthalocyanine/ $\text{ZnIn}_2\text{S}_4$  hybrids. *Chem. Sci.* **10**, 1659–1663 (2019).
31. Xu, L. et al. High-performance electrochemical  $\text{CO}_2$  reduction cells based on non-noble metal catalysts. *ACS Energy Lett.* **3**, 2527–2532 (2018).
32. Choi, J. et al. Steric modification of a cobalt phthalocyanine/graphene catalyst to give enhanced and stable electrochemical  $\text{CO}_2$  reduction to CO. *ACS Energy Lett.* **4**, 666–672 (2019).
33. Kutz, R. B. et al. Sustainion imidazolium-functionalized polymers for carbon dioxide electrolysis. *Energy Technol.* **5**, 929–936 (2017).
34. Dinh, C.-T., García de, Arquer F. P., Sinton, D. & Sargent, E. H. High rate, selective, and stable electroreduction of  $\text{CO}_2$  to CO in basic and neutral media. *ACS Energy Lett.* **3**, 2835–2840 (2018).
35. Verma, S. et al. Insights into the low overpotential electroreduction of  $\text{CO}_2$  to CO on a supported gold catalyst in an alkaline flow electrolyzer. *ACS Energy Lett.* **3**, 193–198 (2018).
36. Li, X. et al. Nanostructured phthalocyanine assemblies with protein-driven switchable photoactivities for biophotonic imaging and therapy. *J. Am. Chem. Soc.* **139**, 10880–10886 (2017).
37. Cao, J. et al. Efficient grain boundary suture by low-cost tetra-ammonium zinc phthalocyanine for stable perovskite solar cells with expanded photoresponse. *J. Am. Chem. Soc.* **140**, 11577–11580 (2018).
38. Manbeck, G. F. & Fujita, E. A review of iron and cobalt porphyrins, phthalocyanines and related complexes for electrochemical and photochemical reduction of carbon dioxide. *J. Porphyr. Phthalocyanines* **19** (01n03), 45–64 (2015).
39. Akyüz, D., Keleş, T., Biyiklioglu, Z. & Koca, A. Metallophthalocyanines bearing polymerizable {[5-((1E)-[4-(diethylamino) phenyl] methylene) amino]-1-naphthyl} oxy groups as electrochemical pesticide sensor. *Electroanalysis* **29**, 2913–2924 (2017).
40. Dodelet, J. P. Oxygen reduction in PEM fuel cell conditions: heat-treated non-precious metal-N4 macrocycles and beyond. In (eds Zagal J. H., Bedioui F. & Dodelet J. P.) *N4-Macrocyclic Metal Complexes*. Ch. 3. 91–99 (Springer, 2006).
41. Li, N., Lu, W., Pei, K. & Chen, W. Interfacial peroxidase-like catalytic activity of surface-immobilized cobalt phthalocyanine on multiwall carbon nanotubes. *RSC Adv.* **5**, 9374–9380 (2015).

### Acknowledgements

M.W. thanks the China Scholarship Council for her PhD fellowship (CSC student number 201606220034). SOLEIL and the MiChem LABEX (Sorbonne Université) are acknowledged for a PhD fellowship to D.M. Partial financial support to M.R. from Air Liquide and from the Institut Universitaire de France (IUF) are also gratefully acknowledged.

### Author contributions

U.I., M.R. and C.P.B. designed and supervised the project. U.I. and F.D. synthesized and characterized the catalysts. M.W., K.T., D.S., D.J. and S.R. carried out the  $\text{CO}_2$  reduction experiments and analyzed the data. D.M. and B.L.-K. performed and analyzed the XAS experiments. All authors discussed the results and assisted during paper preparation.

**Additional information**

**Supplementary Information** accompanies this paper at <https://doi.org/10.1038/s41467-019-11542-w>.

**Competing interests:** The authors declare no competing interests.

**Reprints and permission** information is available online at <http://npg.nature.com/reprintsandpermissions/>

**Peer review information:** *Nature Communications* would like to thank Kyle Grice and other, anonymous, reviewers for their contributions to the peer review of this work.

**Publisher's note:** Springer Nature remains neutral with regard to jurisdictional claims in published maps and institutional affiliations.



**Open Access** This article is licensed under a Creative Commons Attribution 4.0 International License, which permits use, sharing, adaptation, distribution and reproduction in any medium or format, as long as you give appropriate credit to the original author(s) and the source, provide a link to the Creative Commons license, and indicate if changes were made. The images or other third party material in this article are included in the article's Creative Commons license, unless indicated otherwise in a credit line to the material. If material is not included in the article's Creative Commons license and your intended use is not permitted by statutory regulation or exceeds the permitted use, you will need to obtain permission directly from the copyright holder. To view a copy of this license, visit <http://creativecommons.org/licenses/by/4.0/>.

© The Author(s) 2019



## VIP Very Important Paper

# An Iron Quaterpyridine Complex as Precursor for the Electrocatalytic Reduction of CO<sub>2</sub> to Methane

Claudio Cometto,<sup>[a]</sup> Lingjing Chen,<sup>[b]</sup> Daniela Mendoza,<sup>[a, c]</sup> Benedikt Lassalle-Kaiser,<sup>[c]</sup> Tai-Chu Lau,<sup>\*[d]</sup> and Marc Robert<sup>\*[a]</sup>

A Fe quaterpyridine complex was used as a molecular precursor for the electrochemical reduction of CO<sub>2</sub> to CH<sub>4</sub> in acetonitrile in the presence of triethanolamine. CH<sub>4</sub> was produced with a faradaic yield of approximately 2.1% at 25 °C and 1 atm pressure of CO<sub>2</sub> as reactant. Controlled potential electrolysis

coupled to ex situ X-ray photoelectron spectroscopy and X-ray absorption spectroscopy of the electrode surface revealed the formation of metallic iron covered by iron oxides as species responsible for catalysis.

## Introduction

The conversion of CO<sub>2</sub> into fuels represents a promising approach to store the intermittent solar energy produced during daytime. In this regard, CO<sub>2</sub> reduction has been widely studied by many research groups either in a direct photo-stimulated approach or in electrochemical conditions.<sup>[1–4]</sup> Although different catalysts that are cheap, efficient, and selective have been reported for the production of CO and HCOOH,<sup>[5]</sup> systems including only earth-abundant elements and able to selectively reduce CO<sub>2</sub> with more than two electrons are still scarce. Copper is without any doubts one of the most studied metals for the CO<sub>2</sub> reduction reaction (CRR) because it can produce highly reduced species such as CH<sub>4</sub>, C<sub>2</sub>H<sub>4</sub>, and other C<sub>2</sub> products.<sup>[6–10]</sup> However, the limited product selectivity and availability of copper in the Earth's crust make the development of new catalysts necessary. Vigorous efforts have been recently devoted to the development of iron-based catalytic systems employing molecular complexes as catalysts, but in most cases two-

electron products were formed (CO and HCOOH) either in organic solvent or in aqueous solution.<sup>[11–19]</sup>

Notably, there are very few studies concerning the reduction of CO<sub>2</sub> to CH<sub>4</sub>. One case was recently reported: the reaction was performed under photochemical conditions with an iron tetraphenylporphyrin as catalyst, an Ir complex<sup>[20]</sup> or an organic molecule (phenoxazine)<sup>[21]</sup> as photosensitizer, and an amine as sacrificial donor. Regarding heterogeneous catalysis, Hori et al.<sup>[6]</sup> have reported CRR in water in presence of 0.5 M KHCO<sub>3</sub> at a metallic iron electrode at  $E = -1.66$  V vs. saturated calomel electrode (SCE) with a current density of 5 mA cm<sup>-2</sup>. No CH<sub>4</sub> was detected, and only small amounts of HCOOH [2.1% faradaic efficiency (FE)] and CO (1.4% FE) were obtained, whereas H<sub>2</sub> (97.5% FE) was the major product. Recently, Jaramillo and co-workers<sup>[22]</sup> reproduced the experiments performed by Hori et al. They detected traces of CH<sub>4</sub> with a partial current density of approximately 1 μA cm<sup>-2</sup> and 0.01% FE. The formation of a metal-CO adduct was proposed as a necessary step to achieve the reduction of CO<sub>2</sub> with more than two electrons. Further reduction of this adduct in the presence of protons could lead to the formation of highly reduced carbon products (such as CH<sub>4</sub>, methanol, ethylene, etc.) with yield and selectivity that depend on the nature of the metal. In this regard, Jaramillo et al. reported that Au, Ag, Zn, Cu, Ni, Pt, and Fe are able to electrocatalytically reduce CO<sub>2</sub> to CH<sub>4</sub>, CH<sub>3</sub>OH, or both, in water as solvent. They proposed that the strength of the metal-CO bond is a key parameter. Metals that bind CO too strongly are poisoned by it, and small amounts of hydrocarbons or alcohols can be produced; conversely, metals binding the CO weakly release it from the electrode surface before it can be further reduced. The remarkable catalytic activity of copper is thus assigned to an intermediate adsorption energy for CO binding.

The mechanism for the electroreduction of CO<sub>2</sub> to CO catalyzed by a molecular Fe<sup>II</sup> quaterpyridine [Fe(qpy); Figure 1] has been recently studied in acetonitrile (CH<sub>3</sub>CN).<sup>[14]</sup> The one-electron-reduced complex (Fe<sup>I</sup> species) binds to CO<sub>2</sub>, and further

[a] Dr. C. Cometto, D. Mendoza, Prof. M. Robert  
Laboratoire d'Electrochimie Moléculaire, UMR 7591 CNRS  
Université de Paris  
75013 Paris (France)  
E-mail: robert@univ-paris-diderot.fr

[b] Dr. L. Chen  
School of Environment and Civil Engineering  
Dongguan University of Technology  
Guangdong, 523808 (P.R. China)

[c] D. Mendoza, Dr. B. Lassalle-Kaiser  
Synchrotron SOLEIL  
L'Orme des Merisiers, Saint-Aubin, 91192, Gif-sur-Yvette (France)

[d] Prof. T.-C. Lau  
Department of Chemistry  
Institute of Molecular Functional Materials  
City University of Hong Kong  
Tat Chee Avenue, Kowloon Tong, Hong Kong (P.R. China)  
E-mail: bhtclau@cityu.edu.hk

Supporting Information and the ORCID identification number(s) for the author(s) of this article can be found under:  
<https://doi.org/10.1002/cssc.201902040>.

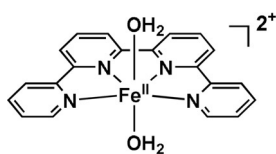


**Figure 1.** Iron quaterpyridine [Fe(qpy)] structure. Counter anions (perchlorate,  $\text{ClO}_4^-$ ) omitted for clarity.

reduction and protonation leads to C–O bond cleavage and formation of an  $\text{Fe}^{\text{I}}(\text{qpy})\text{CO}$  adduct. This intermediate may release the CO to close the catalytic cycle, or it could be further reduced to  $\text{Fe}^0(\text{qpy})\text{CO}$ , from which catalyst deactivation may occur. However, the in situ production of an iron carbonyl adduct could be used as a starting point to-

wards the activation of CO through reduction of this species in suitable acid–base conditions. The choice of the proton source is crucial because CRR always competes with the hydrogen evolution reaction (HER).  $\text{CO}_2$  solubility in the reaction medium is another key issue to be considered and will depend on the solvent nature as well as the partial  $\text{CO}_2$  pressure. For instance, whereas  $[\text{CO}_2]$  is close to 0.04 M in acidic aqueous solution, it is approximately 5 times larger in  $\text{CH}_3\text{CN}$ .<sup>[4]</sup> Hara et al. could increase the selectivity for  $\text{CH}_4$  at an iron electrode (2% FE) by performing controlled-potential electrolysis at high  $\text{CO}_2$  pressure (30 atm) at  $-1.68$  V vs. SCE.<sup>[23]</sup> Another strategy to increase the solubility of  $\text{CO}_2$  and potentially improve the selectivity for CRR is to add alkanolamines [monoethanolamine, diethanolamine, or triethanolamine (TEOA)] that can act as  $\text{CO}_2$ -capture reagents.<sup>[24,25]</sup> Remarkably, Ishitani and co-workers have recently reported  $\text{CO}_2$  insertion in a  $[\text{Re}(\text{bpy})(\text{CO})_3]^+$ /TEOA adduct, in dimethylformamide as solvent.<sup>[26,27]</sup> It led to photocatalytic  $\text{CO}_2$  reduction even at low  $\text{CO}_2$  pressure. In particular, when a  $\text{Ru}^{\text{II}}\text{--Re}^{\text{I}}$  dinuclear complex was used as a photocatalyst with 0.005 atm  $\text{CO}_2$  partial pressure, the gas was reduced with an efficiency equal to 60% of that obtained with pure  $\text{CO}_2$ . The same process was recently transferred to electrochemical conditions.<sup>[28]</sup> Herein we present the direct electrocatalytic reduction of  $\text{CO}_2$  to  $\text{CH}_4$  in mild conditions (25 °C, 1 atm  $\text{CO}_2$  pressure) in  $\text{CH}_3\text{CN}$  by using Fe(qpy) as molecular precursor, in the presence of TEOA as cocatalyst.

## Results and Discussion

A Fe(qpy) solution in a mixture of  $\text{CH}_3\text{CN}$  and TEOA (1 M) was first characterized by cyclic voltammetry (Figure S1 in the Supporting Information) and infrared spectro-electrochemistry (IR-SEC, Figure S2 in the Supporting Information). Briefly, the addition of TEOA under Ar atmosphere induced a positive shift of the first reduction wave (Figure S1 a in the Supporting Information), according to a binding of TEOA to the  $\text{Fe}^{\text{I}}$  species  $[\text{Fe}^{\text{I}}(\text{qpy})]^+$ . Under  $\text{CO}_2$ , an additional anodic shift upon the first reduction wave revealed the  $\text{CO}_2$  binding by  $\text{Fe}^{\text{I}}$  (Figure S1 b in the Supporting Information), confirming previous reports in the literature.<sup>[14]</sup> The  $\text{Fe}\text{--CO}_2$  adduct was then reduced at  $-1.2$  V vs. SCE, and a band at  $1854\text{ cm}^{-1}$  observed by IR-SEC was assigned to the formation of the  $\text{Fe}^0(\text{qpy})\text{CO}$  adduct obtained upon C–O bond cleavage. Setting the potential at more negative values, a huge wave with an onset potential at approximately  $-1.3$  V vs. SCE was observed, corresponding to the further reduction of the carbonyl compound. A 4 h con-

trolled potential electrolysis (CPE) experiment at  $-1.65$  V vs. SCE of a  $\text{CO}_2$ -purged  $\text{CH}_3\text{CN}$  solution containing Fe(qpy) (0.67 mM) and 1 M TEOA revealed the formation of  $\text{H}_2$  as main product (93%), along with CO (4%), HCOOH (1.5%), and  $\text{CH}_4$  (2.3%, corresponding to  $\approx 27\ \mu\text{A cm}^{-2}$  partial current density, Figure 2 and Table 1, entry 2). It is worth noting that very similar results were obtained in terms of FE upon varying the catalyst concentration ( $[\text{Fe}(\text{qpy})]=0.27$  or 1 mM), illustrating the excellent reproducibility of the product distribution [(92.3  $\pm$  0.7)% FE  $\text{H}_2$ , (3.6  $\pm$  0.6)% FE CO, (2.1  $\pm$  0.2)% FE  $\text{CH}_4$ ].

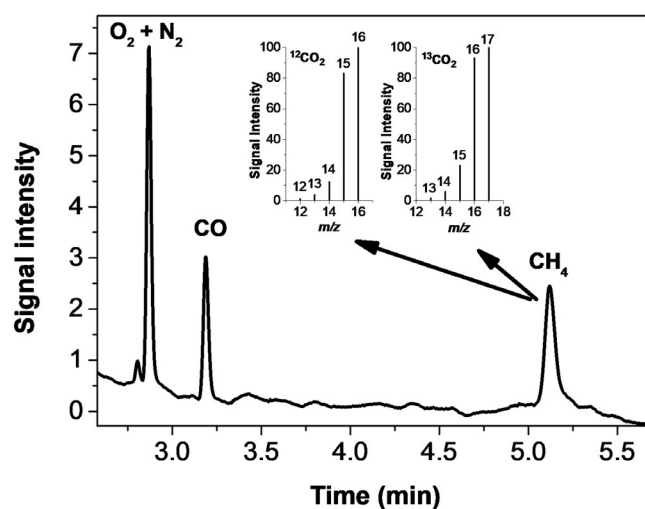


**Figure 2.** GC of gaseous products obtained after a 6.5 h CPE at  $E = -1.65$  V vs. SCE of a 0.67 mM solution of Fe(qpy) in  $\text{CH}_3\text{CN} + 1$  M TEOA. The inset shows the mass spectra of  $\text{CH}_4$  produced from  $^{12}\text{CO}_2$  (left) and  $^{13}\text{CO}_2$  (right) used as substrate.

**Table 1.** CPE experiments (4 h) in  $\text{CO}_2$ -saturated  $\text{CH}_3\text{CN}$  solutions containing Fe(qpy) (0.67 mM).<sup>[a]</sup>

Entry	$E$ [V vs. SCE]	Proton source	FE $\text{H}_2$ [%]	FE CO [%]	FE HCOOH [%]	FE $\text{CH}_4$ [%]
1	-2	TEOA (1 M)	94.4	3.9	2.2	2.6
2	-1.65	TEOA (1 M)	93.1	4.1	1.5	2.3
3	-1.25	TEOA (1 M)	1.5	67.3	n.d.	n.d.
4	-1.65	PhOH (3 M)	95.8	8.9	2.6	n.d.
5 <sup>[b]</sup>	-1.65	TEOA (1 M)	100	n.d.	1	n.d.

[a] FE values calculated at the end of a 4 h experiment. [b] blank experiment without Fe(qpy). n.d. = not detected.

Analysis of the liquid phase by GC-FID (FID = flame ionization detector) did not show any alcohol production (methanol, ethanol). A similar FE value for  $\text{CH}_4$  was achieved at  $E = -2$  V vs. SCE (Table 1, entry 1). Conversely, no methane production was detected at  $-1.25$  V vs. SCE (entry 3). In a blank experiment performed in the absence of catalyst no  $\text{CH}_4$  was produced, showing that the catalyst is essential for methane formation (entry 5).

An electrolysis experiment with  $^{13}\text{CO}_2$  as reactant led to  $^{13}\text{CH}_4$ , confirming that  $\text{CO}_2$  is the source of  $\text{CH}_4$  (Figure 2, inset). When the same CPE experiment was performed under 1 atm

CO or under CO<sub>2</sub> with a significantly different concentration of TEOA (0.1 M or 50% v/v), no methane was detected. No CH<sub>4</sub> was observed by using 3 M phenol (Table 1, entry 4) instead of TEOA as proton supplier. A linear scan performed just after CPE revealed the complete decomposition of the catalyst Fe(qpy) (Figure S3 in the Supporting Information). Moreover, the onset of the catalytic wave after CPE was shifted towards more positive potentials. The production of CH<sub>4</sub> was constant over 6 h, showing the good stability of the catalytic system. A production of approximately 0.23 μmol h<sup>-1</sup> CH<sub>4</sub> was achieved for an initial Fe(qpy) precatalyst concentration of 0.67 mM.

A linear correlation between CH<sub>4</sub> amount and time was constantly observed for other catalyst concentrations (0.27, 0.5, and 1 mM, Figure 3). It is worth noting that FE for CH<sub>4</sub> in-

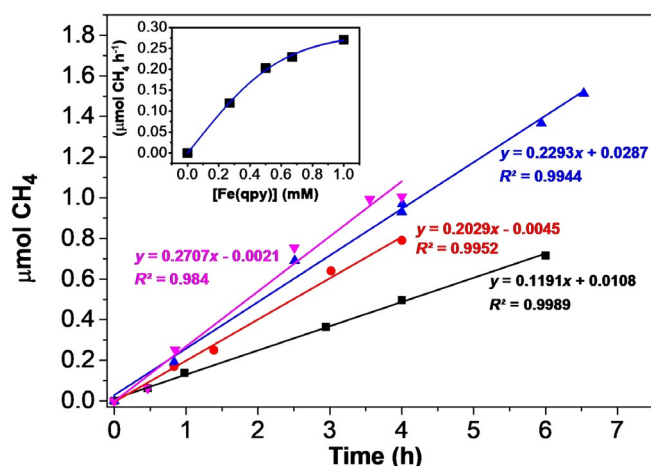


**Figure 3.** CH<sub>4</sub> production as a function of time upon electrolysis ( $E = -1.65$  V vs. SCE) of an CH<sub>3</sub>CN solution containing Fe(qpy) (0.27 mM in black, 0.5 mM in red, 0.67 mM in blue, 1 mM in magenta) and 1 M TEOA. The inset shows the CH<sub>4</sub> production rate versus [Fe(qpy)]; the reported values were obtained from the slope of the linear fittings.

creased over time in all experiments (Figure S4 in the Supporting Information), regardless of the initial Fe(qpy) concentration used. In contrast to CH<sub>4</sub>, the CO formation reached a plateau after approximately 4 h, suggesting that the two gases are produced by two different mechanisms (Figure S5 in the Supporting Information). When the rate of CH<sub>4</sub> production was plotted against the catalyst concentration, a plateau was obtained for [Fe(qpy)] = 1 mM (Figure 3, inset), pointing to the involvement of an adsorbed active species. A rinse test, using the electrode after the CPE experiment and plunging it into a fresh electrolyte saturated with CO<sub>2</sub> but not containing the catalyst, showed that at least an important fraction of the methane production involves an electro-deposited species (Figure S6 in the Supporting Information). Conversely, this adsorbate is not active towards CO evolution, confirming that CO and CH<sub>4</sub> are produced by different catalytically active species. SEM of the glassy carbon electrode obtained after electrolysis of [Fe(qpy)] in a CO<sub>2</sub>-purged CH<sub>3</sub>CN solution (+1 M TEOA) further confirmed the electrodeposition of solid particles on the electrode surface during CPE. Multiple tubular structures with a particle

size of approximately 3 μm were observed (Figure S7 in the Supporting Information).

To better understand the exact nature of the catalytically active form responsible for the CH<sub>4</sub> formation, CPE experiments were performed in solutions containing Fe(ClO<sub>4</sub>)<sub>2</sub> salt instead of Fe(qpy). When 1 M TEOA or 3 M phenol was used as proton donor, some CH<sub>4</sub> was obtained, but its formation rate was significantly lower than if iron quaterpyridine was used (Figure S8 in the Supporting Information). The maximum value for CH<sub>4</sub> production with Fe(ClO<sub>4</sub>)<sub>2</sub> was 0.0968 μmol h<sup>-1</sup>, that is, 2.8 times lower than the rate obtained for 1 mM Fe(qpy) (0.27 μmol h<sup>-1</sup>). The average FE calculated over a range of experiments with both Fe(qpy) and Fe(ClO<sub>4</sub>)<sub>2</sub> (Table S2 in the Supporting Information) revealed that iron quaterpyridine is also a better precursor for CH<sub>4</sub> production in terms of selectivity (2.8-fold increase). Because traces of CH<sub>4</sub> were detected upon using the iron perchlorate salt, we may assign the reduction of CO<sub>2</sub> to CH<sub>4</sub> to electrodeposited Fe particles. Ex situ X-ray photoelectron spectroscopy (XPS) analysis of the electrode surface suggests a de-metalation process occurring during CPE of Fe(qpy) (0.5 mM) solution. Peaks at 724.4 and 711.1 eV could be assigned to the 2p<sub>1/2</sub> and 2p<sub>3/2</sub> energies of Fe<sup>III</sup>, respectively, indicative of a Fe<sub>2</sub>O<sub>3</sub> layer deposited onto the carbon (Figure 4).<sup>[29]</sup>

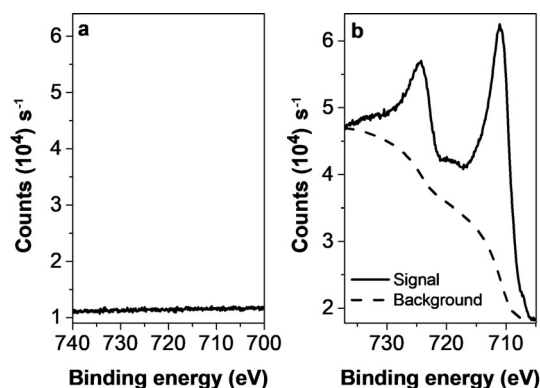


**Figure 4.** XPS spectra (Fe 2p energy levels) at a glassy carbon plate (a) before and (b) after CPE experiments at  $-1.65$  V vs. SCE with a 0.5 mM Fe(qpy) solution (CH<sub>3</sub>CN + 1 M TEOA).

X-ray absorption spectroscopic (XAS) experiments further confirmed these observations. Figure 5 shows the X-ray absorption near-edge structure (XANES) spectra at the Fe K-edge of a glassy carbon electrode after electrolysis in the presence of Fe(qpy) in CO<sub>2</sub>-saturated CH<sub>3</sub>CN (Figure 5, black) and of a reference sample of the same complex before electrolysis (Figure 5, red). The spectrum recorded after electrolysis shows a very different overall shape and is clearly shifted to higher energies ( $\approx 1.63$  eV at half-edge jump). The structure of the starting complex has been altered, and the new species are likely to be more oxidized than the starting one. The shift of the pre-edge peak towards higher energy on going from the starting Fe(qpy) complex to the sample after electrolysis is also indicative of an increased oxidation state (Figure 5, bottom). It should be noted that the XAS signal of a glassy carbon elec-

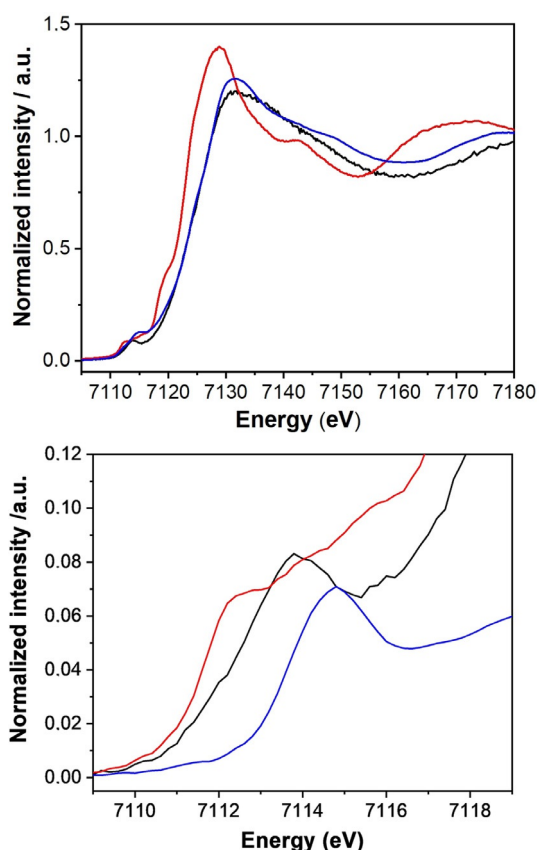


**Figure 5.** Top: XANES spectra at the Fe K-edge of a glassy carbon electrode after CPE experiments at  $-1.65$  V vs. SCE with a  $0.5$  mM Fe(qpy) solution ( $\text{CH}_3\text{CN} + 1$  M TEOA) (black), of the initial complex (red), and of the best linear combination fit obtained with a mixture of iron oxides and metallic iron (blue). Bottom: pre-edge region of the Fe K-edge XANES spectra of a glassy carbon electrode after CPE experiments at  $-1.65$  V vs. SCE with a  $0.5$  mM Fe(qpy) solution ( $\text{CH}_3\text{CN} + 1$  M TEOA) (black) of the starting  $[\text{Fe}(\text{qpy})-(\text{H}_2\text{O})_2]^{2+}$  sample (red) and of ferrihydrite ( $\text{Fe}_2\text{O}_3 \cdot 0.5\text{H}_2\text{O}$ ) (blue).

trode without catalyst did not show any Fe signal (Figure S9 in the Supporting Information). The spectrum recorded after electrolysis was compared to a set of reference iron samples, which were linearly combined to fit the experimental spectrum. The best combination found includes ferrihydrite ( $\text{Fe}_2\text{O}_3 \cdot 0.5\text{H}_2\text{O}$ ; 53.1%), wüstite ( $\text{FeO}$ ; 35.8%), and metallic iron (11.1%) (Figure 5, top (blue), Figure S10 and Table S1 in the Supporting Information). These results suggest that the electrode material consists of metallic iron particles covered by a mixture of iron oxides with a higher proportion of  $\text{Fe}^{\text{III}}$ , in accordance with XPS analysis. The presence of  $\text{Fe}^{\text{III}}$  in the electrodeposited particles could be simply owing to the oxidation during the sample treatment of metallic iron, which is the most probable catalyst for the  $\text{CH}_4$  production during CPE at  $-1.65$  V vs. SCE. Ex situ XPS analysis of the electrode surface excluded any significant presence of the organic ligand in the solid (Figure S11 in the Supporting Information), suggesting that qpy exclusively plays a significant role in the catalyst deposition step. The higher  $\text{CH}_4$  production obtained by using Fe(qpy) as catalyst precursor instead of  $\text{Fe}(\text{ClO}_4)_2$  may be owing to a larger active surface, but the significant increase in

FE (almost independent of the complex concentration, Table S2 in the Supporting Information) shows that a more active catalyst is likely formed with Fe(qpy) as precatalyst.

To summarize, reducing the  $\text{Fe}^0(\text{qpy})\text{CO}$  species produced after  $\text{CO}_2$  reduction in the presence of  $1$  M TEOA resulted in the de-metalation of the molecular compound. The layer of Fe formed on the glassy carbon surface proved to reduce  $\text{CO}_2$  to  $\text{CH}_4$  even in very mild conditions ( $25^\circ\text{C}$ ,  $1$  atm pressure) with a FE for  $\text{CH}_4$  that is analogous to the value reported by Hara et al.<sup>[23]</sup> under  $30$  atm  $\text{CO}_2$  in water at approximately the same potential. When compared to a previous study by Jaramillo and co-workers<sup>[22]</sup> using an iron electrode, an approximately 30- and 200-fold improvement was obtained in terms of current density for the conversion of  $\text{CO}_2$  to  $\text{CH}_4$  and FE, respectively (Table 2). TEOA was essential for the production of meth-

**Table 2.** Comparison between different CRR results with iron-based electrocatalysts.

Entry	$E$ [V vs. SCE]	FE $\text{CH}_4$ [%]	Conditions	Ref.
1	$-1.66$	n.d.	$0.5$ M $\text{KHCO}_3$ in $\text{H}_2\text{O}$	[6]
2	$-1.69$	0.01	$0.1$ M $\text{KHCO}_3$ in $\text{H}_2\text{O}$	[22]
3	$-1.68$	2	$0.1$ M $\text{KHCO}_3$ in $\text{H}_2\text{O}^{\text{[a]}}$	[23]
4	$-1.65$	2.1	$\text{CH}_3\text{CN}$ , $1$ M TEOA <sup>[b]</sup>	this work

[a]  $30$  atm  $\text{CO}_2$ , [b]  $1$  atm  $\text{CO}_2$ .

ane even if its role remains to be further explored. This amine could be involved in the de-metalation process. In addition, reports in the literature suggest that the  $\text{CO}_2$ -adsorbing properties of aqueous and organic solutions of TEOA are owing to the reaction of this molecule with  $\text{CO}_2$  to produce  $\text{HCO}_3^-$  and  $(\text{HOCH}_2\text{CH}_2)_3\text{NH}^+$ .<sup>[24,25]</sup> Small amounts of this acid (its  $\text{pK}_a$  value can be reasonably approximated to  $\approx 19$  in  $\text{CH}_3\text{CN}$ )<sup>[30]</sup> could also be involved in the  $\text{CH}_4$  formation. When a CPE experiment was performed at  $E = -1.65$  V vs. SCE under  $\text{CO}$  atmosphere, no  $\text{CH}_4$  was observed, confirming the fundamental role that  $\text{CO}_2$  could have in the generation of the proton source. In the presence of  $50\%$  v/v of TEOA the current in the CPE experiment largely decreased (reasonably because of the high solution viscosity), accounting for the lack of  $\text{CH}_4$  detection. Conversely, at low TEOA concentration ( $0.1$  M) the absence of  $\text{CH}_4$  may be explained by limited formation of  $(\text{HOCH}_2\text{CH}_2)_3\text{NH}^+$ .

## Conclusions

Electrodeposition of Fe particles from an iron molecular complex precursor in acetonitrile solution containing  $1$  M triethanolamine (TEOA) resulted in a promising method for the direct electroreduction of  $\text{CO}_2$  to  $\text{CH}_4$  in mild conditions. This unprecedented example led to a significant improvement of the results previously reported in the literature for iron-based electrodes. By tuning the ligand structure of the starting complex, it should be possible to develop a new efficient approach for  $\text{CH}_4$  electrogeneration from  $\text{CO}_2$ . Studies along these lines will be further reported.



## Experimental Section

### Chemicals

CH<sub>3</sub>CN (Acros, >99.9%, extra dry over molecular sieves) and supporting electrolyte NBu<sub>4</sub>PF<sub>6</sub> (Fluka, purriss.) were used as received. Fe(qpy) was synthesized as previously reported.<sup>[13]</sup> Phenol, TEOA, and Fe(ClO<sub>4</sub>)<sub>2</sub> were purchased from Sigma–Aldrich and used without further purification.

### Electrochemistry and spectroscopic analysis

All experiments were performed with dry CH<sub>3</sub>CN as solvent and NBu<sub>4</sub>PF<sub>6</sub> as supporting electrolyte. The solution was purged with Ar or CO<sub>2</sub> or CO for 20 min before each experiment.

**Cyclic voltammetry:** The working electrode was a 3 mm-diameter glassy carbon (Tokai) disk carefully polished with diamond paste of various size (15–1 μm), ultrasonically rinsed in absolute ethanol, and dried before use. The counter electrode was a platinum wire, and the reference electrode was an aqueous SCE electrode. All experiments were performed under argon, CO<sub>2</sub>, or CO atmosphere at 20 °C, and the double-wall jacketed cell was thermostated by circulation of water. Cyclic voltammograms were obtained by use of a Metrohm AUTOLAB instrument. Ohmic drop was compensated by using the positive feedback compensation implemented in the instrument.

**Controlled potential preparative-scale electrolysis:** Electrolyses were performed by using a Princeton Applied Research (PARSTAT 2273) potentiostat. Experiments were performed in a two-compartment cell with a glassy carbon plate as working electrode (the volume of the solution was 3 mL, and the active surface area was 1.8 cm<sup>2</sup>). The reference electrode was an aqueous SCE electrode, and the counter electrode was a platinum wire positioned in a bridge separated from the cathodic compartment by a ceramic frit, containing a 4% H<sub>2</sub>O + 0.1 M NBu<sub>4</sub>PF<sub>6</sub> CH<sub>3</sub>CN solution. The electrolysis solution was purged with CO<sub>2</sub> (or CO) for 20 min prior to electrolysis. The ohmic drop between working electrode and reference electrode was minimized by dipping the former directly in the solution and positioning it close to the working electrode. All CPE experiments were performed under stirring.

**GC for detection of CO and CH<sub>4</sub>:** Analyses from the gas evolved in the headspace during electrolysis were performed with an Agilent Technologies 7820A GC system equipped with a thermal conductivity detector. CO and H<sub>2</sub> production were quantitatively assessed by using a CP-CarboPlot P7 capillary column (27.46 m length and 25 μm internal diameter). Temperature was held at 150 °C for the detector and 34 °C for the oven. The carrier gas was argon flowing at 9.5 mL min<sup>-1</sup> at constant pressure of 0.5 bar. Injection was performed through a 250 μL gas-tight syringe (Hamilton). These conditions allowed for separation of H<sub>2</sub>, O<sub>2</sub>, N<sub>2</sub>, CO, CH<sub>4</sub>, and CO<sub>2</sub>. Calibration curves for H<sub>2</sub>, CO, and CH<sub>4</sub> were determined separately by injecting known quantities of pure gas.

Regarding formic acid quantification, a sample (500 μL) of the solution was diluted into H<sub>2</sub>O (9 mL), filtered, and analyzed with a Dionex ICS-1100 Ionic Chromatography System equipped with a IonPac AS15 column (concentration gradient of KOH: 10–30 mM as eluent).

Mass spectra were obtained by a ThermoFisher Scientific TRACE Ultra GC equipped with a CP 7514 column (Agilent Technologies) and coupled to a DSQ II MS in positive ionization mode, using a TriPlus headspace autosampler.

**GC for detection of methanol and ethanol:** At the end of the CPE experiments, 1 μL of the solution was injected into the GC (Thermo Fisher Scientific Trace GC, Split/Splitless) equipped with a column TG/WAXMS (length 15 m, internal diameter 0.25 mm) and an FID detector. The temperature of injector and detector was kept at 150 °C. The column was kept at 50 °C for 2 min, then a 10 °C min<sup>-1</sup> gradient was applied to a final temperature of 150 °C (kept for 5 min). A constant flow of He (1 mL min<sup>-1</sup>) was used as carrier. The peak retention times for methanol (1.8 min) and ethanol (2.1 min) under these analytical conditions were determined by injecting standard solutions of these two compounds.

**IR-SEC:** Experiments were performed with a home-made thin-layer cell, equipped with two KBr windows (radiation path length 0.3 mm). The working electrode was a platinum grid, placed on the infrared beam. An Ag wire was used as pseudo-reference and a platinum grid was employed as counter electrode. A Metrohm AUTOLAB instrument was used for the electrochemical part, and a PerkinElmer 2000 Fourier-transform (FT)IR spectrometer was employed for recording the IR spectra (1 spectrum per minute, 6 scans). A 2 mM solution of Fe(qpy) was used during each experiment, and the solution was preliminary purged with CO<sub>2</sub> for 20 min before the cell was loaded with the liquid and sealed.

**XPS analysis:** An XPS THERMO-VG ESCALAB 250 [RX source K Al (1486.6 eV)] was used.

**XAS analysis:** XAS spectra were collected at the LUCIA beamline of SOLEIL with a ring energy of 2.75 GeV and a current of 490 mA. The energy was monochromatized by means of a Si 311 double-crystal monochromator. Data were collected in a primary vacuum chamber as fluorescence spectra with an outgoing angle of 10° by using a Bruker silicon drift detector. The data were normalized to the intensity of the incoming incident energy and processed with the Athena software from the IFEFFIT package. An E<sub>0</sub> value of 7123 eV was used for the iron K-edge energy, which was measured at the first inflection point.

**SEM images:** SEM was performed by using a Zeiss Supra 40 field-emission gun (SEM-FEG).

## Acknowledgements

*Ph.D. fellowship to C.C. from Université Sorbonne Paris Cité (USPC) and partial financial support to M.R. from the Institut Universitaire de France (IUF) are gratefully acknowledged. SOLEIL and the Michem LABEX are acknowledged for a joint fellowship to D.M. Financial support to T.C.L. by a NSFC/RGC Joint Research Grant (N\_CityU115/18) is also gratefully thanked. G. Thoraval (Université Paris Diderot) and Dr. Solenn Reguer are warmly thanked for the production of the glassy carbon electrodes and for providing iron oxide reference samples, respectively.*

## Conflict of interest

The authors declare no conflict of interest.

**Keywords:** CO<sub>2</sub> reduction • electrocatalysis • Fe complex • methane • solar fuel

[1] C. Costentin, M. Robert, J. M. Savéant, *Chem. Soc. Rev.* **2013**, *42*, 2423–2436.

- [2] H. Takeda, O. Ishitani, *Coord. Chem. Rev.* **2010**, *254*, 346–354.
- [3] B. Kumar, M. Llorente, J. Froehlich, T. Dang, A. Sathrum, C. P. Kubiak, *Annu. Rev. Phys. Chem.* **2012**, *63*, 541–569.
- [4] R. Francke, B. Schille, M. Roemelt, *Chem. Rev.* **2018**, *118*, 4631–4701.
- [5] H. Takeda, C. Cometto, O. Ishitani, M. Robert, *ACS Catal.* **2017**, *7*, 70–88.
- [6] Y. Hori, K. Kikuchi, S. Suzuki, *Chem. Lett.* **1985**, *14*, 1695–1698.
- [7] C. W. Li, M. W. Kanan, *J. Am. Chem. Soc.* **2012**, *134*, 7231–7234.
- [8] K. J. P. Schouten, Y. Kwon, C. J. M. Van der Ham, Z. Qin, M. T. M. Koper, *Chem. Sci.* **2011**, *2*, 1902–1909.
- [9] X. Nie, M. R. Esopi, M. J. Janik, A. Asthagiri, *Angew. Chem. Int. Ed.* **2013**, *52*, 2459–2462; *Angew. Chem.* **2013**, *125*, 2519–2522.
- [10] M. Gattrell, N. Gupta, A. Co, *J. Electroanal. Chem.* **2006**, *594*, 1–19.
- [11] I. Bhugun, D. Lexa, J. M. Savéant, *J. Am. Chem. Soc.* **1996**, *118*, 1769–1776.
- [12] C. Costentin, M. Robert, J. M. Savéant, *Acc. Chem. Res.* **2015**, *48*, 2996–3006.
- [13] Z. Guo, S. Cheng, C. Cometto, E. Anxolabéhère-Mallart, S. M. Ng, C. C. Ko, G. Liu, L. Chen, M. Robert, T. C. Lau, *J. Am. Chem. Soc.* **2016**, *138*, 9413–9416.
- [14] C. Cometto, L. Chen, P. K. Lo, Z. Guo, K. C. Lau, E. Anxolabéhère-Mallart, C. Fave, T. C. Lau, M. Robert, *ACS Catal.* **2018**, *8*, 3411–3417.
- [15] M. D. Rail, L. A. Berben, *J. Am. Chem. Soc.* **2011**, *133*, 18577–18579.
- [16] A. Taheri, E. J. Thompson, J. C. Fettinger, L. A. Berben, *ACS Catal.* **2015**, *5*, 7140–7151.
- [17] I. Azcarate, C. Costentin, M. Robert, J. M. Savéant, *J. Am. Chem. Soc.* **2016**, *138*, 16639–16644.
- [18] C. Costentin, M. Robert, J. M. Savéant, A. Tatin, *Proc. Natl. Acad. Sci. USA* **2015**, *112*, 6882–6886.
- [19] A. Rosas-Hernández, H. Junge, M. Beller, M. Roemelt, R. Francke, *Catal. Sci. Technol.* **2017**, *7*, 459–465.
- [20] H. Rao, L. C. Schmidt, J. Bonin, M. Robert, *Nature* **2017**, *548*, 74.
- [21] H. Rao, C.-H. Lim, J. Bonin, G. M. Miyake, M. Robert, *J. Am. Chem. Soc.* **2018**, *140*, 17830–17834.
- [22] K. P. Kuhl, T. Hatsukade, E. R. Cave, D. N. Abram, J. Kibsgaard, T. F. Jaramillo, *J. Am. Chem. Soc.* **2014**, *136*, 14107–14113.
- [23] K. Hara, A. Kudo, T. Sakata, *J. Electroanal. Chem.* **1995**, *391*, 141–147.
- [24] A. García-Abuín, D. Gomez-Díaz, A. B. Lopez, J. M. Navaza, A. Rumbo, *Ind. Eng. Chem. Res.* **2013**, *52*, 13432–13438.
- [25] E. Sada, H. Kumazawa, Y. Ikehara, Z. Q. Han, *Chem. Eng. J.* **1989**, *40*, 7–12.
- [26] T. Morimoto, T. Nakajima, S. Sawa, R. Nakanishi, D. Imori, O. Ishitani, *J. Am. Chem. Soc.* **2013**, *135*, 16825–16828.
- [27] T. Nakajima, Y. Tamaki, K. Ueno, E. Kato, T. Nishikawa, K. Ohkubo, Y. Yamazaki, T. Morimoto, O. Ishitani, *J. Am. Chem. Soc.* **2016**, *138*, 13818–13821.
- [28] H. Kumagai, T. Nishikawa, H. Koizumi, T. Yatsu, G. Sahara, Y. Yamazaki, Y. Tamaki, O. Ishitani, *Chem. Sci.* **2019**, *10*, 1597–1606.
- [29] R. L. Kurtz, V. E. Henrich, *Surf. Sci.* **1983**, *129*, 345–354.
- [30] J. T. Muckerman, J. H. Skone, M. Ning, Y. Wasada-Tsutsui, *Biochim. Biophys. Bioenerg.* **2013**, *1827*, 882–891.

---

 Manuscript received: July 26, 2019

Revised manuscript received: August 20, 2019

Accepted manuscript online: August 21, 2019

Version of record online: September 12, 2019

**Electrochemistry**

International Edition: DOI: 10.1002/anie.201909257

German Edition: DOI: 10.1002/ange.201909257

# Aqueous Electrochemical Reduction of Carbon Dioxide and Carbon Monoxide into Methanol with Cobalt Phthalocyanine

Etienne Boutin, Min Wang, John C. Lin, Matthieu Mesnage, Daniela Mendoza, Benedikt Lassalle-Kaiser, Christopher Hahn, Thomas F. Jaramillo, and Marc Robert\*

**Abstract:** Conversion of  $\text{CO}_2$  into valuable molecules is a field of intensive investigation with the aim of developing scalable technologies for making fuels using renewable energy sources. While electrochemical reduction into CO and formate are approaching industrial maturity, a current challenge is obtaining more reduced products like methanol. However, literature on the matter is scarce, and even more for the use of molecular catalysts. Here, we demonstrate that cobalt phthalocyanine, a well-known catalyst for the electrochemical conversion of  $\text{CO}_2$  to CO, can also catalyze the reaction from  $\text{CO}_2$  or CO to methanol in aqueous electrolytes at ambient conditions of temperature and pressure. The studies identify formaldehyde as a key intermediate and an unexpected pH effect on selectivity. This paves the way for establishing a sequential process where  $\text{CO}_2$  is first converted to CO which is subsequently used as a reactant to produce methanol. Under ideal conditions, the reaction shows a global Faradaic efficiency of 19.5% and chemical selectivity of 7.5%.

The electrochemical reduction of carbon dioxide ( $\text{CO}_2$ ) into methanol ( $\text{CH}_3\text{OH}$ ) is considered as a major target that could enable a transition from fossil fuels to renewable fuels. To catalyze the six-electron-six-proton reduction of  $\text{CO}_2$  to  $\text{CH}_3\text{OH}$ , efforts have been devoted to the use of metal oxides, metal alloys, or chalcogenide-based catalytic electrodes.<sup>[1–4]</sup> Most of these materials either require the use of rare metals, or are not selective for methanol because they co-generate more reduced products (for example, methane or  $\text{C}_2$  molecules).<sup>[5,6]</sup> Additionally, the thermodynamic stability window of metal oxides is limited<sup>[7]</sup> and the reduced metal electrodes typically have low activity for  $\text{CH}_3\text{OH}$  produc-

tion,<sup>[8]</sup> leading to performance instability. One promising strategy to achieve high selectivity is to use molecular catalysts to precisely control the structure of the active site. Even though such a strategy has been successfully implemented for  $\text{CO}_2$ -to-CO production,<sup>[9,10]</sup> no molecular catalyst has been shown to perform the reaction up to  $\text{CH}_3\text{OH}$  yet. A series of reports with transition-metal complexes were published in the 80s, which, upon assistance from a heterogeneous co-catalyst (Everitt's salt) deposited on a platinum electrode, showed some methanol evolution.<sup>[11–13]</sup> A few papers have reported traces of  $\text{CH}_3\text{OH}$  production when using metal complexes, including cobalt phthalocyanine (CoPc) as a catalyst, but the exact source of the alcohol was not identified<sup>[14]</sup> and no follow-up studies were published.<sup>[15,16]</sup> Here, we demonstrate for the first time that CoPc is able to electroreduce  $\text{CO}_2$  into  $\text{CH}_3\text{OH}$  in aqueous media through a CO intermediate. Since the  $\text{CO}_2$ -to-CO step is very efficient at a neutral pH, further optimization was focused on the CO to  $\text{CH}_3\text{OH}$  step. In basic media (pH 12–13), we used pure CO as a substrate and discovered experimental conditions to reach a nearly 50-fold increase for the Faradaic efficiency (FE) towards methanol generation (from 0.3 to 14.3%). Formaldehyde (HCHO) was also identified as an intermediate. Upon combination of an optimized  $\text{CO}_2$ -to-CO step in a first electrolyzer and the following reduction step of pure CO to methanol in a second electrolyzer, an overall FE from  $\text{CO}_2$  to  $\text{CH}_3\text{OH}$  of 19.5% may be achieved.

CoPc, a well-studied catalyst in electrochemistry,<sup>[17,18]</sup> belongs to the phthalocyanine family that are used as a dye at a large scale in the painting industry. This catalyst is particularly appealing due to its low cost. Upon mixing the cobalt complex with multi-wall carbon nanotubes (MWCNT) and Nafion resin in a mixture of ethanol and ethylene glycol, a colloidal, stable ink was obtained (see Supporting Information). After ink deposition onto porous carbon paper, the material was dried at 100 °C resulting in the porous catalytic film observed from SEM (Supporting Information, Figure S1). The typical CoPc concentration in the film was about  $15.7 \pm 0.7 \text{ nmol cm}^{-2}$ . Electrolyses were then conducted in aqueous solutions under a series of various pH conditions and  $\text{CO}_2$  or CO atmosphere (see Table S1 for a full description). Both the liquid and the gas phases were analyzed following electrolysis by  $^1\text{H}$  NMR and gas chromatography (GC), respectively. The results are summarized in Table 1 and the full set of collected data is reported in the Supporting Information (Tables S1 and S2). After 3 h of electrolysis in a  $\text{CO}_2$ -saturated 0.5 M  $\text{KHCO}_3$  solution (pH 7.2) at an applied potential of  $-0.68 \text{ V}$  vs. RHE, no traces of  $\text{CH}_3\text{OH}$  were detected. However, when decreasing the potential to  $-0.88 \text{ V}$



[\*] E. Boutin, M. Wang, M. Mesnage, D. Mendoza, Prof. M. Robert  
Université de Paris, Laboratoire d'Electrochimie Moléculaire, CNRS  
75013 Paris (France)

E-mail: robert@univ-paris-diderot.fr

J. C. Lin, C. Hahn, T. F. Jaramillo  
SUNCAT Center for Interface Science and Catalysis, Department of  
Chemical Engineering, Stanford University  
Stanford, CA 94305 (USA)

D. Mendoza, B. Lassalle-Kaiser  
Synchrotron SOLEIL, L'Orme des Merisiers  
Saint-Aubin, 91192 Gif-sur-Yvette (France)

C. Hahn, T. F. Jaramillo  
SUNCAT Center for Interface Science and Catalysis, SLAC National  
Accelerator Laboratory  
2575 Sand Hill Road, Menlo Park, CA 94025 (USA)

 Supporting information and the ORCID identification number(s) for the author(s) of this article can be found under:  
 <https://doi.org/10.1002/anie.201909257>.

**Table 1:** Electrolysis results and Faradaic efficiencies for methanol production.

	Substrate	pH	$E$ [V vs. RHE]	$t$ [h]	$j_{\text{total}}$ [ $\text{mAcm}^{-2}$ ]	FE [%]	$\text{CH}_3\text{OH}$ $j$ [ $\text{mAcm}^{-2}$ ]	TON
1	$\text{CO}_2$	7.2	-0.88	3	11.25	0.3	0.03	44
2	$\text{HCOO}^-$	7	-0.89	2	15.85	0	0	0
3	CO	7	-0.89	2	5.34	1.1	0.06	70
4	CO	7	-0.99	2	2.72	2.3	0.06	76
5	CO	13	-0.54	2	1.12	2.9	0.03	40
6	CO	13	-0.64	1.5	4.77	14.3	0.68	556
7	CO	12	-0.70	2	2.68	12.1	0.32	400
8	HCHO	13	-0.54	2	10.16	18.2	1.85	4588
9	HCHO	13	-0.64	1	25.16	11.6	2.91	3621
10	CO	14	-0.63	0.5	3.08	0.9	0.03	10
11	CO	13	-0.99	1	27.77	0	0	0
12 <sup>[a]</sup>	CO	13	-0.64	1	2.01	0	0	0
13 <sup>[b]</sup>	CO	13	-0.64	0.5	0.98	0	0	0

$\text{CO}_2$  and CO were used as reactant substrates upon saturation in water at 25 °C and 1 atm (leading to a concentration of 34 mM and 1 mM, respectively, at neutral pH). Concentration of  $\text{HCOO}^-$  and formaldehyde were 10 and 20 mM, respectively. Except for [a] and [b], CoPc is the catalyst: ([a] catalyst: electrodeposited metallic Co), ([b] catalyst: CoQpy complex).

vs. RHE (Figure 1 a), we detected a small amount of  $\text{CH}_3\text{OH}$  from the  $^1\text{H}$  NMR spectra (Figure S2) of the electrolyte solution. This corresponds to a Faradaic efficiency (FE) of 0.3% and to a partial current density ( $j_{\text{CH}_3\text{OH}}$ ) of  $30 \mu\text{Acm}^{-2}$  (entry 1, Table 1). An isotopic-labelling experiment, conducted in a  $\text{KH}^{13}\text{CO}_3$  solution saturated with  $^{13}\text{CO}_2$  under the same electrochemical conditions as described above provided a clean split of the  $^1\text{H}$  NMR signal which represents the  $\text{CH}_3$  proton peak ( $\delta = 3.35$  ppm) into a doublet with a coupling

constant ( $J_{\text{HC}}$ ) of 142 Hz (Figure S3). This unambiguous signature of the  $^{13}\text{CH}_3\text{OH}$  species confirmed that  $^{13}\text{CO}_2$  is the source of the observed methanol. Since carbon monoxide (CO) and formate ( $\text{HCOO}^-$ ) were also detected after electrolysis under a  $\text{CO}_2$  atmosphere, with FEs of 33.6% and 1.3%, respectively (entry 1, Table S2), electrolyses were performed using both compounds as substrates. At the same pH (7), electrolysis of a formate solution did not produce any traces of  $\text{CH}_3\text{OH}$  (entry 2, Table 1). On the contrary, under

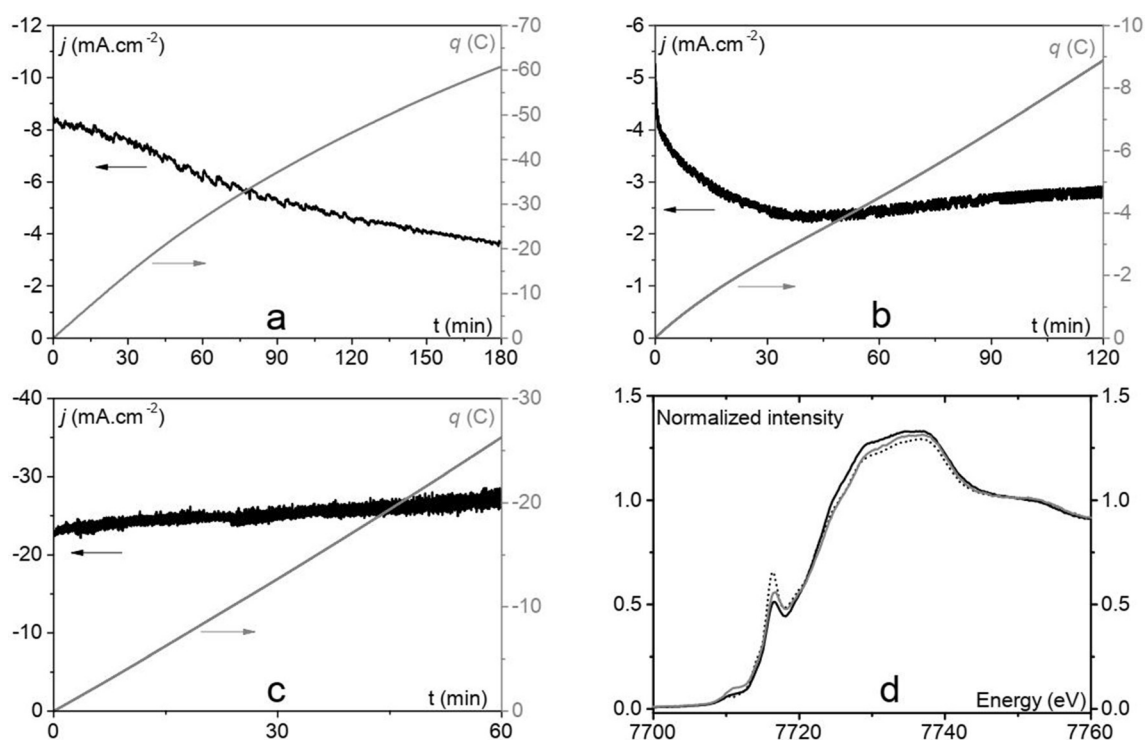


**Figure 1.** Current density and charge vs. time for a) a 3 h electrolysis under a  $\text{CO}_2$  atmosphere (pH 7.2) at -0.88 V vs. RHE, b) a 2 h electrolysis under a CO atmosphere (pH 12) at -0.70 V vs. RHE, c) a 1 h electrolysis with 20 mM formaldehyde (under an argon atmosphere) at -0.64 V vs. RHE. d) Co K-edge XANES spectra of the starting CoPc complex (black dots) and of a CoPc-MWCNT film before (gray) and after (black) 2 h of electrolysis at  $E = -0.64$  V vs. RHE under a CO atmosphere (pH 13).



a CO atmosphere, CH<sub>3</sub>OH was produced with a FE of 1–2% and a partial current density  $j_{\text{CH}_3\text{OH}}$  of 0.06 mA cm<sup>-2</sup>, slightly larger than those obtained from a CO<sub>2</sub>-saturated solution (entries 3–4, Table 1). Upon raising the solution pH to 13 (entries 5–6 in Table 1), the FE for CH<sub>3</sub>OH increased to 14.3% at  $E = -0.64$  V vs. RHE. Similarly, the partial current density for CH<sub>3</sub>OH was enhanced by a factor about 10, increasing up to 0.68 mA cm<sup>-2</sup>, while  $j_{\text{H}_2}$  remained in the same order of magnitude. Concomitantly, the overpotential decreased by 170 mV (from 910 mV to 740 mV) compared to CO<sub>2</sub> electrolysis. A labelled experiment with <sup>13</sup>CO confirmed that the carbon monoxide is the source for the methanol (Figure 2). When the pH value was further increased to 14, the activity decreased.

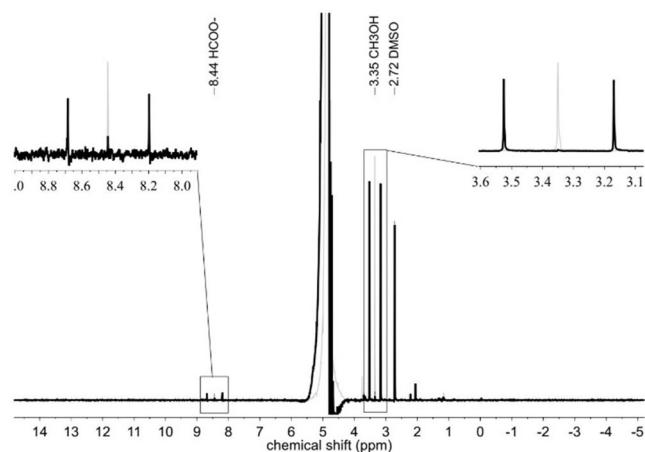


**Figure 2.** <sup>1</sup>H NMR spectra of the solution after controlled potential electrolysis ( $E = -0.64$  V vs. RHE,  $t = 2$  h) in <sup>12</sup>CO- (gray trace) and <sup>13</sup>CO-saturated (black trace) solutions at pH 13.

Following a 2 h electrolysis at  $-0.54$  V vs. RHE and pH 13 under CO, the catholyte solution was analyzed by high-pressure liquid chromatography (HPLC) after derivatization with 2,4-dinitrophenylhydrazine (DNPH) (see Supporting Information). Formaldehyde was detected and the Faradaic efficiency for its formation was 3.3%, leading to a complete FE of 87.6%. No other products than formaldehyde, methanol, and H<sub>2</sub> were detected.

Careful attention has to be paid to the Cannizzaro reaction that may spontaneously take place in alkaline media and even in neutral media in the reaction layer of the cathode where a high pH could build up.<sup>[19]</sup> This reaction, which amounts to formaldehyde disproportionation, may indeed be a source for CH<sub>3</sub>OH and HCOO<sup>-</sup> and can be misleading in product analysis since it does not involve any Faradaic process. In a blank experiment, depolymerized paraformaldehyde was used as a source for formaldehyde in a typical electrolysis solution (0.1 M KOH, pH 13). The formaldehyde solution (20 mM) was then stirred for 2 h and <sup>1</sup>H NMR analysis was performed. In accordance with Cannizzaro's mechanism,<sup>[20]</sup> the ratio between the quantities of CH<sub>3</sub>OH and HCOO<sup>-</sup> is equal to 1 when the reaction occurs (Figure S4). By the end of an electrolysis in a CO-saturated solution at pH 13, the ratio between methanol and formate

concentrations was equal to 16 and even to 27 at pH 12 where Cannizzaro is less favored (Figure S5 and entry 7, Table 1). Therefore, these experiments demonstrate that the Cannizzaro process can only account for a small fraction of the produced CH<sub>3</sub>OH. This conclusion is supported by the fact that cyclic voltammetry of the catalytic film provided a higher catalytic current in the presence of formaldehyde than without (Figure 3).

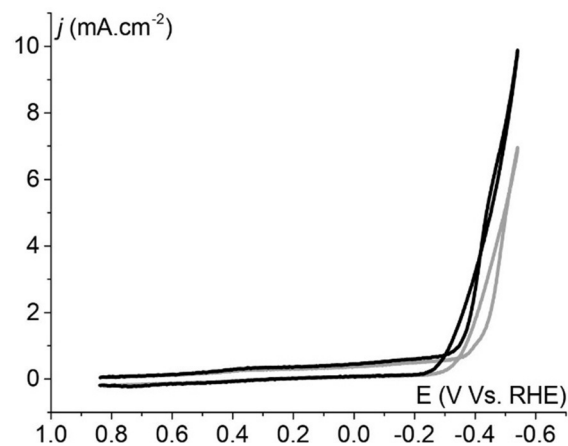


**Figure 3.** Cyclic voltammetry measurements of a CoPc/MWCNT film ( $\Gamma(\text{CoPc}) = 15$  nmol cm<sup>-2</sup>) in a 0.1 M KOH solution under an Ar atmosphere without (gray) and with 20 mM HCHO (black). Scan rate = 20 mV s<sup>-1</sup>, geometric electrode surface  $S_{\text{WE}} = 0.30$  cm<sup>2</sup>.

Also, electrolysis with dissolved formaldehyde performed in an Ar-saturated solution (Figure 1c) gave more than 18% FE for CH<sub>3</sub>OH at a potential of  $-0.54$  V vs. RHE, which corresponds to 770 mV overpotential (entry 8, Table 1). At a slightly more negative electrolysis potential ( $-0.64$  V vs. RHE), a maximum partial current density of 2.91 mA cm<sup>-2</sup> was reached (entry 9, Table 1). In order to properly evaluate both  $j_{\text{CH}_3\text{OH}}$  and  $\text{FE}_{\text{CH}_3\text{OH}}$  values reported in Table 1, the formate production was carefully quantified after each electrolysis and subtracted from the total amount of CH<sub>3</sub>OH as summarized in Equation (1).

$$\begin{aligned} n_{\text{CH}_3\text{OH},\text{Faradaic}} &= n_{\text{CH}_3\text{OH},\text{total}} - n_{\text{CH}_3\text{OH},\text{Cannizzaro}} \\ &= n_{\text{CH}_3\text{OH},\text{total}} - n_{\text{HCOO}^-,\text{total}} \end{aligned} \quad (1)$$

It should be noted that this calculation does not apply for experiments under CO<sub>2</sub>-saturation conditions since it is not possible to distinguish the portion of HCOO<sup>-</sup> originating from the Faradaic reduction of CO<sub>2</sub> and the portion ascribed to the homogeneous Cannizzaro process. Therefore, a fraction of the CH<sub>3</sub>OH reported in entry 1 of Table 1 could come from the Cannizzaro process rather than from a Faradaic reduction of CO<sub>2</sub>, but it should be even smaller than in the above experiments since the Cannizzaro reaction rate is slow at a pH of 7.2.

Identification of formaldehyde as an intermediate provides a rational explanation for the decay of  $j_{\text{CH}_3\text{OH}}$  under CO

atmosphere when the pH was raised from 13 to 14 (see entries 6 and 10 in Table 1). Indeed, methylene glycol (the aqueous form of formaldehyde) has a  $pK_a$  of about 13<sup>[21]</sup> and is mostly deprotonated at pH 14. This is supported by a similar drop in methanol production (< 3 % FE) when starting with formaldehyde as a substrate at pH 14. Interestingly, when methanol itself was used as a starting substrate (20 mM, controlled potential electrolysis at  $-0.64$  V vs. RHE and pH 13 for 2 h), no traces of other products such as methane were detected from GC analysis of the headspace, further illustrating the selectivity of the catalysis towards  $CH_3OH$  formation.

To assess the molecular nature of the catalysis and examine the possibility that the observed reactivity is due to decomposition of CoPc into metallic Co nanoparticles,<sup>[22]</sup> a series of control experiments were performed with various films in CO-saturated solutions at pH 13. The first film was prepared by replacing CoPc with an electrodeposited  $CoCl_2$  film with an equivalent amount of Co atoms. The second film was obtained by replacing CoPc with an identical concentration of cobalt quaterpyridine (CoQpy), a more fragile catalyst<sup>[23]</sup> that demetalates at negative potentials. Finally, a third film was made with CoPc, but was subjected to a more negative potential ( $E = -0.99$  V vs. RHE) to accelerate catalyst decomposition. In all these experiments, no  $CH_3OH$  was found in the catholyte after electrolysis, indicating that the aforementioned catalysis of  $CO_2$  to  $CH_3OH$  is indeed a molecular-driven process. This is also supported by the fact that an anodic scan of the catalytic film right after electrolysis failed to detect any oxidative stripping peak that would correspond to the oxidation of electrodeposited metallic Co (Figure S6). The Co K-edge X-ray absorption near-edge structure (XANES) spectra of the CoPc starting complex as well as the CoPc-MWCNT electrodes before and after electrolysis at  $-0.64$  V vs. RHE under CO atmosphere are shown in Figure 1d. The three spectra present the typical features expected for cobalt phthalocyanine complexes: a first, low-intensity pre-edge peak at 7710 eV which is assigned to the  $1s \rightarrow 3d/4p$  transition and a second intense peak at 7716 eV for the  $1s \rightarrow 4p_z$  transition which is characteristic to Co-N4 interactions.<sup>[24,25]</sup> Only slight changes are observed after catalysis, which can be attributed to changes in the interactions between CoPc and the MWCNTs.<sup>[24]</sup> A comparison of the spectrum obtained after electrolysis with those of reference cobalt species further demonstrates the intactness of the CoPc-MWCNT hybrid (Figure S7). However, it should be noted that the catalytic activity progressively decreased at longer times, as observed from the drop of the Faradaic yield for methanol production after a couple of hours. It may be due to reductive hydrogenation of the C=N double bonds of the phthalocyanine core, which has already been previously reported.<sup>[26]</sup> The exact mechanism of deactivation is under active study but we already know that basic media is not detrimental since a similar cobalt phthalocyanine has recently been shown to be stable for more than 10 h under strongly alkaline conditions (pH 14) for the  $CO_2$ -to-CO step at a gas diffusion electrode.<sup>[27]</sup> Because of the rather fast deactivation and variation in formaldehyde concentration over time (the ratio between electrode surface and electrolyte

volume affects the formaldehyde concentration and thus its reaction rate), the typical uncertainty is in the range of 10–20 %.

All previous results converge to a simple sequential strategy for optimizing methanol production. CoPc can first efficiently catalyze the electrochemical  $CO_2$ -to-CO conversion with a high FE (95 %) in a flow cell with current densities up to  $150$  mA  $cm^{-2}$  as we recently demonstrated.<sup>[28]</sup> Pure CO can then be used as a reactant under basic conditions (pH 13) and be reduced to  $CH_3OH$  with 14.3 % efficiency (740 mV overpotential). The catalyst is the same for each step, while the pH and the electrode potential are adjusted to maximize each partial reduction process. From the total number of transferred electrons, a global Faradaic efficiency of 19.5 % is calculated and the chemical selectivity is about 7.5 % (Figure S8).

In summary, cobalt phthalocyanine was used as a catalyst for the electrochemical conversion of  $CO_2$  to methanol, thanks to the unlocking of the CO-to-methanol step. The simplicity of the catalyst, the facile procedure for preparing the catalytic electrode, and the low loading amounts of the catalyst make the process versatile and easy to implement. Beyond this proof of principle, a tuning of the ligand will rapidly lead to improved performances and will be guided by mechanistic studies that are currently being done in our laboratories. We have thus shown that the electrochemical multi-electron-multi-proton reduction of  $CO_2$  beyond CO and formate can be achieved and controlled with a molecular catalyst. This study illuminates a new field of research for employing earth-abundant metal-based molecular complexes bearing simple ligand structures as cascade electrocatalysts for liquid-fuel production from  $CO_2$  and renewable electricity in mild aqueous conditions.

### Acknowledgements

We thank Dr. S. G. Derouich (Univ. Paris Diderot) for SEM analysis, and G. Le Faucheur and M.-Y. Pinart (Univ. Paris Diderot, Chemistry Department) for performing HPLC analysis. This work was supported by the French National Agency for Research (ANR-16-CE05-0010-01). M.W. thanks the China Scholarship Council for her PhD fellowship (CSC student number 201606220034). Partial financial support to M.R. from the Institut Universitaire de France (IUF) is also gratefully acknowledged.

### Conflict of interest

The authors declare no conflict of interest.

**Keywords:** carbon-monoxide reduction · cobalt phthalocyanine · electrochemistry · methanol · molecular catalyst

**How to cite:** *Angew. Chem. Int. Ed.* **2019**, *58*, 16172–16176  
*Angew. Chem.* **2019**, *131*, 16318–16322

- [1] T.-Y. Chang, R.-M. Liang, P.-W. Wu, J.-Y. Chen, Y.-C. Hsieh, *Mater. Lett.* **2009**, *63*, 1001.
- [2] E. Andrews, M. Ren, F. Wang, Z. Zhang, P. Sprunger, R. Kurtz, J. Flake, *J. Electrochem. Soc.* **2013**, *160*, H841.
- [3] X. Sun, Q. Zhu, X. Kang, H. Liu, Q. Qian, Z. Zhang, B. Han, *Angew. Chem. Int. Ed.* **2016**, *55*, 6771; *Angew. Chem.* **2016**, *128*, 6883.
- [4] J. Albo, A. Sáez, J. Solla-Gullón, V. Montiel, A. Irabien, *Appl. Catal. B* **2015**, *176–177*, 709.
- [5] T. Hatsukade, K. P. Kuhl, E. R. Cave, D. N. Abram, J. T. Feaster, A. L. Jongerius, C. Hahn, T. F. Jaramillo, *Energy Technol.* **2017**, *5*, 955.
- [6] Q. H. Low, N. W. X. Loo, F. Calle-Vallejo, B. S. Yeo, *Angew. Chem. Int. Ed.* **2019**, *58*, 2256; *Angew. Chem.* **2019**, *131*, 2278.
- [7] R. Kas, R. Kortlever, A. Milbrat, M. T. M. Koper, G. Mul, J. Baltrusaitis, *Phys. Chem. Chem. Phys.* **2014**, *16*, 12194.
- [8] K. P. Kuhl, T. Hatsukade, E. R. Cave, D. N. Abram, J. Kibsgaard, T. F. Jaramillo, *J. Am. Chem. Soc.* **2014**, *136*, 14107.
- [9] C. Costentin, S. Drouet, M. Robert, J.-M. Savéant, *Science* **2012**, *338*, 90.
- [10] I. Azcarate, C. Costentin, M. Robert, J.-M. Savéant, *J. Am. Chem. Soc.* **2016**, *138*, 16639.
- [11] K. Ogura, S. Yamasaki, *J. Chem. Soc. Faraday Trans. 1* **1985**, *81*, 267.
- [12] K. Ogura, K. Takamagari, *J. Chem. Soc. Dalton Trans.* **1986**, 1519.
- [13] K. Ogura, I. Yoshida, *J. Mol. Catal.* **1988**, *47*, 51.
- [14] M. Abdinejad, A. Seifitokaldani, C. Dao, E. H. Sargent, X.-a. Zhang, H. B. Kraatz, *ACS Appl. Energy Mater.* **2019**, *2*, 1330.
- [15] K. Kusuda, R. Ishihara, H. Yamaguchi, I. Izumi, *Electrochim. Acta* **1986**, *31*, 657.
- [16] S. Kapusta, N. Hackerman, *J. Electrochem. Soc.* **1984**, *131*, 1511.
- [17] C. M. Lieber, N. S. Lewis, *J. Am. Chem. Soc.* **1984**, *106*, 5033.
- [18] J. H. Zagal, S. Griveau, J. F. Silva, T. Nyokong, F. Bedioui, *Coord. Chem. Rev.* **2010**, *254*, 2755.
- [19] Y. Y. Birdja, M. T. M. Koper, *J. Am. Chem. Soc.* **2017**, *139*, 2030.
- [20] J. F. Walker in *Formaldehyde—Monograph series no. 159*, American Chemical Society, Washington, **1964**, pp. 206–226.
- [21] J. F. Walker in *Formaldehyde—Monograph series no. 159*, American Chemical Society, Washington, **1964**, pp. 106–122.
- [22] J. Huang, X. Guo, G. Yue, Q. Hu, L. Wang, *ACS Appl. Mater. Interfaces* **2018**, *10*, 44403.
- [23] M. Wang, L. Chen, T.-C. Lau, M. Robert, *Angew. Chem. Int. Ed.* **2018**, *57*, 7769; *Angew. Chem.* **2018**, *130*, 7895.
- [24] N. Li, W. Lu, K. Pei, W. Chen, *RSC Adv.* **2015**, *5*, 9374.
- [25] N. Han, Y. Wang, L. Ma, J. Wen, J. Li, H. Zheng, K. Nie, X. Wang, F. Zhao, Y. Li, J. Fan, J. Zhong, T. Wu, D. J. Miller, J. Lu, S.-T. Lee, Y. Li, *Chem* **2017**, *3*, 652.
- [26] F. Gund, *J. Soc. Dyers Colour.* **1953**, *69*, 671.
- [27] M. Wang, K. Torbensen, D. Salvatore, S. Ren, D. Joulié, F. Dumoulin, D. Mendoza, B. Lassalle-Kaiser, U. Işci, C. P. Berlinguette, M. Robert, *Nat. Commun.* **2019**, *10*, 3602.
- [28] S. Ren, D. Joulié, D. Salvatore, K. Torbensen, M. Wang, M. Robert, C. P. Berlinguette, *Science* **2019**, *365*, 367.

Manuscript received: July 24, 2019

Revised manuscript received: August 30, 2019

Accepted manuscript online: September 8, 2019

Version of record online: September 25, 2019



# Achieving Near-Unity CO Selectivity for CO<sub>2</sub> Electroreduction on an Iron-Decorated Carbon Material

Xin-Ming Hu,<sup>[a]</sup> Daniela Mendoza,<sup>[b, c]</sup> Monica Rohde Madsen,<sup>[a]</sup> Dorian Joulié,<sup>[b]</sup> Benedikt Lassalle-Kaiser,<sup>[c]</sup> Marc Robert,<sup>\*,[b, d]</sup> Steen U. Pedersen,<sup>[a]</sup> Troels Skrydstrup,<sup>[a]</sup> and Kim Daasbjerg<sup>\*,[a]</sup>

A straightforward procedure has been developed to prepare a porous carbon material decorated with iron by direct pyrolysis of a mixture of a porous polymer and iron chloride. Characterization of the material with X-ray diffraction, X-ray absorption spectroscopy, and electron microscopy indicates the presence of iron carbide nanoparticles encapsulated inside the carbon matrix, and elemental mapping and cyanide poisoning experiments demonstrate the presence of atomic Fe centers, albeit in trace amounts, which are active sites for electrochemical CO<sub>2</sub> reduction. The encapsulated iron carbide nanoparticles are

found to boost the catalytic activity of atomic Fe sites in the outer carbon layers, rendering the material highly active and selective for CO<sub>2</sub> reduction, although these atomic Fe sites are only present in trace amounts. The target material exhibits near-unity selectivity (98%) for CO<sub>2</sub>-to-CO conversion at a small overpotential (410 mV) in water. Furthermore, the material holds potential for practical application, as a current density over 30 mAcm<sup>-2</sup> and a selectivity of 93% can be achieved in a flow cell.

## Introduction

The enormous consumption of fossil fuels has led to the depletion of this limited energy resource and the excessive emission of CO<sub>2</sub> into the atmosphere, resulting in dramatic climate changes on the global scene. Renewable energy sources, such as solar and wind power, are believed to be carbon-neutral and a promising substitute to fossil fuel. Unfortunately, their intermittent nature calls for effective energy storage solutions.<sup>[1]</sup> To tackle these issues, one of the most promising strategies is CO<sub>2</sub> valorization through the electrochemical CO<sub>2</sub> reduction reaction (eCO<sub>2</sub>RR). This process can possibly contribute to mitigate the atmospheric CO<sub>2</sub> level and allow for storage of renewable energy in the form of CO<sub>2</sub>-derived chemicals.<sup>[2]</sup> Unfortunately, CO<sub>2</sub> is a thermody-

namically and kinetically very stable molecule. As a consequence, the direct reduction of CO<sub>2</sub> at an electrode requires a large overpotential and is often associated with a low selectivity due to the competing hydrogen evolution reaction. Therefore, efficient electrocatalysts with both high activity and selectivity for eCO<sub>2</sub>RR are greatly in demand.<sup>[3]</sup>

Precious metals with various nanostructures and compositions have shown impressive catalytic activity for eCO<sub>2</sub>RR.<sup>[4]</sup> However, the low abundance and high cost present hurdles for their large-scale applications. In this regard, electrocatalysts comprising of earth-abundant elements would be much preferred. One type of such catalysts could be nitrogenated carbon materials, which have been shown to be capable of catalyzing the CO<sub>2</sub>-to-CO conversion at the N sites.<sup>[5]</sup> Unfortunately, the low activity and selectivity make nitrogenated carbon unsatisfactory for eCO<sub>2</sub>RR as things stand now. One typical way to improve the performance is to decorate earth-abundant metal (i.e. Mn,<sup>[6]</sup> Fe,<sup>[7]</sup> Co,<sup>[8]</sup> Ni,<sup>[7b,9]</sup> or Zn<sup>[10]</sup>) atoms in nitrogenated carbon, where the metal centers rather than the N sites become responsible for eCO<sub>2</sub>RR. Among many metals, iron is particularly attractive, being one of the metals showing largest abundance in the Earth's crust and least detrimental effect on environment.<sup>[11]</sup> However, it is still challenging to obtain highly active iron-decorated carbon materials with near-unity selectivity for CO<sub>2</sub>-to-CO conversion.<sup>[7]</sup> To improve the activity and selectivity, previous efforts have been focused on manipulating the coordination environments,<sup>[7e,8b]</sup> and increasing the concentration<sup>[12]</sup> of the atomic metal sites. Impacts coming from different types of metal dopants (such as metal carbide) have not yet been noticed.

In this work, we report a straightforward procedure to synthesize a porous iron-decorated carbon material (Fe-NC). The iron(III) chloride-promoted polymerization enables the


[a] Dr. X.-M. Hu, M. R. Madsen, Prof. S. U. Pedersen, Prof. T. Skrydstrup, Prof. K. Daasbjerg  
Carbon Dioxide Activation Center (CADIAC), Interdisciplinary Nanoscience Center (iNANO) and Department of Chemistry  
Aarhus University  
Gustav Wieds Vej 14, 8000 Aarhus (Denmark)  
E-mail: kdaa@chem.au.dk

[b] D. Mendoza, D. Joulié, Prof. M. Robert  
Université de Paris, Laboratoire d'Electrochimie Moléculaire, CNRS  
75006 Paris (France)  
E-mail: robert@u-paris.fr

[c] D. Mendoza, Dr. B. Lassalle-Kaiser  
Synchrotron SOLEIL, L'Orme des Merisiers, Saint-Aubin  
91192 Gif-sur-Yvette France

[d] Prof. M. Robert  
Institut Universitaire de France (IUF)  
75005 Paris, France.

 Supporting information for this article is available on the WWW under <https://doi.org/10.1002/cssc.202001311>

 This publication is part of a Special Issue entitled "Green Carbon Science: CO<sub>2</sub> Capture and Conversion". Please visit the issue at <http://doi.org/10.1002/cssc.v13.23>.



formation of a highly porous polycarbazole with iron ions trapped in its pores. This renders the formation of encapsulated  $\text{Fe}_3\text{C}$  in a porous carbon material containing trace amount of atomic Fe sites during a subsequent pyrolysis. Such trace amount of atomic Fe sites is active for  $\text{eCO}_2\text{RR}$  and the encapsulation of  $\text{Fe}_3\text{C}$  is found to significantly enhance their activity and selectivity. As a result, Fe-NC exhibits a near-unity selectivity for  $\text{CO}_2$ -to-CO conversion at a small overpotential and can simultaneously achieve a high current density and high selectivity at increased overpotentials in water when inserted in a flow cell.

## Results and Discussion

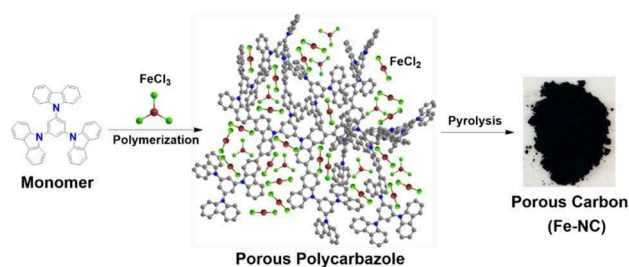
Scheme 1 outlines the protocol for the synthesis of the porous iron-decorated carbon material, Fe-NC. First, oxidative polymerization of 1,3,5-tris(*N*-carbazolyl)benzene by iron(III) chloride produced a highly porous polycarbazole with iron(III/II) chloride filled in its pores.<sup>[13]</sup> Second, this mixture, without isolation steps, was directly pyrolyzed at 1000 °C under inert atmosphere, followed by acid washing and a second pyrolysis, generating the target Fe-NC material. Iron chloride has dual roles in the synthesis, in that it is (1) an oxidant for the C–C coupling among carbazole molecules to form polycarbazole<sup>[14]</sup> and (2) an iron source to produce the Fe-NC material. The acid washing and the second pyrolysis steps are essential to make a high-performance carbon material for  $\text{eCO}_2\text{RR}$ , with the former step removing exposed Fe-based nanoparticles and the latter one minimizing the

oxygenated functionalities. Both kinds of species have been found to favor hydrogen evolution rather than  $\text{eCO}_2\text{RR}$ .<sup>[7a,b]</sup>

For comparison, in a separate experiment we removed the iron(II/III) chloride after the polymerization by thorough acid washing. The polycarbazole was pyrolyzed on its own under the same conditions as for Fe-NC to generate the NC material. Notably, the polymerization process is near quantitative, which, along with the high stability of the cross-linked polycarbazole formed, enables a high-yielding production (> 70% relative to the monomer used) of both NC and Fe-NC. From a yield perspective, this protocol for carbon material synthesis outperforms the typically reported procedures, such as direct pyrolysis of monomeric precursors<sup>[7b]</sup> or coordination-based metal-organic frameworks,<sup>[15]</sup> which usually have as low as 20% yields.

Nitrogen sorption experiments revealed that the two carbon materials have similar specific surface areas ( $826 \text{ m}^2 \text{ g}^{-1}$  for NC and  $1001 \text{ m}^2 \text{ g}^{-1}$  for Fe-NC), being approximately half of that of the polycarbazole ( $2108 \text{ m}^2 \text{ g}^{-1}$ ; see the Supporting Information, Figure S1). In addition, NC and Fe-NC possess similar pore sizes, which, calculated based on density functional theory (DFT), are mainly in the range of micropores (ca. 0.6 and 1 nm) with a small contribution from mesopores (ca. 6 and 9 nm). The pore size distribution of the two carbon materials is distinctly different from that of their precursor, polycarbazole, which features both substantial micro- (ca. 0.9 nm) and mesopores (ca. 3 and 6 nm; Figure 1a). These results suggest that high-temperature pyrolysis leads to reorganization of the polycarbazole structure to form the carbon materials. Notably, the resulting carbon materials retain the highly porous nature originating from their precursors, which would be beneficial for the effective exposure of active sites for catalysis.

X-ray photoelectron spectroscopy (XPS) was employed to determine the composition of the three materials (Figure S2). The polycarbazole contains mainly C (91.0 at%) and an amount of N (6.5 at%). These numbers are close to the theoretically expected C and N percentage in the polymer, thus underlining the high purity of the polymer (Table S1). In line with previous findings,<sup>[16]</sup> chlorination of the polycarbazole seems to occur with each carbazole unit containing approximately one Cl atom. On the other hand, the high-temperature pyrolysis process induces a complete removal of



Scheme 1. Protocol for the synthesis of the porous Fe-NC material.

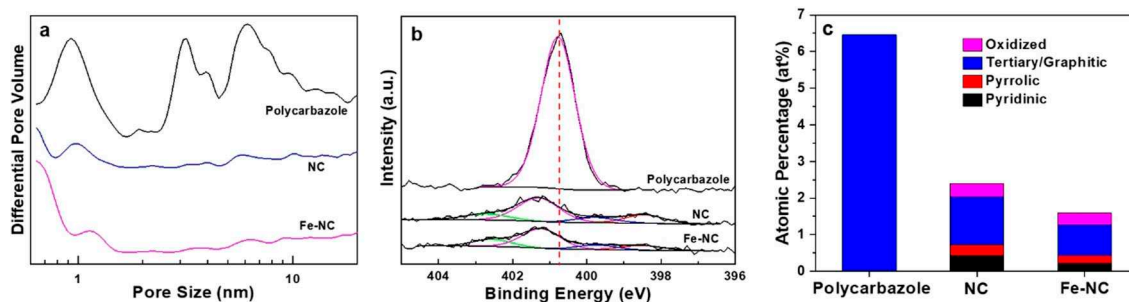


Figure 1. (a) Pore size distribution, (b) N 1s XPS spectra, and (c) percentage of different N species in the polycarbazole, NC, and Fe-NC materials.

Cl along with a partial depletion of N, which further points to the structural reorganization of polycarbazole to form the NC and Fe–NC materials. The two carbon materials possess similar elemental composition, mostly C and a small amount of N.

The high resolution N 1s spectra were further examined. While the polycarbazole only shows the tertiary N as expected, NC and Fe–NC show the same four types of N species (i.e. pyridinic, pyrrolic, graphitic, and oxidized N species; Figure 1b), which can be attributed to the occurrence of disproportionation during the pyrolysis. Although the N content in NC is slightly larger than in Fe–NC (Figure 1c), the relative proportion of N species is, by and large, the same for the two materials. This reveals that the presence of iron(II/III) chloride during the carbon material synthesis does not induce specific differences to the N species.

Initially, we found that polycarbazole and NC contain no Fe due to the thorough acid washing, as shown by both XPS and inductively coupled plasma-optical emission spectroscopy (ICP–OES, Table S1). Surprisingly, neither Fe–NC shows Fe in XPS, whereas ICP–OES reveals a small amount of Fe (0.61 wt%). One possible explanation of this is that all iron species are wrapped by carbon layers. This will exclude them from being detected by XPS which is a surface technique detecting only the elemental composition down to <10 nm

of the material surface. In contrast, ICP–OES analyzes the entire bulk material. This explanation seems to be supported by transmission electron microscopy (TEM), where the encapsulation of the iron-based particles of tens of nanometres in carbon layers is observed with the thinnest part of the carbon layers being ~10 nm (Figure 2a,b). In NC, no Fe<sub>3</sub>C particles but only carbon spheres with similar size to those in Fe–NC are observed (Figure 2c,d). The lattice distance of these particles in Fe–NC is measured to be 0.205 nm, corresponding to the (211) plane of iron carbide (Fe<sub>3</sub>C; Figure S3).<sup>[17]</sup> The presence of Fe<sub>3</sub>C is further confirmed by powder X-ray diffraction (PXRD), where a set of Fe<sub>3</sub>C diffraction peaks in the range of 35–60° is shown (Figure 3a). The strong diffraction peak at 2θ = 26.4° comes from the graphitic carbon in the material.

Another possible explanation of the diverging analysis results is related to the fact that XPS has a detection limit of 0.01 at% for heavy elements (e.g. Fe) in a light element matrix (e.g. C).<sup>[18]</sup> This means that there could be trace amount of atomic Fe sites present in the carbon layers below the detection limit of XPS. This possibility cannot be excluded, as the N atoms, in particular pyridinic and pyrrolic N, in Fe–NC are able to anchor Fe atoms to form atomic Fe sites as widely reported.<sup>[7]</sup> In support of this, the high-angle annular dark-field imaging (HAADF) and the elemental mapping by energy dispersive X-ray spectroscopy (EDX)

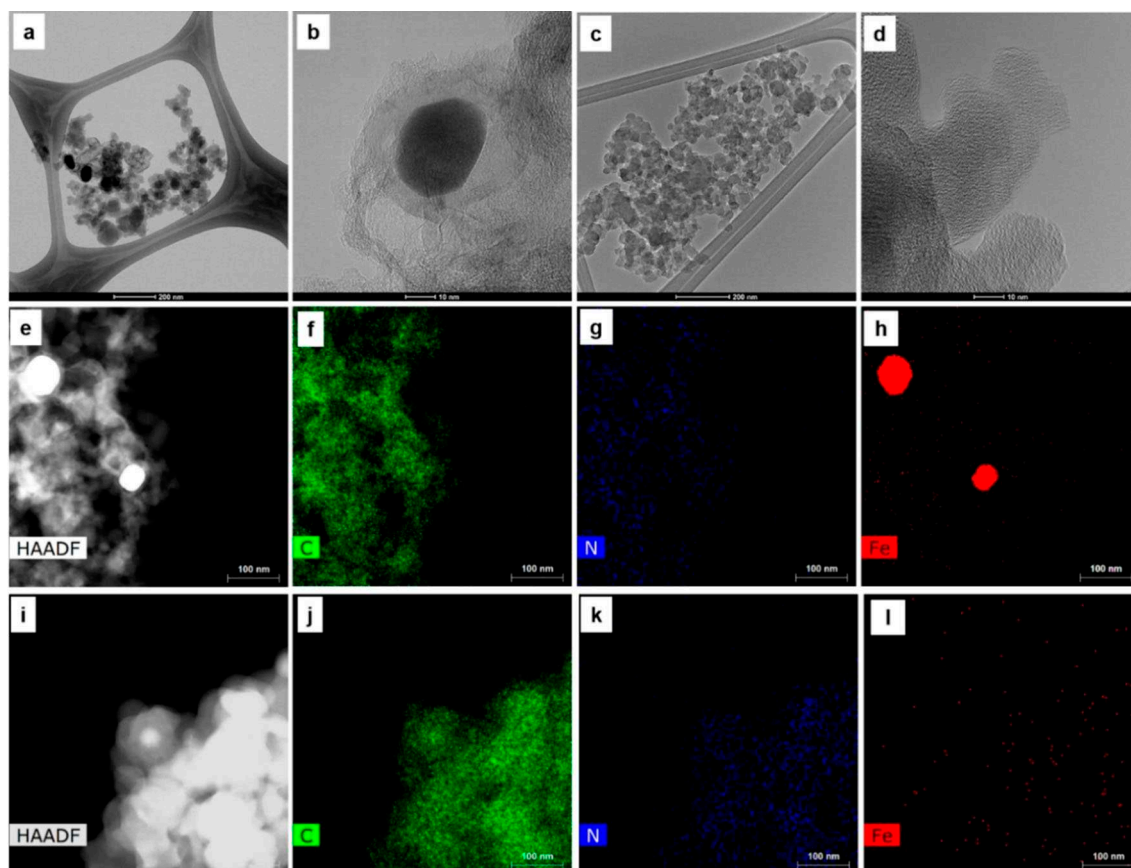
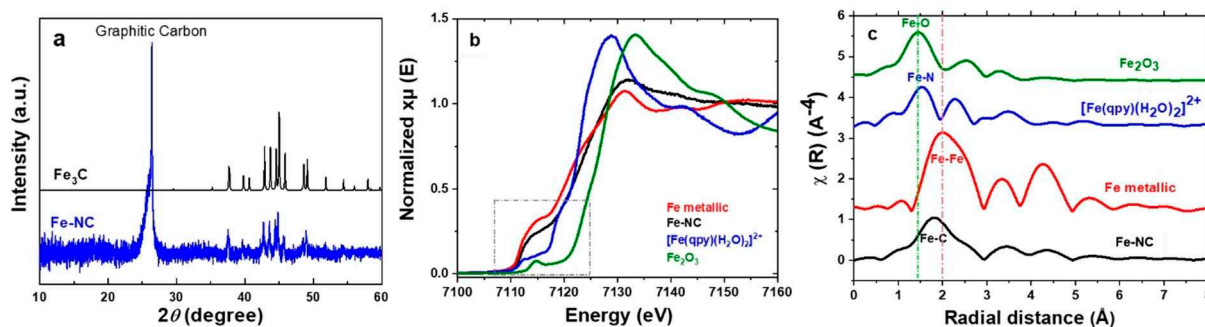


Figure 2. TEM images of (a,b) Fe–NC and (c,d) NC. HAADF images and the corresponding elemental mapping for (e–h) Fe–NC and (i–l) NC.



**Figure 3.** (a) PXRD patterns of Fe-NC along with the diffraction pattern of  $\text{Fe}_3\text{C}$  (No. 9012187 from the Crystallography Open Database). The Fe K-edge (b) XANES and (c) EXAFS spectra of Fe-NC and reference materials (Fe metallic,  $[\text{Fe}(\text{qpy})(\text{H}_2\text{O})_2]^{2+}$ , and  $\text{Fe}_2\text{O}_3$ ).

reveal the presence of sparsely, yet well dispersed Fe sites, in addition to large  $\text{Fe}_3\text{C}$  particles (Figures 2e,h and S4). More surprisingly, the EDX mapping on NC suggests the presence of atomic Fe sites as well (Figure 2l), even though the XPS and ICP-OES do not show positive signals for Fe (Table S1). We notice that few atomic Fe signals are even observed in the blank areas with no Fe-NC or NC (Figure 2h and l). These Fe signals stem from the background noise as also seen in elemental mapping of similar materials.<sup>[19]</sup> Nevertheless, the more densely populated Fe signals in both the two materials compared with the blank areas suggest they contain atomic Fe sites, albeit in trace amount. As another comparison, the presence of a much larger amount of atomic Fe sites is clearly shown by EDX mapping for a previously reported material where the content of Fe is 0.4 wt%, even lower than in Fe-NC (Figure S5).<sup>[7b]</sup>

Taken together, the analysis results show that the overwhelming majority of Fe species in Fe-NC originates from encapsulated  $\text{Fe}_3\text{C}$  nanoparticles, and that atomic Fe sites exist at a trace level in both Fe-NC and NC. While  $\text{Fe}_3\text{C}$  particles seem to be randomly distributed in microscopic TEM and HAADF images, all Fe-NC exhibits magnetism, manifesting the widespread encapsulation of  $\text{Fe}_3\text{C}$  in the material (Figure S6). In contrast, the NC material exhibits no magnetism. Furthermore, N and C elements are uniformly dispersed in both NC and Fe-NC (Figure 2f,g,j,k).

To better understand the chemical environment of the Fe species in Fe-NC, Fe K-edge X-ray absorption near edge structure (XANES) and extended X-ray absorption fine structure (EXAFS) data were recorded (Figure 3b,c). In these analyses, metallic Fe foil, an Fe quaterpyridine molecular complex  $[\text{Fe}(\text{qpy})(\text{H}_2\text{O})_2]^{2+}$  (Scheme S1), and  $\text{Fe}_2\text{O}_3$  were used as references. Notably, the pre-edge position of the Fe-NC material lies in between the one obtained for the metallic Fe foil and the  $[\text{Fe}(\text{qpy})(\text{H}_2\text{O})_2]^{2+}$  complex (Figure 3b). A comparison with the results obtained by Yuan et al. shows that the Fe K-edge XANES for the Fe-NC material matches closely that of  $\text{Fe}_3\text{C}$ ,<sup>[20]</sup> in good agreement with the identification of  $\text{Fe}_3\text{C}$  by TEM and PXRD. It should be pointed out that the XANES cannot rule out the presence of small amount of metallic Fe particles.

Figure 3c shows the Fourier transform of the EXAFS spectra of Fe-NC and the three reference materials. For  $[\text{Fe}(\text{qpy})(\text{H}_2\text{O})_2]^{2+}$  and  $\text{Fe}_2\text{O}_3$  an apparent radial distance is present at  $\sim 1.5$   $\text{\AA}$  corresponding to Fe-N and Fe-O bonds, respectively. This characteristic bond distance for Fe-N is not observed in Fe-NC, thus confirming the low amount of atomic Fe sites with respect to  $\text{Fe}_3\text{C}$  particles, in line with the XPS and EDX mapping results.

The catalytic activity of the synthesized NC and Fe-NC for  $\text{eCO}_2\text{RR}$  was investigated in aqueous 0.5 M  $\text{KHCO}_3$ . Prior to the electrochemical study, each material was deposited (loading =  $0.5 \text{ mg cm}^{-2}$ ) on a glassy carbon plate using a small amount of Nafion as binder. In the case of NC, linear sweep voltammetric recordings exhibit an increase of 5% in the current density ( $|j|$ ) at  $-0.5$  V vs. the reversible hydrogen electrode (RHE) upon saturating the solution with  $\text{CO}_2$  (Figure 4a). This indicates that NC, as also seen for other N-doped carbon materials,<sup>[5]</sup> is active for  $\text{eCO}_2\text{RR}$ . For Fe-NC, a similar 5% increase of  $|j|$  occurs at a less negative potential ( $-0.38$  V vs. RHE) under the same conditions, demonstrating its enhanced activity for  $\text{eCO}_2\text{RR}$ .

The  $\text{eCO}_2\text{RR}$  activity of both NC and Fe-NC was further verified by carrying out controlled potential electrolysis in an H-cell (Figure 4b,c). At the potentials examined, CO and  $\text{H}_2$  were the only products detected by gas chromatography, showing a total faradaic efficiency (FE) close to 100%. No products in the liquid phase could be detected by  $^1\text{H}$  NMR. Using Fe-NC as catalyst, the  $\text{CO}_2$ -to-CO conversion was observed at  $-0.42$  V vs. RHE with  $\text{FE}_{\text{CO}} = 94\%$  and  $|j| = 0.36 \text{ mA cm}^{-2}$ . This represents a small overpotential of 310 mV, consistent with the linear sweep voltammetry experiments. A maximum  $\text{FE}_{\text{CO}}$  of 98% was achieved at  $-0.52$  V vs. RHE along with  $|j| = 1.41 \text{ mA cm}^{-2}$ , corresponding to an overpotential ( $\eta$ ) of 410 mV. Notably, a high  $\text{FE}_{\text{CO}}$  ( $> 92\%$ ) is maintained in the potential range from  $-0.42$  to  $-0.67$  V vs. RHE, showing the high selectivity of Fe-NC towards  $\text{CO}_2$ -to-CO conversion over hydrogen evolution (Figure S7). It has to be pointed out that one cannot directly compare the current densities recorded in linear sweep voltammetry and electrolysis experiments as they are recorded under different experimental conditions. Finally,

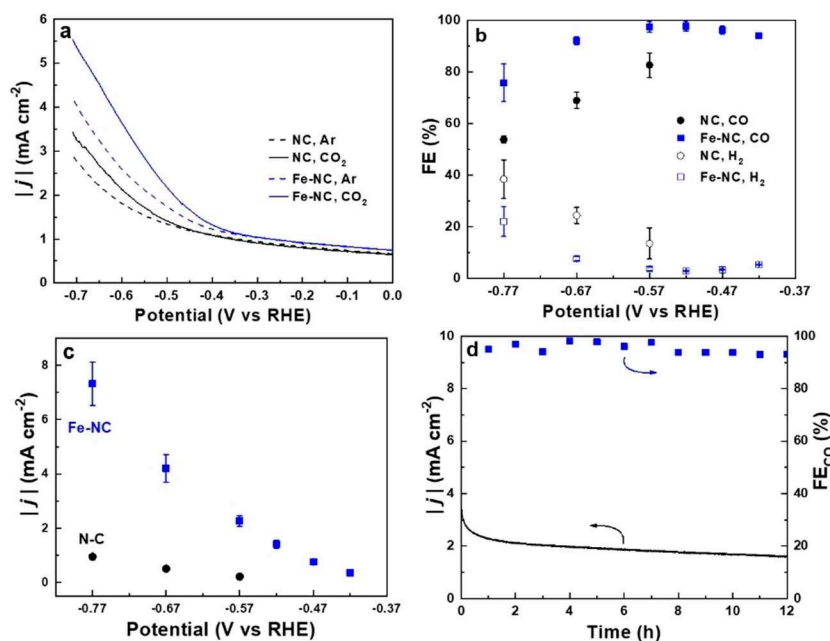


**Figure 4.** (a) Linear sweep voltammetry using NC and Fe-NC materials under Ar and CO<sub>2</sub> atmosphere in 0.5 M KHCO<sub>3</sub>. (b) FE and (c)  $|j|$  using NC and Fe-NC materials during 15 min electrolysis at various potentials in CO<sub>2</sub>-saturated 0.5 M KHCO<sub>3</sub>. (d)  $|j|$  (solid lines) and FE<sub>CO</sub> (symbols) using Fe-NC during 12 h electrolysis at -0.57 V vs. RHE in CO<sub>2</sub>-saturated 0.5 M KHCO<sub>3</sub> solution.

Fe-NC exhibits good long-term stability over 12 h electrolysis of CO<sub>2</sub> at -0.57 V vs. RHE, with a steady FE<sub>CO</sub> ≈ 95% over the entire period and with a decrease of  $|j|$  mainly occurring in the first 2 h (Figure 4d), similar to what is observed for many other carbon-based materials.<sup>[19b,21]</sup>

In the literature, pyridinic N species are known to be active for eCO<sub>2</sub>RR.<sup>[5,21a,b]</sup> At first sight, the most likely active sites in Fe-NC thus would be the N atoms, also considering that they are abundant, whereas the atomic Fe sites are present in trace amount. At the same time, Fe<sub>3</sub>C is encapsulated in the carbon layers which should hinder its direct contact with CO<sub>2</sub>. Yet, the NC material with its higher content of pyridinic N sites (Figure 1c) displays lower FE<sub>CO</sub> and as little as 10% of the current density achieved on Fe-NC (Figure 4b,c). In addition, the double-layer capacitance of Fe-NC was found to be similar to that of NC (Figure S8). This is not

surprising since the two materials also have similar porosity as indicated from N<sub>2</sub> sorption experiments. Such a result excludes the possibility that differences in the electrochemically active surface areas of the materials could be responsible for the eCO<sub>2</sub>RR activity differences. This then leaves with the option that the Fe species are the ones responsible for the enhanced activity of Fe-NC.

To examine the effect of the trace amount of atomic Fe sites in the Fe-NC material, we performed a poisoning test by introducing cyanide ions (CN<sup>-</sup>) into the electrolyte. This is to exploit the ability of CN<sup>-</sup> to block metal centers for catalysis, while there would be no similar poisoning effect on a pure NC material.<sup>[22]</sup> In the presence of CN<sup>-</sup>, we observed for Fe-NC a decrease in FE<sub>CO</sub> accompanied with an increase in FE<sub>H<sub>2</sub></sub>, and more notably, a halving of  $|j|$  (Figures 5a,b and S9). Furthermore, the eCO<sub>2</sub>RR activity could be partly

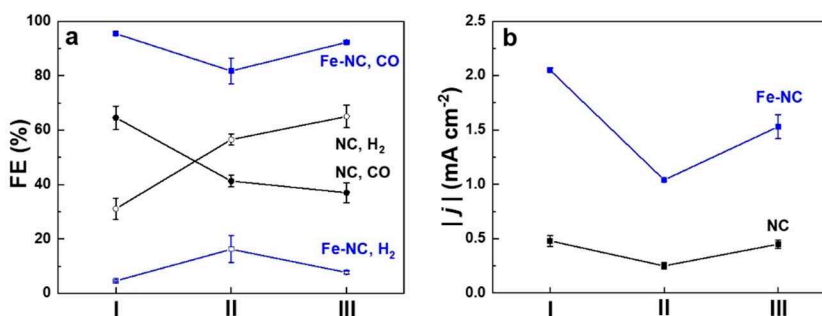


**Figure 5.** (a) FE and (b)  $|j|$  using NC (at -0.67 V vs. RHE) and Fe-NC (at -0.57 V vs. RHE) materials during 15 min electrolysis in CO<sub>2</sub>-saturated 0.5 M KHCO<sub>3</sub> (I) in the absence of CN<sup>-</sup>, (II) in the presence of 30 mM CN<sup>-</sup>, and (III) after being poisoned with CN<sup>-</sup> and then cleaned by washing.



recovered after washing out the  $\text{CN}^-$  and performing the electrolysis under the original conditions. These results suggest that the Fe centers, although only present in trace amount in the carbon matrix, are active sites for the  $\text{eCO}_2\text{RR}$ .

Surprisingly, an appreciable poisoning effect was also seen with the NC material as evidenced from decreases in both  $\text{FE}_{\text{CO}}$  and  $|j|$  upon addition of  $\text{CN}^-$  (Figure 5a,b). In fact, the similar extent of activity decrease (ca. 50%) would indicate that NC and Fe–NC have comparable content of atomic Fe sites. In comparison, the poisoning experiment on an  $\text{Fe}_3\text{C}$ -free carbon material containing more abundant atomic Fe sites led to a  $\sim 20\%$  activity decay in the presence of the same concentration of  $\text{CN}^-$ .<sup>[7b]</sup> In our view, this conveys an important message, namely that trace amount of metal sites in carbon materials, even when undetectable by ICP–OES, could be decisive for the catalytic activity, and that using poisoning of the metal sites, in general, would provide a more reliable way to determine the exact role of the metal. In principle, the Fe in NC could originate from residual Fe trapped in the polycarbazole precursor during the use of  $\text{FeCl}_3$  for the polymerization.

One might raise the question as to why the  $\text{CN}^-$  poisoning only quenches half of the  $\text{eCO}_2\text{RR}$  activity, despite the use of large excess of  $\text{CN}^-$  in respect to the atomic Fe sites in both materials. This result can best be explained by the presence of an equilibrium in the competitive binding of atomic Fe with  $\text{CN}^-$  and  $\text{CO}_2$ . Incomplete blocking of active metal sites by  $\text{CN}^-$  has also been observed for  $\text{eCO}_2\text{RR}$  catalyzed by carbon nanotube-supported cobalt porphyrin, in which the active site for certain is the Co center.<sup>[7b]</sup> Similarly, partial poisoning was reported for  $\text{CN}^-/\text{SCN}^-$  experiments in the case of  $\text{CO}_2$  reduction,<sup>[7b]</sup> oxygen reduction,<sup>[23]</sup> and hydrogen evolution reactions<sup>[24]</sup> using atomic metal sites as catalysts.

Based on these experiments, we may sketch out the structure and active site of Fe–NC, a carbon material with  $\text{Fe}_3\text{C}$  nanoparticles encapsulated and with trace amount of atomic Fe sites anchored (Figure 6a). The atomic Fe sites most likely exist with the stabilization/coordination of N atoms (i.e. Fe–N coordination).<sup>[7]</sup> The low percentage of such Fe sites in Fe–NC (and also NC) is due to the fact that the

materials are synthesized from polycarbazole, which contains only tertiary N species of poor coordinating capability for Fe ions. In contrast, previously reported carbon materials contain abundant Fe–N coordination, since they are synthesized from precursors that possess either amino, pyrrolic, or pyridinic N species, which are prone to coordinate with Fe ions.<sup>[7]</sup> Because of the trace amount of Fe–N coordination, it is difficult to uncover the exact coordination details between N and Fe atoms, even with the most sophisticated characterization techniques such as EXAFS.

At this point we are still left with the observation that the  $\text{eCO}_2\text{RR}$  activity of Fe–NC exceeds that of NC by a large factor (ca. 10 times). We have collected evidence that the two materials contain comparable trace amount of atomic Fe sites as shown by the similarity in the dispersion of the Fe sites (Figure 2h,l) and in the poisoning effect (Figure 5a,b). And these trace amounts are in both cases  $\text{eCO}_2\text{RR}$  active. This then leaves room for another contribution to the  $\text{eCO}_2\text{RR}$  activity in the particular case of Fe–NC. Since the major structural difference between the two materials is the encapsulation of  $\text{Fe}_3\text{C}$  in Fe–NC, we propose the encapsulated  $\text{Fe}_3\text{C}$  to be responsible for the enhanced  $\text{eCO}_2\text{RR}$  activity and selectivity in Fe–NC.

A particularly interesting aspect of the  $\text{Fe}_3\text{C}$  nanoparticles in this work is that they are wrapped by a carbon layers, thus hindering them from having direct contact with electrolyte and  $\text{CO}_2$  molecules. It is important to distinguish this result from that of a recent work, reporting that materials carrying iron carbides and metallic Fe particles are mainly active for hydrogen evolution,<sup>[7a]</sup> because those two types of Fe-based particles are both able to catalyze water reduction by being directly exposed to the electrolyte. In contrast, our Fe–NC material containing  $\text{Fe}_3\text{C}$  (probably minor metallic Fe-particles as well) exhibits minimal activity for hydrogen evolution. This manifests the benefit of having Fe-based nanoparticles encapsulated by a carbon layers if hydrogen evolution is unwanted.

It is also interesting to note that in the oxygen-reduction research field there have been reports on Fe/ $\text{Fe}_3\text{C}$  nanoparticles-encapsulated carbon materials exhibiting enhanced activity.<sup>[25]</sup> Computations therein suggest that the enclosed

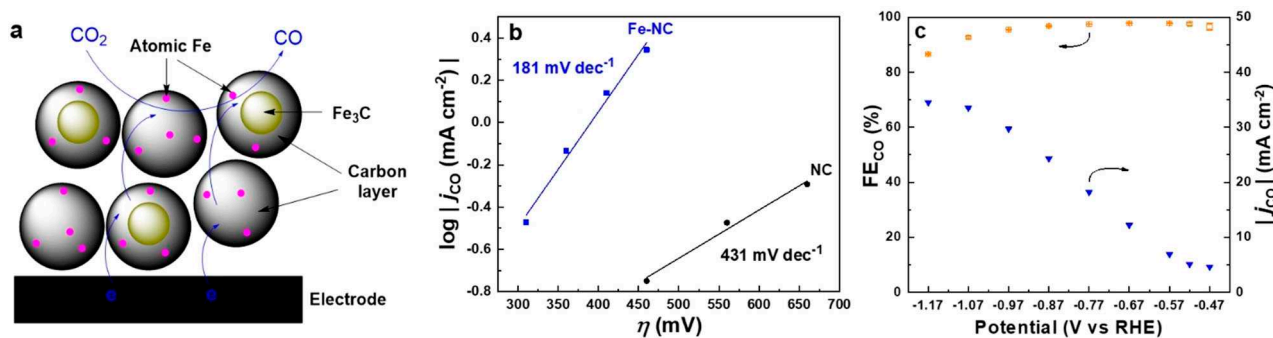


**Figure 6.** (a) Illustration the Fe–NC structure and of the active sites for  $\text{eCO}_2\text{RR}$ . (b) Plot of  $\log |j_{\text{CO}}|$  vs.  $\eta$  in 15 min electrolysis of  $\text{CO}_2$  (0.5 M  $\text{KHCO}_3$  solution) with Fe–NC and NC at various overpotentials in an H cell. (c)  $\text{FE}_{\text{CO}}$  and  $|j_{\text{CO}}|$  measured at various potentials with Fe–NC material in a flow cell (each potential step corresponds to a 20 min electrolysis in a  $\text{CO}_2$  saturated 0.5 M  $\text{KHCO}_3$  solution).

Fe/Fe<sub>3</sub>C nanoparticles facilitate the electron transfer from the atomic Fe sites in the outer carbon layers to O<sub>2</sub>, or similarly in our case, to CO<sub>2</sub>. This hypothesis finds support in a Tafel-plot analysis (Figure 6b), where NC exhibits a slope of 431 mVdec<sup>-1</sup> while it is as low as 181 mVdec<sup>-1</sup> for Fe–NC. The smaller Tafel slope in the latter case suggests that Fe–NC features much more favorable kinetics for the conversion of CO<sub>2</sub> to CO than NC.<sup>[9a]</sup>

Table 1 compares the performance of Fe–NC with that of other carbon materials containing only atomic Fe sites. As it turns out, our Fe–NC exhibits the highest selectivity for CO production at an overpotential comparable to that of the other materials, while  $|j|$  of Fe–NC is comparable or 2–3 times lower. Note that the surface concentration of atomic Fe sites ( $C_{Fe}$ ) for previously reported materials is at least 10–200 times larger. When these numbers are translated into turnover frequency (TOF), Fe–NC shows a TOF that is 1–2 orders of magnitude higher than the other materials. This implies that the intrinsic activity per atomic Fe site in Fe–NC is much higher.

It is important to consider that  $FE_{CO}$ ,  $\eta$ , and  $|j|$  can be affected by a number of other factors, such as the exposure of active sites, mass transport, and effect coming from other dopants. Since the reported materials exhibit comparable surface areas (0.34–1.01 times as large as that of Fe–NC) and double layer capacities (0.65–1.24 times as large as that of Fe–NC), the exposure of the active Fe sites should be comparable. Likewise, the mass transport should be comparable, taking into account that the electrolysis is performed under similar conditions in H-cells using relatively small values of  $|j|$ . This supports the conclusion that the encased Fe<sub>3</sub>C nanoparticles, as a different type of dopants, possess the ability to boost the activity of atomic Fe sites for eCO<sub>2</sub>RR.

Finally, we tested the potential of the material for future practical applications. Fe–NC was deposited on a gas diffusion electrode with a loading of 2 mg cm<sup>-2</sup>, and electrolysis was performed in a flow cell configuration at

various potentials (Figures 6c and S10). Both the current density and the selectivity for CO were significantly improved compared to the H-cell experiments, likely due to the overcoming of the CO<sub>2</sub> mass transport limitation.<sup>[26]</sup> In these conditions, a high selectivity ( $FE_{CO} > 93\%$ ) for the CO<sub>2</sub>-to-CO conversion was achieved in an even wider potential range (from –0.47 to –1.07 V vs. RHE). Notably, a partial current density for CO production of 33.5 mA cm<sup>-2</sup> was measured with a selectivity of 93% at –1.07 V vs. RHE ( $\eta = 960$  mV). These performances highlight the high potential of the Fe–NC material for future applications.

## Conclusion

We have developed a novel eCO<sub>2</sub>RR catalyst consisting of Fe<sub>3</sub>C nanoparticles encapsulated in a carbon material containing a trace amount of atomic Fe sites. The catalyst was prepared by direct pyrolysis of a porous polycarbazole in the presence of iron chloride used to form the polymer. The target Fe–NC catalyst exhibits remarkably high activity and selectivity for eCO<sub>2</sub>RR compared with the Fe<sub>3</sub>C-free NC material. We suggest that the trace amount of atomic Fe sites in the carbon layers is responsible for the reduction of CO<sub>2</sub>, whereas the inner Fe<sub>3</sub>C nanoparticles – although not in direct contact with the electrolyte and CO<sub>2</sub> – promote CO<sub>2</sub> reduction on the atomic Fe sites. This leads to the accomplishment of a high current density (33.5 mA cm<sup>-2</sup>) and selectivity (93%) for the CO<sub>2</sub>-to-CO conversion in water in a flow cell electrolyzer, showing the potential of Fe–NC for practical applications. Producing active carbon materials from intrinsically porous polymers and exploiting the Fe<sub>3</sub>C-enhanced activity for catalytic CO<sub>2</sub> conversion are expected to pave new avenues for the development of high-performance electrocatalysts comprising earth-abundant elements. Even so, continuous efforts are needed to expand the

**Table 1.** Comparison of the catalytic performance of the Fe–NC material and other carbon materials containing atomic Fe sites for electrochemical CO<sub>2</sub>-to-CO conversion.

Material	Cathode material	Electrolyte	$C_{Fe}^{[a]}$ [nmol cm <sup>-2</sup> ]	$FE_{CO}^{[b]}$ [%]	$\eta^{[c]}$ [mV]	$ j ^{[d]}$ [mA cm <sup>-2</sup> ]	TOF <sup>[e]</sup> [s <sup>-1</sup> ]	$S_{BET}^{[f]}$ [m <sup>2</sup> g <sup>-1</sup> ]	$C_{dl}^{[g]}$ [mF cm <sup>-2</sup> ]	Ref.
atomic Fe	glassy carbon	0.1 M KHCO <sub>3</sub>	843	~80	390	~2.5	~0.01	340	N/A	[7c]
atomic Fe	carbon paper	0.1 M NaHCO <sub>3</sub>	268	91	490	4.5	0.08	N/A	N/A	[7a]
atomic Fe	N/A	0.1 M KHCO <sub>3</sub>	235	65	440	~4.5	~0.06	724	67	[7d]
atomic Fe	carbon paper	0.1 M KHCO <sub>3</sub>	49.2	93	470	2.8	0.27	646	N/A	[27]
atomic Fe	glassy carbon	0.5 M KHCO <sub>3</sub>	35.8	85	360	1.5	0.18	742	47	[7b]
atomic Fe	carbon paper	0.1 M KHCO <sub>3</sub>	115	87	380	1.3	0.05	N/A	N/A	[28]
atomic Fe	carbon paper	0.5 M KHCO <sub>3</sub>	300	95	360	20	0.33	772	35	[7e]
atomic Fe	carbon paper	0.5 M KHCO <sub>3</sub>	71.6	95	390	2.8	0.19	1014	N/A	[29]
Fe–NC	glassy carbon	0.5 M KHCO <sub>3</sub>	< 4.1 <sup>[h]</sup>	98	410	1.4	> 1.73	1001	54	This work

[a] Molar concentration of atomically dispersed Fe sites on an electrode calculated with the formula  $C_{Fe} = \xi \times C_{mat} / 55.85$ , where  $C_{mat}$  is the mass concentration of the material on an electrode and  $\xi$  is the weight percentage of the Fe sites in the material. [b] Maximum  $FE_{CO}$  under reported conditions. [c] Overpotential at which the maximum FE is achieved. [d] Current density achieved at the listed  $\eta$ . [e] TOF is calculated from the equation  $TOF = (|j| \times FE_{CO}) / (n \times F \times C_{Fe})$ , where  $n = 2$  is the number of electrons transferred for the CO<sub>2</sub>-to-CO conversion, and  $F = 96485$  C mol<sup>-1</sup> (Faraday's constant). [f] Specific surface area calculated according to the Brunauer–Emmett–Teller (BET) theory. [g] Double layer capacitance. [h] The overwhelming majority of the Fe species in Fe–NC is from encased Fe<sub>3</sub>C. Considering that the atomic Fe sites on the outer carbon layers are not detectable by XPS, with the detection limit being 0.01 at %, <sup>[18]</sup> it is reasonable to assume that the content of atomic Fe in Fe–NC is < 0.01 at %. This can further be translated to a molar concentration of atomic Fe sites on the electrode that is < 4.1 nmol cm<sup>-2</sup>.

understanding of the effect of the dimensions and distribution of Fe<sub>3</sub>C on the catalysis.

## Experimental Section

### Synthesis of materials

**Chemicals.** Anhydrous iron(III) chloride and trifluoroacetic acid were purchased from Riedel-de Haen and Iris Biotech GmbH, respectively. 1,3,5-Tris(*N*-carbazolyl)benzene, Nafion solution (5 wt%), potassium bicarbonate, and the solvents were purchased from Sigma-Aldrich.

**Synthesis of polycarbazole.** Anhydrous iron(III) chloride (282 mg, 1.74 mmol) was suspended in the mixture of dichloromethane (5 mL) and trifluoroacetic acid (0.75 mL). To the above suspension, a solution of 1,3,5-tris(*N*-carbazolyl)benzene (100 mg, 0.17 mmol) in dichloromethane (10 mL) was added dropwise. The mixture was stirred at room temperature under an Ar atmosphere for 20 h and quenched by addition of methanol (5 mL). After filtration, the resulting solid was stirred in 0.5 M H<sub>2</sub>SO<sub>4</sub> at 90 °C for 4 h to remove residual iron chloride. The solid was filtered, washed with deionized water, methanol, and dichloromethane, and dried in vacuum, successively. Finally, yellowish polycarbazole (99 mg) was obtained in a nearly quantitative yield.

**Synthesis of NC.** The isolated polycarbazole was heated to 1000 °C at a ramping speed of 20 °C min<sup>-1</sup> and kept at 1000 °C for 1 h under an Ar atmosphere. Subsequently, the material was stirred in 0.5 M H<sub>2</sub>SO<sub>4</sub> at 90 °C. A second pyrolysis was applied under the same conditions as before to give the target NC material (71 mg) in a 71% yield, calculated relative to the amount used of the organic monomer, i.e. 1,3,5-tris(*N*-carbazolyl)benzene.

**Synthesis of Fe–NC.** Anhydrous iron(III) chloride (282 mg, 1.74 mmol) was suspended in the mixture of dichloromethane (5 mL) and trifluoroacetic acid (0.75 mL). To the above suspension a solution of 1,3,5-tris(*N*-carbazolyl)benzene (100 mg, 0.17 mmol) in dichloromethane (10 mL) was added dropwise. The mixture was stirred at room temperature under an Ar atmosphere for 20 h and quenched by addition of methanol (5 mL). After evaporation of the solvent on a rotary evaporator and subsequently under vacuum at 60 °C for 2 h, the mixture containing the polymer and the iron salt was heated up to 1000 °C at a ramping speed of 20 °C min<sup>-1</sup>. It was kept at 1000 °C for 1 h under an Ar atmosphere. The iron-based particles were washed away in 0.5 M H<sub>2</sub>SO<sub>4</sub> at 90 °C. Finally, a second pyrolysis was applied under the same conditions as before to give the target Fe–NC material (74 mg) in a 74% yield, calculated relative to the amount used of the organic monomer, i.e. 1,3,5-tris(*N*-carbazolyl)benzene.

### Materials characterization

X-ray photoelectron spectroscopy (XPS) was performed on a Kratos Axis Ultra-DLD instrument equipped with a monochromatic Al<sub>Kα</sub> X-Ray source at the power of 150 W. The spectra were recorded with 2 scans accumulation for survey and 4 scans for N 1s spectra at a pass energy of 20 eV. Powder X-ray Diffraction (PXRD) was carried out on a Rigaku SmartLab X-ray diffractometer using a monochromatic Cu<sub>Kα1</sub> radiation ( $\lambda = 1.54056 \text{ \AA}$ ). The sample was ground before measurement. X-ray absorption spectra (XAS) were collected at the LUCIA beamline Synchrotron SOLEIL with a ring energy of 2.75 GeV and a current of 490 mA. The energy was monochromatized by means of a Si 311 double crystal monochromator. Data were recorded in a primary vacuum chamber as fluorescence spectra with an outgoing angle of 10° using a Bruker silicon drift

detector. The data were normalized to the intensity of the incoming incident energy and processed with the Athena software from the IFEFFIT package. An  $E_0$  value of 7112 eV was used for the iron K-edge energy which was measured at the first inflection point. Inductively coupled plasma–optical emission spectroscopy (ICP–OES) was conducted at an AMETEK Spectro Arcos FHS 12 instrument. Prior to the measurement, the Fe–NC material was treated in a plasma-pure concentrated HNO<sub>3</sub> solution at 75 °C for 5 h.

Transmission electron microscopy (TEM) and energy-dispersive X-ray spectroscopy (EDX) were performed on a FEI Talos F200X instrument with an XFEI source at 200 kV. TEM images were recorded in bright field, while the EDX mapping recorded in high-angle annular dark field. Before the measurement, the Fe–NC material was dispersed in methanol by sonication and drop casted onto a lacey carbon film supported on copper grids.

Nitrogen sorption measurements were carried out on an Autosorp iQ from Quantachrome Instruments at 77 K in liquid nitrogen. Prior to the measurement, the materials were degassed at 120 °C in vacuo for 8 h. The adsorption isotherm was evaluated to provide the porosity parameters. The specific surface area was calculated according to the Brunauer-Emmett-Teller (BET) theory in the relative pressure range of 0.01–0.1. The pore size distribution was estimated based on the quenched solid density functional theory (QSDFT), taking into account the presence of various pore shapes, including spherical, cylindrical, and slit-like pores.

### Electrochemical study in the batch cell

Glassy carbon plates (GCPs, supplied by Sigradur G, HTW) were cleaned by sonication in water and acetone, and used as working electrodes. Catalyst ink was prepared by sonication of a mixture of Fe–NC (6 mg), water (450  $\mu\text{L}$ ), isopropanol (90  $\mu\text{L}$ ), and Nafion (60  $\mu\text{L}$ ) for 15 min. A volume of 50  $\mu\text{L}$  of the ink was drop casted on each side of a GCP (in total 100  $\mu\text{L}$  covering 2 cm<sup>2</sup> on both sides) and thoroughly dried in a fume hood, providing the working electrode with a loading of 0.5 mg cm<sup>-2</sup> of Fe–NC material on surface.

Controlled potential electrolysis was performed in an H-cell with the two chambers separated by a glass frit and using a CHI 601D potentiostat. The cathodic compartment contained a GCP coated with the Fe–NC material as working electrode and a Ag/AgCl (ElectroCell LF-1) as reference electrode. The anodic compartment had a platinum mesh as counter electrode. For short-term (15 min) electrolysis, the electrolyte was saturated with CO<sub>2</sub> and sealed for electrolysis at the pre-set conditions under stirring conditions. In poisoning experiments, 30 mM KCN was added to the cathodic compartment. The gases in the headspace were then analyzed on an Agilent Technologies 7890B gas chromatography system equipped with a thermal conductivity detector (TCD). For long-term (12 h) electrolysis, the electrolyte was saturated with CO<sub>2</sub> prior to start. During electrolysis, CO<sub>2</sub> was bubbled to the cathodic solution at a rate of 10 sccm at room temperature and under ambient pressure. The outlet gas containing products was sampled every 30 min by an Agilent gas sampling valve connected to the inlet system of the same Agilent gas chromatography. Prior to recording the electrolysis data at the stated potential, the Fe–NC material was activated by applying a potential (–0.57 V vs. RHE) for 15 min to remove adsorbed oxygen or other reducible species in the pore structure. Linear sweep voltammograms were recorded on the same potentiostat in a one-chamber cell using the same working and reference electrodes and a Pt wire as counter electrode. The potential measured against Ag/AgCl was converted to the reversible hydrogen electrode (RHE) using the formula:  $E(\text{vs. RHE}) = E(\text{vs.}$

Ag/AgCl) + 0.197 V + RT/F × ln10 × pH = E(vs. Ag/AgCl) + 0.63 V. The supporting electrolyte was aqueous 0.5 M KHCO<sub>3</sub> solution with pH = 7.3 when saturated with CO<sub>2</sub>.

### Electrochemical study in the flow cell

The catalyst ink was prepared by sonicating 6 mg Fe–NC and 60 μL Nafion 117 solution (Sigma, 5 wt% in a mixture of lower aliphatic alcohols and water) in a solution of 900 μL water and 180 μL isopropanol for 10 min. Then, 95 μL of the ink was drop-casted on a hydrophobic carbon paper with a microporous layer (Freudenberg paper H23C6) in a fume hood. Once a drop was dried out, another one was added. This process was repeated 4 times to deposit 380 μL of ink corresponding to 2 mg of Fe–NC. The resulting electrode had an area of 1 cm<sup>2</sup> and thus a catalyst loading of 2 mg cm<sup>-2</sup>. Electrolysis (ramping experiments) were performed at varying potentials in CO<sub>2</sub>-saturated 0.5 M KHCO<sub>3</sub> solution. Each step was held at constant potential for 20 min and the products were analyzed after 10 min of electrolysis.

The flow cell electrolyzer (Micro Flow Cell® purchased from Electro-Cell) is composed of a sandwich of flow frames, electrodes, gaskets, and a membrane, which, when assembled as illustrated in Figure S10, constitutes a three-compartment flow cell. One compartment delivers the CO<sub>2</sub> (at 20 sccm) from the back side and through the gas diffusion electrode (GDE, 1 × 1 cm<sup>2</sup>, fixed in a Titanium frame), while another directs the catholyte solution (0.5 M KHCO<sub>3</sub>, flow rate = 16 sccm) in between the GDE and the anion exchange membrane (AEM, Sustainion X37-50). On the other side of the AEM, the anolyte (0.5 M KHCO<sub>3</sub>, flow rate = 16 sccm) is directed between the AEM and the Pt/Ti alloy anode. The flow frames are made of PTFE, and the gaskets of peroxide cured ethylene propylene diene monomer (EPDM) rubber. Catholyte and anolyte were recycled using peristaltic pumps. All tubing was made of PTFE and connected to the cell with polyether ether ketone (PEEK) ferrules and fittings.

### Acknowledgements

We are grateful for financial support from the Danish National Research Foundation (grant no. DNRF118). We are grateful to the France Canada Research Fund (New Scientific Collaboration Support Program) and Institut Universitaire de France (IUF) for partial financial support. SOLEIL and the MiChem LABEX (Sorbonne Université) are acknowledged for a Ph.D. fellowship to D.M. We thank Dr. Marcel Ceccato and Dr. Paolo Lamagni for their kind help with TEM, EDX, and XRD measurements

### Conflict of Interest

The authors declare no conflict of interest.

**Keywords:** CO<sub>2</sub> reduction · electrocatalysis · iron · nanoparticles · porous polymers

- [1] G. Notton, M.-L. Nivet, C. Voyant, C. Paoli, C. Darras, F. Motte, A. Fouillo, *Renewable Sustainable Energy Rev.* **2018**, *87*, 96–105.  
 [2] a) D. T. Whipple, P. J. A. Kenis, *J. Phys. Chem. Lett.* **2010**, *1*, 3451–3458; b) D. M. Weekes, D. A. Salvatore, A. Reyes, A. X. Huang, C. P. Berlin-

- guette, *Acc. Chem. Res.* **2018**, *51*, 910–918; c) T. Haas, R. Krause, R. Weber, M. Demler, G. Schmid, *Nat. Can.* **2018**, *1*, 32–39; d) D. U. Nielsen, X.-M. Hu, K. Daasbjerg, T. Skrydstrup, *Nat. Catal.* **2018**, *1*, 244–254.  
 [3] B. Khezri, A. C. Fisher, M. Pumera, *J. Mater. Chem. A* **2017**, *5*, 8230–8246.  
 [4] a) D. Gao, H. Zhou, J. Wang, S. Miao, F. Yang, G. Wang, J. Wang, X. Bao, *J. Am. Chem. Soc.* **2015**, *137*, 4288–4291; b) M. Liu, Y. Pang, B. Zhang, P. De Luna, O. Voznyy, J. Xu, X. Zheng, C. T. Dinh, F. Fan, C. Cao, F. P. G. de Arquer, T. S. Safaei, A. Mepham, A. Klinkova, E. Kumacheva, T. Filleter, D. Sinton, S. O. Kelley, E. H. Sargent, *Nature* **2016**, *537*, 382–386; c) Z. Cao, S. B. Zacate, X. Sun, J. Liu, E. M. Hale, W. P. Carson, S. B. Tyndall, J. Xu, X. Liu, X. Liu, C. Song, J.-h. Luo, M.-J. Cheng, X. Wen, W. Liu, *Angew. Chem. Int. Ed.* **2018**, *57*, 12675–12679; *Angew. Chem.* **2018**, *130*, 12857–12861.  
 [5] a) J. Wu, R. M. Yadav, M. Liu, P. P. Sharma, C. S. Tiwary, L. Ma, X. Zou, X.-D. Zhou, B. I. Yakobson, J. Lou, P. M. Ajayan, *ACS Nano* **2015**, *9*, 5364–5371; b) P. P. Sharma, J. Wu, R. M. Yadav, M. Liu, C. J. Wright, C. S. Tiwary, B. I. Yakobson, J. Lou, P. M. Ajayan, X.-D. Zhou, *Angew. Chem. Int. Ed.* **2015**, *54*, 13701–13705; *Angew. Chem.* **2015**, *127*, 13905–13909.  
 [6] B. X. Zhang, J. L. Zhang, J. B. Shi, D. X. Tan, L. F. Liu, F. Y. Zhang, C. Lu, Z. Z. Su, X. N. Tan, X. Y. Cheng, B. X. Han, L. R. Zheng, *J. Zhang, Nat. Commun.* **2019**, *10*, 2980.  
 [7] a) T. N. Huan, N. Ranjbar, G. Rouse, M. Sougrati, A. Zitolo, V. Mougél, F. Jaouen, M. Fontecave, *ACS Catal.* **2017**, *7*, 1520–1525; b) X.-M. Hu, H. H. Hval, E. T. Bjerglund, K. J. Dalgaard, M. R. Madsen, M.-M. Pohl, E. Welter, P. Lamagni, K. B. Buhl, M. Bremholm, M. Beller, S. O. Pedersen, T. Skrydstrup, K. Daasbjerg, *ACS Catal.* **2018**, *8*, 6255–6264; c) A. S. Varela, N. R. Sahaie, J. Steinberg, W. Ju, H.-S. Oh, P. Strasser, *Angew. Chem. Int. Ed.* **2015**, *54*, 10758–10762; *Angew. Chem.* **2015**, *127*, 10908–10912; d) W. Ju, A. Bagger, G.-P. Hao, A. S. Varela, I. Sinev, V. Bon, B. Roldan Cuenya, S. Kaskel, J. Rossmel, P. Strasser, *Nat. Commun.* **2017**, *8*, 944; e) J. Gu, C.-S. Hsu, L. Bai, H. M. Chen, X. Hu, *Science* **2019**, *364*, 1091–1094.  
 [8] a) Y. Pan, R. Lin, Y. Chen, S. Liu, W. Zhu, X. Cao, W. Chen, K. Wu, W.-C. Cheong, Y. Wang, L. Zheng, J. Luo, Y. Lin, Y. Liu, C. Liu, J. Li, Q. Lu, X. Chen, D. Wang, Q. Peng, C. Chen, Y. Li, *J. Am. Chem. Soc.* **2018**, *140*, 4218–4221; b) X. Wang, Z. Chen, X. Zhao, T. Yao, W. Chen, R. You, C. Zhao, G. Wu, J. Wang, W. Huang, J. Yang, X. Hong, S. Wei, Y. Wu, Y. Li, *Angew. Chem. Int. Ed.* **2018**, *57*, 1944–1948; *Angew. Chem.* **2018**, *130*, 1962–1966.  
 [9] a) X. Li, W. Bi, M. Chen, Y. Sun, H. Ju, W. Yan, J. Zhu, X. Wu, W. Chu, C. Wu, Y. Xie, *J. Am. Chem. Soc.* **2017**, *139*, 14889–14892; b) H. B. Yang, S.-F. Hung, S. Liu, K. Yuan, S. Miao, L. Zhang, X. Huang, H.-Y. Wang, W. Cai, R. Chen, J. Gao, X. Yang, W. Chen, Y. Huang, H. M. Chen, C. M. Li, T. Zhang, B. Liu, *Nat. Energy* **2018**, *3*, 140–147; c) K. Jiang, S. Siahrostami, T. Zheng, Y. Hu, S. Hwang, E. Stavitski, Y. Peng, J. Dynes, M. Gangisetty, D. Su, K. Attenkofer, H. Wang, *Energy Environ. Sci.* **2018**, *11*, 893–903.  
 [10] F. Yang, P. Song, X. Liu, B. Mei, W. Xing, Z. Jiang, L. Gu, W. Xu, *Angew. Chem. Int. Ed.* **2018**, *57*, 12303–12307; *Angew. Chem.* **2018**, *130*, 12483–12487.  
 [11] <https://www.acs.org/content/acs/en/greenchemistry/research-innovation/endangered-elements.html#table>.  
 [12] a) Y. Cheng, S. Zhao, B. Johannessen, J.-P. Veder, M. Saunders, M. R. Rowles, M. Cheng, C. Liu, M. F. Chisholm, R. Marco, H.-M. Cheng, S.-Z. Yang, S. P. Jiang, *Adv. Mater.* **2018**, *30*, 1706287; b) Q. Yang, C.-C. Yang, C.-H. Lin, H.-L. Jiang, *Angew. Chem. Int. Ed.* **2019**, *58*, 3511–3515; *Angew. Chem.* **2019**, *131*, 3549–3553.  
 [13] Q. Chen, M. Luo, P. Hammershøj, D. Zhou, Y. Han, B. W. Laursen, C. G. Yan, B. H. Han, *J. Am. Chem. Soc.* **2012**, *134*, 6084–6087.  
 [14] A. A. O. Sarhan, C. Bolm, *Chem. Soc. Rev.* **2009**, *38*, 2730–2744.  
 [15] X. K. Pei, Y. F. Chen, S. Q. Li, S. H. Zhang, X. Feng, J. W. Zhou, B. Wang, *Chin. J. Chem.* **2016**, *34*, 157–174.  
 [16] X.-M. Hu, Q. Chen, Z.-Y. Sui, Z.-Q. Zhao, N. Bovet, B. W. Laursen, B.-H. Han, *RSC Adv.* **2015**, *5*, 90135–90143.  
 [17] Y. Hu, J. O. Jensen, W. Zhang, L. N. Cleemann, W. Xing, N. J. Bjerrum, Q. Li, *Angew. Chem. Int. Ed.* **2014**, *53*, 3675–3679; *Angew. Chem.* **2014**, *126*, 3749–3753.  
 [18] A. G. Shard, *Surf. Interface Anal.* **2014**, *46*, 175–185.  
 [19] a) C. Lu, J. Yang, S. Wei, S. Bi, Y. Xia, M. Chen, Y. Hou, M. Qiu, C. Yuan, Y. Su, F. Zhang, H. Liang, X. Zhuang, *Adv. Funct. Mater.* **2019**, *29*, 1806884; b) C. Hu, S. Bai, L. Gao, S. Liang, J. Yang, S.-D. Cheng, S.-B. Mi, J. Qiu, *ACS Catal.* **2019**, *9*, 11579–11588.  
 [20] K. Yuan, S. Sfaelou, M. Qiu, D. Lützenkirchen-Hecht, X. Zhuang, Y. Chen, C. Yuan, X. Feng, U. Scherf, *ACS Energy Lett.* **2018**, *3*, 252–260.  
 [21] a) H. Li, N. Xiao, M. Hao, X. Song, Y. Wang, Y. Ji, C. Li, C. Li, Z. Guo, F. Zhang, J. Qiu, *Chem. Eng. J.* **2018**, *351*, 613–621; b) C. Li, Y. Wang, N.



- Xiao, H. Li, Y. Ji, Z. Guo, C. Liu, J. Qiu, *Carbon* **2019**, *151*, 46–52; c) H. Zhang, J. Li, S. Xi, Y. Du, X. Hai, J. Wang, H. Xu, G. Wu, J. Zhang, J. Lu, J. Wang, *Angew. Chem. Int. Ed.* **2019**, *58*, 14871–14876; *Angew. Chem.* **2019**, *131*, 15013–15018.
- [22] Y. Li, W. Zhou, H. Wang, L. Xie, Y. Liang, F. Wei, J.-C. Idrobo, S. J. Pennycook, H. Dai, *Nat. Nanotechnol.* **2012**, *7*, 394–400.
- [23] M. S. Thorum, J. M. Hankett, A. A. Gewirth, *J. Phys. Chem. Lett.* **2011**, *2*, 295–298.
- [24] H. W. Liang, S. Brüller, R. H. Dong, J. Zhang, X. L. Feng, K. Müllen, *Nat. Commun.* **2015**, *6*, 7992.
- [25] a) W.-J. Jiang, L. Gu, L. Li, Y. Zhang, X. Zhang, L.-J. Zhang, J.-Q. Wang, J.-S. Hu, Z. Wei, L.-J. Wan, *J. Am. Chem. Soc.* **2016**, *138*, 3570–3578; b) D. Deng, L. Yu, X. Chen, G. Wang, L. Jin, X. Pan, J. Deng, G. Sun, X. Bao, *Angew. Chem. Int. Ed.* **2013**, *52*, 371–375; *Angew. Chem.* **2013**, *125*, 389–393.
- [26] S. Ren, D. Joulié, D. Salvatore, K. Torbensen, M. Wang, M. Robert, C. P. Berlinguette, *Science* **2019**, *365*, 367–369.
- [27] F. Pan, H. Zhang, K. Liu, D. Cullen, K. More, M. Wang, Z. Feng, G. Wang, G. Wu, Y. Li, *ACS Catal.* **2018**, *8*, 3116–3122.
- [28] F. P. Pan, W. Deng, C. Justiniano, Y. Li, *Appl. Catal. B* **2018**, *226*, 463–472.
- [29] Z. Zhang, C. Ma, Y. Tu, R. Si, J. Wei, S. Zhang, Z. Wang, J.-F. Li, Y. Wang, D. Deng, *Nano Res.* **2019**, *12*, 2313–2317.

---

Manuscript received: May 23, 2020

Accepted manuscript online: July 16, 2020

Version of record online: September 9, 2020